Salisbury, M.H., Shinohara, M., Richter, C., et al., 2002
Proceedings of the Ocean Drilling Program, Initial Reports Volume 195

4. Site 1201[1]

Shipboard Scientific Party[2]

PRINCIPAL RESULTS

The primary objective at Site 1201 was to drill a cased reentry hole into basement and install a broadband seismic observatory with a battery assembly and data-recording unit. There were also numerous ancillary scientific goals related to cores or wireline logs obtained at the proposed drill site. We hoped to address the following topics: geochemistry, age and isotopic characteristics of the upper ocean crust, Pacific plate paleolatitude and tectonic drift, and Tertiary climate, sedimentation, and ash deposition. The sediment column and igneous basement at Site 1201 were cored successfully, and the borehole seismometer was emplaced as planned. Consequently, it should be possible to accomplish most of the scientific objectives related to coring and placement of the seismic observatory; many were accomplished during the leg itself. The logging program, however, was seriously curtailed owing to technical difficulties and the collapse of the borehole before the logging program in the lower part of the borehole could be completed.

Drilling at Site 1201 yielded a composite 600-m-thick sedimentary and basaltic section through Miocene to Eocene strata with three major unconformities, between 0 and 5 Ma, 14.8 and 24.1 Ma, and in the top section of Biozone NP24. Holes 1201A, 1201B, and 1201C were cored to a maximum depth of 90 meters below seafloor (mbsf) with the advanced piston corer/extended core barrel (APC/XCB) system and recovered soft pelagic sediments. Hole 1201D was cored with the rotary core barrel (RCB) to 600 mbsf with excellent recovery (78%). Hole 1201E consists of a cased reentry hole with the seismometer instrumentation cemented into the basaltic basement.

The sedimentary section at Site 1201 consists of two lithostratigraphic units. The uppermost unit (0–53 mbsf) consists of clays, cherts, and interbedded sandstones and silty claystones that contain a significant red clay content. The underlying unit (53–509 mbsf) is composed

[1]Examples of how to reference the whole or part of this volume.
[2]Shipboard Scientific Party addresses.

Ms 195IR-104

of interbedded dark gray and dark green to gray-green sandstone and silty claystone with breccia and claystone. These sediments are composed of detrital volcaniclastic material from the Palau-Kyushu Ridge that has been reworked by turbidity currents. Turbidites exhibit a downhole trend from high-energy to low-energy turbidites. Changes in sediment supply, basin slope gradient, proximity to the source arc, tectonics (uplift and volcanism), erosion, and sea level could be responsible, in whole or part, for the change in the energetics of the turbidity currents. The diagenetic history is documented by changes in clay mineral and zeolite assemblages with depth that are consistent with changes in pore water composition. A 2.5-m-thick marine claystone is present immediately above the basaltic basement contact at 509 mbsf.

Basement rocks consist of highly altered basaltic pillow lavas. Glassy pillow margin rims are observed in the core, along with hyaloclastite intervals. The rocks are aphyric to moderately plagioclase phyric in discrete intervals. Hypocrystalline rocks are most abundant in the upper part of the core but decrease with depth, correlating with the degree of alteration, which is very high in the upper tens of meters and gradually decreases in the lower part of the core. Alteration products are mainly clay minerals and zeolites in addition to minor carbonate. The original mineralogy consists of plagioclase, clinopyroxene in variable amounts increasing with depth, olivine, and opaque minerals. Preliminary geochemical data suggest a strong arc affinity.

The topmost (0–29 mbsf) and the lowermost (462–509 mbsf) sections are barren of nannofossils. Moderately to poorly preserved nannofossils in the middle section allowed us to recognize six biozones spanning Zones NP19/NP20 to NP25. The turbidites between 53 and 462 mbsf represent an expanded sequence of late Eocene to late Oligocene age. Separated by a short hiatus and lying on top of the turbidites is a 25-m-thick sequence of upper Oligocene (NP25) red claystone. The age of the sediments directly above the basement contact is unknown. Compared to Deep Sea Drilling Project (DSDP) drilling results at Sites 290 and 470, the Eocene sediments (>34.3 Ma) recovered at this site are the oldest so far identified on the sedimentary apron of the Palau-Kyushu Ridge.

Preliminary interpretation of the magnetic inclination record identified 64 reversals of the geomagnetic polarity timescale (GPTS). The top 29 mbsf provides a complete record from the Thvera Subchron (C3n.4n) through late and middle Miocene polarity intervals to Subchron C5Bn.1n, close to the base of the middle Miocene. Strata from the last 5 m.y. are apparently missing at Site 1201. The magnetic inclination record in the RCB section of the turbidite interval between 100 and 500 mbsf defines several long normal and reversed polarity chrons (C12n–C16n.2n) that are well constrained by biostratigraphic ages. Sedimentation rates decreased through time from the late Eocene–Oligocene (100 m/m.y.) to the Miocene–early Pliocene (3 m/m.y.) and reflect the tectonic and environmental history of the West Philippine Basin in the vicinity of the Palau-Kyushu Ridge. Magnetic inclinations in the basaltic basement are shallow and indicate a position of the Philippine plate near the equator at ~7° paleolatitude during the middle Eocene.

The composition of interstitial water at Site 1201 is quite unusual for deep-sea sediments and reflects profound diagenesis of the reworked volcaniclastic material that comprises the lower 350 m of the section. Most of the volcaniclastics have been replaced by clays and zeolites (smectite, heulandite/clinoptilolite, analcime/wairakite, erionite, and chabazite). The most unusual feature is an extremely large increase in

pH, Ca, and chlorinity; whereas seawater is mainly a sodium chloride solution, this altered seawater contains mainly calcium chloride. Calcium increases to 270 mmol/kg, 27 times the concentration in seawater, by leaching from the volcaniclastic material. Chlorinity increases to 645 mmol/kg, 20% higher than the seawater value, by loss of water of hydration to the altered tuffs. The gain in Ca is balanced by a loss of nearly all the Mg and K from the seawater, but mainly by a 70% decrease in Na to 140 mmol/kg. Sulfate decreases as well, from 28 to 15 mmol/kg, by precipitation of gypsum in response to the elevated Ca concentration. Alkalinity falls from the seawater value of 2.4 to <1 meq/kg as it is consumed by precipitation of authigenic minerals. The rise in pH to 10.0 from the seawater value of ~8.1 likewise reflects extreme alteration at the in situ temperatures of 10°C or less.

The results of the multisensor track (MST) measurements showed significant variation in the physical properties of the three main lithostratigraphic units. These measurements show a correlation to individual sequences of turbidites and may provide scaling laws that could be used to characterize the turbidites and constrain depositional environments.

Hole 1201D was logged with the triple combination (triple combo) tool from 80 mbsf to total depth (TD) and with the Formation MicroScanner (FMS)/sonic tool from 80 to 366 mbsf. During the first run, hole conditions appeared to be good in the basement and sedimentary section with the exception of a few tight spots below bit size. Two logging units that correspond to the turbidite sequence and the basaltic basement can be distinguished. The logs show no apparent trends with depth other than a significant step at the contact between the sediment and the basaltic basement. Within the turbiditic sedimentary sequence, fining-upward cycles, which correlate well with the sedimentological description of the cores, can be discerned. It is an important result for the seismometer installation that the basement section is relatively homogenous and shows a slight increase in resistivity and a decrease in gamma ray values with depth, which may indicate a trend toward slightly less altered material.

BACKGROUND AND OBJECTIVES

Seismic Considerations

Site 1201 was devoted to coring and casing a hole in the seafloor at abyssal depths in the Philippine Sea to install a broadband seismometer for a long-term subseafloor borehole observatory. Because the observatory is an important component of the International Ocean Network (ION) seismometer network, the location of the site was dictated primarily by seismic considerations.

The first of these considerations is largely geographic. One of the greatest problems facing seismologists who use teleseismic waves to study the structure and dynamics of the Earth's interior is the uneven distribution of seismic stations, especially the lack of stations in large expanses of ocean such as the Pacific. A global seismic network with at least one seismic observatory every 2000 km is required in the northwestern Pacific to achieve homogeneous coverage of the Earth's surface. One of the most significant gaps in this coverage lies in the center of the Philippine Sea. A major objective of the ION project was to fill this gap by installing a seafloor seismic observatory in the West Philippine

Basin west of the Kyushu-Palau Ridge between existing stations at Ishigaki (ISG) and Baguio (BAG) to the west, Inuyama (INU) and Taejon (TJN) to the north, Minami Torishima (MCSJ) and Chichijima (OGS) to the east, and Pohnpei (PATS) and Jayapura (JAY) to the south (Fig. F1).

A second seismic consideration is to improve the resolution of tomographic imaging of the Mariana subduction zone by placing an observatory in the middle of the Philippine Sea on the overriding plate behind the subduction zone. There are indications that the subducting Pacific plate does not penetrate below the 670-km discontinuity and that it extends horizontally (Fukao et al., 1992; Fukao, 1992), but the resolution of these studies is poor (>1000 km) beneath the Philippine Sea and the northwestern Pacific, especially in the upper mantle. A seismometer at Site 1201 will be crucial to determining whether the Pacific plate is penetrating into the lower mantle in the Mariana Trench but not in the Izu-Ogasawara Trench (van der Hilst et al., 1991; Fukao et al., 1992; van der Hilst and Seno, 1993). In addition, the site will allow imaging of the subducting slab to determine how the stagnant slab eventually sinks into the lower mantle (Ringwood and Irifune, 1988). Better maps of the geometry of the subducting plate and patterns of mantle flow are essential to understanding the dynamics of the mantle and mechanisms of backarc spreading.

Finally, a quiet seafloor observatory at Site 1201 will make it possible to study differences in plate structure under the Philippine Sea and its subbasins (e.g., the Philippine, Shikoku, Japan, and Parece Vela Basins) using surface and body waves. Previous studies with limited resolution in the area suggest that the plate is only ~30 km thick (Kanamori and Abe, 1968; Seekins and Teng, 1977), but this is inconsistent with age vs. heat flow and depth curves (Louden, 1980), and a long-line (500 km) seismic refraction experiment in the West Philippine Basin failed to image the lithosphere/asthenosphere boundary (Goodman and Bibee, 1991).

The site chosen for the seismometer installation is located in the West Philippine Basin ~100 km west of the inactive Kyushu-Palau Ridge and 450 km north of the extinct Central Basin Fault (Fig. F2). Early interpretations of magnetic lineations (Hilde and Lee, 1984) indicate that the site lies on 49-Ma crust near Chron 21 and formed by northeast-southwest spreading on the Central Basin Fault. The spreading direction then changed to north-south at ~45 Ma, and spreading finally ceased at ~35 Ma. Because the earliest magnetic anomalies in the region predate the initiation of subduction at ~45 Ma along the Kyushu-Palau Ridge, Hilde and Lee (1984) considered that the Philippine Sea formed by entrapment of an older Pacific spreading ridge. More recent bathymetric and magnetic surveys (Okino et al., 1999) show that the site lies at the transition from well-defined anomalies south of the Oki-Daito Ridge to more complicated anomalies to the north, which implies that the crust to the north may have formed at a different spreading center.

Site 1201 is located on flat seafloor at a water depth of 5640 m, where the sediments were predicted to be ~400–450 m thick based on recent seismic reflection surveys (Fig. F3) that showed a two-way traveltime to basement of 0.5 s (Fig. F4). Drilling at other sites in the region during DSDP Legs 31 and 59 (Karig, Ingle, et al., 1975; Kroenke, Scott, et al., 1980) recovered a relatively barren, deepwater section dominated by Holocene to Eocene or Paleocene(?) brown pelagic silty clays overlying basement near the Oki-Daito Ridge (DSDP Sites 294 and 295). At DSDP Sites 290 and 447 to the south, the section consists of a barren interval of Pliocene clays underlain by Oligocene nannofossil-bearing silty clays

F1. Seismic station coverage in the northwest Pacific, p. 66.

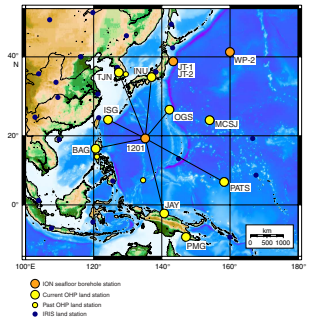

F2. DSDP and ODP sites in the Philippine Sea, p. 67.

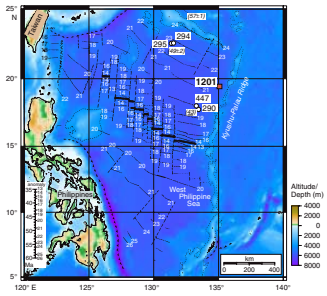

F3. Location of OT97 survey lines, p. 68.

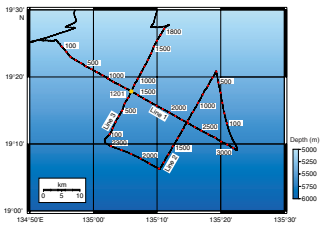

F4. Line OT97 showing the location of Site 1201, p. 69.

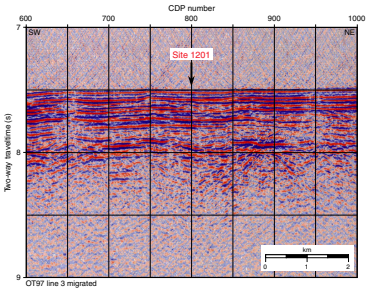

mixed with ash. This was underlain by a thick section of polymict and volcanic breccia presumably derived from the Kyushu-Palau Ridge. The underlying basement consisted of 80% basalt pillows and 20% diabase. Because Site 1201 lies in a similar setting at the foot of the Kyushu-Palau Ridge, it was considered likely that the section would be similar to that at Sites 290 and 447.

Geological Objectives

Although the site was located primarily on the basis of seismic constraints, it was recognized that drilling at Site 1201 would also satisfy many other important geological objectives.

Tertiary Climate Record

Previous drilling in the West Philippine Sea was conducted during DSDP Legs 31 and 59 before the advent of piston coring, and many of the holes were only spot cored. As a consequence, the available core from the region is almost useless for stratigraphic and paleontologic reconstructions. By obtaining a continuous, high-quality record of pelagic sedimentation supplemented by high-quality logs, we hoped to obtain a proxy record of Tertiary climate change for the region. It was anticipated that the upper levels of the section would also contain a record of eolian transport from Eurasia.

Ash Fall Record

Although ash and tuff were present in the sediments recovered in the region during previous legs, it was impossible to reconstruct the ash fall stratigraphy because of core disturbance and the discontinuous nature of the coring. By continuous coring using APC and XCB techniques and correlation with high-resolution FMS and natural gamma spectrometry logs, we hoped to obtain a detailed record of arc volcanism around the Philippine Sea.

Philippine Plate Paleolatitude, Rotation, and Tectonic Drift

Paleomagnetic measurements of sediments and basalt cores are important because oriented samples are difficult to obtain from the oceans. The basalts record the direction of the magnetic field at the time the basalts were emplaced and can be used to infer the paleolatitude of the site (e.g., Cox and Gordon, 1984). Although it was unlikely that enough flow units would be cored at Site 1201 to average secular variation adequately, the results would be useful in determining a Paleogene paleomagnetic pole for the Philippine plate. Sediments are typically a good recorder of the Earth's magnetic field and should contain a continuous record of movement of the Philippine plate through the Cenozoic. By collecting oriented sediment cores, it might be possible to study the rotation of the Philippine plate (Hall et al., 1995) and the initiation of subduction of the Pacific plate.

Age of Basement

Although the age of basement in the northern West Philippine Sea has been estimated from magnetic anomalies, paleontologic confirmation has been imprecise because of spot coring, core disturbance, and

poor preservation of microfossils. By continuous coring to basement using modern coring techniques, we hoped to obtain an accurate basement age from undisturbed microfossils, magnetostratigraphy, or radiometric dating of ash horizons. This information would be of considerable importance in constraining models of backarc spreading.

Basalt Chemistry

Studies of the relationship between mid-ocean-ridge basalt (MORB) chemistry and crustal thickness indicate that the degree of partial melting is strongly controlled by the temperature of the upwelling mantle at the ridge. This means that the temperature of formation and the concentration of major and minor elements in submarine basalts can be estimated from crustal thickness (e.g., Klein and Langmuir, 1987; White and Hochella, 1992). To date, this type of work has been based on the study of young MORBs, and the model has large uncertainties, partly because there are few locations off ridge where rock samples and high-quality seismic data have been collected in the same location. Chemical analysis of the basalts at Site 1201 should provide clues as to why the crust in the Philippine Sea is thinner (3–4 km) than expected and whether it is due to differences in the initial temperature conditions in the lithosphere.

OPERATIONS

Transit to Site 1201 (Proposed Site WP-1B)

The transit to the Guam pilot station covered the 90-nmi distance in just 7.25 hr at an average speed of 12.4 kt. At 0945 hr on 29 March 2001, the *Shamrock* was alongside for a personnel exchange. By 1015 hr, the transfer of all personnel and cargo had been completed and the ship was underway for Site 1201 (proposed Site WP-1B).

During transit in international waters on 30 March at 1900 hr, a poetry reading was held in conjunction with a program sponsored by the United Nations, "Dialogue Among Civilizations." Marine Laboratory Technician Anastasia Ledwon read the poem "Planet Earth" by Marilyn Hacker.

The vessel covered the 652-nmi distance at an average speed of 11.8 kt and arrived at Site 1201 at 1600 hr on 31 March.

Jet-In Testing and Hole 1201A

An APC/XCB bottom-hole assembly (BHA) was assembled, and the vibration-isolated television (VIT) camera was deployed to observe the jet-in test. The seafloor was tagged at 5722.0 meters below rig floor (mbrf) at 0750 hr on 1 April, and jetting continued to a depth of 5762.0 mbrf (40.0 mbsf), where a hard layer prevented further advancement of the jetting assembly. The drill string was pulled out of the hole, and the seafloor was cleared at 1045 hr, ending the jet-in test (see Table T1).

At 1500 hr on 1 April, Hole 1201A was spudded with the APC/XCB. However, the APC shear pins failed prematurely, causing the barrel to fall out under its own weight. With only 1.49 m of recovery, it was decided that another hole should be initiated. Hole 1201A was ended at 1545 hr on 1 April.

T1. Coring summary, Site 1201, p. 189.

Hole 1201B

A problem with the spooling of the coaxial (coax) cable on the winch became apparent during the operations in >5700-m-deep water. Because of the high loads imposed by the deepwater operations at Site 1201, the coax cable was squeezing into the underlying cable wrap at isolated points. This led to uneven spooling and was destined to become further aggravated by each successive layer. Because improper spooling of the cable could lead to internal cable damage and ultimate cable failure, we tried to correct the spooling problem before it became further aggravated.

In an attempt to correct or at least improve the cable spooling situation and avoid or minimize the potential for cable damage, the VIT sleeve was lowered until it came to rest on the drill bit at the end of the BHA. With the core bit ~7 m above the seafloor, the drill ship was offset in dynamic positioning (DP) mode in a constant direction at ~1 kt. Simultaneously, the winch operator played out an additional 125 m of coax cable, letting the cable belly out aft of the ship and then spooled it back on. Cable spooling after this operation was significantly improved; however, the problem still existed to some extent because we were unable to get far enough into the underlying wraps to properly retension the cable.

The vessel was repositioned over the drill site, and Hole 1201B was spudded at 1905 hr on 1 April, establishing a seafloor depth of 5721.3 mbrf. APC coring was initiated and continued through Core 195-1201B-6H to a depth of 46.7 mbsf, where an incomplete stroke on a hard layer signaled the end of piston coring. The XCB core barrel was deployed, and coring continued through Core 195-1201B-11X to a depth of 90.3 mbsf, where coring was terminated because alternating hard and soft turbiditic layers tended to cause jamming in the XCB cutting shoe. Hole 1201B was ended when the drill string cleared the seafloor at 1815 hr on 2 April.

Hole 1201C

The vessel was offset 15 m to the west, and Hole 1201C was spudded at 1935 hr on 2 April. APC coring continued through Core 195-1201C-6H to a depth of 46.7 mbsf. Tensor tool–oriented measurements were taken on Cores 195-1201C-3H through 6H, and Adara temperature measurements were taken on Cores 3H and 5H. The temperature measurement taken on Core 195-1201C-5H was successful; however, the Core 3H measurement recovered no data. The drill string was pulled clear of the seafloor at 0720 hr and was recovered back to the drill ship. The rig floor was cleared, and the vessel was secured for transit by 1715 hr on 3 April.

Deepwater Respooling of Coax Cable

Because of the critical need for the subsea television to achieve the Leg 195 objectives, it was necessary to take steps to correct the deepwater spooling problem. We decided to transit northwest in search of a deepwater pocket on the otherwise relatively flat seafloor. At 1715 hr on 3 April, the ship was under way for a deepwater location identified on the admiralty charts. After failing to locate the desired water depth of >6100 m at our first target location, we continued in a westerly direction to a second target location identified on Japanese hydrographic

charts. After traveling a total of 204 nmi from Site 1201, we located a water depth of 6235.4 mbrf based on a corrected precision depth recorder reading at 20°59.9′N latitude and 133°27.5′E longitude. Deployment of the coax cable to a depth of 6183 m allowed the spooling problems to be corrected and left the coax cable in good condition.

Hole 1201D

At 1715 hr on 4 April, the vessel was in transit back to the drilling location at Site 1201. At 0718 hr on 5 April, the thrusters and hydrophones were lowered and the drill string was tripped to the seafloor. Hole 1201D was spudded at 1630 hr, and a seafloor depth of 5720.0 mbrf was determined. The hole was drilled with a center bit to a depth of 80.4 mbsf where RCB coring was initiated. Coring continued without incident through Core 195-1201D-44R to a depth of 503.3 mbsf. The basement contact was encountered on 9 April while Core 195-1201D-45R was cut at ~510 mbsf. Coring continued in basaltic basement through Core 195-1201D-55R to a depth of 600.0 mbsf.

Logging Operations at Hole 1201D

A wiper trip in preparation for logging up to 80 mbsf and back was uneventful except for a couple of ledges encountered in the basement section of the hole. The hole was displaced with 30 bbl of sepiolite mud, and the pipe was pulled to the logging depth of 80.0 mbsf.

The first run with the triple combo (Lamont-Doherty Earth Observatory temperature/acceleration/pressure [TAP] tool/dual laterolog [DLL]/hostile-environment lithodensity tool/accelerator porosity sonde/hostile-environment natural gamma sonde) reached a depth of 599.0 mbsf. Logging continued up from TD to 450.0 mbsf, where the caliper had to be closed to get through a tight section of hole. When the caliper was closed, current to the DLL tool was lost and logging had to be stopped. Logging was restarted and continued from 415.0 to 120.0 mbsf, where a tight spot directly below the pipe was encountered. The interval from 180.0 to 96.0 mbsf was repeated without incident. The first run was completed and rigged down by 0200 hr on 13 April.

The second tool string run in the hole was the FMS-sonic (micro-electrical scanner tool/long-spaced sonic tool/natural gamma ray spectrometry tool). The tool was lowered until an obstruction that could not be passed was encountered at 355.0 mbsf. Logging continued up to 120.0 mbsf, where the tool was lowered for a second pass. The second pass reached the obstruction at 355.0 mbsf and took another 30 min of working to reach 370.0 mbsf, a gain of 15 m. Logging was then conducted up to the drill pipe at 80.0 mbsf. With the second tool string recovered, rig-down was completed and wireline logging operations were ended at 1330 hr on 13 April.

After completing the wireline logging effort, the pipe could only be lowered an additional 10 m to a depth of 90.0 mbsf before encountering an impassable bridge. At that point, a 15-bbl (50 m) plug of 15.8-pound per gallon (ppg) cement was set to prevent possible future communication with the cased reentry hole and seismometer installation. Upon completion of the cementing operation, the drill string was pulled out of the hole, clearing the seafloor at 1610 hr on 13 April.

Hole 1201E Reentry Cone and Casing Operations

The upper guide horn was laid out, and the reentry cone was moved into position on the moonpool doors. Three joints of 16-in casing were made up with the 16-in casing hanger and latched into the reentry cone. The reentry cone–casing assembly was then lowered to the seafloor, and at 1600 hr on 14 April, Hole 1201E was spudded at 5721.0 mbrf. Ultimately, the reentry cone base was landed at the seafloor and the Drill-Quip (DQ) running tool was released without difficulty at 1830 hr. The 16-in casing shoe was placed at 39.1 mbsf.

At 1945 hr on 15 April, Hole 1201E was reentered and drilling of the 14.75-in hole commenced. Drilling proceeded without incident, and at 0845 hr on 17 April, basement was contacted at a depth of 512.0 mbsf. Basement drilling continued at a slower rate but without difficulty. At 2100 hr on 17 April, drilling was terminated at a depth of 543.0 mbsf (31.0 m into basement).

A wiper trip back to the 16-in casing shoe at 39.1 mbsf was performed. There was no fill identified on the bottom, and the hole was judged to be in excellent condition. The top drive was set back, and the drill string was pulled clear of the reentry cone at 0300 hr on 18 April. Rig-up and running of the 10.75-in casing string went exceptionally well. A total of 43 joints of casing was made up to the casing hanger by 1700 hr on 18 April.

Hole 1201E was reentered for the second time at 0624 hr on 19 April, and the casing string was washed to a depth of 528.7 mbsf, where it landed on the casing hanger. Fifty barrels of 15.8-ppg cement was mixed up and displaced downhole with the mud pumps. The cementing operation was completed, and by 1112 hr the DQ running tool was released. Hole 1201E was reentered again at 1052 hr on 20 April. It took 3.5 hr to drill out the cement and wash to the bottom of the 14.75-in hole at 543.0 mbsf.

At 1645 hr, drilling of the 9.875-in ION installation hole began, and by 1600 hr on 21 April, the hole had reached a total depth of 580.0 mbsf. At 1945 hr on 21 April, the pipe cleared the reentry cone/seafloor, ending the reentry cone/casing/drilling operations at Hole 1201E.

Hole 1201E Seismometer Installation

After laying out the upper guide horn, preparations for deployment of the ION seismometer package began. The instrument carrier was made up to a joint of 4.5-in casing. At 0930 hr on 22 April, the 4.5-in casing and cable deployment operation began. Each joint of 4.5-in casing was run with two electrical cables strapped to the outside and secured with tie wraps and duct tape. Approximately every 1.5 m, a 4.5-in casing centralizer (measuring ~9 in outside diameter [OD]) was attached. A total of 23 additional joints of casing were run, making the total string length ~279 m. A circulating sub (~0.3 m) was then installed, followed by another 23 joints (~268 m) of casing. This was followed by the riser/hanger assembly.

At this point, electrical continuity checks were made, and the long and tedious cable terminating process was begun at 1915 hr on 22 April. By 1230 hr on 23 April, the instrument string was assembled and final electrical integrity checks were completed. Hole 1201E was reentered for the fourth and final time, and the instrument package was lowered into the hole without incident. The riser/hanger was landed at 0100 hr on 24 April, and a 50-bbl slurry of 15.8-ppg cement was mixed

and displaced using the rig pumps. The instrument string was cemented in place with the end of the stinger located at a depth of 568.4 mbsf, or 56.4 m into basaltic basement. The top of the uppermost seismometer was placed at ~558.4 mbsf, or ~46.4 m below the basement contact. Using theoretical hole volumes and displacements, the top of the cement slurry should have reached a level of 142.6 m above the 10.75-in casing shoe (384.4 mbsf).

Hole 1201E Battery Frame Deployment

Preparations for deployment of the battery frame included bolting and tack welding the frame structure and rigging the deployment bridle, the glass balls for cable retraction, the redundant acoustic release package, and the wire cables for transferring the weight of the platform to the logging line. Lowering the platform through the moonpool was a complicated procedure in which the deployment of cables or the platform could snag on the open lower guide-horn structure. At 0830 hr on 24 April, once the final rig-up of the logging line had been completed and all final electrical checks had been performed, the platform was lowered through the moonpool and started on its descent to the seafloor. The 5.5-hr trip ended at 1400 hr when the platform landed in the reentry cone. A handheld acoustic command transducer was deployed, and within 10 min the release confirmation signal was received. At the same time, the winch operator reported losing ~700 lb of weight. Slowly raising the logging line confirmed that a satisfactory platform release had been achieved. The VIT system was lowered to survey the platform installation and observe the J-tool release from the riser/hanger. By 2010 hr on 24 April, the camera reached the seafloor, proper platform installation was verified, and in <5 min, the J-type running tool was released.

By 1100 hr on 25 April, the ship was secured for transit and underway for alternate Site 1202 (proposed Site KS-1).

LITHOSTRATIGRAPHY

At Site 1201, sedimentary successions were recovered in four holes, 1201A, 1201B, 1201C, and 1201D. Recovery was good (88%), and a nearly complete sedimentological succession was recovered from the seafloor to the basement at 509 mbsf. Hole 1201A was abandoned after the first core because of mechanical difficulties. A very short interval (1.6 m) of pelagic sediment was recovered. Pelagic sediments and cherts were recovered in Holes 1201B and 1201C. Hole 1201B penetrated deeper (81.07 mbsf) than Hole 1201C (48.10 mbsf) by using the XCB after APC refusal and recovered interbedded sandstones and bioturbated silty claystones. Hole 1201D was drilled down to 80.40 mbsf before core recovery began and then penetrated to a depth of 591.06 mbsf. The contact between the sedimentary succession and basaltic basement was present at 509 mbsf. The sedimentary succession in Hole 1201D is characterized by interbedded volcaniclastic sandstone and bioturbated silty claystone with rare breccia intervals. A short interval of claystone immediately overlies the basement contact (Fig. **F5**).

The sedimentary succession at Site 1201 has been divided into two lithostratigraphic units. Unit I consists of clays, cherts, and interbedded sandstones and silty claystones that contain a significant red clay content. The uppermost portion of Unit I is characterized by pelagic clays

F5. Representative graphic lithology log, p. 70.

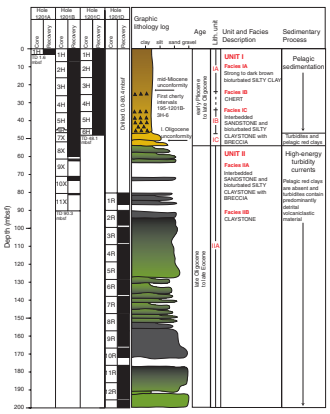

with increasing silica diagenesis downcore, indicated by the presence of cherty intervals. The lowermost portion of Unit I is characterized by interbedded pelagic claystones, with sandstone and silty claystone turbidites. Unit II underlies Unit I and consists of interbedded sandstones and silty claystones. These sediments are composed of detrital volcaniclastic material that has been reworked by turbidity currents. The lowermost portion of Unit II consists of quiescent marine claystone. This claystone facies is present immediately above the basaltic basement contact. Interpillow material in the underlying basalts includes sedimentary material with an unclear relation to the sediments of Unit II.

Lithostratigraphic Unit I

Interval: Sections 195-1201A-1H-1, 0 cm, to 1H-CC, 18 cm; 195-1201B-1H-1, 0 cm, to 8X-1, 150 cm; and 195-1201C-1H-1, 0 cm, to 6H-CC, 27 cm
Depth: 0–1.49; 0–53.40; and 0–48.10 mbsf
Age: early Pliocene to late Oligocene

Unit I consists of the uppermost 53 m of sediments recovered in Holes 1201A, 1201B, and 1201C. These sediments are predominantly strong brown to yellowish brown and contain a significant pelagic red clay content. Three distinct sedimentary facies can be identified. Facies IA is present in the uppermost 25 m of Site 1201 and is characterized by bioturbated and massive silty clays with manganese nodules. Facies IB consists of yellowish brown to dark brown cherts that are interbedded with the silty clays of Facies IA above and are also present as massive intervals in Cores 195-1201B-6H and 195-1201C-6H. Facies IC consists of interbedded sandstones and bioturbated silty claystone (Figs. F5, F6).

Facies IA

Facies IA is present in the uppermost 25 m of Site 1201 (Hole 1201A; Sections 195-1201B-1H-1, 0 cm, through 3H-6, 115 cm [0–25.35 mbsf]; and Sections 195-1201C-1H-1, 0 cm, through 3H-6, 94 cm [0–24.54 mbsf]) (Figs. F5, F6). Facies IA is characterized by strong brown to dark brown, bioturbated, massive silty clays with manganese nodules (Fig. F7). The silty clays contain a significant red clay content typical of pelagic sediments. A large (>3 cm) fragmented manganese concretion is present in intervals 195-1201A-1H-1, 64–67 cm, 195-1201B-1H-1, 28–36 cm, and 195-1201C-1H-1, 20–37 cm, and sand-sized manganese nodules are abundant throughout. Isolated rare, soft, fine-grained green nodules are present throughout Facies IA (e.g., Section 195-1201B-2H-5, 73 cm). An interval of white sand-sized fragments is present in interval 195-1201B-3H-4, 18–21 cm. These green and white fragments have been identified in smear slides and by X-ray diffraction (XRD) analysis as authigenic zeolites. A discrete interval of soft green zeolites suggests a possible hiatus surface in Holes 1201B and 1201C (intervals 195-1201B-3H-6, 56–58 cm, and 195-1201C-3H-6, 80–82 cm). This zeolite-rich hiatus surface is overlain by clay-rich sediments with abundant bioturbation and is underlain by coarser sediments (Fig. F8). The location of this hiatus surface is consistent with the middle Miocene unconformity identified at a depth of 24.8 mbsf in the age-depth plot for this site (see "Paleomagnetism," p. 28, and "Biostratigraphy," p. 23).

F6. Lithology, units and facies, color reflectance, natural gamma count, and mineral composition, p. 73.

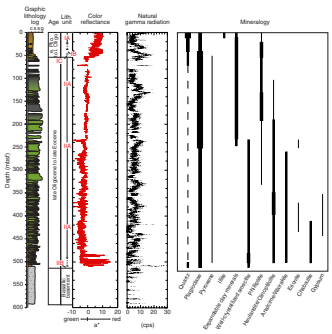

F7. Bioturbated silty clays typical of Facies IA, p. 74.

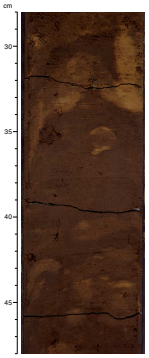

F8. Possible middle Miocene hiatus, p. 75.

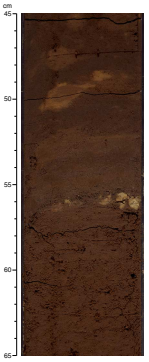

Facies IB

Facies IB is characterized by chert (Figs. F5, F6). Chert is present as isolated dark brown to yellowish brown firm to hard intervals within the silty clays of Facies IA (Fig. F9). The first isolated cherts are present in intervals 195-1201B-3H-6, 117–120 cm, and 195-1201C-3H-6, 94–96 cm, and become increasingly abundant downcore, culminating in massive chert in Cores 195-1201B-6H and 195-1201C-6H. The chert intervals contain abundant sand-sized manganese nodules. Rare intervals contain moderate bioturbation and sedimentary structures, such as planar and cross laminations.

F9. Chert interval typical of Facies IB, p. 76.

Facies IC

Facies IC consists of interbedded sandstone and bioturbated silty claystone with rare breccia. It is present in Sections 195-1201B-7X-1, 0 cm, through 8X-1, 150 cm (46.70–53.40 mbsf). The claystones contain a significant red clay content similar to the pelagic sediments of Facies IA identified above. The sediments are yellowish brown to dark brown. They are often normally graded, and the sandstones are often planar and cross laminated (Fig. F10). There is microscopic evidence to suggest that these sediments incorporate reworked material from underlying Unit II sediments (see "Smear Slide Analyses," p. 14). A pumice ash layer was identified in smear slides from an interval of sand-sized alternating black-and-white laminae (interval 195-1201B-8X-6, 76–78 cm). This material appeared to be less consolidated than the surrounding sediments. This is significant, as this was the only unreworked ash layer positively identified at Site 1201. The reworking of most of the sedimentary succession at Site 1201 likely obliterated most primary tephra layers.

F10. Sandstone and silty claystone turbidites, p. 77.

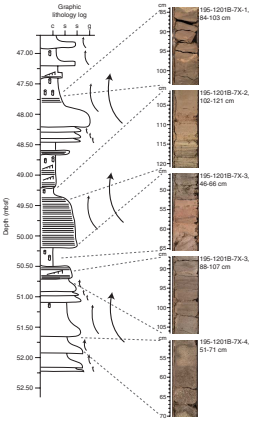

Lithostratigraphic Unit II

Interval: Sections 195-1201B-8X-2, 0 cm, to 11X-CC, 37 cm, and 195-1201D-1R-1, 0 cm, to 45R-5, 90 cm
Depth: 53.40–81.07 and 80.40–509.76 mbsf
Age: late Oligocene to late Eocene

Unit II constitutes the remaining recovered sedimentary section below Unit I at Site 1201. The transition from Unit I to Unit II is indicated by an abrupt color change from brown to greenish gray. This color change is associated with a change in the mineralogical composition of the sediments (Figs. F5, F6). In Unit I, a major component of the sediments is red clays. In Unit II, the red clays are absent and the sediments are composed primarily of reworked detrital volcaniclastic material (see "Smear Slide Analyses," p. 14, and "X-Ray Diffraction Analyses," p. 16). Two distinct sedimentary facies can be identified. Facies IIA is the predominant sedimentary facies of Unit II and extends from the boundary with Unit I down to within 2.5 m of the contact with basaltic basement at 509 mbsf. Facies IIA is characterized by interbedded volcaniclastic sandstones, bioturbated silty claystones, and breccia. Facies IIB is characterized by reddish brown bioturbated claystone with some faint planar laminations. It occurs interbedded with Facies IIA near the base of the recovered sedimentary section at Site 1201 and then as a predominantly massive unit for the remaining 2.5 m immediately overlying basaltic basement (Figs. F5, F6). Sediments are present as interpillow mate-

rial in the underlying basalts, but their relation to Facies IIB sediments is unclear.

Facies IIA

Facies IIA is characterized by interbedded sandstones, bioturbated silty claystones, and breccia consisting of volcaniclastic material. Texturally, it is very similar to the overlying sediments of Facies IC (e.g., Fig. F11); however, a marked color and mineralogical change denotes the unit boundary. Facies IIA extends through the remaining recovered interval of Hole 1201B (Sections 195-1201B-8X-2, 0 cm, through 11X-CC, 37 cm [53.40–81.07 mbsf]) and through the majority of the sedimentary succession recovered from Hole 1201D (Sections 195-1201D-1R-1, 0 cm, through 45R-3, 90 cm [80.40–507.20 mbsf]). Facies IIA is predominantly dark greenish gray and becomes increasingly grayish green downhole (Figs. F5, F6). Pelagic red clays are absent. Detrital volcaniclastics and authigenic zeolites are the primary constituents of the sediment (Fig. F6).

Much of the succession is normally graded at multiple scales (Figs. F11, F12). In these fining-upward sequences, bioturbated silty claystones overlie sandstones that often exhibit planar, cross, wavy, and rare trough cross-laminations. Basal contacts are sharp and erosional. Fining-upward sequences become increasingly finer grained downhole, with fewer intervals of massive sandstone and no breccia intervals (Fig. F5). Rare inversely graded intervals are present (e.g., interval 195-1201B-14R-1, 2–53 cm). Calcareous intervals in silty claystone and calcareous sand-sized fragments in sandstone (overcalcified foraminifers) (see "Biostratigraphy," p. 23) are present throughout Facies IIA.

Rounded green clasts of zeolite-cemented sandstone are present in Section 195-1201D-1R-2 as rare isolated clasts and increase in abundance downhole. Fine-grained bright green zeolite-cemented intervals are first observed in Section 195-1201D-17R-3 (Fig. F13). These isolated intervals (with a maximum thickness of 42 cm in interval 195-1201D-356R-2, 52–94 cm) increase in abundance downhole. Thin (<5 cm) white gypsum-bearing intervals are rare and are first observed in Section 195-1201D-32R-6. Thin (<5 mm thick) white zeolite veins oriented oblique to laminae are rare and are first observed in interval 195-1201D-14R-5, 99–103 cm. They are encountered again in Cores 195-1201D-24R, 30R, and 37R. Lastly, unusual thick laminae first occur in Section 195-1201D-31R-5. Sand-sized grains within the laminae are "inflated" by alteration. The laminae are 2 to 3 mm thick and have sharp upper and lower contacts that are wavy. The primary planar and cross laminations of the sediment are still identifiable, but the altered thick, wavy laminae make the structures appear "fuzzy" or out of focus (Fig. F14) (see "Smear Slide Analyses," p. 14, and "X-Ray Diffraction Analyses," p. 16).

Facies IIB

Facies IIB consists of reddish brown bioturbated claystone with rare faint planar laminations. It occurs interbedded with Facies IIA in Sections 195-1201D-43R-1, 0 cm, through 44R-7, 71 cm (484.10–503.41 mbsf), then as a predominantly massive unit in Sections 195-1201D-45R-4, 0 cm, through 45R-5, 90 cm (507.36–509.76 mbsf), with the exception of faint planar laminations in the uppermost portion of Section 45R-4. A thin (<5 mm thick) white quartz layer is present in interval

F11. Dark greenish gray volcaniclastic sandstone and silty claystone turbidites, p. 78.

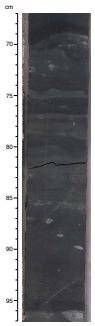

F12. Sandstone and bioturbated silty claystone turbidites, p. 79.

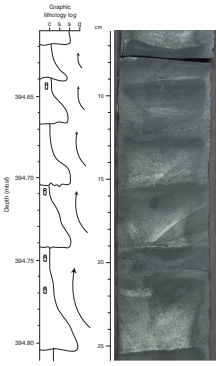

F13. Fine-grained bright green zeolite-cemented interval, p. 80.

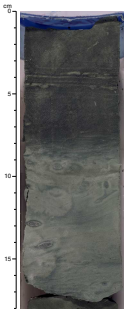

F14. "Inflated" laminae in sandstone, p. 81.

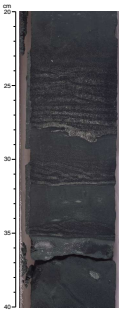

195-1201D-45R-5, 63–63.5 cm (Fig. F15). The lowermost massive interval of Facies IIB is reddish brown and becomes dark brown toward the basement contact in Section 195-1201B-45R-5, 90 cm (Fig. F16). Similar fine-grained sediments are present as interpillow material in the underlying basalts. These sediments are mustard yellow, strongly altered, and include encrusted radiolarians. No age assignments or genetic relationships with the overlying Facies IIB sediments could be determined at this stage of investigation.

Smear Slide Analyses

Besides visual core description and XRD analyses, the textural and compositional characteristics of the unconsolidated to semiconsolidated sediments of Unit I and uppermost Unit II in Holes 1201A and 1201B were inferred from smear slide analyses (see "Site 1201 Smear Slides," p. 90). The reddish to brownish silty clays generally have high clay concentrations, which mostly vary between 80% and 95%. Higher concentrations of silt-sized (15%–30%) and sand-sized (1%–5%) quartz, feldspar, and heavy-mineral grains in the reddish to brownish silty clays are confined to the uppermost 2 m of the recovered sediment succession. Down to ~10 mbsf, the red silty clays include small but ubiquitous portions of volcanic glass shards, which disappear downhole. Authigenic phillipsite crystals become common at the expense of volcanic glass. This distribution pattern might indicate the possible dissolution of volcanic glass and a related neoformation of zeolite promoted by low sedimentation rates.

The calcareous intervals of Unit I, encountered in Sections 195-1201B-4H-3, 5H-4, 9X-CC, and 10X-1, are mainly composed of calcareous nannofossils. The cherts of Facies IB include abundant opaline particles, which partly originate in encrusted radiolarian tests. The XRD results show no indication of the transformation of amorphous opal to a higher degree of crystal ordering. The cherts, therefore, actually represent protocherts or so-called "porcellanites." Furthermore, phillipsite lathes appear to be concentrated and amalgamated in the opal layers.

The interbedded sandstone–silty claystone succession of Facies IC again includes volcanic glass shards. The sandstones may bear detrital zeolite grains, which apparently were reworked from diagenetic cements of the underlying sandstones of Unit II (Fig. F17). One distinct laminated ash layer with pumice glass shards was identified in Section 195-1201B-7X-2 (Fig. F17).

Thin Section Analyses

Microscopic investigations of thin sections were carried out to verify the textural and compositional variations of the lithified sedimentary rocks of Unit II and to gain insights into their diagenetic alteration (see "Site 1201 Thin Sections," p. 94).

From a sediment-petrographic view, the immature sandstones and fine-grained breccia of Unit II can be classified as lithic arenites with almost no quartz, high abundances of feldspar, and dominant rock fragments (lithoclasts). The detrital material is mostly derived from volcanic sources and was redeposited by sedimentary processes. This is demonstrated by current bedding and the admixture of volcanic clasts of different origins in a given sample, which is not consistent with pure tephra that should show a more homogenous composition. Furthermore, exotic clasts, such as light gray clasts of fossiliferous shallow-

F15. Dark brown claystone containing a white quartz interval, p. 82.

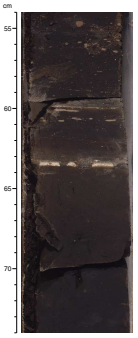

F16. Contact of the sediments with basaltic basement, p. 83.

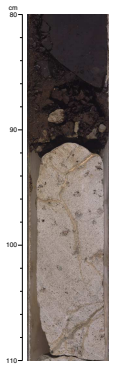

F17. Reworked zeolite grain and glass shards from a pumice ash layer, p. 84.

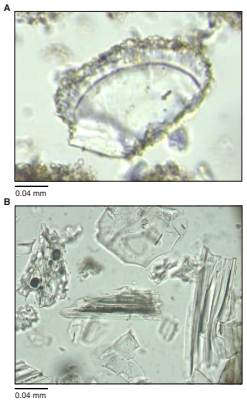

water limestone, are occasionally associated with the volcaniclastic material (Figs. F18, F19). Some of the samples include foraminifers and calcareous nannofossils that indicate open-marine conditions. Their scarcity can be related to high sedimentation rates of detrital material that dilutes the pelagic rain of biogenic matter.

The composition of the lithic arenites is consistent with the provenance and detrital input from an undissected magmatic arc source (Fig. F20) (Dickinson, 1985). An undissected arc represents a juvenile magmatic arc that was not eroded and unroofed to its roots where coarse-grained intrusive rocks prevail. Sediment supply from such a source provides a large amount of fine crystalline, sand-sized volcanic rock fragments. Alternatively, the erosion of plutonic rocks from a dissected arc produces more sand-sized quartz and feldspar.

The volcanic clasts of Unit II are diverse in texture and appear to be of similar basaltic to andesitic composition. They comprise more or less vesicular porphyries and vitrophyres that include plagioclase, clinopyroxene, and, to a lesser extent, hornblende and orthopyroxene phenocrysts embedded in a glassy to hypocrystalline groundmass (Figs. F18, F19). The plagioclase crystals are typically zoned with sodium-rich margins and calcic cores, pointing to hypabyssal crystallization of the phenocrysts (Fig. F21). Tentatively, four volcanic rock varieties were distinguished, although transitional types are also present. The most abundant and variable type is black to grayish brown plagioclase-augite porphyry/vitrophyre with relatively few vesicles and a dark tachylitic groundmass. This rock type also appears as an oxidized reddish scoria, which represents a minor but ubiquitous component in the arenites of Unit II (Fig. F19). Another subordinate rock variety of more dacitic composition is made up of aligned plagioclase laths in a dark, fine groundmass (pilotaxitic "trachytic" texture). The most conspicuous rock type consists of vitric fragments of sideromelane with abundant bubble-shaped vesicles separated by wide glassy bubble walls and low concentrations of crystalline phenocrysts (Fig. F18). Fragments of phenocrysts from these diverse rock types are also present as single detrital grains in the sandstones, particularly in the fine-grained sandstones. The siltstones consist almost exclusively of fine detrital glass shards of sideromelane.

The downhole distribution of these diverse rock fragments shows high variability. From the analysis of a few thin section samples, there seems to be a crude trend toward more abundant porphyries/vitrophyres in the upper part of Unit II and larger amounts of sideromelane in the deeper part (see "Site 1201 Thin Sections," p. 94). This trend might be attributed to an uphole grain size coarsening, as porphyries/vitrophyres tend to be enriched in the coarse sand– to granule-sized fraction. According to the criteria proposed by Fisher and Schmincke (1984), this might indicate a change in the overall mode of volcanism. Subaqueous and subaerial explosive eruptions at an early stage are documented by the sideromelane fragments. A higher contribution of eroded subaerial tephra and effusive rocks during a later stage are indicated by the tachylitic porphyries/vitrophyres. The presence of red oxidized scoria throughout the section, however, indicates that subaerial volcanics were also produced during the early stage. This type of scoria forms around terrestrial volcanic vents, where lithified lava is maintained at high temperatures for extended periods while in contact with the atmosphere.

Another important aspect of Unit II is a high degree of diagenetic alteration, which shows a depth-dependent pattern, especially in the

F18. Fresh lithic arenite and siltstone, p. 85.

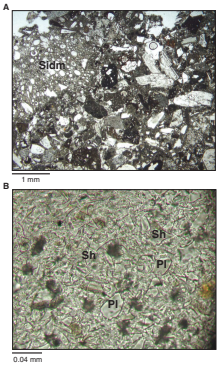

F19. Oxidized scoria; plagioclase-rich vitrophyre and limestone fragment, p. 86.

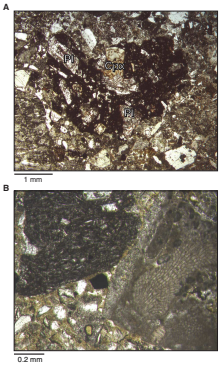

F20. Tectono-genetic provenance of sandstones, p. 87.

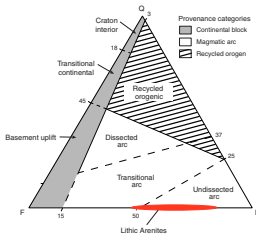

F21. Zoned and twinned plagioclase; prismatic lathes of phillipsite and clay, p. 88.

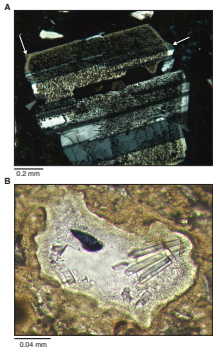

paragenesis of zeolite minerals. Although the exact identification of zeolite and clay minerals awaits further confirmation by shore-based studies, some general downhole trends seem to be evident on the basis of shipboard findings from thin sections and XRD results. The upper clastic rocks of Unit II are relatively fresh and grade into strongly altered sequences farther downhole. Throughout the unit, pore-lining clay rims around the detrital grains, which also form the coatings of vesicles in the sideromelane clasts, likely initiated the cementation and induration of the sediments (Fig. F21). Authigenic phillipsite crystals, which characterize the red silty clays of Unit I, also appear in the sedimentary rocks of upper Unit II, where they are present as prismatic lathes in the pore spaces (Fig. F21). Below ~100 mbsf, zeolite minerals in the pore spaces occasionally appear as pore-filling fibrous spherolites composed of phillipsite and, possibly, clinoptilolite and analcime (Fig. F22). In some samples, carbonate patches replace detrital grains or appear as pore fillings.

Intergranular to poikilotopic cementation of pore spaces and the replacement of glass in the sideromelane clasts by sparry zeolites is evident below ~180 mbsf and becomes pervasive below 250 mbsf (Fig. F23). The remaining lower part of Unit II, with its bright green layers, shows increasing palagonitization of silt-sized glass shards to zeolites and green clay minerals. Larger grains in many of the sandstones are also affected by strong alteration. They were replaced by zeolites and only show the ghosts of their former detrital precursors, which likely consisted of unstable vitric clasts (Fig. F24). Since the plagioclases and augites are not affected by alteration at this depth, the high abundance of altered sand grains gives further evidence for compositional variations of source materials through time, with a higher contribution of pure volcanic glass during an earlier stage of volcanism. Below 400 mbsf, several generations of zeolite minerals (chabazite and erionite) are associated with sulfate minerals (Fig. F25).

X-Ray Diffraction Analyses

Results from semiquantitative XRD analyses on the composition of the sediments and sedimentary rocks of Units I and II confirm the findings from the other applied methods, with additional detail (Table T2; Figs. F26, F27). The XRD results provide further insight into the downhole distribution of quartz, which is difficult to identify in the smear slides and thin sections. Higher quartz abundances are confined to the uppermost silty clays of Unit I down to 15–20 mbsf and decline progressively toward the upper part of Unit II at ~80 mbsf. In the upper 5 m, quartz is associated with illite, which is not present in the remaining part of the section, pointing to a higher proportion of terrigenous dust in the uppermost sediments. In most clastic components of Unit II, quartz ranges near the limit of detection, consistent with sediment provenance from basic to intermediate volcanic sources. Slightly higher quartz concentrations are again present in the lowermost red claystones of Unit II.

The mineralogical patterns inferred from the XRD results nicely illustrate the downhole change of diagenetic assemblages with an increase of gypsum and Ca-rich zeolites such as chabazite ($CaAl_2Si_4O_{12}·6H_2O$) and erionite ($[Ca,K_2,Na_2]_2Al_4Si_{14}O_{36}·15H_2O$) at the expense of phillipsite ($[K,Na,Ca]_{1–2}[Si,Al]_8O_{16}·6H_2O$), analcime ($NaAlSi_2O_6·H_2O$), and clinoptilolite ($[Na,K,Ca]_6[Si,Al]_{36}O_{72}·20H_2O$) below 250 mbsf. At this depth, a

F22. Diagenetic features in sandstone and pore-filling zeolite spherolites, p. 89.

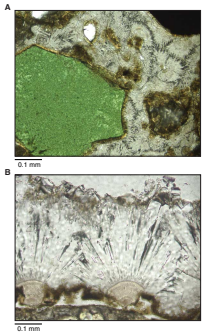

F23. Advanced stage of diagenesis in sandstones, p. 90.

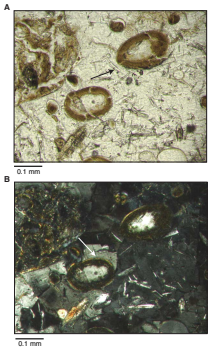

F24. Strongly altered sandy siltstone, p. 91.

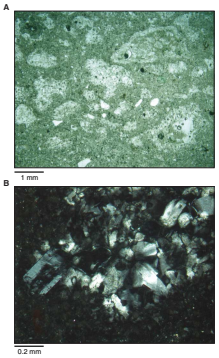

F25. Diagenesis in siltstones, p. 92.

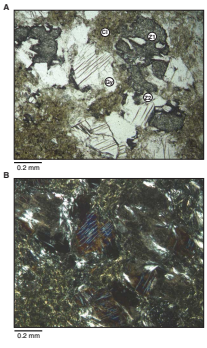

marked change in clay mineralogy is evident with the first appearance of well-crystallized smectite downhole. Conversely, the upper portion of the section is dominated by various types of expandable and poorly crystallized clay minerals. The changes in diagenetic minerals are consistent with pore water profiles at Site 1201, which exhibit the presence of extremely CaCl-rich interstitial waters below 250 mbsf (see "Geochemistry," p. 33). Similar diagenetic patterns and pore water profiles were reported from lithic arenites of the Izu-Bonin forearc sedimentary basin (Egeberg et al., 1990; Marsaglia and Tazaki, 1992).

Environmental Interpretation

Site 1201 is located just west of the Palau-Kyushu Ridge axis along the eastern edge of the western Philippine Basin. Deposits similar to those encountered at Site 1201 have been described from earlier drilling in the West Philippine Basin during DSDP Leg 31 (Site 290) (Karig, Ingle, et al., 1975), DSDP Leg 59 (Site 447) (Kroenke, Scott, et al., 1981), and in the Izu-Bonin forearc sedimentary basin during ODP Leg 126 (Sites 792 and 793) (Shipboard Scientific Party, 1990a, 1990b). The paleoenvironmental setting for the sedimentary succession recovered at Site 1201 is summarized in Figure F28. Our model of sedimentation is similar to others constructed for basins in the West Pacific (e.g., Marsaglia et al., 1995 [their fig. 20]; Clift et al., 1994; Rodolfo, 1980). The remainder of this section is discussed within the context of the stages of sedimentation outlined in Figure F28, starting with the oldest sediments recovered at Site 1201. The final paragraph addresses the history of diagenesis at Site 1201.

Stage 1 (Late Eocene)

The sedimentary succession at Site 1201 begins immediately above the contact with basaltic basement at 509 mbsf (Fig. F16). Claystones of Facies IIB were deposited in a quiescent marine environment with a possible eolian component (Figs. F6, F15, F28). Facies IIB claystones contain quartz and clay minerals and are derived from the erosion of a source that is different from that of the overlying turbidite facies, which is composed of detrital volcaniclastic material. Facies IIB sediments are fine grained and largely structureless. The brown color of the sediments can be attributed to many possible factors. The claystones may have originated as terrigenous sediments that were oxidized subaerially and subsequently redeposited in the marine environment. Alternatively, slow sedimentation rates may have enabled oxidation of the sediments to occur with circulating bottom waters. The brown color may also be the consequence of the influence of hot pore fluid from the basement interacting with the claystones. Geochemical gradients suggest that the latter scenario is likely the case for the lowermost sediments (see "Geochemistry," p. 33). Although the claystone includes a high proportion of iron, which might indicate metalliferous sediments, the high aluminum concentration is inconsistent with this assertion and could reflect the high concentration of pelagic clay minerals in the sediment. The cause of the high concentration of manganese in the claystones (up to 6%) was not determined on board ship and will be investigated in postcruise studies.

T2. XRD data for soft sediments and sedimentary rocks, p. 192.

F26. XRD of major sediment and sedimentary rock types, p. 93.

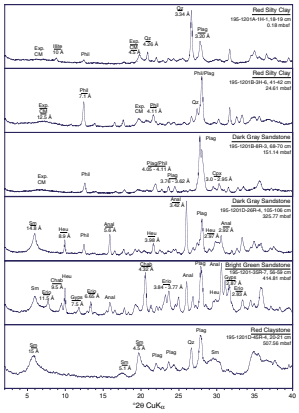

F27. XRD of clay minerals and zeolites, p. 94.

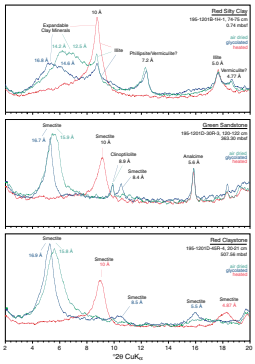

F28. Environmental interpretations from the sedimentary succession, p. 95.

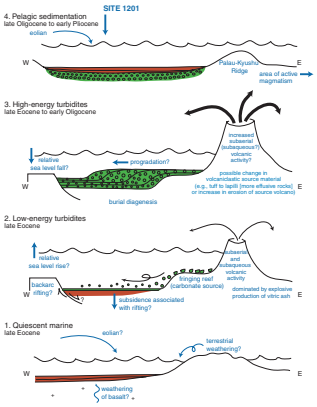

Stages 2 and 3 (Late Eocene to Late Oligocene)

The majority of the sedimentary succession at Site 1201 records deposition of detrital volcaniclastic (Unit II, Facies IIA), and pelagic (Unit I, Facies IC) sediments by turbidity currents (Fig. F28). In Figure F28, subaqueous and subaereal volcanism is proposed as the source of the volcaniclastic material and a fringing reef/shelf environment is a likely source of the reworked carbonate material observed throughout Facies IIA. This is consistent with the timing of the growth and maturity of the Palau-Kyushu magmatic arc proposed in studies from the West Pacific (e.g., Bloomer et al., 1995 [their fig. 4]).

Eruption-driven turbidity current sequences were continuously pumped into basins surrounding the arc as described by Underwood et al. (1995 [their fig. 1]). The petrographic composition of Facies IIA sediments with almost no quartz and abundant plagioclase feldspars and lithic fragments (Fig. F20) is consistent with a nearby sediment supply from an undissected arc environment (Dickinson, 1985; Valloni, 1985). Sediment supply from a relatively young magmatic arc is also inferred by the composition of feldspars and lithoclasts that indicate basaltic to andesitic volcanism.

The turbidites in the sedimentary succession at Site 1201 exhibit an uphole trend from low-energy turbidites to high-energy turbidites (Figs. F5, F6). This uphole trend can be attributed to many possible factors; these are indicated in Figure F28. Changes in sediment supply, slope gradient, proximity to source, tectonics, erosion, and sea level could all be responsible, in whole or in part, for the energetics of the turbidity currents.

A higher relative sea level farther down in the section is consistent with a backarc basin environment experiencing rapid initial rifting and subsidence. Subsidence associated with rifting followed by uplift associated with the growth of the magmatic arc could greatly increase the slope gradient over time and would result in high-energy turbidites characterized by coarser sediments higher in the section. This interpretation may be supported by preliminary observations of seismic profiles that suggest a graben structure underlying Site 1201. Shore-based studies of seismic profiles are required to further substantiate this observation. Coarser sediments could also be produced by an increase in volcanic activity or an increase in erosion of the source volcanic rocks, as indicated in Figure F28.

Stage 4 (Late Oligocene to Early Pliocene)

Unit I sediments are indicative of a pelagic environment. Pelagic sediments are incorporated into the uppermost turbidite sequences. Over time, however, the sediment supply from the volcanic arc ceased. The lack of sediment feeding the depositional system caused the turbiditic environment to be replaced by one that is characterized by slow pelagic sedimentation with an eolian component (Fig. F28). The increase in terrigenous quartz and illite in Unit I might be an indication of stronger dust supply from Eurasia during late Cenozoic climate deterioration.

Post–Stage 4

According to the age-depth plot from Site 1201, the sediments at the top of the sedimentary succession are early Pliocene in age but the rest of the section is missing (see "Biostratigraphy," p. 23, and "Paleomag-

netism," p. 28). To determine whether bottom currents at Site 1201 might be responsible for this hiatus, the position of a sonar beacon was tracked during its release and ascent from the seafloor on two occasions using the ship's DP system. On one occasion, the beacon rose straight to the surface, but on a second, it encountered an 8-cm/s current bearing 200° south-southwest throughout the bottom 1000 m of the water column. A bottom-water current with this velocity could hold pelagic sedimentation in suspension, thereby depleting the site of pelagic sediments younger than the onset of the current. In any case, the absence of pelagic sedimentation since the early Pliocene suggests a significant change in the paleoceanographic regime in the region at that time.

Diagenetic History

Unit I sediments underwent increasing levels of silica diagenesis downcore, with firm to hard cherty intervals high in opal content (Fig. F9) culminating in massive chert (porcellanite) intervals in Cores 195-1201B-6H and 195-1201C-6H.

Many features of the Facies IIA sediments are indicative of increased diagenetic alteration of the sediments with depth. The general color trend downhole from dark greenish gray to grayish green indicates increased zeolite content with depth. Green sandstone clasts cemented with zeolites and fine-grained bright green zeolite-cemented intervals increase in abundance downhole. White zeolite veins and gypsum-bearing intervals also increase in abundance, although they remain rare. Unusual inflated laminae in which primary planar and cross-laminar structures are distorted by sand-sized grains that are inflated by diagenetic alteration are first observed in Core 195-1201D-31R and increase in abundance downhole. These "zeolitized" sediments indicate increasing alteration with depth.

Three possible causes might explain the diagenetic pattern at Site 1201: (1) fluids derived from seawater and hydrothermal fluids from the underlying basalts could meet and interact with solid phases in the sediment pile, (2) burial diagenesis may promote the alteration of unstable glass shards with depth, and (3) the degree of diagenetic alteration may be related to compositional and textural changes, with stronger alteration in the deeper section, where abundant silt-sized glass shards favor chemical attack because of their larger particle surface area. A combination of the second and third processes seems most likely. The composition of the pore water appears to be the result of the diagenetic reactions and indicates a present state of equilibrium between the interstitial fluids and the solid phases. The rough estimate of the modern geothermal gradient of 12.5°C/100 m at Site 1201 (see "Physical Properties," p. 36) supports the assumption of burial diagenesis under moderately elevated temperatures. Accordingly, the thermal exposure of the strongly altered material reached at least 50°C. The observed paragenetic assemblage, on the other hand, suggests burial temperatures of 85° to 125°C (see Fisher and Schmincke, 1984, and references therein). This difference suggests that the geothermal gradient at Site 1201 may have been higher in the past, for instance, during a time when this location was a focus of magmatic arc development during the Eocene to Oligocene.

IGNEOUS PETROLOGY

The basement drilled at Site 1201 is composed of a 94-m-long sequence of volcanic rocks (recovery = 32%). Evidence for pillow lava structures, such as glassy margins, hyaloclastite fragments, and interpillow sedimentary material, as well as radiating fractures and vesicles (Fig. F29) are visible throughout the sequence. Examples of preserved pillow margins are found in intervals 195-1201D-48R-4, 12–26 cm, and 52R-1, 18–44 cm (Fig. F30). Hyaloclastite fragments are observed, for example, in interval 195-1201D-46R-4, 24–29 cm (Fig. F31A), and traces of biogenic material are found in interpillow sediments containing hyaloclastite fragments (Fig. F31B). Section 195-1201D-55R-1 is massive with no evidence for pillow margins and may therefore represent a lava flow.

In Section 195-1201D-47R-3 there are intervals of pillow breccia containing fragments of lava cemented in brown sedimentary material (Fig. F32). The latter is brown (10YR 4/3) to yellowish brown (10YR 5/4) and has been found throughout the core, for instance, in Sections 195-1201D-47R-1, 48R-1, 52R-2, and 54R-1 (Fig. F33). The sedimentary material is found both as single pieces containing fragments of green volcanic glass and infilling veins and fractures in the lava.

The lavas are highly altered, especially at the contact with the overlying sediments. In general, the degree of alteration decreases slightly with depth, as indicated by a decrease in the percentage of secondary minerals (see "Petrography," p. 20) and a decrease in the loss on ignition (LOI) (see "Geochemistry," p. 33). The alteration gives different colors to the rocks, from light gray (5Y 6/1) to bluish gray (5B 6/1–5B 5/1) in most of the sections and reddish gray (10R 5/1) in the lowermost cores. Veins and amygdules are widespread between Cores 195-1201D-45R and 48R, becoming less frequent in the deeper cores, where only a few thin veins are present. The veins are usually filled by one or more of the following secondary minerals, identified in thin section: zeolites, iron oxyhydroxides, carbonate, and clay minerals. They are accompanied by large halos in which the color of the rock is generally lighter, such as gray (5Y 6/1) or reddish brown. The veins are often filled with brownish sedimentary material with dark red rims and contain a late-stage carbonate precipitate (Fig. F34). The amygdules are filled by green clay minerals and/or zeolites and sometimes also by carbonate. No quartz vein fillings were observed.

In hand specimen, the basement igneous rocks are generally very fine grained (borderline aphanitic) and aphyric. Only rare brownish red pseudomorphs of olivine can be observed. The groundmass appears glassy with signs of devitrification ("rosette texture") in the upper cores and more microcrystalline in the deeper cores.

Petrography

The petrography of the basement rocks has been defined on the basis of 38 thin sections, covering all representative rock types observed throughout the core. The thin section samples were selected to characterize different textures, primary and secondary mineral phases, crystal content and size, and amygdule and vein mineralogy and size. All observations are reported in the thin section tables (see "Site 1201 Thin Sections," p. 94), following the guidelines illustrated in "Thin Section Descriptions," p. 11, in "Igneous Petrology" in the "Explanatory

F29. Aphyric basalt exhibiting radiating vesicles, p. 96.

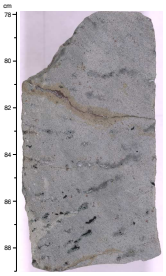

F30. Basalt pillow reconstruction and basalt piece with glassy pillow margin, p. 97.

F31. Hyaloclastite and pillow piece with biogenic clast in interpillow material, p. 98.

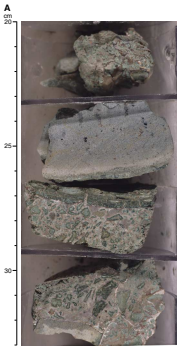

F32. Pillow breccia consisting of angular fragments of aphyric basaltic glass, p. 100.

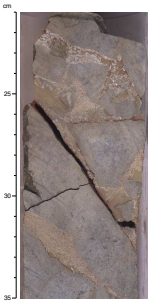

Notes" chapter. On the basis of both visual and microscopic observations, the basement rocks are classified as basalts.

In thin section, the basalts range from aphyric to sparsely porphyritic to moderately porphyritic with up to 7% phenocrysts (crystals longer than 0.5 mm). They show variable crystallinity, from almost completely glassy along pillow rims to hypohyaline and coarser grained in pillow interiors. A general trend of increasing crystallinity is observed with depth. The grain size is generally fine (average length of microliths in the groundmass = <0.2 mm) and tends to increase slightly with depth. In most cases, the glass is completely devitrified (palagonitized), but the devitrification products cannot be identified easily under the microscope. Different colored clay minerals and zeolites are tentatively identified as the most common secondary minerals after glass. Based on XRD data, mixed-layer clay minerals and zeolites such as phillipsite, natrolite, and analcite are common alteration products (see **"Lithostratigraphy,"** p. 10).

The main primary minerals observed in the basalts include plagioclase, olivine, clinopyroxene, and opaque minerals. Clinopyroxene is the only well-preserved primary mineral. Its morphology is commonly anhedral or subhedral. In glass-rich rocks, the clinopyroxene microliths show anomalous undulatory extinction, due to fast cooling. Based on its colorless or pale green color, the clinopyroxene should be Mg rich. Olivine is always completely replaced by secondary minerals and its original composition cannot be determined, but its relics are easily recognized by their common euhedral morphology. Olivine alters to clay minerals, iron oxyhydroxides (including hematite), and carbonate (Fig. **F35**). The plagioclase exhibits elongate skeletal morphology, often swallow-tailed, due to fast cooling (Fig. **F36**). Plagioclase appears highly altered in many thin sections. It is most commonly replaced by zeolites and alkali feldspar and less commonly by either clay minerals or carbonate (Fig. **F37**). In most cases, Na-rich rims are preserved, reflecting original chemical zoning (Fig. **F38**). In several thin sections, the primary plagioclase core has also been preserved, and its composition, determined using the Michel-Levy method, ranges from An_{75} to An_{49}, with little or no difference between phenocrysts and small microliths in the groundmass. Opaque minerals are present as small euhedral or skeletal grains in the groundmass; the composition is presumably titanium-rich magnetite. Opaque grains often observed in the groundmass of glass-rich basalts outline branching or spherulitic (clay mineral?) patches of devitrified glass. The secondary minerals observed in thin section and those identified by XRD analysis suggest that alteration of the basalts in Hole 1201D occurred within the zeolite metamorphic facies (Table **T3**).

Devitrification of glass often leads to a spherulitic texture, corresponding to the "rosette" texture visible in hand specimen or by lens. Spherulites made up of radiating clinopyroxene and plagioclase microliths are common (Fig. **F39**). Other types of textures exhibited by glass-rich basalts are hyalopilitic and branching textures. In hyalopilitic textures, devitrified glass, vesicles, and clinopyroxene and plagioclase microliths show subparallel alignment along flow directions (Fig. **F35**), whereas in branching textures, the microliths and/or the devitrified glass are bent and show featherlike shapes, suggesting fast cooling (Fig. **F40**). In a few cases, the rocks display two or more of the above textures, sometimes exhibiting a gradual transition from spherulitic at the pillow margins to branching textures further away.

Basalts with a higher degree of crystallinity show a textural variation from felty to intersertal to intergranular to subophitic, with progres-

F33. Fragments of aphyric basaltic glass and pillow margin, p. 101.

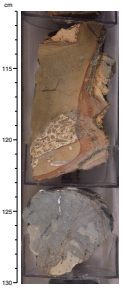

F34. Vesicular, hydrothermally altered, aphyric basalt, p. 102.

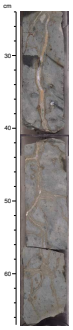

F35. Hyalopilitic texture and completely replaced olivine, p. 103.

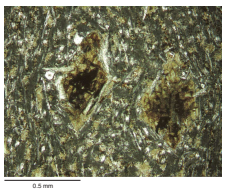

F36. Skeletal plagioclase exhibiting "swallow-tail" morphology, p. 104.

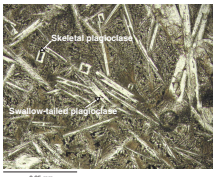

F37. Plagioclase lath, clinopyroxene, and amygdules, p. 105.

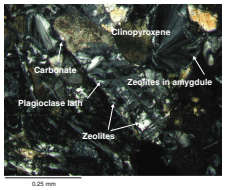

sively decreasing glass and increasing amounts of crystals. In felty and intersertal textures, euhedral plagioclase microliths are distributed randomly, with variable amounts of devitrified glass occupying the angular spaces between them. In intergranular texture, the spaces between plagioclase microliths are occupied by olivine, clinopyroxene, and opaque grains, whereas in subophitic rocks, euhedral plagioclase microliths are partially enclosed by anhedral clinopyroxene or olivine grains (Fig. F41).

The textural relationships exhibited by the basalts and the morphologies displayed by the different minerals have allowed us to infer an order of crystallization of the original minerals. Plagioclase crystallized first, often together with olivine, followed by clinopyroxene, and finally, opaque minerals. Evidence for plagioclase being crystallized before or along with olivine suggests a shallow depth of crystallization as well as high P_{H_2O} conditions (Johannes, 1978).

Geochemistry

A total of 30 samples from Hole 1201D were analyzed using inductively coupled plasma–atomic emission spectroscopy for major and trace elements. The selected samples are either plagioclase ± clinopyroxene ± olivine phyric to aphyric basalts. A few hyaloclastites and glassy pillow basalt margins were also analyzed to study the effects of seawater alteration on the bulk rock geochemistry. The basement samples are altered to various degrees (see **"Petrography,"** p. 20), so LOI values vary considerably (0.85–11.85 wt%); moreover, many of the rocks have gained alkalis, as reflected by the appearance of nepheline in their CIPW norms (see Table T4). The upper 20 m of the pillow basalts are highly altered, with LOI values up to 12 wt% (average = 6.4 wt%). Below this depth, LOI drops to relatively constant lower values (average = 1.84 wt%), reflecting less extensive seawater alteration and less veining and fracturing of the basalts (see also Fig. F42). These deeper basalts are also hypersthene rather than nepheline normative (Table T3). Some of the major and trace element abundance vs. depth patterns correlate well with the LOI values (Fig. F43). In fact, by examining the behavior of elements easily mobilized during seafloor alteration (K, Na, Sr, Ca, and Fe) in samples that are visually altered, it has been possible to assess the effect of alteration on the bulk chemistry. The content of Si, Al, and Ti remains relatively unchanged with depth, whereas P is highly variable throughout the entire sequence (Table T4) and shows no correlation with depth. The remaining major elements show different behavior patterns above and below ~525 mbsf. Compared with the deeper basalts, the shallow basalts exhibit lower average CaO (9.7 vs. 13.3 wt%), higher Na_2O (3.8 vs. 2.1 wt%), and highly variable K_2O (0.9 to 2.8 wt%) and Sr (41 to 223 ppm) contents. This suggests significant seawater alteration. In the basalts below 525 mbsf, all of the above-mentioned elements except K_2O show only minor variations. As expected, the immobile trace elements Zr, Y, V, and Cr show no significant variations with depth, their average values being 48.3, 24.4, 261, and 390 ppm, respectively. The effect of seawater alteration is also demonstrated by comparing the more altered light-colored basalt in interval 195-1201D-46R-1, 134–136 cm, with the adjacent darker, presumably fresher, basalt in interval 46R-1, 138–140 cm (Table T4). The two samples, respectively, show decreasing values of Na_2O (from 5.5 to 4.0 wt%), Fe_2O_3 (from 9.8 to 8.8 wt%), and LOI (from 6.5 to 5 wt%), as well as increas-

F38. Plagioclase lath replaced by secondary minerals, p. 106.

T3. XRD data on selected basement samples, p. 194.

F39. Spherulite of clinopyroxene and plagioclase in vesicular groundmass, p. 107.

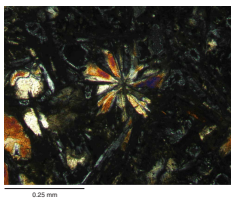

F40. Branching clinopyroxene and skeletal plagioclase in basalt, p. 108.

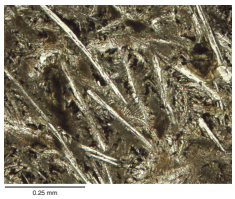

F41. Subophitic texture with plagioclase enclosed by clinopyroxene and olivine, p. 109.

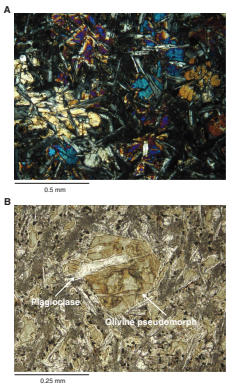

T4. Major, minor, and trace element content, p. 195.

ing CaO (from 7.35 to 9.7 wt%), Sr (from 26 to 64 ppm), and P_2O_5 (from 0.13 to 0.20 wt%) contents.

Overall, the basement rocks recovered from Site 1201 are primitive basalts, as confirmed by their overall high MgO and Cr contents (averages = 7.8 wt% and 400 ppm, respectively) and high Mg number values (average = 64.2, ranging from 55 to 68). These features are indicative of mantle-derived primary magmas (BVSP, 1981). Plotted on a total alkalis vs. silica diagram (LeBas et al., 1986), the majority of the analyzed samples fall in the basalt field with a few falling in the trachybasalt field (Fig. **F43**). The basalt samples have low contents of TiO_2 (0.77–1.02 wt%; average = 0.93 wt%) and Zr (43–52 ppm; average = 48 ppm).

The two samples of hyaloclastite (intervals 195-1201D-46R-4, 24–27 cm, and 46R-4, 31–33 cm) are geochemically similar to the basalts except for the higher concentration of alkalis (average Na_2O = 4.7 wt%; average K_2O = 2.0 wt%). Sample 195-1201D-46R-4, 31–33 cm, has an LOI value of almost 12 wt% and unusually low values of Cr, V, and Y.

The chemical composition of the basalts from Site 1201 has been plotted on tectonic discrimination diagrams using major and trace elements of proven immobility to infer their tectonic affinity. The basalt suite from Site 1201 straddles the MORB and island arc tholeiite (IAT) fields on both (Ti/100)-Zr-(Y×3) (Fig. **F44**) and Ti vs. V (Fig. **F45**) tectonic discrimination diagrams. On the other hand, the same samples plot in the IAT field on the TiO_2-(MnO×10)-(P_2O_5×10) (Fig. **F46**) but in the MORB field on the Y vs. Cr (Fig. **F47**) diagrams (Pearce, 1982; Pearce and Cann, 1973; Shervais, 1982; Mullen, 1983).

The basalts at Site 1201 lack the orthopyroxene typical of island arc basalts and display early crystallization of plagioclase, suggesting a fertile island arc mantle source (e.g., Wilson, 1989, and quoted references). Based on this and the proximity of Site 1201 to the Palau-Kuyshu Ridge remnant arc, it is likely that the mantle from which these rocks originated had geochemical features transitional between typical arc and backarc basin mantle (see DSDP Leg 59; Kroenke, Scott, et al., 1981). The basalts at Site 1201 are depleted in Zr (which is typical for island arc basalts) (Taylor et al., 1995) but are enriched in Cr and Mg (which is typical for primitive MORB and backarc basin basalt [BABB]). An arc affinity is also suggested by the low Ti content, which is uncommon for BABBs such as those from the Sumisu Rift (Gill et al., 1992) and the Lau Basin (Hawkins, 1995). Furthermore, the Site 1201 basalts have high Zr/Y ratios (average = 1.9 vs. 2.5–5.0 for typical MORBs) (Taylor et al., 1995) and low Ba/Zr ratios (average = 0.32). Both the Zr/Y and the Ba/Zr ratios are virtually identical to the Palau-Kyushu arc values of Wood et al. (1980). Taylor et al. (1995) reported rocks with arc affinities from sills penetrating the forearc basement of both the Mariana (ODP Site 781) and Izu-Bonin (Site 793) regions. Studies of the Kasuga Seamounts in the Mariana Trough by Fryer et al. (1997) have shown that arc volcanism can also occur on the backarc side of the frontal arc. The transitional arc affinity of the basalts recovered at Site 1201 is possibly a result of a similar tectono-magmatic setting.

BIOSTRATIGRAPHY

Of the five holes drilled at Site 1201, Holes 1201B, 1201C, and 1201D recovered a nearly continuous sedimentary succession. Smear slides were made from core catchers and selected intervals of these three holes for nannofossil examination. Because one major objective of this site

F42. Plot of Sr, CaO, K_2O, Na_2O, and LOI in basalt, p. 110.

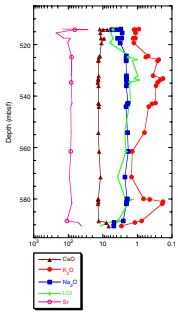

F43. Total alkalis vs. silica diagram for volcanic rocks, p. 111.

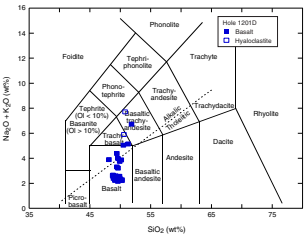

F44. (Ti/100)-Zr-(Y+3) discrimination diagram, p. 112.

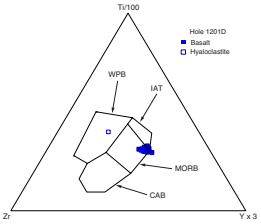

F45. Ti/1000 vs. V discrimination diagram, p. 113.

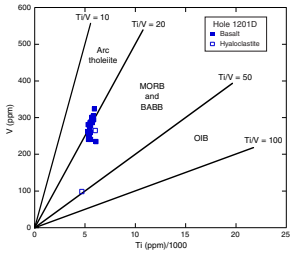

F46. TiO_2-(MnO×10)-(P_2O_5×10) discrimination diagram, p. 114.

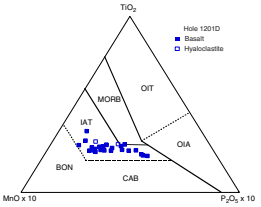

was to date the sediments contacting the basement, sediments that were situated immediately above the basalt and those sandwiched occasionally within the basalt were also examined.

Nannofossils are scarce in most of the core catchers we examined. Extra samples were taken from various carbonate-bearing intervals detected by HCl tests of the sediments. Moderately to well-preserved nannofossil assemblages were found in the bioturbated pelagic clays and mudstones intercalated within the turbidite sequence (see **"Lithostratigraphy,"** p. 10) (Table **T5;** Fig. **F48**). The fossil assemblages indicate that an expanded section of late Eocene–middle Oligocene age was recovered (Fig. **F49**). A detailed zonation of the sedimentary succession was difficult to prepare, partly because of the sporadic nature of the fossil occurrences and partly because of the inevitable reworking of old nannofossils into younger sections via turbidity currents. The frequent reworking makes the last occurrence (LO) of species less reliable for age determination. Unfortunately, the zonation scheme of the late Eocene–middle Oligocene sequence relies conventionally on many LOs of species.

To prepare a sensible zonation of the cored succession, special caution was taken to evaluate each of the first occurrences (FOs) and LOs of the age-diagnostic species. In the following section, we will first lay out our general consideration and weighing of the various datum levels in our record before giving the detailed description of the individual holes.

Upper Eocene and Oligocene Datum Levels Used at Site 1201

Dictyococcites bisectus

Almost every single nannofossil-bearing sample in the studied section contains this easily identified, morphologically distinctive species (Table **T5;** Fig. **F49**). *Dictyococcites bisectus* has a long range, between 38.0 and 23.9 Ma (Berggren et al., 1995). Both the FO and LO are considered reliable age markers (Wei, 1992; Berggren et al., 1995). The persistent presence of this species in our record ensures that the sequence belongs to the late Eocene–Oligocene.

Discoaster barbadiensis and *Discoaster saipanensis*

In calcareous nannofossil biostratigraphy, the Oligocene/Eocene boundary (33.6 Ma) is conventionally approximated by the extinction of *Discoaster barbadiensis* and *Discoaster saipanensis*. The LO of *D. saipanensis* has been preferred as a more reliable marker near the middle of Subchron C13r at 34.2 Ma (Wei and Wise, 1989; Berggren et al., 1995). The LOs of both species were designated in Sample 195-1201D-40R-6, 10 cm (462.36 mbsf). However, in the entire 510-m-thick sedimentary succession, there are only two samples near 462.4 mbsf containing good quantities of both species (Table **T5;** Fig. **F49**). The designation of the LOs and thus the boundary between Zones NP20 and NP21 at this level is circumstantial. Nevertheless, the common occurrence of both species in two consecutive samples, 195-1201D-40R-6, 10 cm (462.36 mbsf), and 40R-6, 25 cm (462.51 mbsf) ensures that the upper Eocene occurs in our record. The lack of *Isthmolithus recurvus* appears to indicate that the interval is still younger than 34.8 Ma (Berggren et al., 1995).

F47. Cr vs. Y discrimination diagram, p. 115.

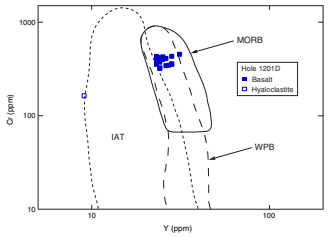

T5. Distribution of calcareous nannofossils, p. 197.

F48. Preservation and abundance of calcareous nannofossils, p. 116.

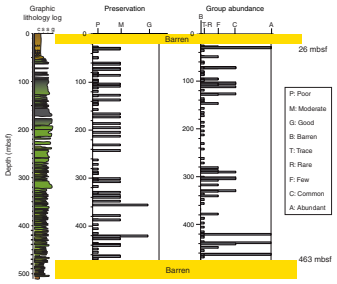

F49. Occurrence of age-diagnostic calcareous nannofossils, p. 117.

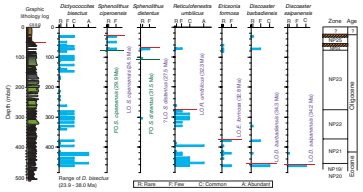

It is noticeable that a few reworked specimens of *D. barbadiensis* were spotted in various samples in the upper sections (Fig. F49; Table T5).

Ericsonia formosa

The LO of *Ericsonia formosa* has been widely used to define the Zone NP21/NP22 boundary. This datum level, near the bottom of Chron C12r at 32.8 Ma (Berggren et al., 1995), has been considered geologically synchronous and an excellent marker in the low and mid-latitudes (Wei and Wise, 1989). The presence of *E. formosa* at Site 1201 has not been abundant or persistent (Fig. F49; Table T5). Judging from the absence of this otherwise optically distinctive species in the long interval between Cores 195-1201D-1R and 30R, we anchored its last occurrence at 31R-CC (378.19 mbsf) (Fig. F49).

Reticulofenestra umbilicus

The LO of *Reticulofenestra umbilicus* has been widely used to mark the upper boundary of Zone NP22 in the upper Oligocene (Martini, 1971). Wei and Wise (1989) determined that the datum is located two-thirds of the way down in Chron C12, at ~32.3 Ma (Berggren et al., 1995). To ensure taxonomic consistency with previous work, we followed the commonly accepted cutoff size of 14 µm (Backman and Hermelin, 1986) to separate this species from the smaller but similar form termed *Reticulofenestra samodurovii* (= *Reticulofenestra dictyoda* or *Reticulofenestra coenura,* according to Wei and Wise, 1989). *R. umbilicus* is common to abundant in the lower sections of Hole 1201D, with its LO designated at 261.96 mbsf (Sample 195-1201D-19R-CC, 13–19 cm) (Fig. F49).

Spenolithus predistentus–Sphenolithus ciperoensis Lineage

The *Spenolithus predistentus–Sphenolithus ciperoensis* lineage evolved through the late Eocene and Oligocene. The evolution of this lineage provides three important datum levels for the nannofossil zonations of Martini (1971) and Okada and Bukry (1980). The first appearance of descendant species in such an evolutionary series has a great advantage over other age markers in assigning ages for the turbidite succession under study. However, the gradual evolution of this lineage hampers a consistent differentiation of the successive species by workers in the field when subjectivity gets involved in taxonomy (see discussions in Roth et al., 1971a, 1971b; Haq, 1972; Lang and Watkins, 1984; Moran and Watkins, 1988; Wei and Wise, 1989). Moreover, as noted by Wei and Wise (1989), the FO of *Sphenolithus distentus* in many localities is well below the LOs of *R. umbilicus* and *E. formosa* and is therefore in conflict with the original zonation scheme of Okada and Bukry (1980).

To circumvent the "*Sphenolithus* problem," we have adopted the criteria suggested by Moran and Watkins (1988) to differentiate species. They found that the most accurate characteristics for separating *S. ciperoensis* from *S. distentus* are the "extinction" lines of the proximal shield (basal disc of spines) under cross-polarized light using a light microscope and the width of the proximal shield (as originally proposed by Bramlett and Wilcoxon, 1967; Roth, 1970). Specifically, the descendant species, *S. ciperoensis,* is characterized by the following: (1) the proximal shield is wider than any point on the apical spine and (2) the "extinction" lines of the proximal shield are "chevronlike" and do not cross each other when the apical spine is at 45° to either polarizer. In con-

trast, the proximal shield of *S. distentus* is rarely wider than the base of the apical spine and the "extinction" lines are V-shaped and crossed (Moran and Watkins, 1988). Similarly, we differentiated *S. predistentus* from *S. distentus* by the criteria stated in Roth (1971b): "If the angle between the extinction line and the median axis is 90° or less, (the) forms are assigned to *S. predistentus*" (p. 1106 of Roth, 1971b).

At Site 1201, *S. predistentus* is the most common and long-ranged species within the lineage, rendering it less useful in subdividing the sequence into zones. The marker of the top boundary of Zone NP24 (27.5 Ma), the LO of *S. distentus,* was found at 71.78 mbsf (Fig. **F50**) (Section 195-1201B-10X-1, 68 cm), together with the last appearances of several other species, including *Bramletteius serraculoides, Discoaster tani ornatus, S. pseudoradians,* and *Helicosphaera compacta* (Fig. **F50**). The truncation of so many species simultaneously appears to suggest the existence of a hiatus.

The FO of *S. ciperoensis,* the marker of the base of Zone NP24, was observed at 72.98 mbsf, only slightly below the LO of *S. distentus* (the top of Zone NP24) (Fig. **F49**). Zone NP24 in Hole 1201B, defined accordingly, is therefore extremely short. In view of the shortness of Zone NP24, as well as the truncation pattern of many concurrent species, we interpret that a hiatus exists at about this level and that Zone NP24 is truncated. The truncation of ranges at 71.78 mbsf, however, is an artifact caused by the poor recovery of Cores 195-1201B-10X and 9X (Fig. **F49;** also see **"Lithostratigraphy,"** p. 10). The inferred hiatus, instead, is placed at 53.4 mbsf in Section 195-1201B-8X-4, where a distinct lithologic and color change separates lithologic Unit I from the underlying Unit II (see **"Lithostratigraphy,"** p. 10).

Figure **F50** summarizes our interpretation of the ranges of these age-diagnostic species as well as several additional species. The range chart shows clearly that six NP zones were recognized throughout the sedimentary succession.

F50. Ranges of selected age-diagnostic nannofossil species, p. 118.

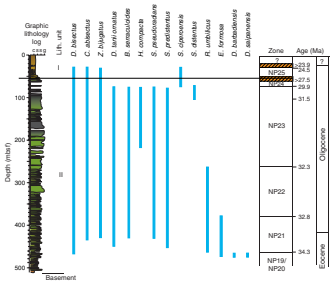

Hole 1201B

Nannofossils are generally scarce within the 90 m of Hole 1201B. Most core catchers are barren of nannofossils, except for a few samples in which traces or only a few specimens were spotted. Careful inspection and extensive sampling through the cored sections eventually yielded a few samples that contained sufficient nannofossils for biostratigraphic investigation (Figs. **F48, F49**). Section 195-1201B-4H-3 is exceptional in that it contains abundant, diversified, but only moderately preserved assemblages (Table **T5**). The consistent occurrence of *Dictyococcites bisectus* in Hole 1201B constrains the succession to be older than 23.9 Ma (late Oligocene). Indeed, the assemblages are dominated by *Cyclicargolithus floridanus,* with common occurrences of *Sphenolithus moriformis* and *Discoaster deflandrei,* typical of Oligocene tropical flora. Sample 195-1201B-4H-3, 68 cm (29.88 mbsf), witnessed the LO of *S. ciperoensis,* indicating an age older than 24.5 Ma (Berggren et al., 1995) (see also **"Biostratigraphy,"** p. 14, in the "Explanatory Notes" chapter). The lingering occurrence of *S. ciperoensis* continues downsection to Sample 195-1201B-10X-CC, 38–43 cm (72.98 mbsf), with the coexistence of *S. distentus*. The concurrent range of these two age-diagnostic species brackets an age of 27.5–29.9 Ma in Zone NP24 for the interval 71.8–73 mbsf. The shortness of Zone NP24 and the simultaneous truncation pattern of species, together with the distinct lithologic change at 53.4 mbsf, collectively suggest the existence of a minor

hiatus. We infer that the upper part of Zone NP24 is missing (Figs. F49, F50).

Hole 1201C

Hole 1201C is barren of nannofossils except for a few intervals that show traces of coccoliths (Table T5). Although lithology and various physical properties (e.g., magnetic susceptibility, color reflectance, and velocity) indicate that Hole 1201C is almost identical to Cores 195-1201B-1H to 5H, the nannofossil-bearing intervals in Section 195-1201B-4H-3 do not have corresponding counterparts in Hole 1201C. Such a discrepancy indicates that nannofossils were favorably preserved in certain localized pockets or patches and that these pockets were not laterally continuous.

Hole 1201D

Because of the high sedimentation rates and quick burial associated with turbidites, the long sedimentary succession in Hole 1201D consistently yields moderately to poorly preserved nannofossils. Except for the successive appearances of *D. saipanensis, E. formosa,* and *R. umbilicus,* the assemblages are almost monotonous throughout the succession. Variation in the nannofossil composition, if any, is dictated by dissolution intensity (Fig. F48). Despite the nuisance caused by dissolution and reworking, the nannofossil record allowed us to subdivide the sequence into four zones: NP19/NP20, NP21, NP22, and NP23 (Figs. F49, F50). Most of Hole 1201D (80 to ~425 mbsf) belongs to the lower Oligocene, but the part of the succession below 462 mbsf is definitely older than 34.3 Ma (Table T6).

T6. Estimated ages of nannofossil datum levels, p. 203.

The lack of any nannofossils in the lowermost section (195-1201D-40R-7 to 53R [463–523 mbsf]) makes it impossible to gauge an age for the basement. In middle Eocene–early Oligocene time, Site 1201 would have been located in the equatorial zone (using the paleogeographic reconstruction of Cambray et al., 1995). The occurrence of abundant sphenoliths and discoasters in the succession and the lack of any high-latitude dwellers such as *Chiasmolithus* is consistent with this paleogeographic reconstruction. The lack of any calcareous microfossils in the lower section also fits the history of the calcite compensation depth (CCD) in the equatorial Pacific. Van Andel et al. (1975) documented clearly that the CCD dropped during the Eocene–Oligocene transition. It is likely that the shallow CCD during the Eocene prevented calcareous microfossils from being preserved. On the other hand, we have observed Eocene nannofossils from Zone NP19/NP20 for the first time on the sedimentary apron of the western flank of the Palau-Kyushu Ridge. In comparison, the oldest sediments above the basalt contact drilled at DSDP Site 447 are middle Oligocene (NP23) in age (Martini, 1981), whereas at Site 290 they are latest Eocene in age (NP20) (Ellis, 1975).

Section 195-1201D-44R-4, 140 cm (499.6 mbsf), contains radiolarians in red clay (or porcellanite). Potential utility of the radiolarians for biostratigraphic age determination at this site awaits further exploration. Despite extensive sampling and close examination of sediments sandwiched in the basalt section in Cores 195-1201D-45R to 53R, no nannofossils were found. Instead, examination of thin sections of interpillow fillings in the basalt sections revealed traces of microfossils, possibly radiolarians (e.g., see Fig. F31B for a biogenic clast found in the in-

terpillow sediments). These biotic remains possess great potential for revealing the ages of these sediments.

Discussion and Conclusions

At Site 1201, a 509-m-thick sedimentary succession was recovered above the basaltic basement. The topmost (0–26.5 mbsf) and lowermost (462–509 mbsf) sections are barren of nannofossils. Although traces of diatoms and ichthyoliths were spotted in the top section, the lack of calcareous nannofossils in the upper 26 m makes it impossible to assign any ages for the top section. The upper pelagic clay of Unit I is thinner than similar units cored at DSDP Sites 290 (~90 m) and 477 (37.5 m) located south of Site 1201. The uppermost unit at DSDP Site 290 was thought to be early Pliocene, underlain by Oligocene nannofossil-bearing clay, whereas the top unit in DSDP Hole 477 was regarded to be early Miocene in age based on fossil fish teeth. It is premature to correlate the top section (0–26.5 mbsf) of Site 1201 to either of the DSDP sites or to draw any conclusion about the nature of the hiatus based on the shipboard biostratigraphic investigation. The lack of post-Oligocene-age calcareous microfossils in the top section of Site 1201 has been attributed to the submergence of the ocean floor through the CCD after the early late Oligocene (Scott et al., 1980).

Moderately to poorly preserved nannofossils in the turbidite succession (lithostratigraphic Unit II) allowed us to recognize six biozones spanning from Zone NP19/NP20 to NP25 (Fig. **F50**). The estimated ages of the major bioevents are listed in Table **T6.** The turbidites between 54 and 462 mbsf represent an expanded sequence of late Eocene–early Oligocene age consisting of the top of Zone NP19/NP20, Zones NP21, NP22, NP23, and a truncated Zone NP24. Separated by a short hiatus, lying on top of the turbidites, is a 25-meter-thick sequence of upper Oligocene (29.4–54.3 mbsf) (NP25) red claystone (Fig. **F50**). The age of the basal 47 m of sediments above the basement contact is unknown. Nevertheless, compared to the previous drilling results from DSDP Sites 290 and 477, the Eocene sediments (>34.3 Ma) recovered at this site are the oldest observed so far on the sedimentary apron of the Palau-Kyushu Ridge. Radiolarians found in Section 195-1201D-44R-4, 140 cm (499.6 mbsf), may have potential for constraining the age of the bottom sediments.

Overall, the recovered succession at Site 1201 is similar to the material recovered from DSDP Sites 290 and 447 located south of this site. However, Site 1201 is unique in having an expanded early Oligocene section, which provides a detailed high-resolution record of the history of the Palau-Kyushu Ridge.

PALEOMAGNETISM

All core archive halves from Holes 1201A, 1201B, 1201C, and 1201D were measured on the shipboard pass-through superconducting rock magnetometer. Natural remanent magnetization (NRM) and remanent magnetization after 5-, 10-, 15-, and 20-mT alternating-field (AF) demagnetization steps were measured at 5-cm intervals. In situ orientation data were collected with the Tensor tool for all APC cores from below 30 mbsf.

A total of 311 oriented discrete samples (standard 8-cm^3 plastic cubes from Hole 1201B and 8-cm^3 cubes cut with a nonmagnetic parallel saw

from Hole 1201D) were collected from the working halves at a resolution of one to two samples per core section for progressive AF and thermal demagnetization and for rock magnetic studies. Samples from the turbidite sequence from Hole 1201D were taken from the fine-grained parts of the turbidites (see "Lithostratigraphy," p. 10). The basaltic basement (509–600 mbsf) was sampled at a frequency of one per section and was complemented with samples taken at the same frequency for the physical properties measurement program. All discrete samples were demagnetized at successive peak fields of 5, 10, 15, 20, 25, 30, 35, 40, 50, 60, 70, and 80 mT to verify the reliability of the split core measurements. Two hundred forty-six of the 273 sediment samples yielded good principal component analyses (PCAs) (Kirschvink, 1980) with fits having an average maximum angular deviation (MAD) of 4.4°. The PCA of all 38 basalt samples yielded excellent results with an average MAD of 1.8°. Twelve discrete samples were also progressively thermally demagnetized at temperatures of 100°, 200°, 300°, 350°, 400°, 450°, 500°, 550°, 570°, 580°, 590°, 600°, and 640°C to assess the effectiveness of thermal vs. AF demagnetization and for mineral magnetic analyses.

A composite paleomagnetic record was constructed for Site 1201 using data from Holes 1201B (0–81 mbsf) and 1201C (80–509 mbsf). Data from Hole 1201C repeat the APC section of the record for Hole 1201B and for this reason are not incorporated in the composite record presented in this site report.

Both magnetic declination and inclination were used when possible for the magnetostratigraphic interpretation at this site. The geomagnetic field at the latitude of Site 1201 (19.28°) has an inclination of 35°, assuming a geocentric axial dipole model, which is sufficiently steep to determine magnetic polarity in APC, XCB, and RCB cores that lack a horizontal orientation.

Mineral magnetic analyses were performed on discrete samples after AF demagnetization. The low-field magnetic susceptibility and the anhysteretic remanent magnetization (imparted using a 100-mT alternating field and a 0.05-mT bias field) were routinely measured on all samples. On selected samples, we measured the acquisition of an isothermal remanent magnetization (IRM) up to 1.0 T and the coercivity of backfield remanence (B_{cr}).

Rock Magnetism and Paleomagnetic Behavior

The magnetic susceptibility and anhysteric remanent magnetization (ARM) (Fig. F51) are concentration-dependent measurements that are sensitive to the amount of magnetic material present. The ARM is more sensitive to the fine-grained magnetic grains, whereas the magnetic susceptibility measures coarser-grained magnetic particles. The lowest values and the least variability of these parameters are recorded in the upper 50 mbsf of the core and are directly related to lithologic variation (brown clays of lithostratigraphic Unit I) (see "Lithostratigraphy," p. 10). Between 50 and 509 mbsf, the base of the sedimentary section, the variability of both parameters is dominated by the lithologic variations within the turbidite sequences (lithostratigraphic Unit II). With the exception of an interval of higher magnetic concentration, recorded by both magnetic susceptibility and ARM between 100 and 120 mbsf, both parameters appear to be related to small- and large-scale turbidite cycles. The ARM/*k* ratio is a concentration-independent parameter that provides an estimate of relative magnetic grain-size changes (Thompson and Oldfield, 1986; Verosub and Roberts, 1995). The small-

F51. Concentration-dependent parameters and magnetic grain-size proxy, p. 119.

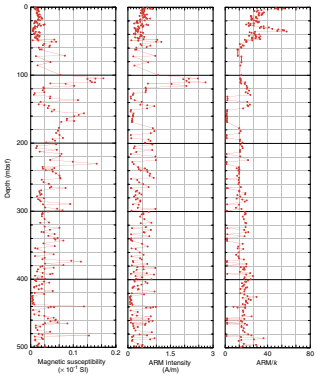

est magnetic grain sizes are found in the brown pelagic clays of lithostratigraphic Unit I (Fig. F51), with peaks within the top few meters and at 35 mbsf. The turbidite sequence is characterized by alternating intervals of very coarse grained magnetic minerals (low ARM/*k* ratio) with finer-grained material.

Figure F52 shows representative curves of acquired IRM to saturation IRM (SIRM) and backfield SIRM. Samples from both lithostratigraphic units and the underlying pillow basalt exhibited very uniform behavior, were saturated by 300–500 mT, and had B_{cr} values of 8–24 mT. AF demagnetization of these samples (Fig. F53) demonstrated moderate to soft magnetization, with ~50%–90% of the intensity of magnetization lost by the 20- to 30-mT demagnetization step. Samples from lithostratigraphic Unit II had a harder magnetization, in general.

Thermal demagnetization of sediments from both lithostratigraphic units and pillow basalts shows two sharp decreases in magnetization, indicating the presence of at least two carrier minerals of magnetic remanence (Fig. F54). The inflection point at ~450°C suggests that minerals such as goethite or maghemite, which undergo thermal unblocking at these temperatures, contribute to the magnetic signal. At present, we do not have enough evidence to distinguish between these two possibilities. All measured samples display Curie temperatures (T_c) of 570°C, suggesting that the dominant magnetic mineral is magnetite with minor substitution of other elements (e.g., Ti, Al, or Mg), which decreases the Curie temperature from that of pure magnetite (T_c = 585°C). One basalt sample from the deepest part of the section (Section 195-1201D-55R-2, 10 cm) displays a T_c of 585°C and retains a few percent remanence up to 640°C, indicating the presence of impure hematite. Therefore, it is likely that Ti-bearing magnetite is the dominant carrier of magnetic remanence and susceptibility, with varying contributions from goethite(?) or maghemite(?) and hematite.

Average NRM intensities are 0.102 A/m in lithostratigraphic Unit I, 0.058 A/m in the turbidite sequence of Unit II, and 4.76 A/m in the pillow basalts (Fig. F55). The NRM measurements display inclinations ranging between –84° and +89° (mean = 33°). Inclination values after 20-mT demagnetization are skewed toward positive (downcore) values that are consistent with a steeply positive drill string overprint induced during coring. These values show that the 20-mT demagnetization step has not been completely effective in removing the overprint from the split-core archive halves.

The demagnetization behavior of discrete samples that yielded good PCA results from all lithologies is illustrated in Figure F56. Most, but not all, samples displayed a soft magnetic overprint that was removed between 5 and 25 mT. PCA of the entire whole-core record is possible with the four demagnetization steps applied during the paleomagnetic measurements program and will identify where additional cleaning of the paleomagnetic data and demagnetization of discrete samples will aid in elucidating the characteristic remanent magnetization (ChRM) at Site 1201.

Magnetostratigraphy

The interpretation of magnetic polarity from the composite inclination and declination record for Site 1201 (Fig. F57) is well constrained by key nannofossil datums spanning Biozones NP19/NP20 to NP25 between 29 and 462 mbsf (see "Biostratigraphy," p. 23; also see "Bio-

F52. IRM and backfield acquisition curves, p. 120.

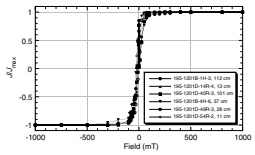

F53. Magnetic intensity as a function of increasing AF field, p. 121.

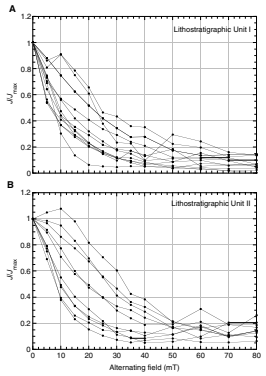

F54. Thermal demagnetization data from sediment and basalt, p. 122.

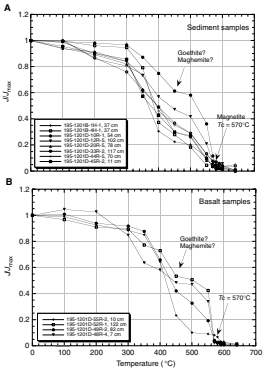

F55. Magnetic susceptibility, intensity, and inclination, p. 123.

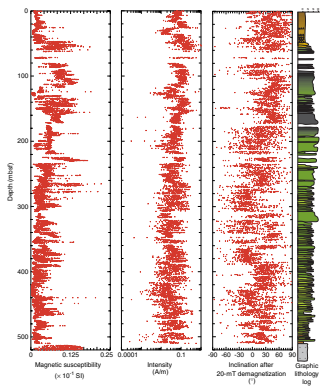

stratigraphy," p. 14, in the "Explanatory Notes" chapter). The top 29 mbsf is barren of nannofossils, and the preliminary magnetostratigraphic interpretation of this interval (Fig. F57A) is not constrained by any biostratigraphic datums. The inclination record for this interval, when compared with the GPTS (Cande and Kent, 1995; Berggren et al., 1995), assuming constant sedimentation rates, provides a complete record from the Thvera Subchron (C3n.4n) through late and middle Miocene polarity intervals to Subchron C5Bn.1n, close to the base of the middle Miocene (Table T7). This part of the magnetic record is characterized by sharp 180° reversals of the magnetic declinations, which allow the identification of magnetic chrons and subchrons. The magnetic inclination record, on the other hand, is ambiguous and strongly biased toward positive values and can, for the most part, only be interpreted with the help of discrete samples (Fig. F57A). The magnetic polarity reversals and the correlation with the GPTS show that the upper and middle Miocene record at Site 1201 is remarkably complete and possesses strikingly uniform sedimentation rates. The characteristic reversal patterns of the Brunhes, Matuyama, Gilbert, and Gauss Chrons are not discernible at the top of the section, which suggests that the last 5 m.y., consisting of the entire Pleistocene and most of the Pliocene, are missing at Site 1201. This hiatus implies that there is currently no sediment being deposited at Site 1201 or that sediment has been or is being eroded.

The reversed polarity chron below Subchron C5Bn.1n (24–26 mbsf) contains the LO of nannofossils *Dictyococcites bisectus* (>23.9 Ma) and *Spenolithus ciperoensis* (24.5 Ma), constraining this interval to Chron C6Cr. Sedimentological evidence (see **"Lithostratigraphy,"** p. 10) for a hiatus in Section 195-1201B-3H-6, 56 cm (24.8 mbsf), and the absence of continuity in the correlation with the GPTS suggest that the lower part of the normal polarity chron between 24 and 26 mbsf belongs to the late Oligocene Subchron C6Cn.3n. The middle Miocene to late Oligocene unconformity, defined by a combination of magnetostratigraphic, biostratigraphic, and sedimentological evidence spans ~10 m.y.

The normal polarity event between 31.7 and 35.1 mbsf correlates with Subchron C7n.2n. The upper Oligocene record below Chron C7n cannot be interpreted because the magnetic signal is noisy, the correlation between magnetic declination and polarity that guided the magnetostratigraphic interpretation in the top 25 mbsf of the section is missing, the sampling resolution of the discrete samples is not sufficient, and biostratigraphic datums have not been identified. Poor recovery at the bottom of Hole 1201B caused a coring gap between Holes 1201B and 1201D that complicates the magnetostratigraphic interpretation between 60 and 80 mbsf.

The truncation of several nannofossil species at a distinct lithologic change between lithostratigraphic Units I and II (see **"Lithostratigraphy,"** p. 10) defines a hiatus at 53.4 mbsf within the upper part of nannofossil Zone NP24 (see **"Biostratigraphy,"** p. 23).

The LO of *S. distentus* (27.5 Ma) occurs in the normal polarity chron between 50 and 60 mbsf, which probably correlates this interval with one of the subchrons of Chron 10n. The FO of *S. ciperoensis* (29.9 Ma) within Core 195-1201B-10X constrains this short normal polarity interval to Subchron C11n.2n.

The magnetic inclination record in the RCB section of the turbidite interval between 100 and 500 mbsf defines several long normal and reversed polarity chrons (Fig. F57B). The normal polarity interval between 90 and 173 mbsf contains the FO of *S. distentus* (31.5 Ma), which

F56. Vector component diagram with normalized intensity decay plots, p. 124.

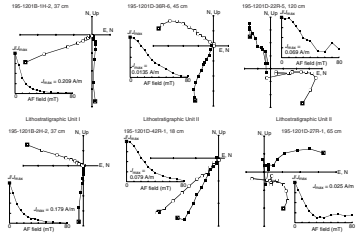

F57. Magnetostratigraphic record from 0 to 509 mbsf, p. 125.

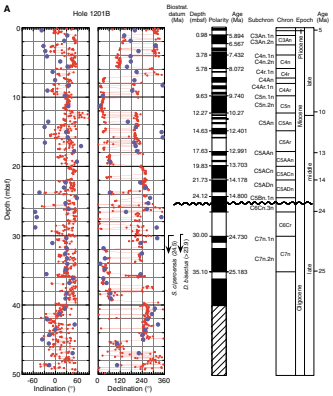

T7. Compilation of magnetostratigraphy, p. 204.

constrains this interval to Chron 12n. The long reversed polarity interval between 173 and 389 mbsf correlates to Chron C12r and is well constrained by the LO of *Reticulofenestra umbilicus* (32.3 Ma) and *Ericsonia formosa* (32.8 Ma).

The transition to the upper Eocene occurs at the well-defined polarity transition at 423.4 mbsf, the onset of Chron C13n. Three normal polarity intervals can be distinguished in the upper Eocene strata that are assigned to Chron 15n and the two subchrons of Chron 16n. Two nannofossil events at 462 mbsf, the LO of *Discoaster barbadiensis* (34.3 Ma) and *D. saipanensis* (34.2 Ma) constrain Chron C15r between 468 and 458 mbsf. The termination of Subchron 16n.2n at 35.685 Ma, more than 20 m above the basaltic basement, is the oldest and lowermost magnetostratigraphic event that can be identified at Site 1201. The onset of Subchron 16n.2n could not be determined, but the normal polarity continues right to the contact with the basement.

In the 509-m Neogene–Paleogene composite record of Site 1201, 65 subchrons of the GPTS are present. The record is interrupted by three major hiatuses, between 0 and 5 Ma, 14.8 and 24.1 Ma, and in the top section of Biozone NP24 in the uppermost Oligocene (see **"Biostratigraphy,"** p. 23). A paleomagnetic age model for Site 1201, listing depths and ages of magnetic polarity reversal events, is given in Table **T7**.

Sedimentation Rates

An age-depth summary for Site 1201, using the GPTS reversal polarity ages given in Berggren et al. (1995) and the nannofossil events (see **"Biostratigraphy,"** p. 23), is provided in Figure **F58A** (entire record) and **58B** (0–60 mbsf). The average sedimentation rate for lithostratigraphic Unit I above the Miocene/Oligocene unconformity (0–24.8 mbsf) is 3 m/m.y. Above the unconformity, the average sedimentation rate decreases from 4 m/m.y. in the middle Miocene to 2 m/m.y. in the late Miocene at a well-defined inflection point at 15 mbsf (12.5 Ma). The average sedimentation rates in the interval between the two hiatuses (24.8–51 mbsf) is 8 m/m.y. and increases to >100 m/m.y. in the turbidites between 100 and 420 mbsf. An inflection point at 420 mbsf (33.5 Ma) denotes a change to lower sedimentation rates (35 m/m.y.) between 420 and 485 mbsf. The lack of biostratigraphic and magnetostratigraphic ages directly above the basement precludes the assessment of sedimentation rates for this important part of the section.

The trend to decreasing sedimentation rates from the late Eocene to the early Pliocene reflects the environmental history of the West Philippine Basin in the vicinity of the Palau-Kyushu Ridge with extensive amounts of reworked arc-derived volcaniclastic material deposited from the late Eocene through the early Oligocene and a transition to a deep-water environment with slower pelagic sedimentation in the middle to late Miocene. The onset of a bottom-water current sometime after the early Pliocene could be responsible for the nondeposition or erosion of sediments <5 Ma.

Basaltic Basement

PCA of 38 basalt samples revealed magnetically extremely well-behaved samples (Fig. **F59**). A soft magnetic overprint was easily removed with AF demagnetization techniques. A comparison between AF and thermal demagnetizations carried out on two basalt samples (Fig. **F59**) demonstrates that although a small high-temperature and high-

F58. Age model and correlation of the composite magnetic polarity, p. 127.

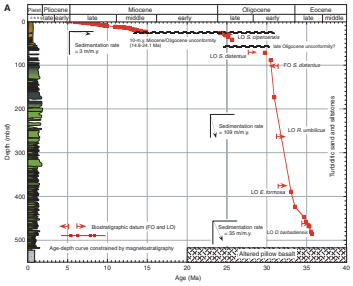

F59. Demagnetization behavior of representative basalt samples, p. 129.

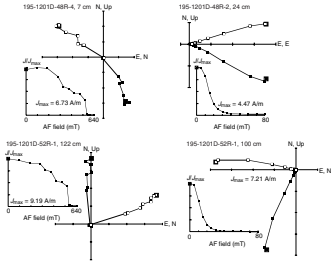

coercivity component can be present, the AF technique is more effective in isolating the ChRM. The magnetic inclination record shows a mean inclination of 13.9° between the top of the basement at 509 mbsf and 530 mbsf (Fig. F60). Inclinations between 530 and 550 mbsf are shallow, with both positive and negative polarity. The bottom part of the basalt sequence (550–600 mbsf) is characterized by shallow inclinations with negative polarity. The mean inclination for this part of the section is –12.8°. Although the basalt has been severely altered, the thermoremanent magnetization carried by the (titano) magnetites is not affected.

The age of the basement at Site 1201 was estimated from seafloor anomalies (Chron 21) to be middle Eocene (~48 Ma). The inclination record of the basalts suggests the existence of a magnetic reversal at 550 mbsf. Magnetic inclinations above and below this reversal are shallow (13°–14°) and pass the reversal test by being perfectly antipodal. They indicate a position of the Philippine plate near the equator, at ~7° paleolatitude, during the middle Eocene. This supports the model of a major northward movement of the plate proposed by Hall et al. (1995), based on earlier coring results, to the current position of 19° latitude at Site 1201.

F60. Magnetic inclinations of discrete basalt samples, p. 130.

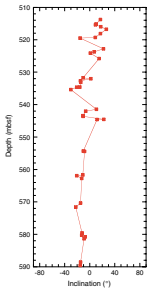

GEOCHEMISTRY

The shipboard geochemistry program focused on inorganic constituents in interstitial water (Table T8). Six samples of the basal sediment from Hole 1201D were also analyzed (Table T9). Routine headspace gas samples were collected, but none contained methane above the detection limit of 3 ppmv.

T8. Composition of interstitial water, p. 205.

T9. Composition of basal sediment and lithogenous pelagic clay, p. 207.

Interstitial Water

Fifty-three samples of interstitial (pore) water were recovered by squeezing whole rounds from 34 cores, 1 from Hole 1201A, 9 from Hole 1201B, and 24 from Hole 1201D. The deepest pore water was sampled from just above basement, at 510 mbsf in Hole 1201D. The three holes constitute a single section because they were drilled within ~60 m of one another and their total depths overlap.

Changes in pore water chemistry at Site 1201 reflect lithologic changes. The sedimentary section can be divided into three parts: (1) red to tan silty clay from the seafloor to ~55 mbsf, (2) gray to green volcaniclastic breccia and sandstone and siltstone turbidites from 55 to 507 mbsf, and (3) reddish brown claystone from 507 to 510 mbsf. The volcaniclastic materials are increasingly altered to clays and zeolites with depth (see "Lithostratigraphy," p. 10).

Results

The composition of the interstitial water at Site 1201 is quite unusual for deep-sea sediments and reflects the extreme alteration of the volcaniclastic materials and sandstones that comprise the lower 250 m of the section. The most unusual feature is the large increase in pH, Ca, and chlorinity. Calcium increases to 270 mmol/kg, 27 times the concentration in seawater, by leaching from the volcaniclastic material. Chlorinity increases to 645 mmol/kg, 20% higher than the seawater value, by loss of water of hydration to the altered basalts. The gain in Ca is bal-

anced by the loss of nearly all of the Mg and K from seawater, but mainly by a 70% decrease in Na, to 140 mmol/kg. As a result, the pore water from Site 1201 at 190 mbsf and below contains far more Ca than Na (Table **T9**). In seawater, Na comprises about 78% of the cations and chloride about 90% of the anions on a milliequivalent basis (Fig. **F61**). Subordinate cations are Mg (18%), Ca (3%), and K (1%), whereas subordinate anions are sulfate (9%) and bicarbonate ([alkalinity] 1%). In the average pore water from Site 1201, by contrast, Ca comprises 38% of the cations and, in a Ca-rich sample from 499.7 mbsf, 67% of the cations (Fig. **F61**). The proportion of chloride increases to 92% in the average pore water from Site 1201 and to 95% in the Ca-rich pore water. The large increase in Ca inevitably saturates the solution with gypsum, causing sulfate to decrease from 28 to 15 mmol/kg as gypsum precipitates. Alkalinity falls from the seawater value of 2.4 to <1 meq/kg as it is consumed by formation of authigenic minerals. These reactions likewise cause the rise in pH to 10.0 from the seawater value of ~8.1, reflecting extreme diagenesis or perhaps zeolite facies metamorphism accompanied by extensive authigenesis.

Between 83 and 147 mbsf in Hole 1201D, the sandstone and siltstone turbidites and breccia were too indurated to yield pore water. Fortunately, this sampling hiatus does not interrupt the smooth depth profiles exhibited by most of the dissolved constituents (Figs. **F62, F63, F64, F65**). Exceptions are sulfate, Na, and K. Unfortunately, the major inflection point in cross-plots of Ca vs. Na, Cl, Mg, K, sulfate, and alkalinity (not shown) occurs within this interval, connecting generally linear segments above and below. The linear segments are consistent with diffusion as the major process within these depth intervals, whereas the inflection points imply the presence of a chemical reaction zone. Below the hiatus, the decreases in Mg, K, and sulfate with increasing Ca become less steep, whereas the decrease in Na and increase in chlorinity become steeper. (In keeping with these trends, the slope of Na vs. chlorinity is essentially constant with depth.) The slope of alkalinity vs. Ca actually changes from negative (decreasing alkalinity with increasing Ca) within the depth interval of 0–73 mbsf sampled in Hole 1201B to positive (increasing alkalinity) within the interval 147–510 mbsf sampled in Hole 1201D. (The uppermost pore water sample from 83 mbsf in Hole 1201D falls at an intermediate point that is not on either line.) These observations suggest that the most intense uptake of Mg, K, and sulfate is occurring within the upper reaction zone centered at ~110 ± 30 mbsf, whereas the most intense hydration, uptake of Na, and release of Ca is occurring within the basal sediments and possibly within basement. Reactions include alteration of feldspar and glass to smectite and Na-Ca-K zeolites and precipitation of gypsum (see **"Lithostratigraphy,"** p. 10).

The reality of an upper reaction zone is confirmed by large, broad maxima in dissolved Si, Sr, and Mn and a smaller maximum in fluoride in this depth interval (Fig. **F64**). These elements are all known to be quite reactive in deep-sea sediments. The Si maximum results from dissolution of silica and/or silicate phases. The Mn maximum implies suboxic to reducing conditions at that depth, and a Sr maximum is typically associated with recrystallization of calcium carbonate. The Li and B profiles resemble those for Na and K, except that the concentrations of Li and B increase slightly with depth between ~150 and 500 mbsf. Aluminum increases steadily with depth between 83 and ~300 mbsf and then levels out.

F61. Major anions and cations compared with seawater, p. 131.

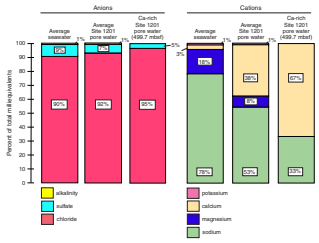

F62. Interstitial water pH, alkalinity, ammonia, sulfate, and chlorinity, p. 132.

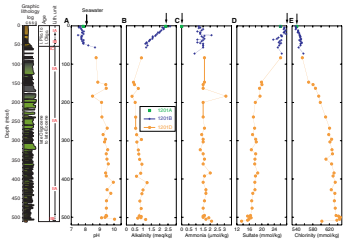

F63. Interstitial water Mg, Ca, Na, and K, p. 133.

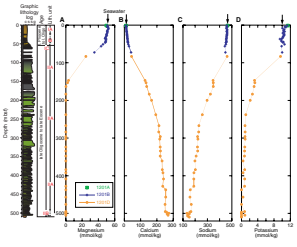

F64. Interstitial water Si, Sr, Mn, and F, p. 134.

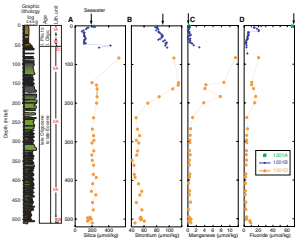

Comparisons among pore water compositions can also be made on the basis of equilibrium mineral assemblages calculated from thermodynamic principles. The computer code PHREEQC simplifies these calculations (Parkhurst and Appelo, 1999). Pore water precipitates minerals when it is oversaturated with the mineral's chemical constituents and dissolves minerals when it is undersaturated with those constituents. Pore water in equilibrium with minerals neither precipitates nor dissolves those phases. The stability of minerals in aqueous solutions is quantified with the saturation index (SI), which is >0 for minerals that precipitate, <0 for minerals that dissolve, and 0 for equilibrium. Increases in the relative values of negative SIs are also significant because they point to closer approach of mineral precipitation. The uncertainty of SI values is variable because some aqueous systems are well characterized, whereas others are not. For example, calcite SIs are accurate to about ±0.1 SI units, but the uncertainty for zeolites is ±1–2 SI units. The calculations were made for temperature = 3°C and pH = 8.5.

Saturation indices for selected minerals reveal three general trends (Table **T10**). One is an increase in sepiolite SIs with depth, sepiolite representing a Mg sink. Note, however, that smectite is the true magnesian clay likely to precipitate under alkaline conditions, such as those in the deeper pore water from Site 1201. Saturation indices for this more complex clay are not calculated by PHREEQC. Second, zeolite SIs increase with depth, particularly those of laumontite and leonhardite, which are not present at Site 1201 but were used to model zeolite behavior because they are among the most silica-poor and water-rich zeolites. These zeolites can accommodate Na in exchange for Ca. The sodic zeolite analcime could also accommodate Na. Precipitation of hydrous minerals such as clays and zeolites causes increased chloride concentrations in residual water (Fig. **F63A**). A third trend is increased SIs with depth for anhydrite and gypsum. Gypsum SIs increase substantially across the indurated zone, implying increased amounts of gypsum precipitation within and below this interval. Gypsum takes up Ca, sulfate, and H_2O.

Discussion

Diagenesis of volcanic sediments has been documented in several western Pacific basins (e.g., Gieskes and Lawrence, 1981; Egeberg et al., 1990; Torres et al., 1995). These findings are based on pore water recovered from DSDP and ODP drill sites. Calcium enrichment accompanied by Mg depletion with increased depth below the seafloor is the characteristic chemical pattern. The same pattern is present at Site 1201.

Fresh volcanic ash, glass, and shards from the Mariana arc contain ~2–13 wt% CaO and 0–10 wt% MgO (Arculus et al., 1995). These materials provide a rich source of Ca in the sediments. An alternative Ca source is carbonate in the sediments. Carbonate dissolution would cause an increase in alkalinity, as is seen in Hole 1201D, between ~200 and 500 mbsf. Smectite was identified in XRD analyses of volcanic materials at Site 1201 (see **"Lithostratigraphy,"** p. 10). This clay is the likely sink for Mg. Increases in Ca require Na decreases that are twice as large to maintain charge balance. Sodium can enter clays, zeolites, albitized plagioclase, and other secondary phases. Diagenetic changes such as these can account for the major patterns of pore water chemistry in the altered volcanic sediments at Site 1201.

F65. Interstitial water Li, B, and Al, p. 135.

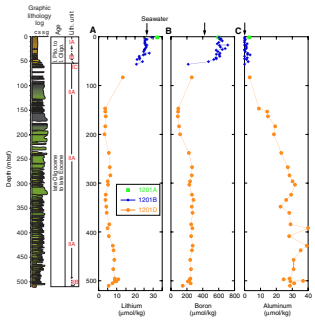

T10. Mineral saturation indices vs. depth, p. 208.

Sediment Geochemistry

Six samples of the basal sediment from Hole 1201D were analyzed because of their unusual appearance (Table T9). The basal layer immediately above basement (two samples) is a dark chocolate-brown claystone. This layer grades upward into grayish brown uniform to laminated claystone (two samples) and laminated dark gray claystone (one sample) with pink interlayers (uppermost sample). In general, the uppermost two samples are similar to the lithogenous pelagic clays of Chester and Aston (1976) (Table T9). They have similar amounts of Si, Al, Fe, Mg, Na, and P but only one-half as much Ti and K, and three to five times as much Mn and Ca. The other four samples are progressively more dissimilar. Compared with the lithogenous pelagic clays, the lowermost two have only 80% of the Mg, two-thirds of the Si, Al, and Na, and less than one-half the Ti and K. They are enriched 3-fold in Fe, 6-fold in Ca and P, and up to 12-fold in Mn. Whereas all six samples from Site 1201 are relatively depleted in Ti and K and enriched in Mn and Ca, for the other elements they could be modeled as mixtures of lithogenous pelagic clay, goethite (identified by XRD) (see "Lithostratigraphy," p. 10), Mn oxide/hydroxide, and apatite.

PHYSICAL PROPERTIES

All whole-round core samples from Holes 1201A, 1201B, 1201C, and 1201D longer than 40 cm were run through the MST. The XCB cores from Hole 1201B and the RCB cores from Hole 1201D have a diameter of ~5.75 cm, smaller than the nominal 6.6-cm core diameter recovered by the APC at Site 1201. The values measured by the MST are corrected for the reduced core diameter as at Site 1200 (see "Physical Properties," p. 40, in the "Site 1200" chapter), with the exception of the magnetic susceptibility logger (MSL) measurements (σ), which were corrected for the reduced sample volume using Equation 1:

$$\sigma_{corr} = (\sigma_{meas}/1.03) \times 10^{-5}. \quad (1)$$

The values in the database do not reflect these corrections.

The *P*-wave velocity logger was able to obtain *P*-wave velocity measurements only through the APC cores. The degree of consolidation in the sediment at depths >46 mbsf prevented both discrete *P*-wave velocity measurements using the insertion transducers (PWS1 and PWS2) and formation factor measurements on split core samples. At depths >46 mbsf, *P*-wave velocity was measured along the x-, z-, and, occasionally, the y-axis of the core using discrete minicore samples and the contact transducers (PWS3). The minicore samples were subsequently used for index properties measurements.

RCB cores from Hole 1201D were recovered in pieces ranging in length from a few centimeters to in excess of 1 m; very little of the core was affected by biscuiting. The gaps, or fractures, between each piece reduce the magnetic susceptibility values by a small amount at a distance of up to ~10 cm on either side. Gamma ray attenuation (GRA) density values are reduced almost to zero by the presence of a gap. As at Site 1200, the effect of the gaps was not removed from the MSL data set but anomalously low density values (<1.0 g/cm^3 or values obviously outside the local trend) were eliminated from the GRA data set by hand (see "Physical Properties," p. 40, in the "Site 1200" chapter).

Results from the corrected MST runs are presented in Figure F66, and results with the depth scale expanded in 100-m intervals are presented in Figures F67, F68, F69, F70, F71, and F72. Holes 1201B and 1201C cored a similar depth interval, and results from the MST are very similar (Fig. F73). Index and physical properties measurements are presented in Tables T11 and T12.

Volume Magnetic Susceptibility

The values of volume magnetic susceptibility measured in the pelagic muds are relatively low and constant at ~200 × 10^{-5} (SI units). The values increase at the boundary between the pelagic muds and the turbidites. The mean value for the turbidites is ~500 × 10^{-5}. The variability of the susceptibility values is higher in the turbidites compared to the muds, with values ranging from near zero to >2000 × 10^{-5}. High values occur only over very short intervals, giving the data a "spiky" appearance. The spikes likely correspond to greater concentrations of magnetite, which may be present at the base of turbidite sequences because of magnetite's higher than average grain density or because of better preservation of magnetite in the coarser clasts. The sharp decreases in magnetic susceptibility at depths of 341.0 and 347.0 mbsf correlate with boundaries between larger-scale turbidite sequences. The values of magnetic susceptibility increase below the boundary between the sedimentary succession and basaltic basement. Although the highest values of magnetic susceptibility in the basalts are less than high values in the turbidites, the values in the basalts have a higher mean value of ~800 × 10^{-5} and are more evenly distributed.

It is possible to identify several scales of turbidite sequences in the magnetic susceptibility data measured by the MST. For example, the interval between 340 and 347 mbsf contains one large-scale turbidite sequence (~6 m thick) (Fig. F74). Evident within this sequence are smaller-scale sequences on the order of 1–2 m, and within these sequences are smaller sequences on the order of 0.2 m.

Density

Whole-core density measurements obtained on the MST (Figs. F67, F68, F69, F70, F71, F72) are in close agreement with the bulk density measured on discrete samples. Grain density was also measured on the discrete samples.

Figure F75A and F75B show the grain and bulk densities as a function of depth. The bulk density of the pelagic mud shows little variation with depth and has a mean value of 1.28 g/cm³. The mud has a mean grain density of 2.66 g/cm³ and an average porosity of ~85%. The bulk density increases rapidly as the lithology changes from pelagic mud to turbidites. The mean bulk density for the turbidites is 1.86 g/cm³, and the mean grain density is 2.54 g/cm³. There is a general trend of decreasing grain density with increasing depth in the turbidites, which can be attributed to increasing diagenesis (see "Lithostratigraphy," p. 10). At a smaller scale, there are several intervals where the grain density increases almost linearly with depth (e.g., 340–350 mbsf). These trends likely correspond to sorting of more dense minerals and clasts toward the bottom of larger-scale turbidite sequences. However, from 100 to 140 mbsf within the turbidites, there is a clear decrease in grain density with increasing depth.

F66. Compiled MST results, Holes 1201B and 1201D, p. 136.

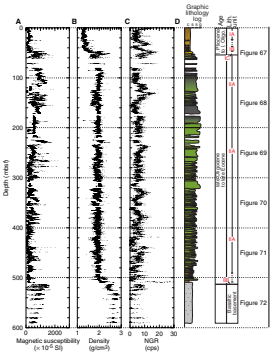

F67. MST results in Holes 1201B and 1201D (0–100 mbsf), p. 137.

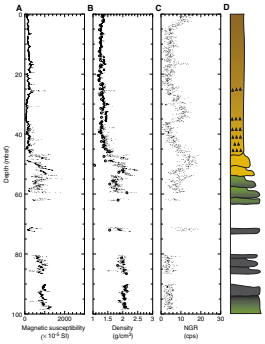

F68. MST results, Hole 1201D (100–200 mbsf), p. 138.

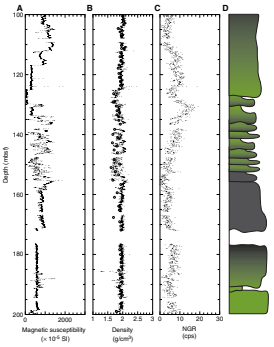

F69. MST results, Hole 1201D (200–300 mbsf), p. 139.

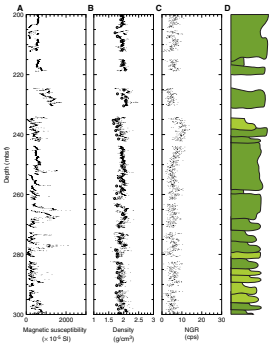

At the interface between the turbidites and the basalt, bulk density increases significantly from ~2.0 to ~2.5 g/cm³. At a depth of ~20 m below the top of the basalt, the bulk density increases to a mean value of 2.70 g/cm³ for the remainder of the section. The grain density of the basalt shows similar variability with depth and has a mean value of 2.79 g/cm³ at depths >20 m below the top of the basalt. The relatively low density in the top 20 m of the basalt may be due to alteration. The mean porosity of the basalt is 5.1%.

Porosity values (Fig. F75C) decrease from a mean of 84% in the pelagic mud to 44% in the turbidites and 9% in the basalt. On the scale of the whole core, porosity appears to be inversely related to the bulk density. This relationship follows from the generally low variability in the grain density with depth, as the large variations observed in the bulk density must be related to the water content.

Natural Gamma Radiation

Natural gamma ray (NGR) emissions (Figs. F66, F67, F68, F69, F70, F71, F72) show significant variations in the pelagic mud. Count rates are highest at the seafloor, with nearly 50 counts per second (cps), compared to an average count rate of ~5 cps at this site. Three large increases in the count rate occur in the muds, at 16.5, 30–35, and 45–50 mbsf. In the turbidites, NGR emission variations appear to follow the same general trends as the density log, except that where the density decreases, the NGR count rate increases.

Toward the bottom of the turbidites between 505 and 510 mbsf, an interval with relatively high count rates can be identified. The high count rates coincide with intervals of reddish brown silty claystone.

Count rates in the basalt are slightly higher in the top 15–20 m, with an average of ~6 cps. At depths greater than ~530 mbsf, the NGR emissions reduce to ~4 cps then appear to increase slightly toward the bottom of the section. Overall, in comparison to the sediments, NGR emissions in the basalt are relatively low and uniform throughout the interval.

P-Wave Velocity

P-wave velocity increases in discrete steps from ~1.6 km/s at the seafloor, to ~2.5 km/s in the turbidite sequences, and ~5.5 km/s in the basalts (Fig. F75D). The velocities measured in the pelagic muds are relatively uniform, varying ±0.1 about an average of 1.63 km/s. In contrast, the velocities of the turbidites vary much more, ±0.8 about an average of 2.46 km/s. This variation is due to the changes in porosity, mineralogy, and cementation within individual turbidite sequences and within the entire turbidite section. Within a single turbidite sequence, for example the more massive sequence between 90 and 130 mbsf, velocities decrease with increasing depth. In general though, the velocities are aliased, that is, the sampling interval for the velocity measurements was too large to show the individual turbidite sequences. Also, because the velocity depends on both mineralogy and porosity, a decrease in velocity toward the top of an individual turbidite sequence due to the presence of clay minerals might be offset by a concomitant decrease in porosity. The velocities of the basalts increase from just over 4.0 km/s at the top of the basalts to >5.0 km/s ~10 m into the basement. This increase in velocity is likely due to decreased alteration of the basalts with depth.

F70. MST results, Hole 1201D (300–400 mbsf), p. 140.

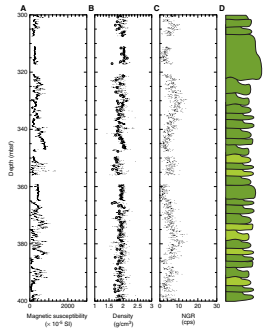

F71. MST results, Hole 1201D (400–500 mbsf), p. 141.

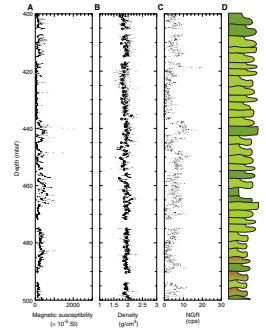

F72. MST results, Hole 1201D (500–591 mbsf), p. 142.

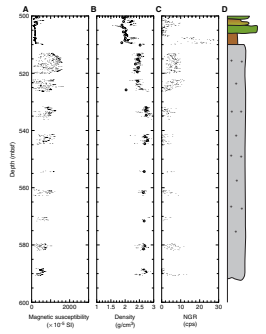

F73. MST results, Holes 1201B and 1201C, p. 143.

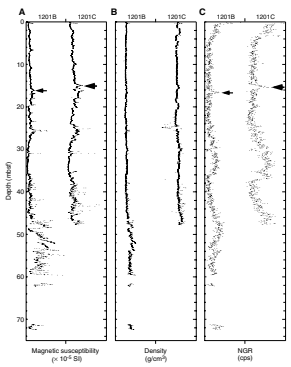

Acoustic impedance (Z), defined as the product of density (ρ) and velocity (V) (Equation 2), is calculated for each index properties sample (Fig. F75E):

$$Z = \rho \times V. \quad (2)$$

Major changes in impedance coincide with changes in lithology from pelagic mud to turbidite to basalt. The reflection coefficient (R), defined as the ratio between the amplitude of the incident and reflected seismic waves (Equation 3), was determined at the interface between each lithologic unit (Fig. F75E):

$$R = (Z_{lower} - Z_{upper})/(Z_{upper} + Z_{lower}). \quad (3)$$

Although the seismic record shows strong reflections at these interfaces, it also shows reflections with as great or greater strength throughout the entire top half of the turbidite succession. Because the impedances of the turbidites vary widely, these strong reflections are likely caused by the constructive interference of seismic waves reflected within the turbidites. Figure F76 compares the seismic record to a synthetic trace that convolves the impedances shown in Figure F75E with a 15-Hz sine wavelet. The synthetic trace does not include the effects from attenuation, multiples, or gain control imposed during analysis of the seismic data. It does, however, show that many of the reflections shown in the seismic record are caused by the rapidly varying impedance contrasts.

Seismic anisotropy, measured as the ratio of the horizontal P-wave velocity (V_h) to the vertical P-wave velocity (V_z), is shown in Figure F77. The pelagic muds show a slight anisotropy ($V_h/V_z \approx 1.03$) with little variation. The anisotropy in the turbidites is initially very close to unity, with values ranging from 0.95 to 1.1. At ~300 mbsf, the variability and magnitude of the anisotropy in the turbidites increases. These increases correspond to smaller-scale and finer-grained turbidite sequences, as shown in the sedimentary record (Fig. F66D). The anisotropy of the basalts varies from 0.9 to 1.04. The values of anisotropy are likely caused by microcracks created either by thermal stresses as the basalt cooled or possibly by stress relief and fracturing during recovery of the core.

Shear Strength

The shear strength of the pelagic muds was measured once per section on the working half of the core from Hole 1201B within 30 min of splitting the core. The measured peak shear strengths are relatively constant, with values ranging between 3.9 and 24.0 kPa at depths of <40 mbsf. From 40 to 46 mbsf, the peak shear strength rapidly increases to a maximum of nearly 100 kPa as the interface between the pelagic muds and the turbidites is crossed (Fig. F78).

Formation Factor

The formation factor was determined from resistivity measurements made using a four-probe array with a 13.3-mm probe spacing. The probes were inserted to their full 15-mm length in the split core surface to provide consistent apparent resistivity measurements but not abso-

T11. Index properties of discrete samples, p. 209.

T12. Physical properties, p. 215.

F74. Magnetic susceptibility, Hole 1202D, p. 144.

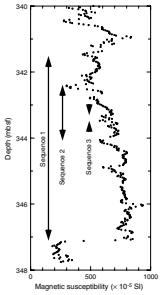

F75. Density, porosity, velocity, and acoustic impedance, p. 145.

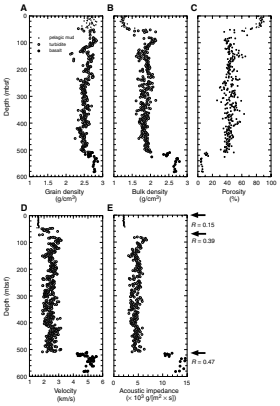

F76. Comparison of the seismic record to a synthetic trace, p. 146.

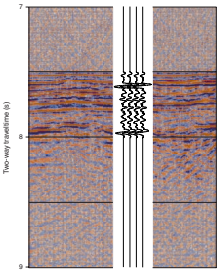

lute values. Pore water was assumed to have the same electrolytic properties as surface seawater.

Formation factors range from 1.92 to 3.67, with a mean value of 2.62 (Fig. F79). The formation factor does not vary linearly with increasing depth. There appears to be a region between 20 and 35 mbsf where the formation factor is reduced by ~25%.

Thermal Conductivity

Thermal conductivity measurements fall into three distinct ranges that are defined by major changes in lithology. Measurements vary between 0.73 to 0.86 W/(m·K) in the pelagic muds, between 0.94 and 1.21 W/(m·K) in the turbidites, and between 1.41 and 1.74 W/(m·K) in the basement (Fig. F80). The thermal conductivity values vary little with depth in each lithologic layer, with the possible exception of the basement, which shows a slight increase in thermal conductivity within the first 50 m.

Temperature Measurements

In situ temperature measurements were made in Hole 1201C using the Adara temperature probe. The temperature record is shown in Figure F81. Also shown on the figure are the seafloor or mudline temperature (T_{ml}) and the estimated sediment temperature at depth (T_{sed}).

The sediment temperatures at depth were determined using the curve fitting program TFIT. The estimates of sediment temperatures can vary several degrees depending on the value of the thermal conductivity of the sediment and the region of the decay curve chosen for the estimation. The estimated sediment temperature shown in Figure F80 was found using only the latter portion of the middle temperature series, the temperature decay curves.

The mudline temperature was determined to be 1.51°C. The sediment temperature at a depth of 44.6 mbsf was measured to be 7.08°C, yielding a thermal gradient of 0.12°C/m. A mean thermal conductivity for the pelagic mud of 0.786 W/(m·K) was determined from the measured values in Table T12. Because there was negligible variation of the thermal conductivity with depth in the pelagic muds (Fig. F79), the integrated thermal resistivity was not calculated. Instead, the heat flow was calculated directly using Equation 4:

$$q = -K(\delta T/\delta z), \quad (4)$$

where,

q = the heat flow,
K = the thermal conductivity, and
$\delta T/\delta z$ = the thermal gradient.

It should be noted that this value of heat flow assumes that all heat flow is due to conduction. The heat flow in Hole 1201C of 98 mW/m² is higher than the global average of ~50 mW/m² (Garland, 1979).

F77. Seismic velocity anisotropy from velocity measurements, p. 147.

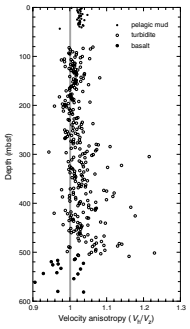

F78. Peak shear strength in pelagic muds, p. 148.

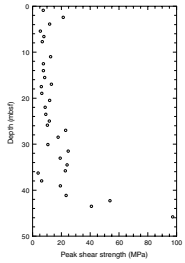

F79. Formation factor, Holes 1201A and 1201B, p. 149.

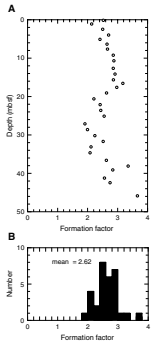

F80. Thermal conductivity, p. 150.

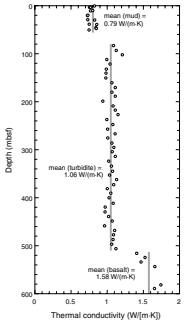

DOWNHOLE MEASUREMENTS

Operations

Wireline logging operations were carried out in Hole 1201D, the pilot hole that was drilled prior to installation of the seismometer package. During logging, the base of the drill string was kept at 76.5 mbsf to prevent borehole collapse in the upper soft sediment section (Fig. **F82**). The depth to the seafloor was determined to be 5723 mbrf, based on changes in the density and porosity logs at that depth. Two tool strings were run during wireline logging operations: the triple combo (temperature, resistivity, density, porosity, and natural gamma) and the FMS/sonic combination (Formation MicroScanner, sonic wave velocity, and natural gamma ray) (Table **T13**).

The first downlog run with the triple combo tool string reached TD at 591 mbsf after encountering sticky intervals at ~107 mbsf, just below where the drill string was set, and between 417 and 467 mbsf (Table **T13**). There was no apparent geological reason from the recovered cores why this interval should have been sticky and difficult to penetrate. The hole was logged up from TD, past the basement contact at 512 mbsf and up to ~417 mbsf, where the caliper was closed to get through the deepest tight spot. When the caliper was closed, the current to the dual laterolog tool was lost and one of the telemetry modules had to be exchanged to restore power. Logging ceased at this point and restarted again just above the tight spot; as a result, there is a gap in the data over this interval (see Table **T14;** also see **"Data Quality,"** p. 41). No problems were encountered logging from there up to 127 mbsf, the sticky interval below the pipe. Logging continued with the caliper open up to the seafloor at 5723 mbrf; however, no dual laterolog data were recorded in the uppermost interval (see **"Data Quality,"** p. 41). An interval was repeated from 177 to 93 mbsf without any further difficulty.

The run with the FMS/sonic tool string was more routine than the first run with the triple combo. Initially, some difficulty was encountered getting the tool string out of the pipe, and applying pump pressure with circulation was necessary to wash material out of the end of the pipe. While the tool was lowered for the first logging pass, an obstruction that could not be passed was encountered at 352 mbsf, higher up than the tight interval found on the first run. On the first logging pass, the FMS calipers did not open fully until 250 mbsf. The hole was logged up to 117 mbsf, at which point the tool string was lowered again for a second pass. The second pass commenced 15 m deeper, at 366 mbsf, and was successfully logged up to the pipe depth at 82 mbsf.

Data Quality

Hole conditions were good in the basement, with the caliper measurements showing a hole diameter varying between 10 and 11.5 in. In the sediment section, the caliper measurement varied from 12 to 18.5 in, with occasional tight spots below bit size. There were several washed-out zones where the density and porosity tools lost contact with the borehole wall, resulting in degradation of the data. Resistivity logs are relatively insensitive to borehole size; however, the natural gamma ray and density logs were corrected for borehole size during acquisition.

During logging operations in Hole 1201D, a speed correction was applied automatically by the Schlumberger acquisition software. However,

F81. Temperature measurements, Hole 1201C, p. 151.

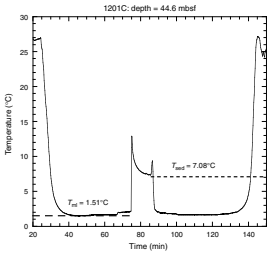

F82. Logging operations diagram, p. 152.

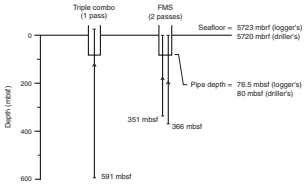

T13. Logging operations summary, p. 223.

T14. Logging data quality summary, p. 224.

when the speed correction was removed and the data were restored to measured depth because of a software error, some of the high-resolution data were lost, resulting in straight-line sections on the high-resolution density and porosity curves. The FMS images and natural gamma ray measurements from the FMS/sonic tool string were particularly affected by this loss of data. There are many stretched or compressed intervals and spikes in the data (Fig. F83), and much of the textural detail on the images has been lost. Although it appears that the data loss is irretrievable, preliminary observation suggests that the conventional standard logs are still of reasonable quality.

The logging data recorded on the run down to TD are the only data without the default speed correction. The downlogs are recorded at a faster speed than the uplogs, too fast for reliable gamma ray measurements, and they are run with the caliper retracted so that no correction for borehole size can be applied to the gamma and density logs. Neutron porosity is not measured on the downlog because bombardment of the formation with fast neutrons on the way down would affect the gamma ray measurement on the subsequent uplog run. The resistivity data, however, are more reliable because they are not as adversely affected by borehole size and logging speed. These data were used for depth matching with the speed-corrected data from the uplog runs during onshore processing.

The data from the two uplog runs that were recorded above and below the tight spot were spliced at 396.5 mbsf, although some gaps in the gamma ray and porosity log data remain. The gaps are different for each tool because the tools are situated at different depths along the tool string. Table T14 shows the depths of the first and last readings and the data gap for each tool in the triple combo string. The readings on the gamma ray curve, measured just above the tight spot during the second uplog, may be slightly elevated because of prior activation of the formation by the neutron source (see Fig. F83). The density logs are unreliable over a short interval between 451 and 444 mbsf, where the long-spacing voltage became unstable. The short-spacing curves over this interval are unaffected. There is one erroneous spike on the shallow laterolog curve between 412 and 417 mbsf, caused by the splice with the downlog data over this interval, and a second feature at 297 mbsf that was not observed on the downlog. Despite these minor problems, the repeat measurements of all logs compare well and demonstrate the good quality of the standard resolution geophysical logs.

F83. Downhole logging results, p. 153.

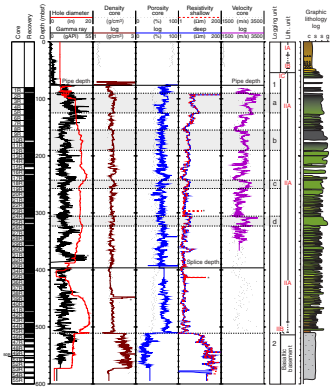

Logging Units

Two logging units have been identified (Figs. F83, F84). Logging Unit 1 corresponds to lithostratigraphic Unit II, and logging Unit 2 corresponds to the underlying basaltic basement. Lithostratigraphic Unit I was not logged because it only extends to ~60 mbsf, and the base of the pipe was set at 76.5 mbsf during logging. The log data show a good correlation with the physical properties measurements made on cores, particularly the discrete sample density and velocity measurements (Fig. F83). The porosity measurements from the logs are higher than the measurements made on discrete core samples because the neutron porosity log responds to the presence of hydrogen in the formation and also measures bound water and fracture porosity (Schlumberger, 1989; Rider, 1996). The logs show no obvious trends with depth other than a step change at the contact between the sediment and the basaltic basement, which is marked by a sharp increase in resistivity and density and

F84. Natural gamma ray logs, p. 154.

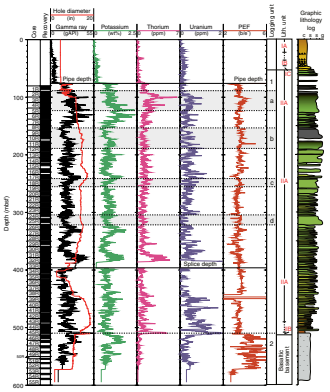

a corresponding decrease in porosity. Both logging units appear to be relatively homogeneous but include subtle variations that reflect changes in lithology.

Logging Unit 1—Turbiditic Sediments

This unit extends from 76.5 mbsf, the position of the pipe during logging, to the basement contact at 512 mbsf. The logs are consistent over this entire interval, which demonstrates the fairly homogenous nature of the reworked volcaniclastic sediments that dominate the unit. Recovery in the RCB hole was high (>80%), which facilitates detailed core-log correlation studies. The sediments consist of a series of low- to high-energy turbidite sequences characterized by alternating claystone-rich and coarser sandstone-rich or breccia intervals (see "Lithostratigraphy," p. 10). The logging data show small variations in resistivity, velocity, density, porosity, and gamma ray values, reflecting changes in lithology, porosity, and grain size. In logging Unit 1, four intervals that correspond to thicker, coarser turbidite packages can be recognized in the logging data (see gray shaded intervals a–d present at 90–124, 155–190, 242–257, and 305–322 mbsf in Figs. F83 and F84). These intervals are generally characterized by higher and more consistent velocity, density, and resistivity values and slightly lower and more consistent natural gamma ray values. They correspond to more massive sandstone or breccia intervals. but smaller-scale grain-size variations can also be identified in the log response. Between these intervals, the logs corresponding to the interbedded finer-grained units show more rapid fluctuations, with generally lower velocity, density, and resistivity values and slightly higher and more variable gamma ray values.

The FMS images in Figure F85 are from a coarse turbidite-claystone sequence between 240 and 320 mbsf. Despite the fact that the images have been adversely affected by the default speed correction, the resistivity difference between the coarser massive units and the finer interbedded sequences is immediately obvious on the static normalized image. Individual bed boundaries can be delineated and used for core-log integration studies, assuming that a good depth match to the triple combo data can be achieved.

F85. Pressure and temperature from the TAP tool, p. 155.

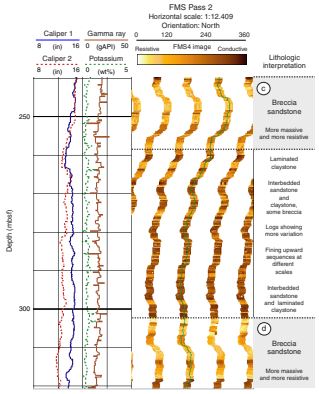

Logging Unit 2—Basement

Logging Unit 2 extends from 512 mbsf down to a total logging depth of 591 mbsf and is marked by a significant increase in density, resistivity, and velocity values and a corresponding decrease in porosity values. The resistivity values, although significantly higher than those recorded in logging Unit 1, are not as high as expected for a massive basalt lava sequence. Instead, they are comparable to values that have been reported from pillow lavas with interpillow breccia. Core recovery in basement was relatively poor (<23.1%) and included small pieces (<30 cm) of highly veined basalt with glassy pillow margins and interpillow material, including highly altered hyaloclastite. This is consistent with the interpretation of this unit as a pillow sequence with some interpillow breccia as opposed to massive basalt flows (see "Igneous Petrology," p. 20). The basement section is relatively homogenous and contains no obvious boundaries, although there appears to be a slight increase in resistivity and a decrease in gamma ray values with depth, which may indicate a trend toward slightly less altered material deeper in the basement section.

Temperature Log

The Lamont-Doherty Earth Observatory TAP tool recorded the temperature of the fluid in Hole 1201D as part of the triple combo tool string (Fig. F86). Temperature and pressure are plotted against elapsed time because the computer that records the depth-time relationship failed during acquisition, resulting in a loss of the depth information. The temperature measurement lags behind the pressure measurement, reflecting the slow response of the thermistor. The measurement is an underestimate of the true formation temperature, as the borehole fluid did not have time to equilibrate to the formation temperature during the logging operation. The pressure and temperature curves illustrate well the different stages of the logging operation in Hole 1201D. Recording started ~300 m above the seafloor, and a temperature of ~5°C was recorded at the seafloor (Fig. F86). Pressure and temperature both increased steadily during downlog acquisition, and a maximum temperature of 16.4°C was recorded at the bottom of the hole (595 mbsf). The return path to the seafloor highlights the two stages of uplog acquisition, and the perturbations on the pressure curve correspond to intervals where tool sticking was experienced. During the repeat run, the pressure and temperature both increased slightly and then decreased again. The final pressure-temperature peak on the graph corresponds to an attempt that was made to lower the tool string again to assess whether further sticking would be encountered if the FMS/sonic tool was run.

F86. FMS images from a coarse turbidite-laminated claystone, p. 156.

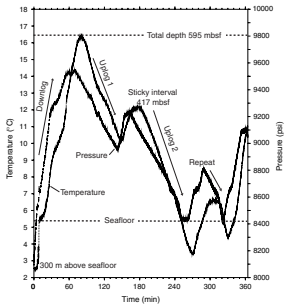

Summary and Conclusions

Despite the problems that hampered logging operations at Site 1201, good data were obtained over the entire open hole interval (76.5–591 mbsf) with the triple combo tool string and reliable sonic data were recorded down to 366 mbsf during the second run with the FMS/sonic tool string. The logging data correlate well with core physical properties measurements. Although lithostratigraphic Unit I was not present within the logged interval, the boundary between lithostratigraphic Unit II (logging Unit 1) and the underlying basement (logging Unit 2) can be clearly delineated. The upper section (logging Unit 1) is characterized by a sequence of turbidites with varying proportions of sandstone or breccia and silty claystone intervals. No obvious trend in density, porosity, resistivity, or velocity with depth is apparent. However, the downhole logs show subtle but significant variations within this turbiditic sedimentary sequence, and fining-upward units that correlate well with sedimentological units described in the cores can be identified. The basement section (logging Unit 2) is relatively homogenous, although there may be a trend toward slightly less altered material with depth.

BOREHOLE INSTRUMENTATION

System Overview

Objectives

A major limitation of our understanding of active tectonic processes largely comes from the fact that we lack in situ long-term observations

in the oceans where many areas of major tectonic activity are found. Since the DSDP era, there have been many attempts to utilize boreholes for such observations. For example, recent circulation obviation retrofit kit (CORK) deployments to measure pressure and temperature changes in sealed boreholes are beginning to produce interesting results. ODP continues to recognize the importance of long-term observatory objectives (Ocean Drilling Program, 1996). Tomographic studies using earthquake waves propagating through the Earth's interior have revolutionized our understanding of mantle structure and dynamics. Perhaps the greatest problem facing seismologists who wish to improve such tomographic models is the uneven distribution of seismic stations, especially the lack of stations in large expanses of ocean such as the Pacific. The ION project, an international consortium of seismologists, has identified gaps in the global seismic net and is attempting to install digital seismometers in those locations. One of the highest priorities of ION is to install a station beneath the deep seafloor of the northwest Pacific. A primary objective of Leg 195 was to install a permanent seismic observatory (WP-1) at Site 1201, situated in the western Philippine Basin (Fig. **F87**), which would become a long-term borehole seismological observatory. The WP-1 seismic observatory is surrounded by Inuyama and Taejon stations to the north, Ishigakijima and Baguio stations to the west, Davao City and Jayapura stations to the south, and Guam, Minami Torishima, and Ogasawara stations to the east.

A global seismographic network was envisaged by the Federation of Digital Seismographic Networks to achieve homogeneous coverage of the Earth's surface with at least one station per 2000 km radial distance in the northwestern Pacific area. Thus, the WP-1 seismic observatory at Site 1201 will provide invaluable data, obtainable in no other fashion, for global seismology. Data from this observatory will help revolutionize studies of global earth structure and upper mantle dynamics by providing higher-resolution imaging of mantle and lithosphere structures in areas that are now poorly imaged (Fig. **F88**). In addition, this observatory will provide data from the backarc side of the Izu-Ogasawara and Mariana Trenches, giving greater accuracy and resolution of earthquake locations and source mechanisms. The observations of seismic surface waves as well as various phases of body waves from earthquakes at the Philippine Sea plate margins will provide sufficient data to map differences in plate structure among different basins comprising the plate (e.g., the West Philippine, Shikoku, and Parece Vela Basins). There are only a few studies with limited resolution on the lithospheric structure of these areas (Kanamori and Abe, 1968; Seekins and Teng, 1977; Goodman and Bibee, 1991).

There are indications that the subducting Pacific plate does not penetrate below the 670-km discontinuity and that it extends horizontally (Fukao et al., 1992; Fukao, 1992), but the resolution of these studies is poor (>1000 km) beneath the Philippine Sea and the northwestern Pacific, especially in the upper mantle, where significant discontinuities and lateral heterogeneities exist (Fukao, 1992). The WP-1 seismic observatory is a crucial network component in determining whether the Pacific plate is penetrating into the lower mantle in the Mariana Trench but not in the Izu-Ogasawara (Bonin) Trench (van der Hilst et al., 1991; Fukao et al., 1992; van der Hilst and Seno, 1993). In addition, the WP-1 seismic observatory will allow imaging of the subducting slab to determine how the stagnant slab eventually sinks into the lower mantle (Ringwood and Irifune, 1988).

F87. Seismic station coverage in the Philippine Sea, p. 157.

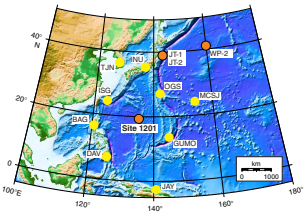

F88. Location of the WP-1 observatory in relation to global seismicity, p. 158.

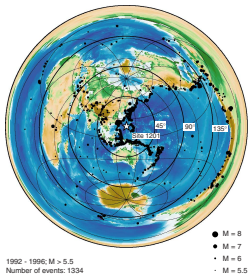

NEREID-195 System Outline

We outline the NEREID-195 system of the WP-1 borehole broadband seismic observatory in this section (Fig. F89). The details of each component are described in separate sections. Like other existing oceanic borehole observatories (JT-1 and JT-2) (Sacks, Suyehiro, Acton, et al., 2000), there is a nearby coaxial transoceanic telephone cable (TPC-2) to use for data recovery and power. However, the WP-1 observatory installation is designed as a stand-alone system with its own batteries and recorder. Thus, once instruments are installed in the hole, they will be serviced for data analyses, distribution, and archiving. We plan to connect data, control, and power lines to the TPC-2 cable owned by University of Tokyo after confirmation of data retrieval.

The two seismometers are designed to be placed near the bottom of the hole, each housed in a separate pressure vessel. Both sensors are feedback-type broadband seismometers (Guralp Systems, Ltd., CMG-1T). Two separate cables are required to connect the sensors uphole. The signals are digitized in the sensor packages and sent in digital form to the seafloor packages. The seafloor package (multiple-access expandable gateway [MEG]-195) (see Table T15 for abbreviations) serves to combine the digital data from the two seismometers to a single serial data stream. It also distributes power to the individual seismometers. The data are stored in digital format in a separate module (the storage acquisition module [SAM]-195) after being sent via an RS-232C link using Guralp Compressed Format (GCF) protocol. The SAM-195 has four 6-GB SCSI 2.5-in hard disks capable of storing more than six channels of 0.5-yr-long continuous data of 24-bit dynamic range at 100-Hz sampling rate. In this case, there are three channels for each of the seismometers. We plan to change the hard disks in the SAM-195 to those with a capacity of 15 GB. Using four 15-GB hard disks, the recording period of the SAM-195 is extended to ~1.5 yr. The seismometers are emplaced in the borehole permanently; they are cemented into the hole to assure good coupling. The MEG-195, on the other hand, may be serviced by a remotely operated vehicle (ROV) or submersible. The MEG-195 can be physically replaced and accepts commands and software upgrades through the SAM-195. The SAM-195 must be replaced by an ROV or submersible before the hard disks become full, which is ~1.5 yr with the future design. The SAM-195 also provides a communication link to the borehole system while the station is being serviced by the ROV or submersible. The SAM-195 can send part of the data to the surface across a serial link to check the health of the system. The SAM-195 measures the time difference between the clocks in the SAM-195 and the MEG-195. Before deployment and after retrieval of the SAM-195, the time difference between the SAM-195 and the Global Positioning System (GPS) clocks is measured on board. Because the MEG-195 controls the timing of the whole borehole system, we can adjust the system timing to universal time coordinated using the data from the SAM-195. All the necessary power is supplied from the lithium battery unit (LBU). The LBU consists of two units. Each unit is composed of 16 cells provided by Yuasa, Japan (model CL-1300L). Each cell has a voltage of 2.7 V at 0°C with a capacity of 1300 Ah. We connected eight cells in series and two series in parallel; therefore, each unit has a dominant voltage of 21.6 V at 0°C with a capacity of 2600 Ah. Each battery unit has two titanium spheres with a diameter of 65 cm because eight cells are housed in one titanium sphere. It is expected that the battery system will provide power to the system for ~2.5 yr.

F89. Schematic view of the NEREID-195 system, p. 159.

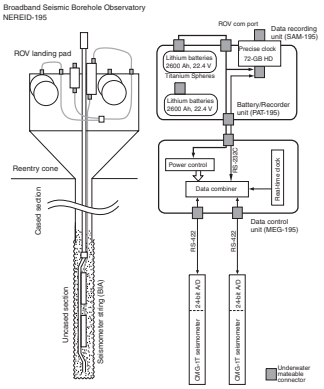

T15. Glossary of the NEREID-195 system, p. 225.

Environmental Requirements

Site 1201 is geographically situated in a large gap of the global seismic network (Fig. F87) where no seismic observatory exists within 1000 km. The seismic image of the Earth's structure beneath this area, especially in the upper mantle, will remain ambiguous without a seismic station in this area. There are several requirements that must be fulfilled for the permanent installation of a seismic observatory so that the expansion of the global network to the ocean is truly effective. The seismic noise of an observatory should be as small as possible. The number of observed seismic phases depends on the magnitude of the seismic noise in the same frequency band as the seismic phases from earthquakes. Therefore, the reduction of seismic noise at the site directly enhances the value of the observatory. There are many sources of seismic noise. Environmental seismic noise caused by microseisms, infragravity waves, and water currents at the sea bottom are commonly recorded by ocean seafloor observatories. Each environmental seismic noise has a significant characteristic frequency band. At frequencies <0.1 Hz, seafloor seismic observations are significantly degraded by the noise caused by water currents at the seafloor. The magnitude of this type of noise can be higher than that of almost any long-period teleseismic phase. Escaping the noise due to water currents by shallow burial of the seismometer in sediment or borehole installation was suggested and was tried in several pilot experiments (e.g., Stephen et al., 1999). Because a lower noise level is expected in a borehole rather than at the seafloor or in shallow sediment, especially long term, permanent seismic observatories should be installed in boreholes at the sea bottom. Installation in a deep borehole seems to eliminate the effect of flow noise, but noises characteristic of borehole installation, such as turbulence in the water column of the borehole, might reduce that advantage. For high-sensitivity measurements, pressure fluctuations resulting from ocean long waves or temperature changes can be noise sources. Any water motion near the sensor is also a potential noise source. Therefore, the seismometers must be grouted inside the borehole to avoid noise from water motion and to be optimally coupled to the surrounding rocks. From the experience of Leg 186, during which borehole geophysical observatories were installed on the inner slope of the Japan Trench, it was determined that the infragravity wave was the dominant noise source, with frequencies between 0.004 and 0.02 Hz (Araki, 2000). Using theoretical estimation of strains, it was found that the acceleration of the ground as a result of tilt by the infragravity wave is largest in a sediment layer but becomes negligible below the top of the basement. This is because the sediment has a large *P*-wave velocity (V_P)/*S*-wave velocity (V_S) ratio, whereas the V_P/V_S ratio of the basement is smaller. The depth of the horizontal traction maximum is mostly determined by the wavelength of the applied pressure signal at the seafloor, although shear strength is also an important parameter. The wavelength of infragravity waves is more than a few kilometers in the frequencies of interest. Consequently, the horizontal stress takes a maximum value at the bottom of the sediment column unless the sediment thickness is extreme. Horizontal traction is maximum at the bottom of the sediment layers, whereas the vertical traction is maximum at the seafloor, a consequence of the traction-free boundary condition at the seafloor. A seismometer in deep sediment will suffer from large horizontal infragravity wave noise, whereas a seismometer in shallow sediment will suffer from large vertical infragravity noise. Therefore, it is necessary to install a

seismometer in igneous basement rather than in sediment to reduce the noise caused by infragravity waves; the seismic noise from infragravity waves in the horizontal component is smaller by >40 dB in basement than in sediments. During Leg 191, broadband seismometers were installed ~70 m below the sediment/basement interface in the northwestern Pacific Basin (Kanazawa, Sager, Escutia, et al., 2001). Although we have only 1-hr records from the seismometer at present, the noise level in the horizontal component estimated to be caused by the infragravity wave decreased by at least 20 dB.

Installation Techniques

Requirements

To obtain high-quality data, a suitable instrument, as described in "Borehole Instruments," p. 50, must be in intimate contact with the host rock. This is accomplished by cementing robust instruments in the bottom of an open hole in competent, indurated rock. At Site 1201, we installed and cemented the seismic instruments into the basaltic basement.

One of the complications of subseabottom installations arises from having to cope with irreducible ship heave during hole entry. Because heave may be a meter or more, cables linking the instruments with the seafloor data handling units have to be protected from stresses arising from relative motion between the units and the hole wall and between the units and any insertion tools. Although the passive and active heave compensators can be used during hole entry, the instrument string has to hang from the rig floor without compensation while pipe is being added. Pipe is added every 10 to 30 m for ~580 m of hole penetration. In addition, for the cement to set properly, the instrument package has to be completely undisturbed for about a day after the cement is introduced.

Methods

The technique we have developed to satisfy the installation requirements listed above is illustrated in Figure F90. The instrument package is supported on 4.5-in diameter casing pipe that hangs on the base of the reentry cone at the seafloor. This has two advantages: (1) the pipe provides a conduit for cement pumping and (2) it also keeps the package stationary once its support (riser/casing hanger) lands on the hanger at the base of the cone. After cementing, the drill pipe from the ship can be uncoupled and withdrawn, leaving the casing pipe in the hole. The cables are protected by strapping them to the casing pipe and are also protected from wall contact by centralizers (see Fig. F91). Therefore, there is no motion between the cables and the support tube (casing pipe) and no contact with the borehole walls. Strapping the cables to the support tube minimizes the tension in the cables. Armored cables are not required, and the cable structure is such that it is almost neutrally buoyant in seawater, further minimizing long-term stress on the cables.

It has been found that cement pumped through a pipe into a water-filled hole does not penetrate much below the pipe opening, tending rather to force its way upward. To make a strong plug below the seismometers, a 3.2-m-long extension tube called a stinger is coupled to the bottom of the borehole instrument assembly (BIA) that supports

F90. BIA installation schematic, p. 160.

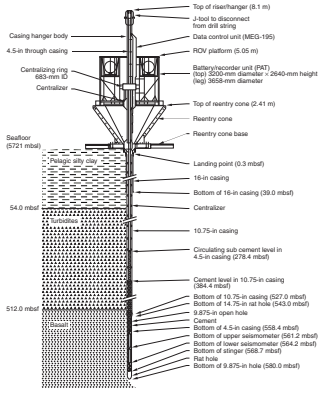

F91. Cable strappings and centralizer, p. 161.

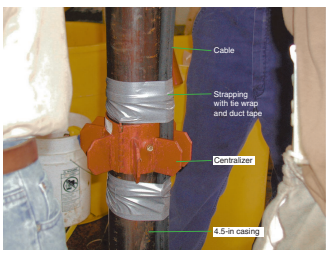

the seismometers. This ensures that the seismometers are sealed off from the bottom of the hole and that a strong cement plug extends well below the lower seismometers.

The cement is pumped through the casing pipe, the BIA, the stinger, and then up around the BIA into the 10.75-in casing. In Hole 1201E, the open hole length was 53.0 m, the top end of the stinger was 14.5 m above the bottom of the hole, and cement was pumped up from the bottom of the stinger, filling ~184.3 m of the hole (Fig. F90).

To avoid water circulation in the borehole column, which may cause seismic noise, the entire hole should be filled with cement. However, a long column of cement makes an overpressure at the position of the seismometers because of the cement density of ~2.0 g/cm^3. The cables from seismometers may be damaged by the overpressure because the pressure limitation of the borehole cables is ~6500 m. Therefore, we adopted a length of ~200 m for the cement fill, a compromise between filling the hole and limiting the overpressure.

Figure F92 shows the BIA. Each of the two sensors has its own cable to the seafloor unit. There are a number of reasons why this plan was adopted rather than having a single armored cable carrying all the signals. Because we do not know the exact depth of installation until the hole has been drilled and the formation evaluated, the downhole cable cannot be cut and terminated ahead of time. Cable termination with an underwater mateable connector (UMC) is a delicate operation and took ~14 hr for the two connectors used during Leg 195. With flexible cable, enough slack can be provided that errors in the termination operation can be tolerated. With armored cable, this would be impossible and the termination would be extremely difficult to accomplish onboard ship.

An overriding concern has been the long life of the installation. A 10-yr goal is necessary if we are to achieve all the scientific objectives. Our experience with long-term land installations is that cable leakage and electronic component failure are the most likely sources of data termination. For this reason, we use multiple cables and much of the electronic circuitry is contained in a removable seafloor unit (see "Seafloor Instruments," p. 52).

Borehole Instrument Assembly

The BIA is designed to prevent the instruments from being damaged during the installation in the borehole and to secure a conduit for cement pumping. The main frame of the BIA is a 0.076-m-diameter × 7.1-m-long steel pipe with two blades, which have an angle of 62° between them (Figs. F92, F93, F94). The steel pipe serves as a conduit for cement. The 5.5-m-long middle part of the pipe is shifted toward the outside so that two ocean borehole seismometer (OBH) sensors (S/N T1023 and T1038) and their cables can be emplaced there. Two OBH sensors are situated and fixed on the frame pipe in the area between two blades. The two blades protect the instruments from being hit and abraded by the hole. The surface of the frame pipe, where the pressure vessels of the OBH sensors touch, is covered with fiberglass cloth to insulate the instruments from the frame pipe. A 3.2-m-long stinger pipe with centralizers is bolted onto the bottom of the BIA. Cement pumped into the hose flows through the drill pipes, the BIA frame pipe, and the stinger. At the bottom, cement floods out from the lower end of stinger and rises upward to fill the space between the instruments and the borehole.

F92. BIA with two OBHs, p. 162.

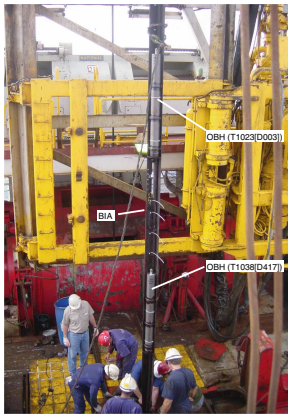

F93. An OBH sensor was emplaced on the BIA, p. 163.

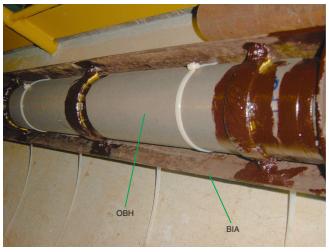

F94. BIA with two OBHs is lowered to the sea, p. 164.

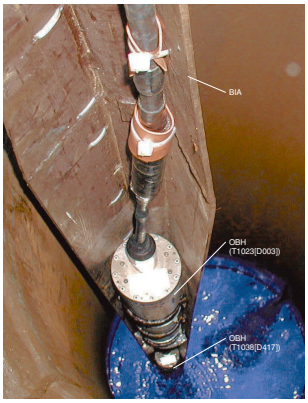

Borehole Instruments

Ocean Borehole Seismometer

The OBH package consists of a three-component seismometer and a 24-bit digitizer (DM24) assembled in a 1.2-m-long grade five titanium pressure cylinder (12.7 cm OD). The cylinder is designed to withstand pressures at 10,000 m water depth, and the T1023 cylinder was tested at a pressure of 72 MPa. The two seismometers are model CMG-1T units made by Guralp Systems, Ltd. Each consists of three orthogonal sensors stacked vertically in the canister with a vertical sensor above two horizontal sensors (Figs. F95, F96). Two OBHs were mounted on a BIA frame lengthwise with 3-m spacing.

Mechanically, the vertical OBH sensors are of the Ewing type and the horizontal sensors are of an inverted pendulum type. Mechanical details of the vertical sensor are shown in Figure F97. The inertial mass is a boom supporting a transducer coil. The boom consists of a solid machined beam. The vertical sensor mass is supported by a prestressed triangular spring to compensate for its weight and has a natural period of ~0.5 s. The horizontal sensor mass is centered by an unstressed flat triangular spring and has a natural period of ~1 s. The effective mass of each sensor is ~250 g. The springs are connected to the frames with a temperature compensating thread that minimizes the effect of temperature variation. A compact design is achieved chiefly by the short stiff springs and short boom.

The adjustments required for operation consist of leveling the boom of the vertical sensor and tilting the bases of the horizontal sensors to center the mass movements in their equilibrium positions. Adjustments are made by small (1 cm diameter × 3 cm long) direct current (DC) motors operating gear mechanisms to tilt the bases of the horizontal sensors and to apply a small extra force to the vertical sensor's boom.

Before and during borehole installation, the instrument may be subjected to severe motion that can damage the mass support hinges. Consequently, the masses have to be locked securely in their frames and the hinges released. This operation is performed by a small motor-driven clamp, which is controlled by a command to the DM24 digitizer.

The sensors employ feedback to expand their bandwidth and dynamic range. The response of the sensor is determined by the characteristics of the feedback loop. The mass position is sensed by a capacitative position sensor. The voltage from the sensor, which is proportional to the displacement of the mass from its equilibrium position, is amplified and fed to a coil on the mass. The current in the coil forces the mass to its equilibrium position. With a high loop gain, motion of the mass is essentially prevented and the feedback voltage is then a measure of the force, and thus the acceleration, applied to the mass.

Figure F98 shows block diagrams of the feedback system. To obtain stable performance over the whole frequency range, the feedback-loop phase shift has to be carefully controlled by compensation components in the forward and feedback paths in the system. There are two feedback paths; one consists of a single capacitor in parallel with a resistor, and the other consists of a noninverting integrator in series with a resistor. The arrangement gives a double pole at specific frequencies. The system velocity responses are defined by a transfer function identical to that of a conventional long-period sensor with a velocity transducer whose natural resonance period is set at 360 s with the damping factor at 0.707. The velocity output (flat to 100 Hz) is fed through a low-pass

F95. Components of the OBH, p. 165.

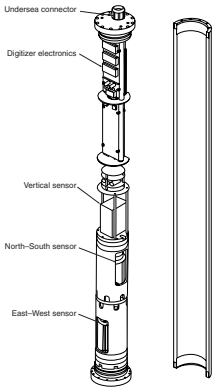

F96. Spectra of the instrument ground and self-noise, p. 166.

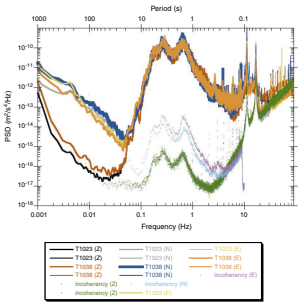

F97. Cutaway drawing of the CMG-1T vertical sensor, p. 167.

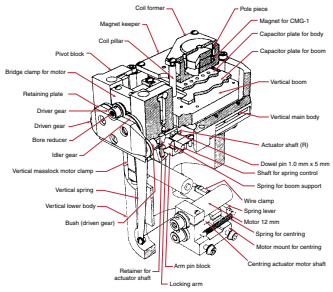

F98. Schematic diagram for the CMG-1T sensors, p. 168.

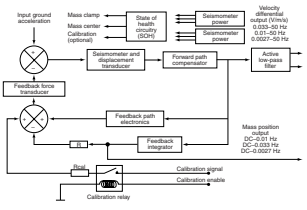

filter (<50 Hz) before the digitizer. The mass position output can be used for periods >360 s.

The single-end output signals, such as velocity and mass position, are digitized by the DM24 digitizer. A detailed description of the DM24 digitizing module is given later in this section. The velocity outputs are digitized at 100 samples per second (sps), and the mass position outputs are digitized at 4 sps. The digitizer was programmed to produce decimated optional velocity outputs at 20 sps, although the sampling frequencies of velocity channels can be changed by commands. The sensitivities are ~5.0×10^{-10} m/s/bit for the velocity outputs and 8.0×10^{-8} m/s^2/bit for the mass position outputs (Table **T16**). The DM24 also digitizes the signal from a temperature sensor in the OBH cylinder at a resolution of 12.87 mK/bit. All the digital data are sent to the MEG-195 seafloor data module through a 560-m-long cable. The communication link to the MEG-195 is a four-wire, 38,400-bit per second (bps) RS-422 serial link. As well as sending the signal data, the DM24 receives the time reference signal from the MEG-195 and synchronizes the OBH clock to the MEG-195 clock. The precision of the OBH synchronization is typically within 200 µs. The OBH clock is resynchronized to the reference if the time offset between the OBH and the MEG-195 clocks becomes >20 ms. The OBH clock in the DM24 records the time in the digitized records (Fig. **F99**).

T16. Sensor sensitivity of Guralp seismometer, p. 226.

F99. Seismometer clock offset and drift, p. 169.

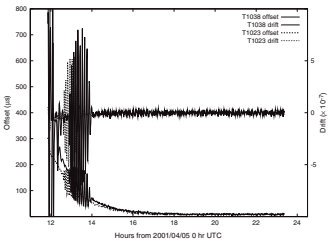

The voltage range for the OBH is 10–36 V. Because the 560-m-long cable resistance is ~11 Ω, the supply voltage can be varied in response to the power consumption of the OBH instrument. A large power consumption is required when the sensor mass unlock/lock is performed. This large current in the power line may cause damage to the DM24 processor. Therefore, an electrolytic capacitor with 4700 µF of capacitance and 63 V of resisting voltage is employed to eliminate undesirable effects caused by voltage fluctuation. A 100-Ω resistor is connected in series with the capacitor to limit the charging current of the capacitor. The limitation of current in the power line is important to protect the power supply. A diode is also connected to the resistor in parallel for discharge of the capacitor. The capacitor must discharge quickly when power is turned off. The 560-m cable that contains both the power supply and the data link is connected to the OBH by an eight-way underwater connector (SEACON MSSK-8-BCR) attached to the top bulkhead. The power consumption of the OBH instrument is ~2.5 W during regular operation of the sensor. Power loss in the long cable is expected to be ~0.15 W. The OBH power is supplied through a DC/DC converter in the MEG-195 to isolate the power ground from that in the MEG-195, and its efficiency is ~80%. The overall power consumption of the OBH is ~2.9 W during normal operation. When the masses are locked, each OBH consumes 0.3 W more power.

The microprocessor in the DM24 controls various functions of the sensors such as unlocking/locking the masses and bases of the horizontal sensors and centering the masses. These controls are initiated by a command sent from the MEG-195 or automatically by the program in the OBH system. The OBH system is programmed to start unlocking the sensors and centering the masses after a programmed date, which must be set after deployment. During Leg 195, this date was set to 6 May 2001 for all sensors. Another task related to control of the sensor is auto centering. The masses are recentered whenever they deviate from the center position by a more than half the range of the mass movement.

DM24 Digitizer

The DM24 is a modular intelligent digitizer developed by Guralp Systems, Ltd. The schematic diagram of the DM24 is shown in Figure F100. Each DM24 has three single-ended analog input channels to 24-bit analog-to-digital (A/D) converters, as well as additional eight-component 16-bit A/D channels. Each DM24 consists of rectangular printed circuit boards in the OBH. The 24-bit digitizer utilizes the Crystal Semiconductor CS5321/2 chipset and the Motorola 56002 DSP. The CS5321/2 digitizes signal at 2000 sps, and the data are processed by the 56002 DSP to give lower sample-rate data. The high sample-rate data are filtered and decimated in four cascaded stages. The first stage decimates the data by 10 to give 200 sps. The following three stages can have various individual decimation factors that allow multiple data output rates to be selected simultaneously. Sampling by the CS5321/2 is triggered by a Hitachi H8 16-bit microprocessor. The H8 processor receives data from the DSP, buffers it in 512 KB of S-RAM memory, and sends it through the serial link outside the module in GCF (see "Seafloor Instruments," p. 52). Transmission of the data by the processor is intelligent, so that even a lost packet during transmission can be recovered by handshaking upstream in a block recovery protocol.

Seafloor Instruments

MEG-195

The MEG-195 is composed of a combiner/repeater module (CRM) and power conditioning/distribution module (PDM) (Fig. F101). The major role of the MEG-195 is to acquire signals from each sensor and send out the converted digital data to the SAM-195 data recorder across a single serial link.

Mechanical Design of the MEG Frame

In the MEG-195, all of the electrical components are stored in an 8.5-in OD titanium pressure vessel (Fig. F102). The vessel is sealed at the top and bottom by bulkheads. On the top bulkhead, a UMC from Ocean Design, Inc. is installed. The UMC, which has four conductor pins, is an interface to the SAM-195 and the LBU and is joined by a 20-ft-long ROV cable to the power access terminal (PAT), in which the LBU and SAM-195 are stored. On the bottom bulkhead, four titanium UMCs are installed and connected to the long cables that connect the seismometers to the seafloor electronics. The UMCs at the bottom of the MEG-195 (Fig. F103) connect each OBH at the bottom of the borehole to the MEG-195.

The UMC on the top bulkhead has a latch mechanism, whereas the bottom UMCs are stab-mating connectors that require continuous stabbing force to maintain connection. The required stabbing force is 36.4 kg total for the four connectors, which is provided by the weight of the MEG pressure vessel (70.9 kg in air; 37.3 kg in water without contents). The vessel is inserted to a MEG frame (Fig. F102). The MEG frame is part of the riser/hanger assembly that stands up in the center of the reentry cone. The MEG frame holds the vessel and aligns the bottom bulkhead connectors to the UMC receptacles on the stab plate, which is at the bottom of the frame. The MEG pressure vessel can be removed from the frame. The bottom UMC connections can be disengaged safely by oper-

F100. Schematic diagram of the DM24 digitizer, p. 170.

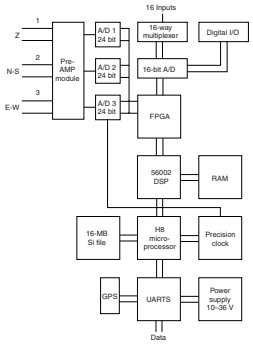

F101. MEG-195 system block diagram, p. 171.

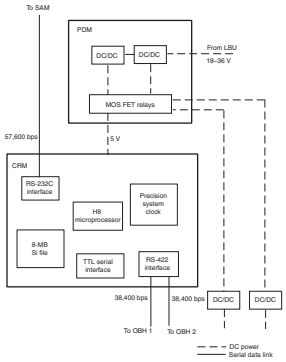

F102. MEG-195 vessel installed in the MEG frame, p. 172.

F103. Allocation of the UMCs on the MEG vessel, p. 173.

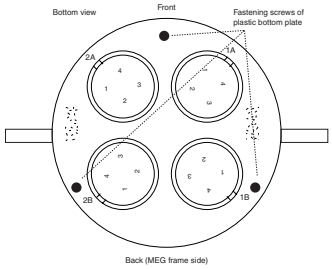

ating a lever attached to the MEG frame. At the bottom of the frame, a set of flippers with a latch mechanism is linked to the lever to push the vessel out. After UMC disconnection, the vessel can be safely pulled out of the frame with a rope. Thus, the MEG-195 may be replaced even after being deployed on the seafloor. The retrieval of the MEG-195 may be necessary if it malfunctions.

To guide the vessel correctly into the MEG frame, four 12.7-mm-diameter titanium pins are attached to the sides of the vessel. Two pins are at the top and two are at the bottom. The pins slide into the slots of the MEG frame and define the orientation of the vessel, which allows the UMCs at the bottom of the vessel to mate smoothly upon insertion. There are also two plastic wedges on the top side of the vessel, which together with wedges on the MEG frame side, are designed to increase the space between the vessel and the frame side members. This allows the vessel to be easily reinserted into the frame if replacement by ROV is necessary. The MEG pressure vessel is electrically isolated from the frame to prevent electric corrosion. The plastic wedges at the top of the vessel meet with the titanium wedges at the top of the frame, and the bottom of the titanium vessel meets with the lower plastic wedges at the frame because a plastic-plastic contact may become stuck by increasing the friction during insertion or extraction of the vessel.

Guralp Compressed Format

GCF is a format that allows many different time-series data channels to share a single transmission line. The format is used to transfer data throughout the NEREID-195 system. It can also transfer status messages in ASCII characters. Each GCF-format data transmission is an information packet containing either a data block or a status block. The GCF packet consists of an identification character (G), transmission serial identifier (ID), data/status block contents, and 2-byte checksum characters. The transmission serial ID increments by one for every packet. The serial number enables the receiver to recognize a lost GCF packet and will result in a request for the lost packet to be resent. The data block is used for time-series data transfer, and the status block is used for the sensor status information. Each data block stores data in multiples of a full second, starting on an exact second. The data block consists of a header and compressed data. In the 16-byte header, the most basic attributes of the data are stored, such as system ID, stream ID, date and time of the observation data, number of samples per second, number of data in the block, and type of compression in the data block that follows. The set containing system ID and stream ID identifies the source of the data. The assignments of the system ID/stream ID by each source are listed in Table **T17.** Simple data compression is made by the first and last complete values in each block and the difference values between adjacent samples. The bit lengths of the difference values are all the same in a data block and are 8, 16, or 32 bits, depending on the maximum first difference in the signal in that data block. The status block has the same header as that of data blocks, but its samples-per-second field is set to zero and the compression byte has a value of four. After the header, status information in ASCII characters follows. The status block transfers many different types of information, such as boot messages, progress reports of seismometer mass control, and measurements of clock offset between the CRM and the DM24s.

Each DM24 has a clock that adds time information to the data sent to the CRM. These clocks are independent from the precision clock in

T17. Mapping between sensor channels and stream ID in GCF, p. 227.

the CRM, which is the reference. The DM24 clocks have less accuracy; therefore, the clocks in the DM24s must always be synchronized to the accurate clock in the CRM. Each DM24 receives the time reference signal and adjusts its clock oscillator to synchronize with the reference.

The adjustment to the external clock can be performed by either GPS or stream-sync time-base signal; however, all the DM24 clocks in the MEG-195 and OBHs are set up to use the stream sync. The stream-sync signal is a set of clock synchronization characters sent by an upstream module through the serial data link to the DM24. The signal consists of 2-byte characters sent every second; date and time information is transmitted over 1 min. The first character (0x10) of each 2-byte character represents the timing reference, which is accurately synchronized to each second of the clock in the transmitter. The second character represents a part of a date or time. Although the first character is synchronized to the second, the processor actually needs the second character to compare with its own clock. Therefore, the receiver's internal clock will be delayed for the little time it takes to send the 10-bit data in the serial data link (~0.2 ms in a 38,400-bps line between the OBHs and the MEG frame). The difference between the clocks is measured every minute. The adjustment of the clock oscillator is also performed every minute. The time difference between the clocks is typically kept within 200 µs. When the difference between the clocks becomes >20 ms, the DM24 clock is resynchronized to the standard in the CRM.

The DM24s report the time difference in a unit of 25/1536 µs in the GCF status block. The DM24 can be interactively configured or commanded through the same serial link that is used for data transmission. With a simple command line, control of the sensor attached to the DM24 in the DM24 is possible (e.g., mass unlock/lock and mass centering). The system programs are customized to fit the sensor attached to the DM24.

As well as the control on demand of a command from outside, some of the DM24s can have a task that automates the control of the sensors. For example, the DM24 for the CMG-1T seismometer has a process to monitor the mass positions and centers the masses when they deviate by more than half the full scale from the zero position.

Combiner/Repeater Module

The CRM collects digital data from all the DM24s in the OBHs. The serial link between the CRM and the DM24 in the MEG-195 is a transistor-transistor-logic level interface to minimize power consumption in its line driver/receivers. A 38,400-bps RS-422 serial interface is used to connect the CRM to the OBH to ensure a link of sufficient quality over a cable length of 550 m. The serial links from the CRM to the DM24s in the OBHs are optically isolated. The downhole power lines are also isolated with DC/DC converters. Complete electrical isolation of each component is necessary to avoid corrosion in case of accidental electrical leakage to seawater. The data collected by these serial interfaces are handled by a Hitachi H8 microprocessor. The data are buffered in an 8-MB silicon file in order and are transmitted to the SAM-195 recorder through a high-speed 57,600-bps RS-232C serial interface.

The H8 processor controls a precision reference real-time clock (RTC) in the same manner as the DM24. The reference RTC is a temperature-compensated precision clock, and the trimming of the oscillator by the processor makes its accuracy on an order of 1×10^{-8} (Fig. F104).

F104. Time difference between the MEG-195 and the SAM-195, p. 174.

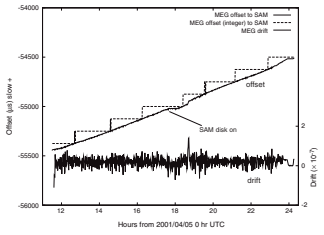

When the ROV plug from the battery frame is connected to the MEG-195, the CRM boots the whole system upon system power up. The CRM runs a boot loader in its EPROM first, and the boot loader reads the actual program from EEPROM in its CMOS memory to run the system. The CRM will also allow the system program to be loaded from the high-speed serial data link to update the one in EEPROM. After the system program is started, the CRM begins to handle data transmission and powers up all the seismometers sequentially. The CRM in the MEG-195 executes the command at the time-determined running state, whose number increases every minute from boot time. The CRM controls all the power for itself and the OBH. All of the supplied current for the OBHs connected to the MEG-195 is monitored by the CRM every minute. If the average current for the OBH over 1 min exceeds the preset limit (160 mA), the CRM in the MEG-195 shuts down the power of the OBH with overcurrent and will not automatically power on the OBH for the protection of the power supply circuit. The MEG-195 also checks the hourly supplied voltage average from the LBU. If the average voltage over two successive hours falls below the "good" threshold (20.0 V), the CRM in the MEG-195 shuts off one of the running OBHs to conserve power consumption. The CRM confirms that the LBU has little power using two successive measurements of the voltage from the LBU. Because the SAM-195 needs a large current for writing data to the disk, there is a possibility that the voltage of the LBU can drop temporarily. Writing data to the disk typically takes ~43 min. When the voltage of the LBU is greater than the "good" threshold over 2 hr (e.g., the CRM obtains two successive measurements of an average voltage above the threshold) after shutting down one OBH, the CRM in the MEG-195 switches on the OBH that had been shut down. When the CRM in the MEG-195 finds that the hourly average voltage is smaller than the "low" threshold (18.8 V), the MEG-195 and the OBHs will be completely shut off for 24 hr. After 24 hr, the CRM will try to boot again and see the supply gets back to a "good" condition.

The CRM produces a GCF status message every minute to report the condition of each system. The status message is composed using ASCII strings (Table **T18**) and reports the status of power distribution, clock synchronization, and intermodule communication. The status message from the CRM in the MEG-195 contains ~400 bytes, and the CRM in the SAM-195 contains an additional ~100 bytes of information about the data buffer status.

T18. Status messages from the CRM in the MEG/SAM, p. 228.

When the CRM in the MEG-195 receives a set of characters to request a command session from the upstream SAM-195, it stops sending data and switches to command session mode. In command session mode, the CRM provides features to control many other modules such as the master RTC or the PDM in a simple command set. The available commands (those of the DM24s, SAM-195, and CRM) are summarized in Table **T19.** The command session is finished by a "close" command from upstream or by a time-out of 1 min. The command session can be established between a DM24 and upstream modules over the CRM through the high-speed link, in what is called a pass-through. When an upstream unit requests the CRM for a connection to a DM24, the CRM stops sending data to the unit and relays the connection request to the DM24. The CRM continues to maintain the command session link until the upstream unit finishes the session. Stream-sync characters from the upstream module are sent even during the command session to maintain stable clock synchronization over the modules.

T19. Available command set in the CRM, OBH, and SAM, p. 229.

The watchdog fail-safe timer, which is a part of the H8 microprocessor reset circuit, is employed to reset the CRM. The timer needs to be triggered at least every 1.5 s. The CRM system multitasker normally does this every second. If there is some failure of the CRM program, a failure to trigger the timer results in a system reboot.

Power Distribution Module

The PDM is a unit that switches and distributes power to all the sensors and the CRM. The PDM measures the supply voltage and currents and sends that information to the CRM. The PDM can have a maximum of seven channels of power switches independently controlled by the CRM. The CRM in the MEG-195 utilizes two channels for the OBHs; the CRM in the SAM-195 uses two channels for hard disk units.

Each power channel is switched by separate MOS FET (LH1517) relays. Channels 1 and 2 are different from the others in that they employ two LH1517s to double the switchable load. Current through each power channel is monitored by the CRM every second. To protect other modules, the CRM shuts down a channel if it draws an unexpectedly large average current over 1 min. Shutdown criteria can be different for each component and are configured in the CRM system CMOS memory.

The PDM controls power to the CRM, which controls power to the sensors. This is done by the power management circuit along with a battery backup RTC, which can run on a very small power supply. The PDM monitors the LBU voltage, and if the voltage drops to <17.5 V, the PDM switches off the CRM (and thus all the sensors) to prevent the system from running into an unstable condition. If this situation should occur, the system is kept down until the voltage is restored to 20.0 V or for 24 hr. Within this shutdown period of 24 hr, the system can be restarted by cycling power for 2 min until the PDM automatically shuts the system back off. If there is the need to operate the system intentionally under this situation, we can change the status of the system by sending a "manual" command to the normal sequence of operation. The PDM can also be configured to power the system on a preset date with a wake-up command.

Downhole Link

Two 550-m-long cables, which are tied to the 4.5-in casing pipes, supply power for each downhole OBH as well as transfer data for the MEG-195. The cables have eight conductors each. Each of the long cables is branched to terminate with two, four-conductor female UMCs 1 m below the connectors. Two UMCs for each OBH were necessary because there were no UMCs with more than four conductors that can withstand 6000-m-depth pressures. The OD of all cables is 19.5 mm. The structure of the cable from the center is two layers of conductors covered with an inner jacket made from high-density plastic elastomer (HDPE) and a tension member made of aramyd fibers covered with an HDPE outer jacket. The fiber tension member provides good tensional protection of conductors up to 1800 kgf (N) of maximum tensional load. These cables retain enough mechanical flexibility to allow a bending radius as small as 12 in. The cables are designed to have a low specific gravity (1.05 g/cm^3) in seawater. Thus, these cables experience minimal tension in the borehole. They are also strapped to the 4.5-in casing at 1.5-m intervals with centralizers. The cross-sectional area of

the conductors is 1.25 mm². The cable resistance for a 700-m length is 11.3 Ω.

The cable for the OBH consists of three DC power supply wires (two negative and one positive), four data transmission line wires, and one signal ground. The electrical characteristics of the data transmission line conform to RS-422 serial communication standards. The digitized seismic signal and the seismometer status are transmitted through the uplink in GCF format. The acknowledge characters for the uplink data and clock synchronization signal are sent by the CRM to the MEG-195 through the downlink. Commands to control the seismometer, which may be issued manually during ROV operations, can also be sent through the downlink. The GCF acknowledge characters, the clock synchronization characters, and the command characters have different formats so that the seismometer can distinguish them.

The assignment of the cable wires, as well as the pin assignment of connector pins on both the MEG-195 UMC and the sensors, is summarized in Table **T20.** The OBH T1023 and T1038 are terminated by the UMC sets 1 and 2 (as shown by Fig. **F103**), respectively.

T20. Pin assignments of the UMCs, p. 231.

SAM-195

The SAM-195 is the recorder that is mounted on a frame located on top of the PAT battery frame. The SAM-195 is connected through an ROV-operated cable to the MEG-195. When the SAM-195 storage becomes full after ~1.5 yr of recording, an ROV can replace it with an empty SAM-195. Ejection of the SAM-195 is facilitated by a lever mechanism on the frame.

The power to the SAM-195 is supplied in parallel with power to the MEG-195 directly from the LBU, with a typical voltage of 22.4 V at 0°C. The SAM-195 receives data from the MEG-195 through a high-speed (57,600 bps) RS-232C serial link. The four-pin stab-mating male UMC at the bottom of the SAM-195 cylinder connects the LBU power supply and data link for the MEG-195. The SAM-195 buffers the received data in a silicon file that consists of 64 MB of flash memory. The flash file is nonvolatile memory so that data will not be lost even during power loss. When 56 MB of data is buffered, flushing of the buffered memory into a hard disk drive (HDD) is initiated (Fig. **F105**). The amount of data incoming to the SAM-195 is expected to be ~15 kbps in a standard recording configuration, as summarized in Table **T21.**

F105. Usage of flash memory in the SAM-195, p. 175.

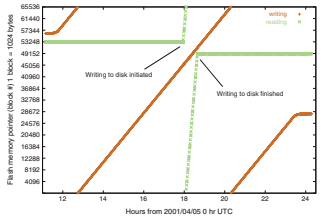

T21. Recording configuration and data amount estimation, p. 232.

The SAM-195 has four SCSI 2.5-in HDDs, which gives a total of 22.8 GB of storage. These HDDs are powered only on the memory flush. The speed of data transfer is ~1.30 MB/min.

Thus, it takes ~43 min to flush out the 56-MB buffer memory. The directory of the data written on the disk can be browsed by a "dir" command on the CRM in the SAM-195, although the data itself cannot be replayed through the serial link. On the "dir" command, the SAM-195 will reply with a list of system ID, stream ID, date of first data, date of last data, and total amount of data for a stream. The disk drives can be connected to a PC-compatible computer (PC) with a SCSI interface. A PC program called "scsiread" can replay the data written on the SCSI disk GCF format.

In parallel to saving the received data into the buffer memory, the SAM-195 also hands the data to another serial link for communication with an ROV via the four-pin female UMC. The UMC provided by Ocean Design Inc. is on top of the SAM canister. Because we assume an ROV may have a relatively slow link, such as 9600 bps, only slow data

channels (those of 20 sps or slower) and status messages are passed to the ROV serial port. When the SAM-195 receives a pass-through request from the upstream ROV, it will organize the session. If the request is addressed to downstream modules, the SAM-195 passes the request to the MEG-195 to reach the addressed module.

Power consumption of the SAM-195 is ~1.0 W in the interval between disk transfers. When the SAM-195 disk is running, the power consumption increases up to an average of 11.0 W. The SAM-195 manages power in a similar way to the MEG-195. During disk operations, the LBU voltage is monitored against a preset threshold (20 V), and if it falls below this for 10 min the disk transfer is aborted. This is done in an orderly way; the disk flushing task stops and the disk supply switches off. If this fails to finish in 5 min, the disk supply switches off. The SAM-195 also monitors the average voltage against a limit of 18.8 V and will automatically power down after 2 hr and remain shutdown for 24 hr, as in the MEG-195.

During the disk transfer period, the large power consumed in the SAM vessel results in a rapid increase of the temperature in the vessel by 20°C, as shown in Figure **F106.** This rapid temperature increase affects the precision clock, as seen in Figure **F104,** although the effect is minimized by the effective temperature compensation mechanism built into the clock module. The large current drain into the SAM also drops the supply voltage by 0.6 V at the SAM and by 0.35 V at the MEG (Fig. **F107**).

F106. Temperature in the SAM-195 and MEG-195 pressure vessels, p. 176.

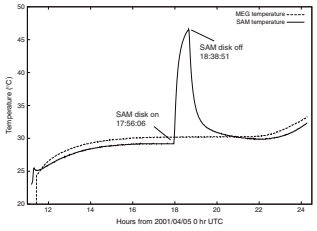

F107. Supply voltage at the MEG-195 and SAM-195, p. 177.

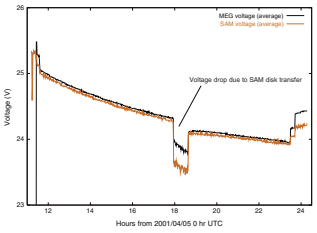

System Power Consumption

The power for the whole system is supplied by limited LBU power. We initially record the data in the SAM, which is recovered by an ROV. Switching the LBU to the other battery unit when it becomes empty is also performed by an ROV. To plan the schedule of the ROV visits properly, it is important to have a precise knowledge of the power consumption of the whole system, which varies with many parameters, such as the number of running OBHs and sample intervals of the seismic channels.

Table **T22** summarizes the result of the power consumption measurement for the NEREID-195 system in Hole 1201E. When all the OBHs are running, we expect the power consumption of the whole system over a long period to be 7.73 W. If we confirm the functionality of both OBHs, we can shut one of them off to run the system at ~4.7 W, saving as much as 3.0 W for one OBH.

T22. Power consumption of the NEREID-195 system, p. 233.

Power Supply

Lithium Battery Unit

The power for the NEREID-195 system is supplied by the LBU. The LBU consists of two identical units, which are composed of 16 lithium cells. The lithium cells are housed in a titanium sphere vessel with a diameter of 65 cm. Each unit has two titanium sphere vessels.

The cell is a manganese dioxide/lithium primary battery. Manganese dioxide and lithium are used as anode and cathode, respectively (Fig. **F108**). The battery uses lithium as a cathode because it has a larger energy density and a smaller self discharge than other types of primary batteries. The manganese dioxide/lithium battery has an advantage of being safer than other types of lithium batteries because the anode is

F108. Structure of a manganese dioxide/lithium primary battery, p. 178.

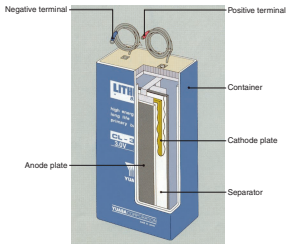

solid. Therefore, it is easy to construct a large-capacity battery using the manganese dioxide–lithium chemical process. We use the Yuasa model CL-1300L as a cell. The CL-1300L has a capacity of 1300 Ah and has a dominant voltage of 3.0 V at 25°C and 2.7 V at 0°C. The battery cells can operate between –20° and 60°C. The weight and dimension of the CL-1300L is 13.7 kg and 224 mm × 241 mm × 127 mm, respectively. The CL-1300L battery can supply a current of up to 2.6 A continuously and has a thermostat for protection against overcurrent and high temperatures. The thermostat is bimetallic and breaks a circuit at temperatures of >80°C, which corresponds to a current of >16 A passing through the circuit. The thermostat closes the circuit again at a temperature of <65°C after shutting down. The weight and volume are 10 times less than those of a lead battery, and the self-discharge rate is <1% per year. The batteries are sealed hermetically in a stainless steel canister. Therefore, the CL-1300L can be housed in a closed vessel. The discharge characteristics of the CL-1300L are shown in Figures **F109** and **F110.** The voltage of the cell is more than the dominant voltage just after start of the discharge but rapidly decreases to the dominant voltage. After reaching the dominant voltage, the voltage of the cell gradually decreases with the amount of discharge. At the end of the discharge, the voltage of the cell rapidly drops to 2.0 V. The power control units in both the MEG-195 and SAM-195 are determined by these discharge characteristics.

Titanium Sphere Battery System

The CL-1300L cells are housed in a spherical titanium pressure vessel with a diameter of 65 cm, which was developed at the Experimental Design Bureau of Oceanological Engineering, Russian Academy of Sciences. The spherical vessel is made from titanium alloy and consists of two hemispheres that are the same size. The weight in air and buoyancy in water of the sphere are 89 and 73 kg, respectively. The sphere houses eight CL-1300L cells on a rack (Figs. **F111, F112**). To increase the total capacity of the power supply, two spheres are used for an LBU. Eight CL-1300L cells in one sphere are connected in series, and two series are connected in parallel; therefore, each unit has a dominant voltage of 21.6 V at 0°C with a capacity of 2600 Ah. For the parallel connection of two series of CL-1300Ls, a diode is connected in series for each series for safety reasons (Fig. **F113**). A cable with a dry-mate connector connects each sphere for the parallel connection, and one sphere has a UMC on the top for supplying the power to the entire system. Two spheres are mounted on a titanium frame (Figs. **F114, F115**). The top and bottom of the LBU are flat panels made of fiber-reinforced plastic drainboard for compatibility with the top panel of the PAT. The top drainboard of the LBU has an access hole for the UMC. The LBU is put into a hole on the top of the PAT-195 and can be pulled out by an ROV after complete discharge. The frame of the LBU is designed for easy replacement by an ROV. Because the PAT-195 has two LBUs, the total capacity of the LBU is ~112 kWh, which corresponds to ~2.5 yr of operation with one OBH, MEG-195, and SAM-195.

At testing of the equipment before the deployment, the LBU supplied the power to the whole system. During the testing, voltage and current from the LBU were measured by the seafloor equipment, as described in **"Seafloor Instruments,"** p. 52. The testing was carried out on the deck of the ship on 5 April 2001. Because the temperature was >25°C, the voltage from the LBU without a load was >25.0 V. After con-

F109. Variation of the voltage of the CL-1300L cell, p. 179.

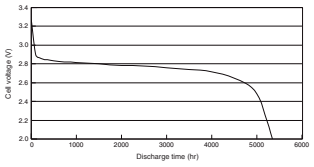

F110. Voltage of the CL-1300L cell at constant loads, p. 180.

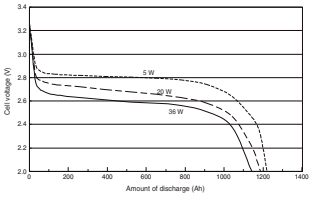

F111. Schematic of the titanium sphere, p. 181.

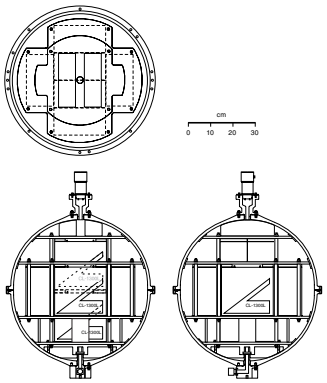

F112. Perspective view of lithium cells and rack, p. 182.

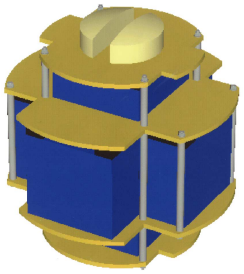

necting the equipment, the voltage of the LBU immediately started to decrease. During a large load (~1.5 A of current) caused by the power-up of the disks in the SAM-195, the LBU showed a temporary decrease of output voltage.

Battery Frame

The LBU is mounted on the cylindrical PAT frame, as shown in Figure F116. Two units of the LBU are stored in holes in the upper part of the PAT. The PAT frame is made of ordinary steel and is coated with epoxy paint to protect it from corrosion. The titanium frames of the LBUs are isolated from the PAT with polyvinyl chloride insulators. The top of the PAT is a flat panel made of fiber-reinforced plastic drainboard. The top of the LBU is the same level as that of the PAT at its proper position. The wide, flat panel serves as the ROV platform. The panel is reinforced by a metal frame and is circular when viewed from above. The diameter of the top panel is 3.2 m. The basal "leg" of the PAT is also circular and the diameter is 3.66 m, which corresponds to the diameter of the reentry cone. The basal leg is 0.24 m in height. The leg keeps the PAT stable on the reentry cone. In the center of the PAT frame, coaxial rings are placed to guide the PAT smoothly over the riser assembly during the installation. The hole in the center of the top panel provides space for the MEG frame. The total height of the PAT is 2.64 m to avoid contamination of seafloor mud during an ROV operation. The vertical position of the MEG-195 on the riser is set to allow ROV operations. The top of the MEG-195 is 608 mm above the top panel of the PAT. The PAT also holds the SAM-195 recorder beneath its top panel. The top part of the SAM-195 sticks out of the panel. The UMC at the bottom of the SAM bulkhead is mated by gravity into a UMC receptacle, mounted on the stab plate placed at the bottom of the SAM hole, when the SAM-195 is dropped into the hole. During the dropping operation, the hole keeps the SAM-195 canister in the upright position. The SAM-195 key is lowered to the guiding wedges prepared inside the hole. At this time, the connectors on the bottom bulkhead of the SAM-195 canister are correctly positioned to the mating orientation of the UMC. The SAM-195 can be set and ejected by an ROV-operated lever mechanism in the recorder frame (Fig. F117). The lever can be locked at two positions, one at the mated position of the SAM-195 and the other at the released position. By the use of the locking positions, an ROV can easily replace the SAM-195 canister. The cable from the UMC at the bottom of the SAM hole receptacle has a T-junction; one branch is for connection to the LBU, and the other goes to the MEG-195. Both branches are terminated with UMCs, which are mounted on the PAT top panel. Two other cables (the ROV cables) are installed on the panel; one is used to connect the UMC receptacle on the top panel to the MEG-191 canister, and the other cable is for connection between the UMC plug to the LBU. The ROV cables are fastened to the top panel initially by fastening mechanisms. The ROV cable end for the MEG-195 canister is fixed at a parking connector for the ROV UMC receptacle. An ROV will take off the fasteners and connect the ROV UMC receptacle to the MEG-195 canister. The other end of the T-junction branch cable is connected to the LBU during the deployment. After complete discharge of one LBU, an ROV must change the connection to the other LBU.

F113. Block diagram of a lithium battery system unit, p. 183.

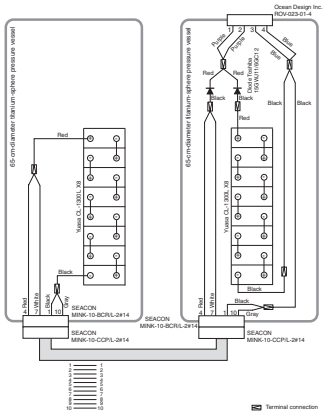

F114. LBU during assembly, p. 184.

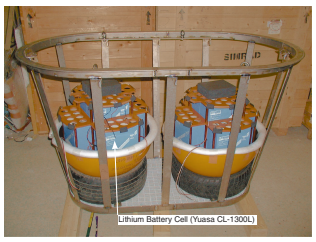

F115. Photograph of the LBU, p. 185.

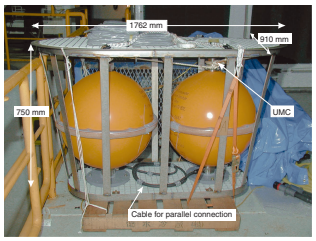

F116. PAT in the moonpool area, p. 186.

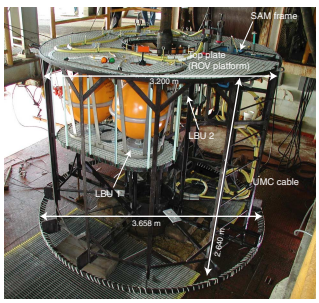

ROV Operations

Operation of WP-1 Observatory

The downhole OBH sensors (see "Borehole Instruments," p. 50) are not functioning until the NEREID-195 system is activated by an ROV. *Kaiko* (Fig. F118), a Japan Marine Science and Technology Center (JAMSTEC) ROV designed to operate in water depth up to 11,000 m, is scheduled to visit Site 1201 to activate the WP-1 observatory.

The operations by the ROV are as follows:

1. Dive to Site 1201 with the SAM-195.
2. Remove the dummy SAM from its seating frame located on the top of the PAT.
3. Insert the SAM-195 onto the seating frame.
4. Make a connection between the MEG-195 and the PAT.
5. Check the status of the NEREID-195 system using the SAM/ROV interface.
6. Return to the surface.

(See "Seafloor Instruments," p. 52, for MEG and SAM information; see "Power Supply," p. 58, for PAT information.)

An ROV dive depends on sea conditions. Poor sea conditions may prevent the ROV from diving to activate the WP-1 observatory during its planned March 2002 visit to Site 1201. The SAM-195 can record automatically using its timer. If the SAM-195 were installed on the PAT at the time of installation and the WP-1 observatory is not activated at the scheduled time, the SAM would start to work and consume battery power while the OBH sensors and the MEG were inactive. For this reason, the SAM-195 will be installed at the time of the ROV visit.

After the SAM-195 is installed on the PAT, the NEREID-195 system activates as soon as the electrical connection between the MEG-195 and the PAT is made using the UMCs. Power is supplied to the OBH sensors, the MEG-195, and the SAM-195 from the LBU. Once this connection is made, data from the OBH sensors start to flow into the SAM-195 on the PAT, which can store 60 GB of data, sufficient to record 490 days of observations.

The ROV can check the status of the system via a SAM/ROV interface that allows RS-232C communication between the SAM-195 and the ROV. If there are no problems, the ROV needs to swap the SAM-195 at least once every year to ensure no loss of data continuity. The battery life is estimated to be ~1.5 yr. After the first observation period, the ROV will change the connection from LBU 2 to LBU 1 and recover LBU 2, which was used for the first observation period. After complete consumption of LBU 1, we will deploy a new LBU to continue observations.

The seafloor downhole observatory is still in the pilot study stage. There is no routine setup that one can rely on. In our design, the OBH sensor string is unrecoverable for the reasons given in "Installation Techniques," p. 48. This necessitates that the string be composed of highly reliable instruments (see "Borehole Instruments," p. 50). On the other hand, the seafloor components are virtually all replaceable and serviceable by an ROV. The SAM-195 is replaced at each ROV visit. The MEG-195 can be pulled out of its seating frame and reinserted by an ROV, although the operation is more complex than other tasks.

F117. Top of the PAT-195 and the recorder frame, p. 187.

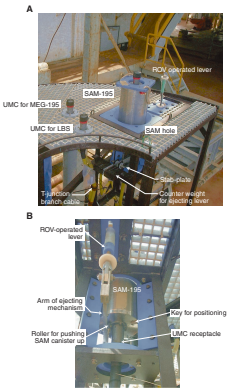

F118. Photograph of JAMSTEC's ROV, the *Kaiko,* p. 188.

REFERENCES

Araki, E., 2000. Geophysical nature of broadband seismic signals in deep oceans [Ph.D. Thesis]. Univ. of Tokyo, Japan.

Arculus, R.J., Gill, J.B., Cambray, H., Chen, W., and Stern, R.J., 1995. Geochemical evolution of arc systems in the western Pacific: the ash and turbidite record recovered by drilling. *In* Taylor, B., and Natland, J. (Eds.), *Active Margins and Marginal Basins of the Western Pacific*. Geophys. Monogr., Am. Geophys. Union, 88:45–65.

Backman, J., and Hermelin, J.O.R., 1986. Morphometry of the Eocene nannofossil *Reticulofenestra umbilicus* lineage and its biochronological consequences. *Palaeogeogr., Palaeoclimatol., Palaeoecol.,* 57:103–116.

Basaltic Volcanism Study Project (BVSP), 1981. *Basaltic Volcanism on the Terrestrial Planets:* New York (Pergamon Press).

Berggren, W.A., Kent, D.V., Swisher, C.C., III, and Aubry, M.-P., 1995. A revised Cenozoic geochronology and chronostratigraphy. *In* Berggren, W.A., Kent, D.V., Aubry, M.-P., and Hardenbol, J. (Eds.), *Geochronology, Time Scales and Global Stratigraphic Correlation*. Spec. Publ.—Soc. Econ. Paleontol. Mineral., 54:129–212.

Bloomer, S.H., Taylor, B., MacLeod, C.J., Stern, R.J., Fryer, P., Hawkins, J.W., and Johnson, L., 1995. Early arc volcanism and the ophiolite problem: a perspective from drilling in the western Pacific. *In* Taylor, B., and Natland, J. (Eds.), *Active Margins and Marginal Basins of the Western Pacific*. Geophys. Monogr., Am. Geophys. Union, 88:1–30.

Bramlette, M.N., and Wilcoxon, J.A., 1967. Middle Tertiary calcareous nannoplankton of the Cipero Section, Trinidad, W.I. *Tulane Stud. Geol.,* 5:93–132.

Cambray, H., Pubellier, M., Jolivet, L., and Pouclet, A., 1995. Volcanic activity recorded in deep-sea sediments and the geodynamic evolution of western Pacific island arcs. *In* Taylor, B., and Natland, J. (Eds.), *Active Margins and Marginal Basins of the Western Pacific*. Geophys. Monogr., Am. Geophys. Union, 88:97–124.

Cande, S.C., and Kent, D.V., 1995. Revised calibration of the geomagnetic polarity timescale for the Late Cretaceous and Cenozoic. *J. Geophys. Res.,* 100:6093–6095.

Chester, R., and Aston, S.R., 1976. The geochemistry of deep-sea sediments. *In* Riley, J.P., and Chester, R. (Eds.), *Chemical Oceanography* (2nd ed.): New York (Academic Press).

Clift, P.D., and ODP Leg 135 Scientific Party, 1994. Volcanism and sedimentation in a rifting island-arc terrain: an example from Tonga, SW Pacific. *In* Smellie, J.L. (Ed.), *Volcanism Associated with Extension at Consuming Plate Margins*. Spec. Publ.— Geol. Soc. London, 81:29–51.

Cox, A., and Gordon, R.G., 1984. Paleolatitudes determined from paleomagnetic data from vertical cores. *Rev. Geophys. Space Phys.,* 22:47–72.

Dickinson, W.R., 1985. Interpreting provenance relations from detrital modes of sandstones. *In* Zuffa, G.G. (Ed.), *Provenance of Arenites:* Dordrecht (D. Riedel), 333–361.

Egeberg, P.K., and Leg 126 Shipboard Scientific Party, 1990. Unusual composition of pore-waters found in the Izu-Bonin fore-arc sedimentary basin. *Nature,* 344:215–218.

Ellis, C.H., 1975. Calcareous nannofossil biostratigraphy—Leg 31, DSDP. *In* Karig, D.E., Ingle, J.C., Jr., et al., *Init. Repts. DSDP,* 31: Washington (U.S. Govt. Printing Office), 655–676.

Fisher, R.V., and Schmincke, H.-U., 1984. *Pyroclastic Rocks:* New York (Springer-Verlag).

Fryer, P., Gill, J.B., and Jackson, M.C., 1997. Volcanologic and tectonic evolution of the Kasuga Seamounts, northern Mariana Trough: *Alvin* submersible investigations, *J. Volcanol. Geotherm. Res.,* 79:277–311.

Fukao, Y., 1992. Seismic tomogram of the Earth's mantle: geodynamic implications. *Science,* 258:625–630.

Fukao, Y., Obayashi, M., Inoue, H., and Nenbai, M., 1992. Subducting slabs stagnant in the mantle transition zone. *J. Geophys. Res.,* 97:4809–4822.

Garland, G.D., 1979. *Introduction to Geophysics:* Philadelphia (Saunders).

Gieskes, J.M., and Lawrence, J.R., 1981. Alteration of volcanic matter in deep-sea sediments: evidence from the chemical composition of interstitial waters from deep sea drilling cores. *Geochim. Cosmochim. Acta,* 45:1687–1703.

Gill, J.B., Seales, C., Thompson, P., Hochstaedter, A.G., and Dunlap, C., 1992. Petrology and geochemistry of Pliocene–Pleistocene volcanic rocks from the Izu Arc, Leg 126. *In* Taylor, B., Fujioka, K., et al., *Proc. ODP, Sci. Results,* 126: College Station, TX (Ocean Drilling Program), 383–404.

Goodman, D., and Bibee, L.D., 1991. Measurements and modelling of possible mantle constituents from a long-line seismic refraction experiment in the West Philippine Basin. *Geophys. J. Int.,* 106:667–675.

Hall, R., Fuller, M., Ali, J., and Anderson, C., 1995. The Philippine Sea plate: magnetism and reconstructions. *In* Taylor, R.B., and Natland, J. (Eds.), *Active Margins and Marginal Basins of the Western Pacific.* Geophys. Monogr., Am. Geophys. Union, 88:371–404.

Haq, B.U., 1972. Paleogene calcareous nannoflora, Part III: Oligocene of Syria. *Stockholm Contrib. Geol.,* 21:99–127.

Hawkins, J.W., 1995. Evolution of the Lau Basin—insights from ODP Leg 135. *In* Taylor, B., Natland, J. (Eds.), *Active Margins and Marginal Basins of the Western Pacific.* Geophys. Monogr., Am. Geophys. Union, 88:125–173.

Hilde, T.W.C., and Lee, C.S., 1984. Origin and evolution of the West Philippine Basin: a new interpretation. *Tectonophysics,* 102:85–104.

Johannes, W., 1978. Melting of plagioclase in the system Ab-An-H_2O and Qz-Ab-An-H_2O at P_{H_2O} = 5 kbar, an equilibrium problem. *Contrib. Mineral. Petrol.,* 66:295–303.

Kanamori, H., and Abe, K., 1968. Deep structure of island arcs as revealed by surface waves. *Bull. Earthquake Res. Inst.,* 46:1001–1025.

Kanazawa, T., Sager, W.W., Escutia, C., et al., 2001. *Proc. ODP, Init. Repts.,* 191 [CD-ROM]. Available from: Ocean Drilling Program, Texas A&M University, College Station TX 77845-9547, USA.

Karig, D.E., Ingle, J.C., Jr., et al., 1975. *Init. Repts. DSDP,* 31: Washington (U.S. Govt. Printing Office).

Kirschvink, J.L., 1980. The least-squares line and plane and the analysis of palaeomagnetic data. *Geophys. J. R. Astron. Soc.,* 62:699–718.

Klein, E.M., and Langmuir, C.H., 1987. Global correlations of ocean ridge basalt chemistry with axial depth and crustal thickness. *J. Geophys. Res.,* 92:8089–8115.

Kroenke, L., Scott, R., et al., 1981. *Init. Repts. DSDP,* 59: Washington (U.S. Govt. Printing Office).

Lang, T.H., and Watkins, D.K., 1984. Cenozoic calcareous nannofossils from DSDP Leg 77: biostratigraphy and delineation of hiatuses. *In* Buffler, R.T., Schlager, W., et al., *Init. Repts. DSDP,* 77: Washington (U.S. Govt. Printing Office), 629–648.

LeBas, M.J., Le Maitre, R.W., Streckeisen, A., and Zanettin, B., 1986. A chemical classification of volcanic rocks based on the total alkali-silica diagram. *J. Petrol.,* 27:745–750.

Louden, K.E., 1980. The crustal and lithospheric thickness of the Philippine Sea as compared to the Pacific. *Earth Planet. Sci. Lett.,* 50:275–288.

Marsaglia, K.M., Boggs, S., Jr., Clift, P., Seyedolali, A., and Smith, R., 1995. Sedimentation in the western Pacific backarc basins: new insights from recent ODP drilling. *In* Taylor, B., and Natland, J. (Eds.), *Active Margins and Marginal Basins of the Western Pacific*. Geophys. Monogr., Am. Geophys. Union, 8:291–314.

Marsaglia, K.M., and Tazaki, K., 1992. Diagenetic trends in Leg 126 sandstones. *In* Taylor, B., Fujioka, K., et al., *Proc. ODP, Sci. Results,* 126: College Station, TX (Ocean Drilling Program), 125–138.

Martini, E., 1971. Standard Tertiary and Quaternary calcareous nannoplankton zonation. *In* Farinacci, A. (Ed.), *Proc. 2nd Int. Conf. Planktonic Microfossils Roma:* Rome (Ed. Tecnosci.), 2:739–785.

————, 1981. Oligocene to recent calcareous nannoplankton from the Philippine Sea, Deep Sea Drilling Project 59. *In* Kroenke, L., Scott., R., et al., *Init. Repts. DSDP,* 59: Washington (U.S. Govt. Printing Office), 547–565.

Moran, M.J., and Watkins, D.K., 1988. Oligocene calcareous-nannofossil biostratigraphy from Leg 101, Site 628, Little Bahama Bank Slope. *In* Austin, J.A., Jr., Schlager, W., et al., *Proc. ODP, Sci. Results,* 101: College Station, TX (Ocean Drilling Program), 87–103.

Mullen, E.D., 1983. $MnO/TiO/P_2O_5$: a minor element discriminant for basaltic rocks of oceanic environments and its implications for petrogenesis. *Earth Planet. Sci. Lett.,* 62:53–62.

Ocean Drilling Program, 1996. *Understanding Our Dynamic Earth through Ocean Drilling: Ocean Drilling Program Long Range Plan Into the 21st Century:* Washington (Joint Oceanographic Institutions).

Okada, H., and Bukry, D., 1980. Supplementary modification and introduction of code numbers to the low-latitude coccolith biostratigraphic zonation (Bukry, 1973; 1975). *Mar. Micropaleontol.,* 5:321–325.

Okino, K., Ohara, Y., Kasuga, S., and Kato, Y., 1999. The Philippine Sea: new survey results reveal the structure and the history of marginal basins. *Geophys. Res. Lett.,* 26:2287–2290.

Parkhurst, D.L., and Appelo, C.A.J., 1999. User's guide to PHREEQC (version 2)—a computer program for speciation, batch-reaction, one-dimensional transport and inverse geochemical calculations. *Water-Resour. Invest. Rep. (U.S. Geol. Surv.),* 99–259.

Pearce, J.A., 1982. Trace element characteristics of lavas from destructive plate boundaries. *In* Thorpe, R.S. (Ed.), *Andesites: Orogenic Andesites and Related Rocks:* New York (Wiley), 525–548.

Pearce, J.A., and Cann, J.R., 1973. Tectonic setting of basic volcanic rocks determined using trace element analyses. *Earth Planet. Sci. Lett.,* 19:290–300.

Rider, M., 1996. *The Geological Interpretation of Well Logs* (2nd ed.): Caithness (Whittles Publishing).

Ringwood, A.E., and Irifune, T., 1988. Nature of the 650 km seismic discontinuity: implications for mantle dynamics and differentiation. *Nature,* 331:131–136.

Rodolfo, K.S., 1980. Sedimentological summary: clues to arc volcanism, arc sundering, and back-arc spreading in the sedimentary sequences of Deep Sea Drilling Project Leg 59. *In* Kroenke, L., Scott, R., et al., *Init. Repts. DSDP,* 59: Washington (U.S. Govt. Printing Office), 621–624.

Roth, P.H., 1970. Oligocene calcareous nannoplankton biostratigraphy. *Eclogae Geol. Helv.,* 63:799–881.

Roth, P.H., Baumann, P., and Betolino, V., 1971a. Late Eocene–Oligocene calcareous nannoplankton from central and northern Italy. *In* Farinacci, A. (Ed.), *Proc. 2nd Int. Conf. Planktonic Microfossils Roma:* Rome (Ed. Tecnosci.), 2:1069–1097.

Roth, P.H., Franz, H.E., and Wise, S.W., 1971b. Morphological study of selected members of the genus *Sphenolithus* Deflandre (*Incertae sedis,* Tertiary). *In* Farinacci, A. (Ed.), *Proc. 2nd Int. Conf. Planktonic Microfossils Roma:* Rome (Ed. Tecnosci.), 2:1099–1119.

Sacks, I.S., Suyehiro, K., Acton, G.D., et al., 2000. *Proc. ODP, Init. Repts.,* 186 [CD-ROM]. Available from: Ocean Drilling Program, Texas A&M University, College Station TX 77845-9547, USA.

Schlumberger, 1989. *Log Interpretation Principles/Applications:* Houston (Schlumberger Educ. Services), SMP–7017.

Scott, R.B., Kroenke, L., Zakariadze, G., and Sharaskin, A., 1980. Evolution of the south Philippine Sea: DSDP Leg 59 results. *In* Kroenke, L., Scott, R., et al., *Init. Repts. DSDP,* 59: Washington (U.S. Govt. Printing Office), 803–816.

Seekins, L.C., and Teng, T.L., 1977. Lateral variations in the structure of the Philippine Sea plate. *J. Geophys. Res.,* 82:317–324.

Shervais, J.W., 1982. Ti-V plots and the petrogenesis of modern and ophiolitic lavas. *Earth Planet. Sci. Lett.,* 59:101–118.

Shipboard Scientific Party, 1990a. Site 792. *In* Taylor, B., Fujioka, K., et al., *Proc. ODP, Init. Repts.,* 126: College Station, TX (Ocean Drilling Program), 221–314.

———— 1990b. Site 793. *In* Taylor, B., Fujioka, K., et al., *Proc. ODP, Init. Repts.,* 126: College Station, TX (Ocean Drilling Program), 315–403.

Stephen, R.A., Collins, J.A., and Peal, K.R., 1999. Seafloor seismic stations perform well. *Eos,* 80:592.

Taylor, R.N., Marlow, M.S., Johnson, L.E., Taylor, B., Bloomer, S.H., and Mitchell, J.G., 1995. Intrusive volcanic rocks in western Pacific forearcs. *In* Taylor, B., Natland, J. (Eds.), *Active Margins and Marginal Basins of the Western Pacific.* Geophys. Monogr., Am. Geophys. Union, 88:41–43.

Thompson, R., and Oldfield, F., 1986. *Environmental Magnetism:* London (Allen and Unwin).

Torres, M.E., Marsaglia, K.M., Martin, J.B., and Murray, R.W., 1995. Sediment diagenesis in Western Pacific Basins. *In* Taylor, B., and Natland, J. (Eds.), *Active Margins and Marginal Basins of the Western Pacific.* Geophys. Monogr., Am. Geophys. Union, 88:241–258.

Underwood, M.B., Ballance, P.F., Clift, P.D., Hiscott, R.N., Marsaglia, K.M., Pickering, K.T., and Reid, R.P., 1995. Sedimentation in forearc basins, trenches, and collision zones of the western Pacific: a summary of results from the Ocean Drilling Program. *In* Taylor, B., and Natland, J. (Eds.). *Active Margins and Marginal Basins of the Western Pacific.* Geophys. Monogr., Am. Geophys. Union, 88:315–353.

Valloni, R., 1985. Reading provenance from modern marine sands. *In* Zuffa, G.G. (Ed.), *Provenance of Arenites:* Dordrecht (D. Riedel), 309–332.

Van Andel, T.H., Heath, G.R., and Moore, T.C., Jr., 1975. Cenozoic tectonics, sedimentation and paleoceanography of the central equatorial Pacific. *Mem.—Geol. Soc. Am.*, 143:187–194.

van der Hilst, H., Engdahl, R., Spakman, W., and Nolet, G., 1991. Tomographic imaging of subducted lithosphere below northwest Pacific island arcs. *Nature,* 353:37–43.

van der Hilst, R.D., and Seno, T., 1993. Effects of relative plate motion on the deep structure and penetration depth of slabs below the Izu-Bonin and Mariana island arcs. *Earth Planet. Sci. Lett.,* 120:395–407.

Verosub, K.L., and Roberts, A.P., 1995. Environmental magnetism: past, present, and future. *J. Geophys. Res.,* 100:2175–2192.

Wei, W., 1992. Paleogene chronology of Southern Ocean drill holes: an update. *In* Kennett, J.P., and Warnke, D.A. (Eds.), *The Antarctic Paleoenvironment: a Perspective on Global Change.* Antarct. Res. Ser., 56:75–96.

Wei, W., and Wise, S.W., 1989. Paleogene calcareous nannofossil magnetobiochronology: results from South Atlantic DSDP Site 516. *Mar. Micropaleont.,* 14:119–152.

White, A.F., and Hochella, M.F., 1992. Surface chemistry associated with the cooling and subaerial weathering of Recent basalt flows. *Geochim. Cosmochim. Acta,* 56:3711–3721.

Wilson, M., 1989. *Igneous Petrogenesis: A Global Tectonic Approach:* London (Unwin Hyman).

Wood, D.A., Joron, J.-L., Marsh, N.G., Tarney, J., and Treuil, M., 1980. Major- and trace-element variations in basalts from the North Philippine Sea drilled during Deep Sea Drilling Program Leg 58: a comparative study of back-arc-basin basalts with lava series from Japan and mid-ocean ridges. *In* Klein, G. deV., and Kobayashi, K., et al., *Init. Repts. DSDP,* 58: Washington (U.S. Govt. Printing Office), 873–894.

Figure F1. Location map of seismic station coverage in the northwest Pacific. At least five major plates with consuming boundaries interact in the northwest Pacific, causing subduction, backarc opening, slab collisions, terrane accretion, and island arc development. Blue and yellow circles = land seismic stations: TJN = Taejon, South Korea; INU = Inuyama, Japan; ISG = Ishigakijima, Japan; OGS = Chichijima, Japan; MCSJ = Minami Torishima, Japan; BAG = Baguio, Philippines; PATS = Pohnpei, Micronesia; JAY = Jayapura, Indonesia; PMG = Port Moresby, Papua New Guinea. Orange circles = International Ocean Network (ION) seafloor observatories: JT-1 and JT-2 (Japan Trench), WP-2 (northwest Pacific), and Site 1201 (this site). OHP = Ocean Hemisphere Project, IRIS = Incorporated Research Institutions for Seismology.

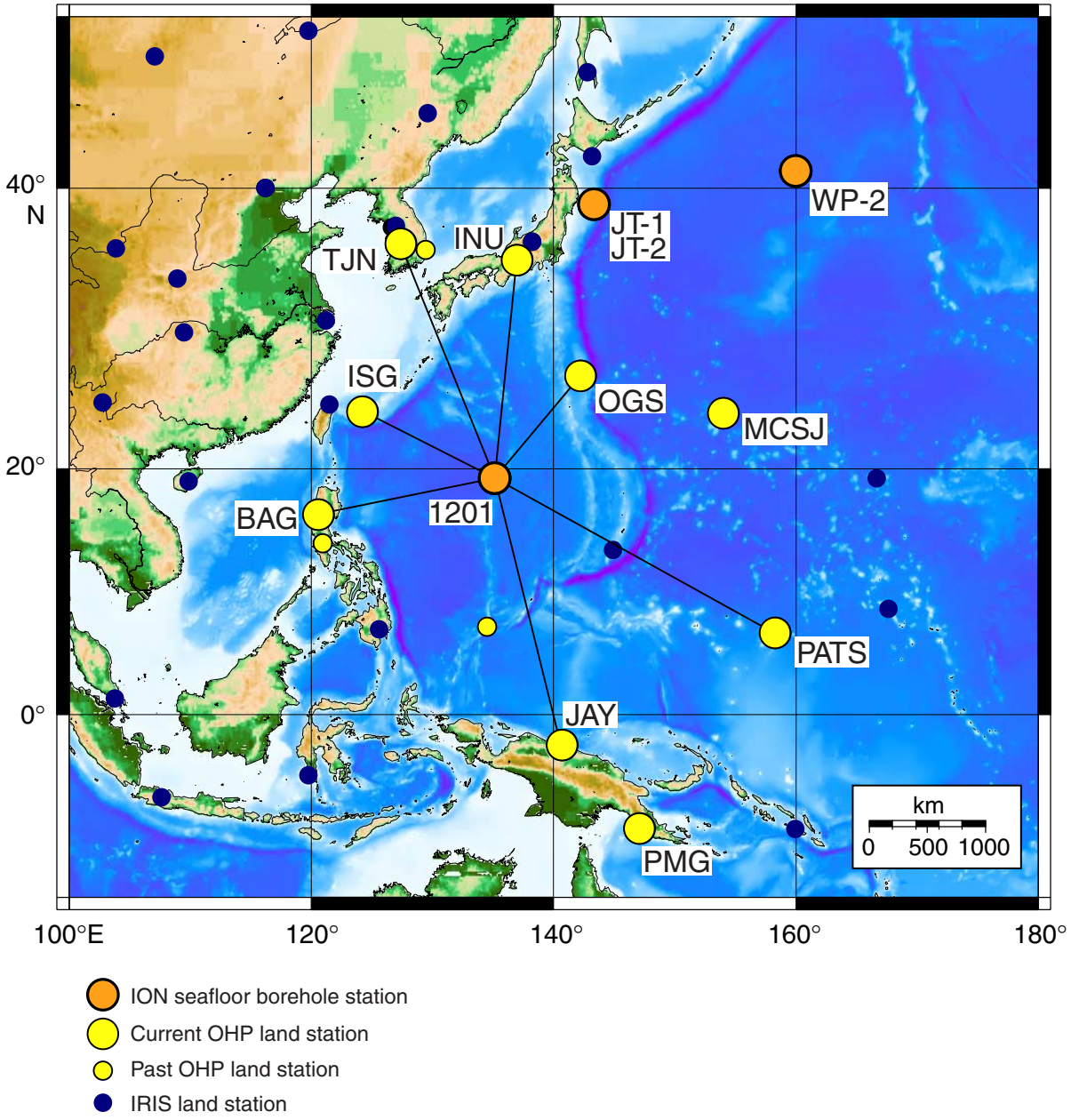

Figure F2. Location map showing DSDP Sites 290, 294, 295, and 447 and ODP Site 1201 in the Philippine Sea. Also shown are magnetic anomalies from Hilde and Lee (1984). Basement ages are in parentheses.

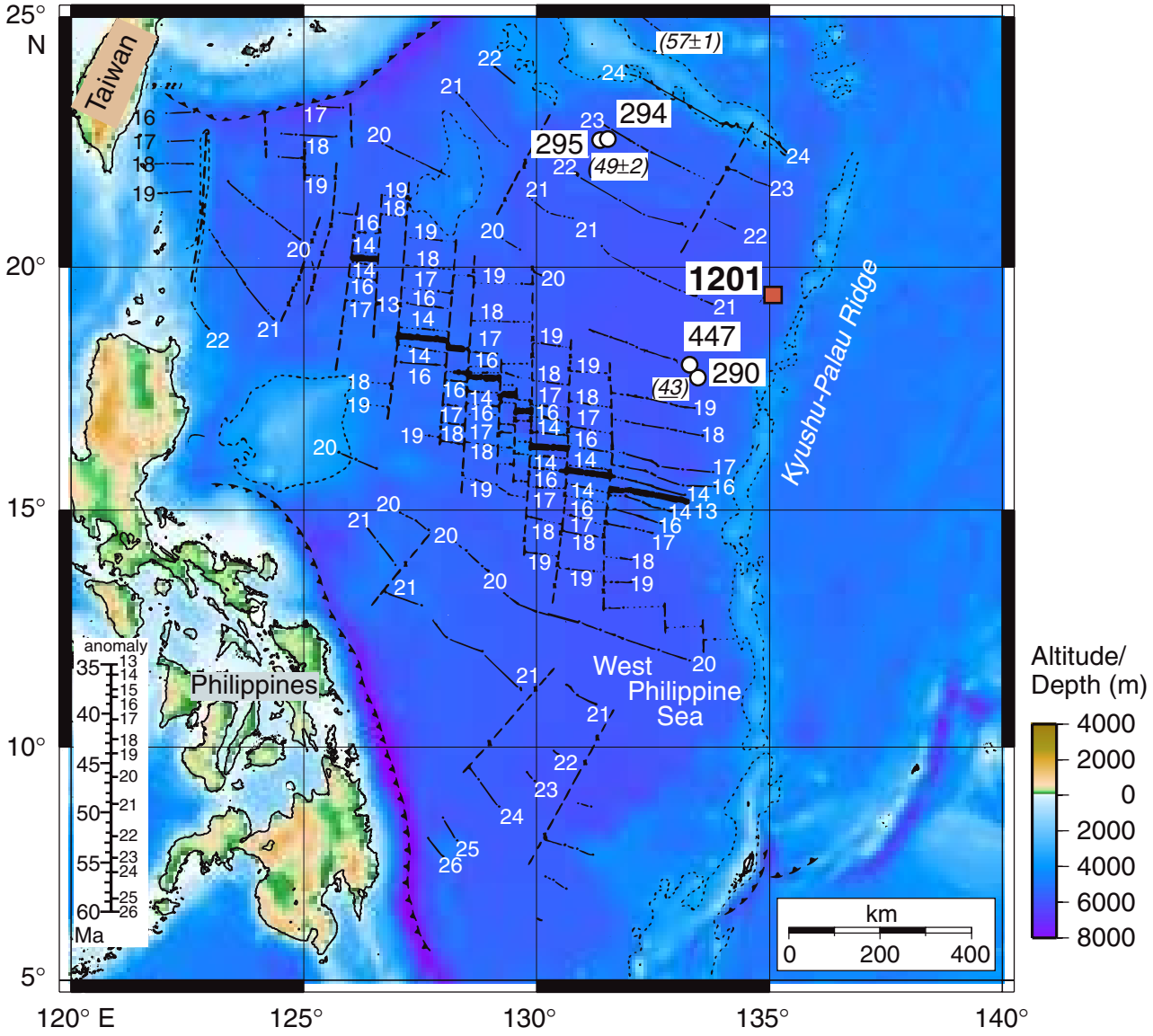

Figure F3. Location of OT97 survey lines in the vicinity of Site 1201. The seismic reflection profile for reflection line 3 is shown in Figure F4, p. 69.

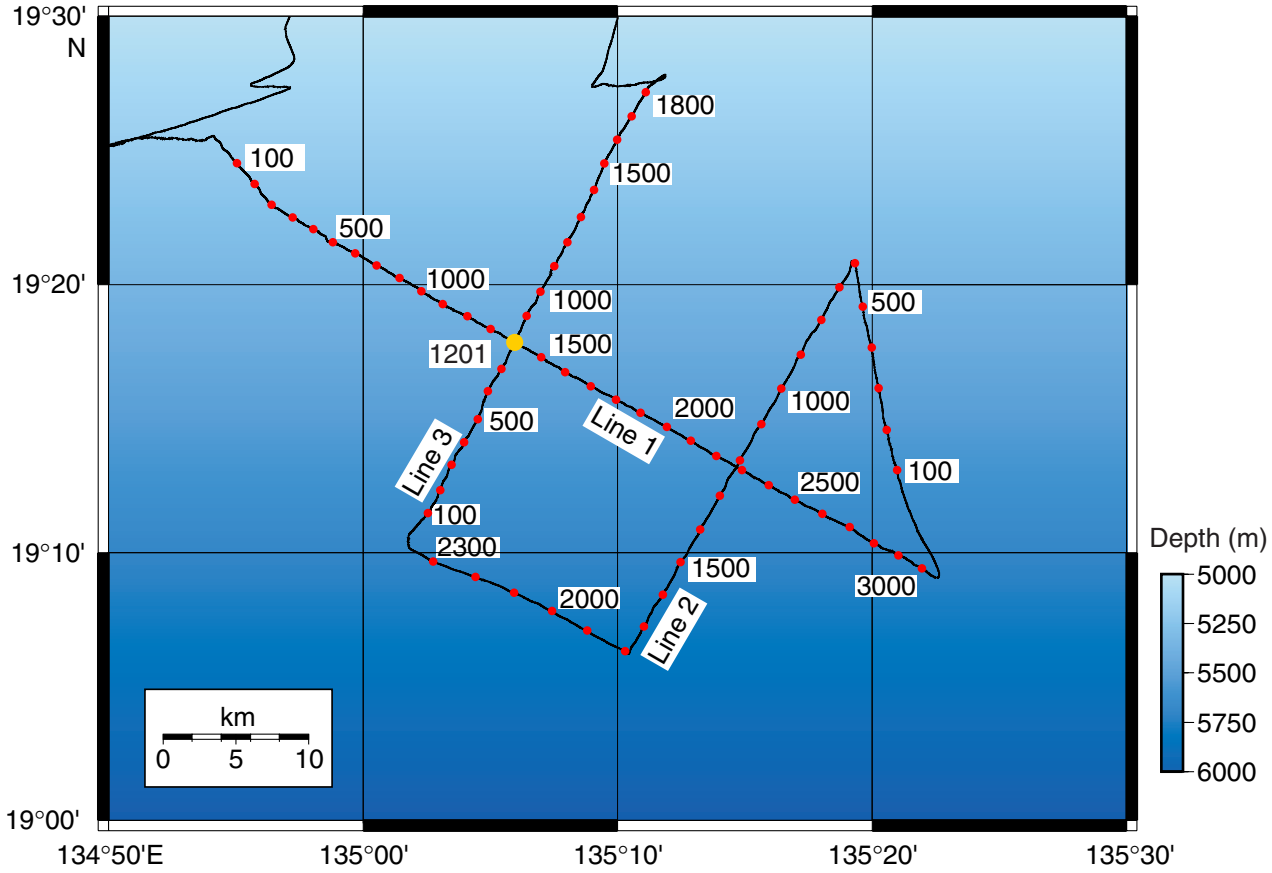

Figure F4. Reflection line OT97 showing the location of Site 1201. Basement lies ~0.5 s (two-way traveltime) below seafloor. CDP = common depth point.

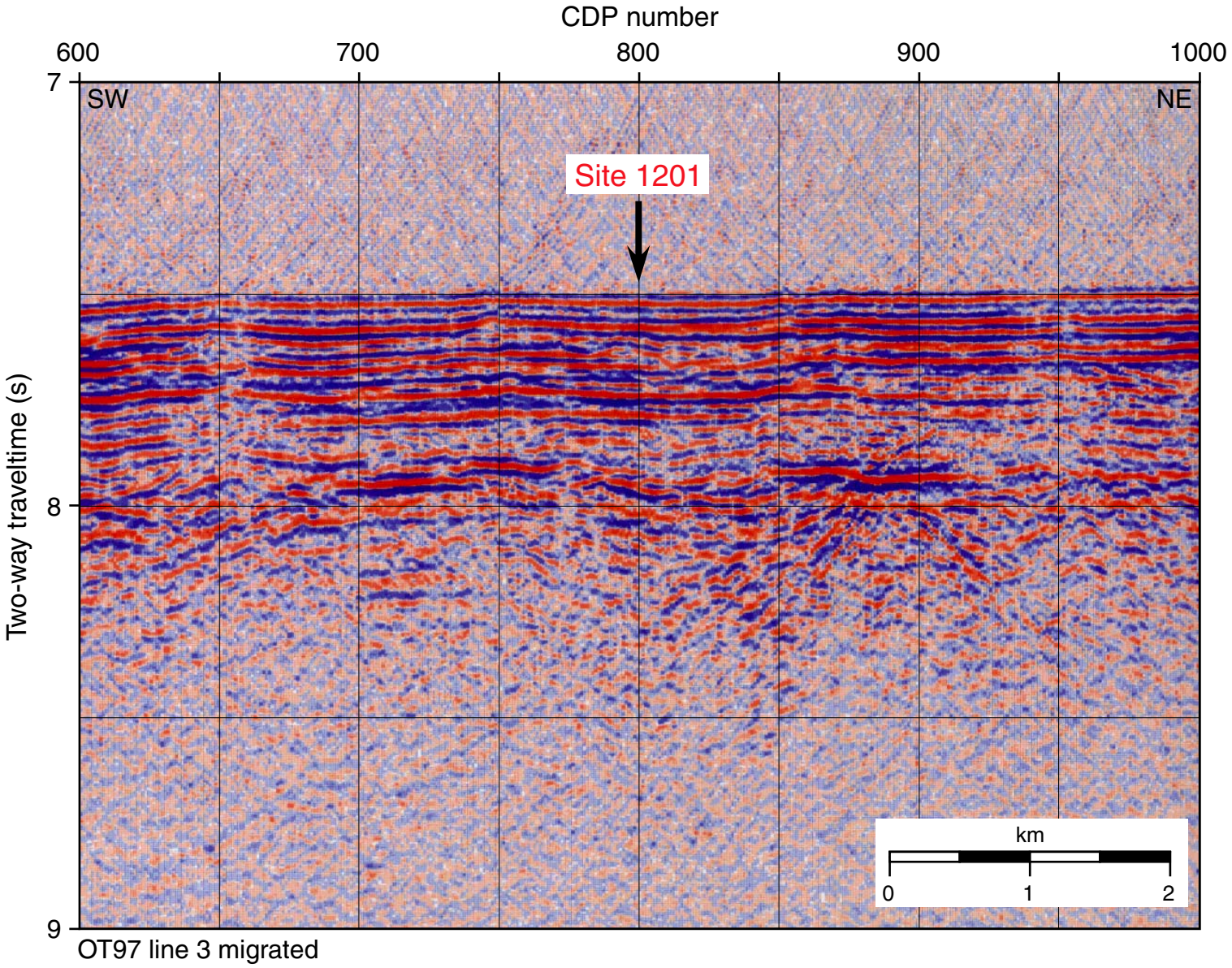

Figure F5. Representative graphic lithology log for Site 1201 including recovery, age, unit and facies descriptions, and sedimentary processes. Individual fining-upward sequences are not drawn to scale. For more detailed graphic logs, see Figures **F10,** p. 77, and **F12,** p. 79. TD = total depth. (Continued on next two pages.)

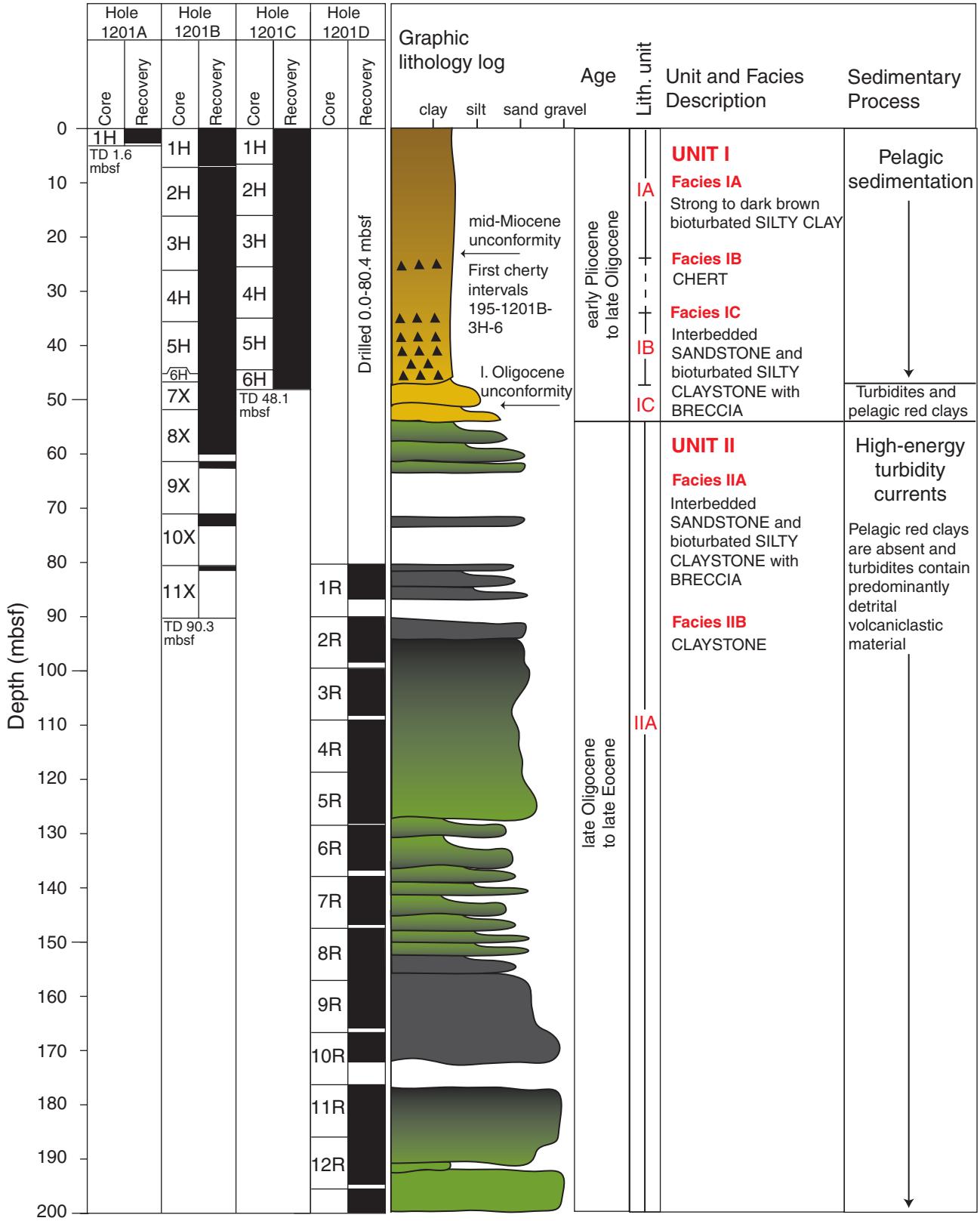

Figure F5 (continued).

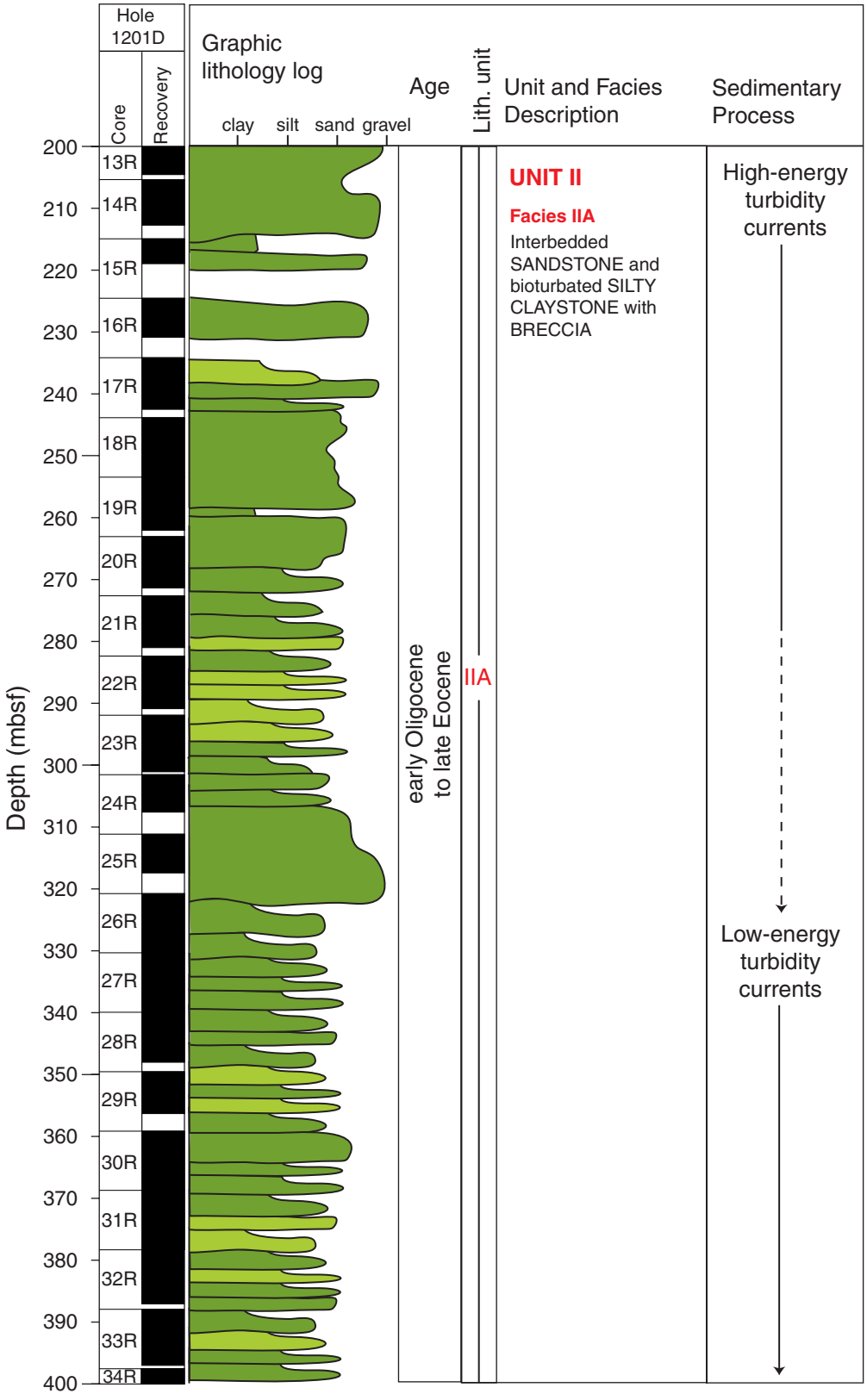

Figure F5 (continued).

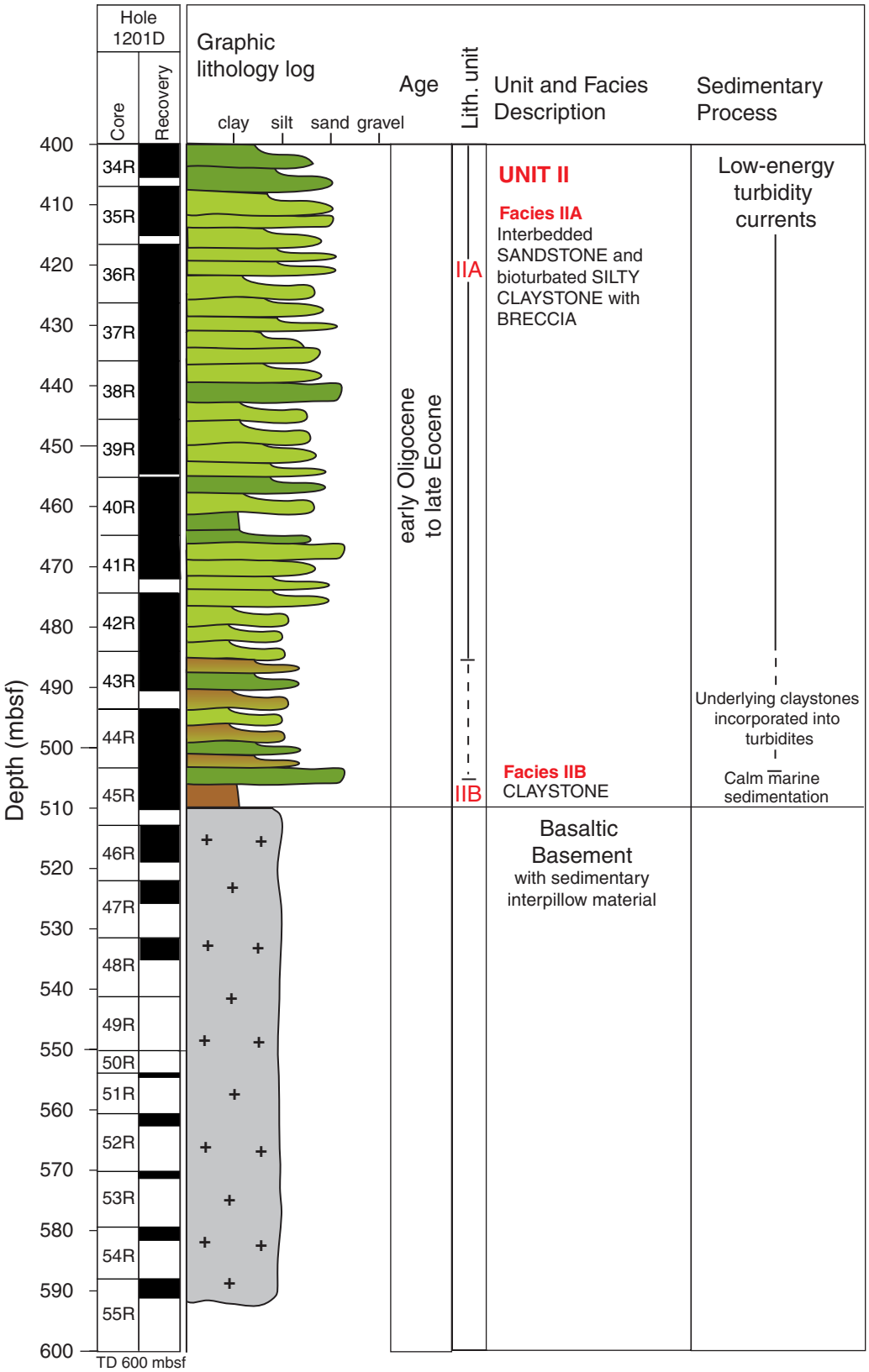

Figure F6. Summary figure for Site 1201 including lithology, units and facies, color reflectance, natural gamma count, and mineral composition. The color reflectance parameter a* measures the amount of reflectance in the green vs. red spectra. Natural gamma counts were obtained from physical properties measurements performed on the MST. Mineral composition is derived from a compilation of results from smear slide, thin section, and XRD analyses. All parameters coincide well with the lithostratigraphic boundary between Units I and II. Color reflectance data is consistent with facies changes that are associated with a change of color, whereas the natural gamma counts reflect both the large-scale and the tightly packed multiple fining-upward sequences found throughout the succession. In the graphic lithology log, c = clay, s = silt, s = sand, g = gravel.

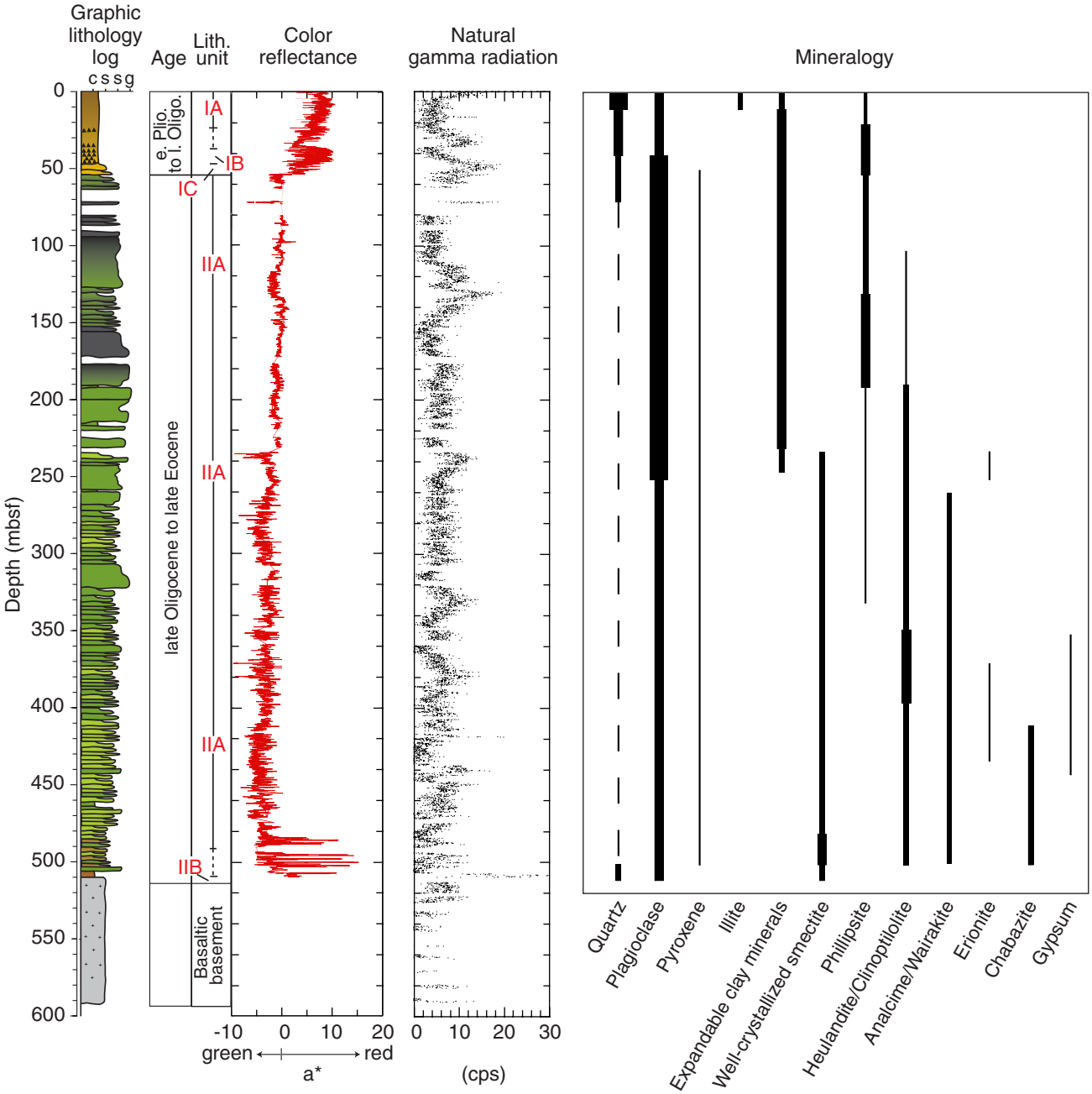

Figure F7. Bioturbated silty clays typical of Facies IA (interval 195-1201B-3H-6, 28–48 cm).

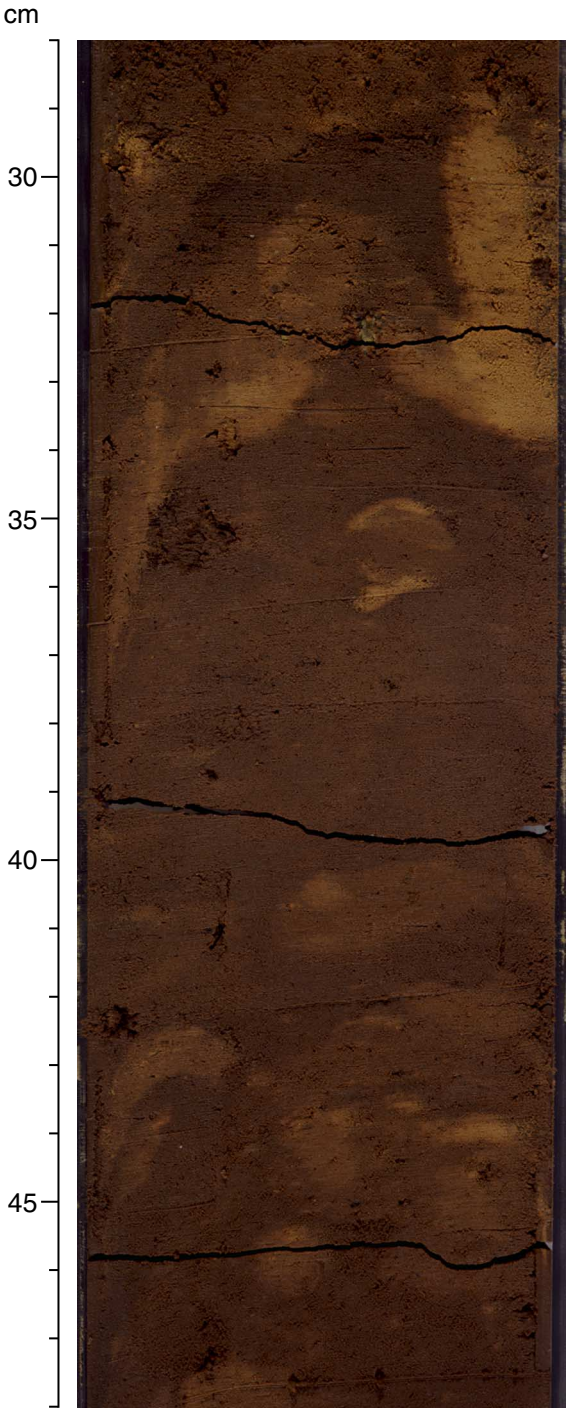

Figure F8. Possible middle Miocene hiatus in Core 195-1201B-3H. An interval of soft green zeolite nodules (55–57 cm) is overlain by fine-grained, bioturbated silty claystone and underlain by coarser sediments (interval 195-1201B-3H-6, 45–65 cm).

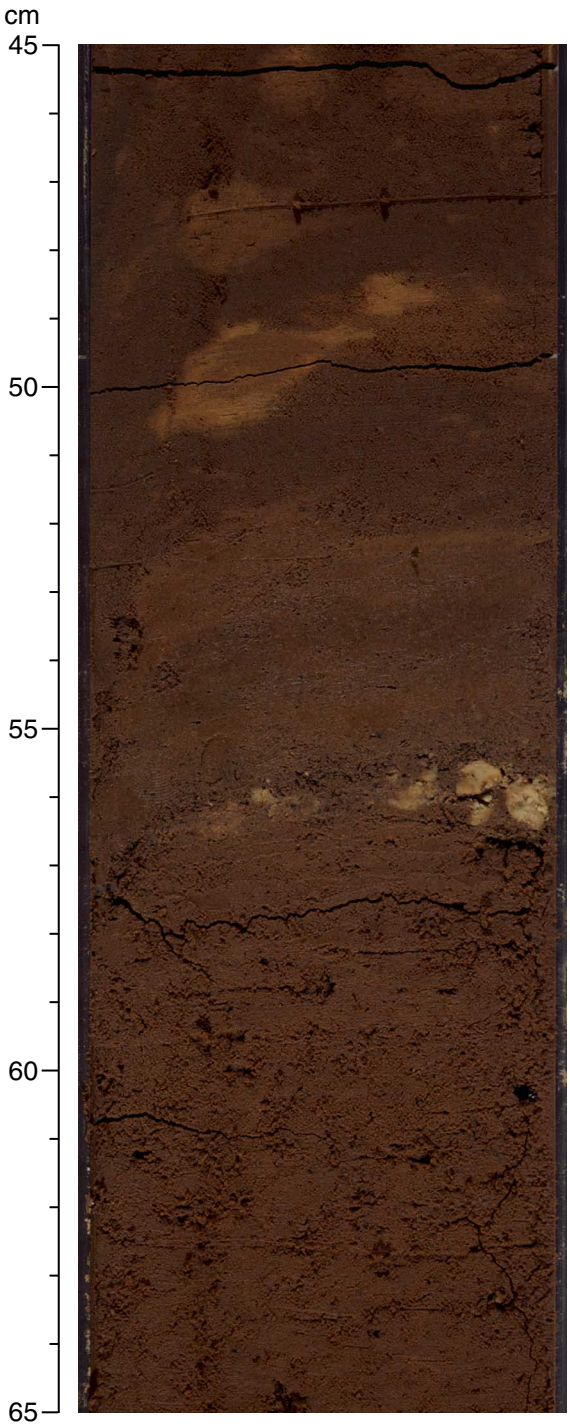

Figure F9. Chert interval typical of Facies IB within dark brown silty claystone (interval 195-1201B-5H-4, 40–70 cm).

Figure F10. Representative graphic lithology log and core photos of sandstone and bioturbated silty claystone turbidites in Core 195-1201B-7X. Structures are drawn to scale. Arrows indicate the different scales of fining-upward sequences. In the graphic lithology log, c = clay, s = silt, s = sand, g = gravel.

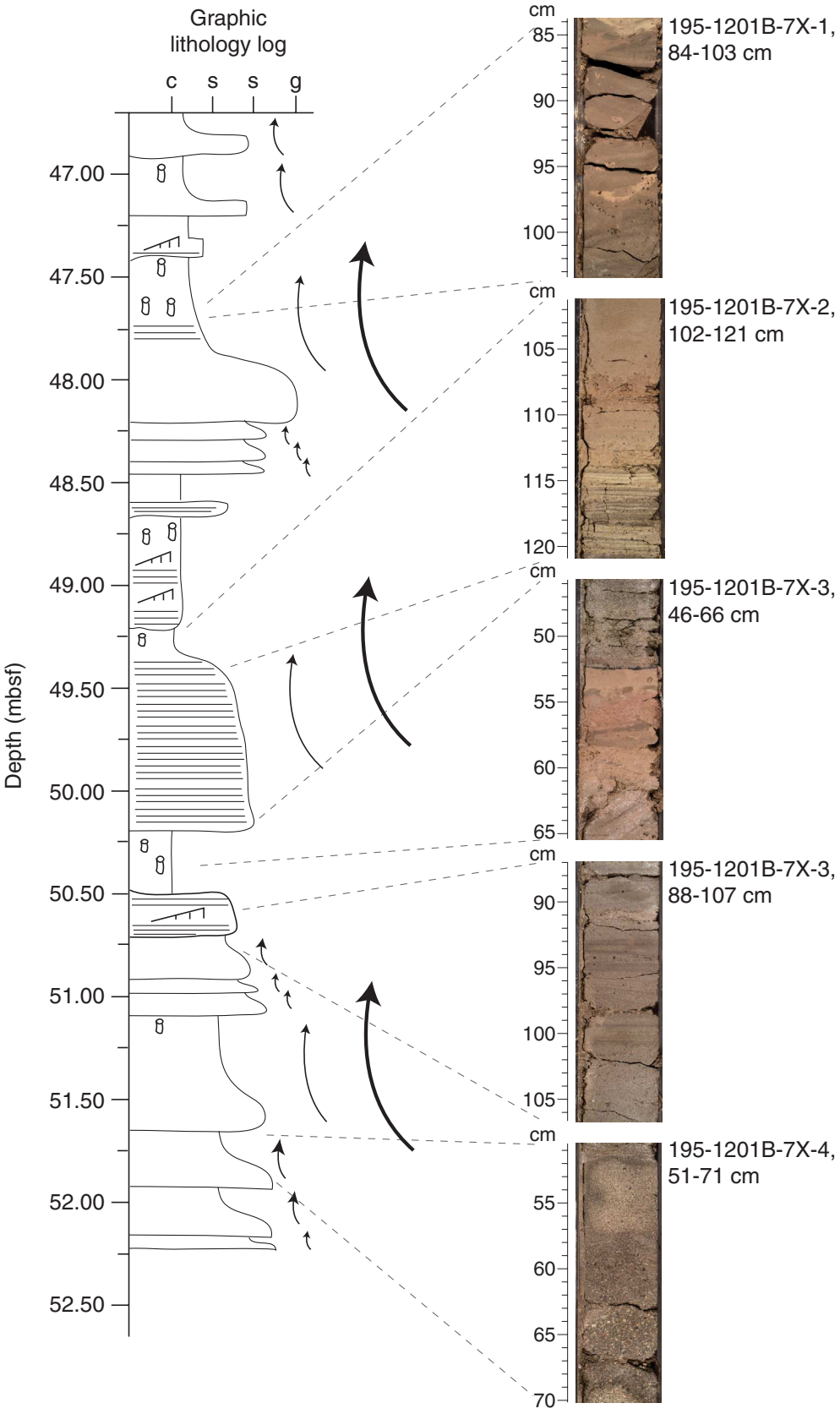

Figure F11. Dark greenish gray volcaniclastic sandstone and silty claystone turbidites typical of Facies IIA (interval 195-1201D-22R-6, 67–97 cm).

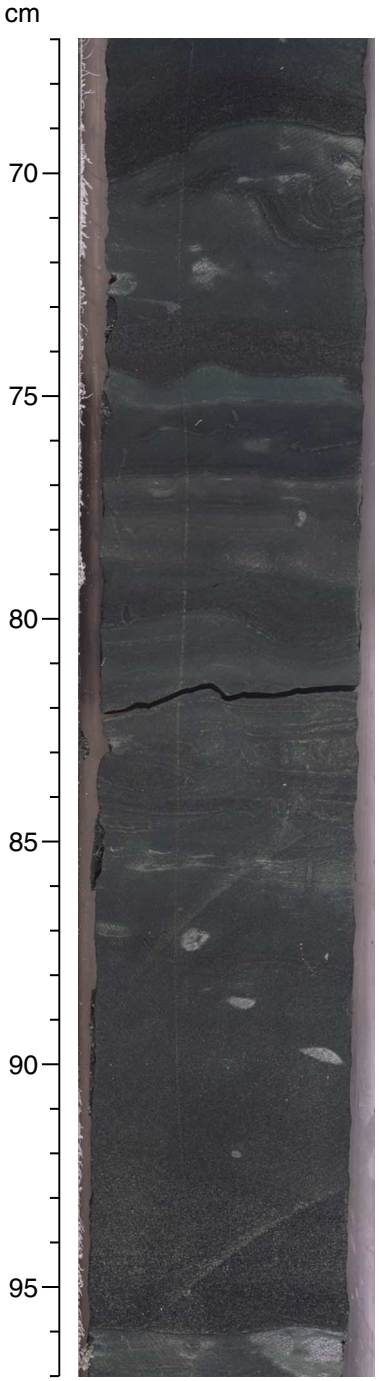

Figure F12. Representative graphic lithology log and core photo of sandstone and bioturbated silty claystone turbidites in interval 195-1201D-33R-5, 6–26 cm, with multiple fining-upward sequences drawn to scale. In the graphic lithology log, c = clay, s = silt, s = sand, g = gravel.

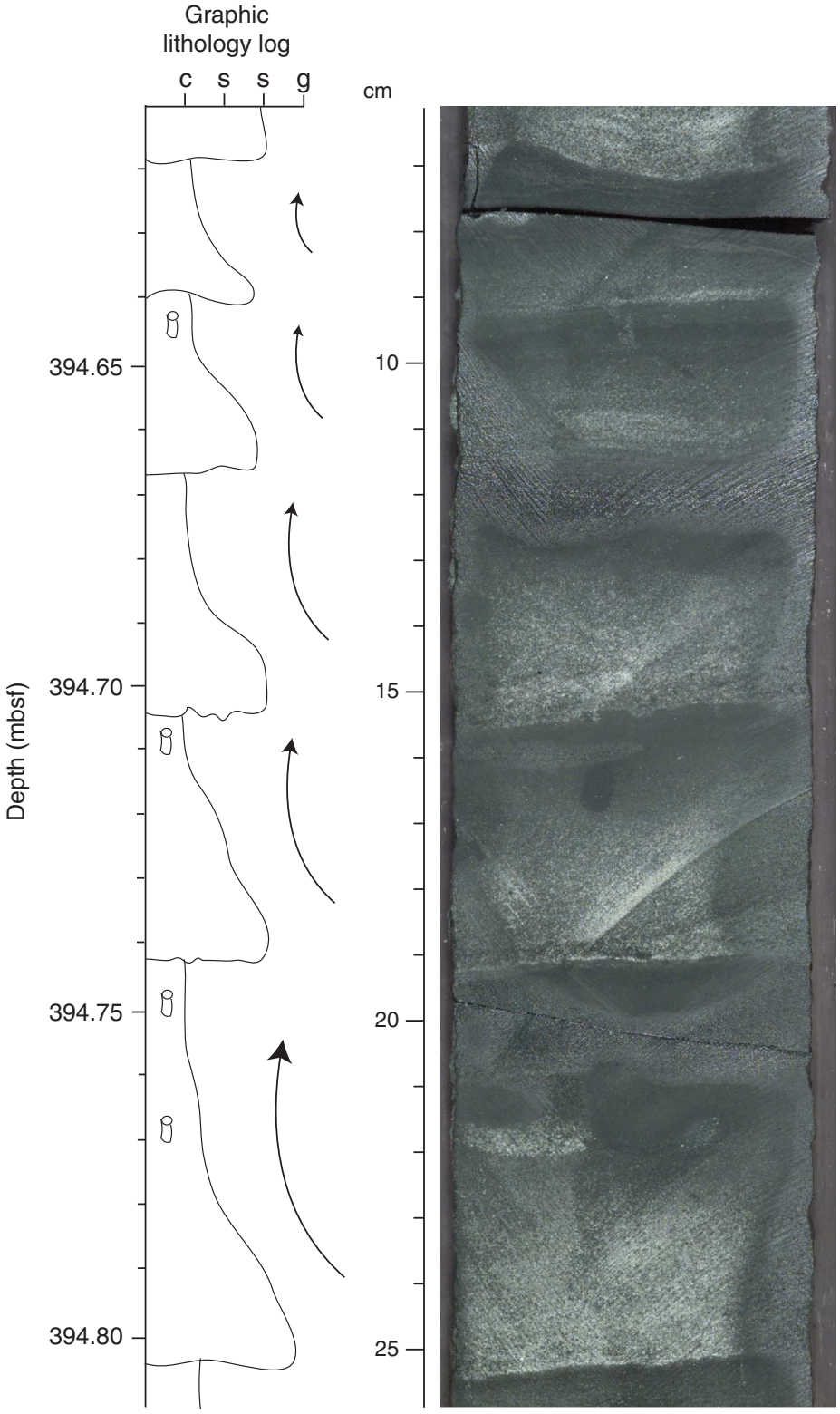

Figure F13. Fine-grained, bright green, zeolite-cemented interval (8–17 cm). These diagenetically altered intervals increase in abundance downhole (interval 195-1201D-21R-3, 0–18 cm).

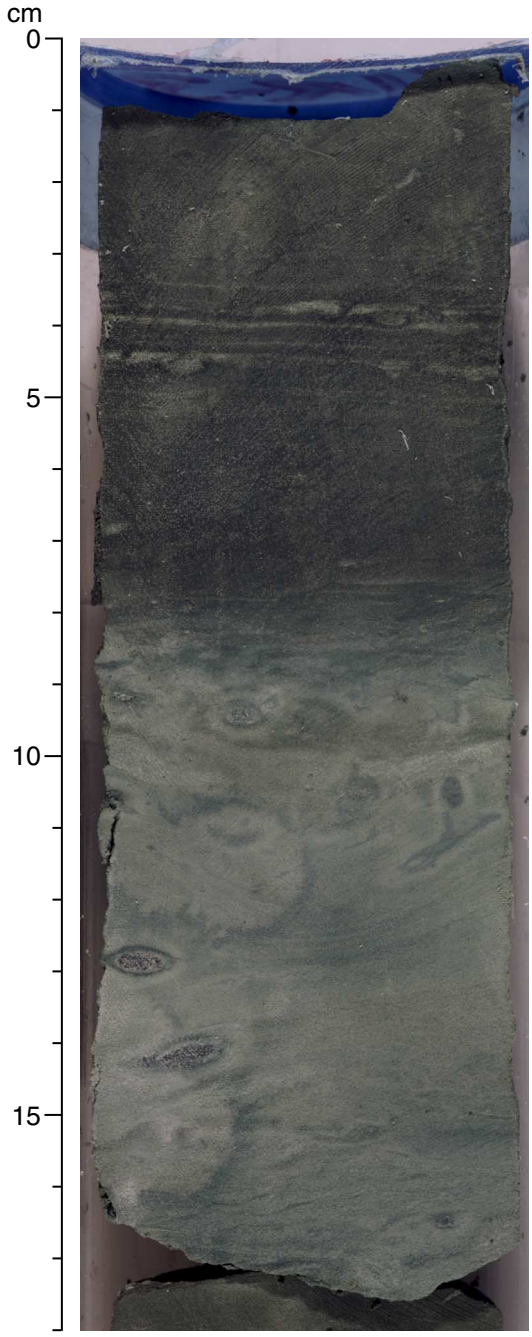

Figure F14. "Inflated" laminae in sandstone. Sand-sized grains have been altered by diagenetic alteration and primary sedimentary structures, like planar and cross laminations, now appear "fuzzy" (interval 195-1201D-35R-4, 20–40 cm).

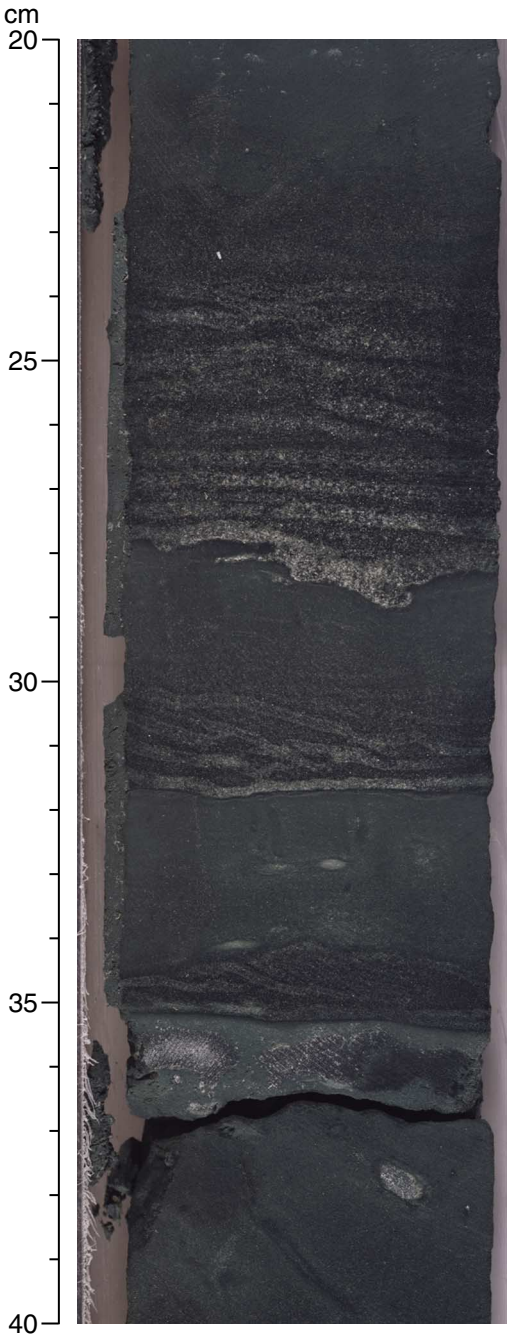

Figure F15. Dark brown claystone of Facies IIB containing a white quartz interval (63–64 cm) (interval 195-1201D-45R-5, 54–74 cm).

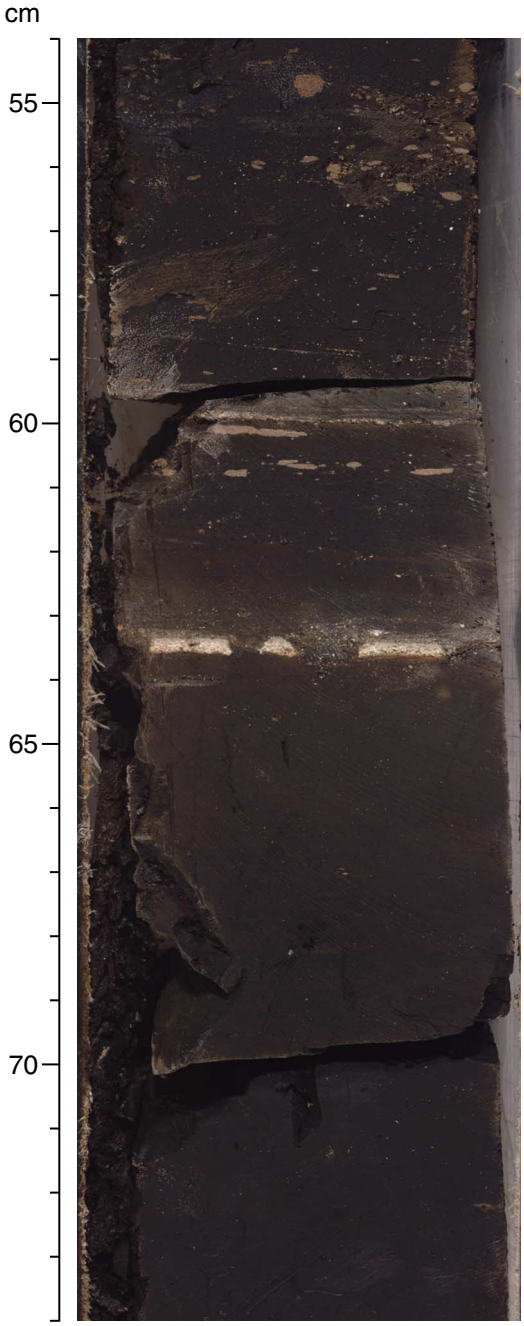

Figure F16. Contact of the sedimentary succession at Site 1201 (Facies IIB) with underlying basaltic basement (interval 195-1201D-45R-5, 80–110 cm).

Figure F17. A. Reworked zeolite grain in sandstone of Facies IC. The detrital zeolite grain originated in the spherolite cements of Unit II sandstones (see Fig. **F21,** p. 88) and thus indicates erosion of older sedimentary rocks (smear slide from Sample **195-1201B-7X-2, 147 cm** [49.67 mbsf]). **B.** Glass shards from a pumice ash layer within Facies IIA. Most shards show abundant pipe or bubble vesicles (smear slide from Sample **195-1201B-8X-6, 7 cm;** 58.97 mbsf). Both photomicrographs were taken in plane-polarized light.

Figure F18. A. Fresh lithic arenite of Unit II, showing abundant porphyry and vitrophyre rock fragments. The upper left part of this section is occupied by a sideromelane fragment (Sidm) with abundant bubble-shaped vesicles (thin section from Sample **195-1201D-1R-CC, 14–17 cm** [86.82 mbsf]). **B.** Fresh siltstone of Unit II dominated by bubble-wall glass shards (Sh) and infrequent plagioclase grains (Pl) (thin section from Sample **195-1201B-8X-6, 26–28 cm** [59.16 mbsf]). Both photomicrographs were taken in plane-polarized light.

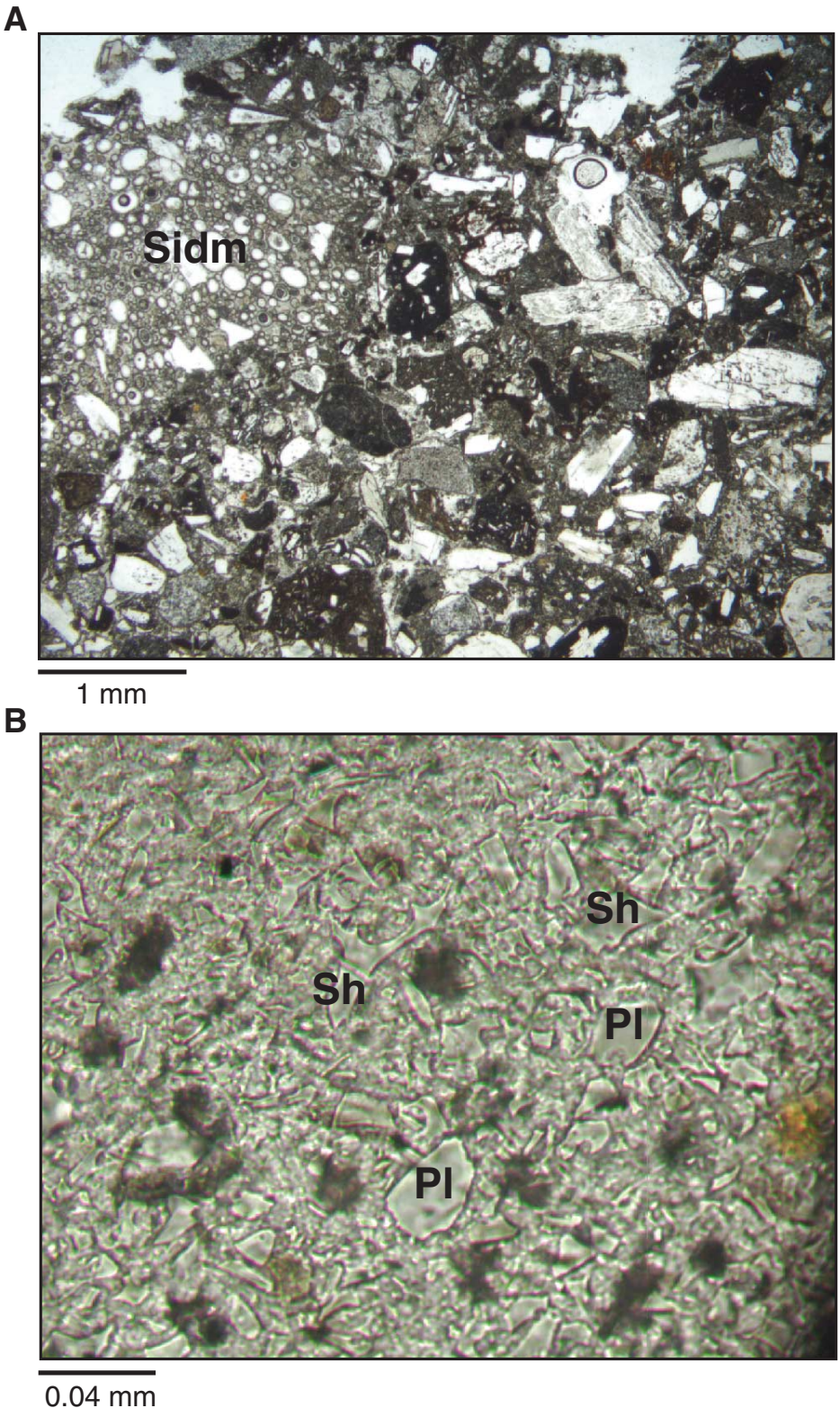

Figure F19. A. Reddish oxidized scoria vitrophyre with phenocrysts of zoned clinopyroxene (Cpx) and zoned plagioclase (Pl) (thin section from Sample **195-1201B-8X-2, 22–24 cm** [53.62 mbsf]). **B.** Black plagioclase-rich vitrophyre fragment (left) and shallow-water limestone fragment with skeletons of bryozoa and calcareous algae(?) (thin section from Sample **195-1201D-20R-4, 140–142 cm** [268.56 mbsf]). Both photomicrographs were taken in plane-polarized light.

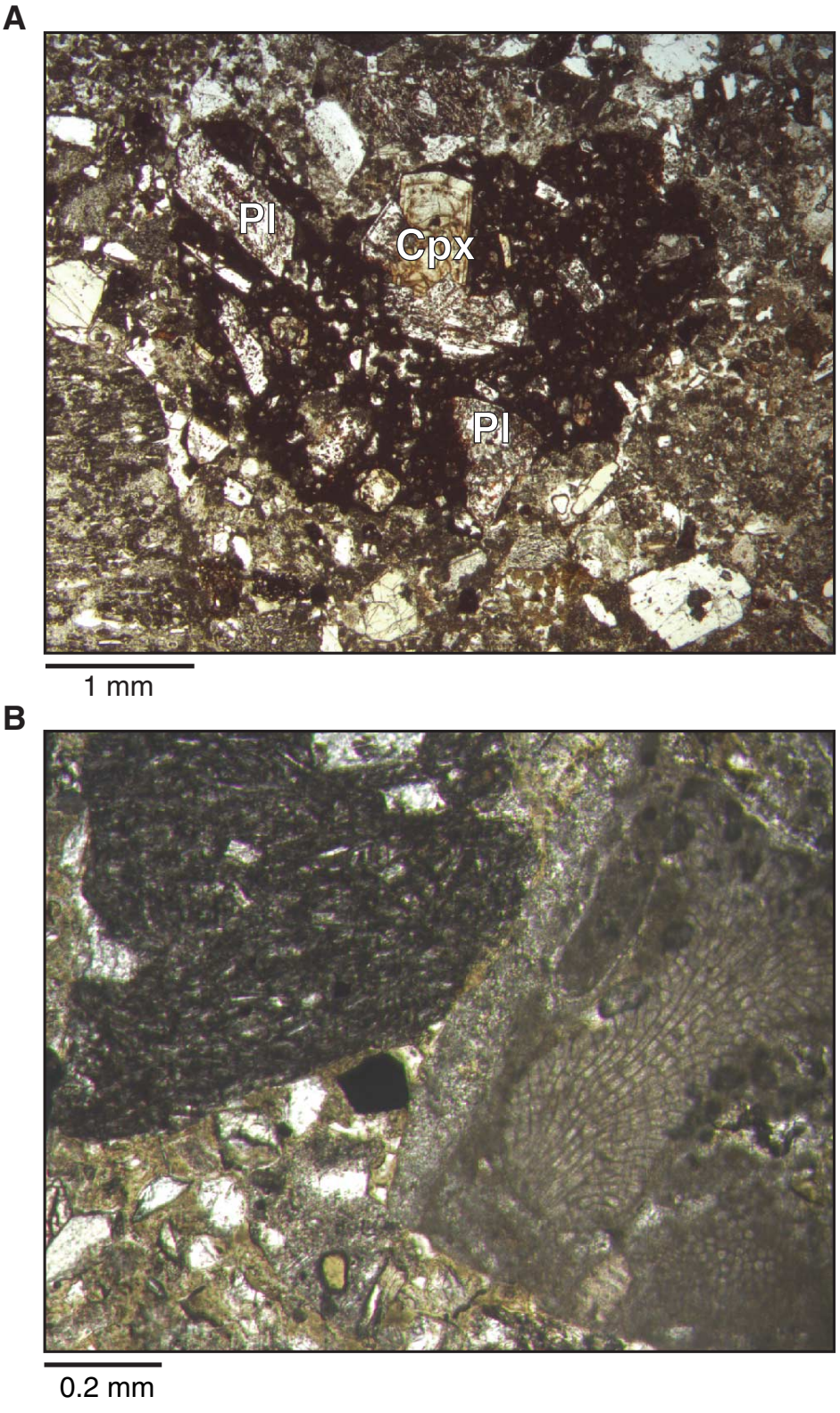

Figure F20. Empirically deduced tectono-genetic provenance of sandstones according to their framework composition, displayed in terms of quartz (Q), feldspar (F), and lithoclast (L) grains (Dickinson, 1985). The framework composition of the lithic arenites from Unit II plots in the "Undissected arc" field.

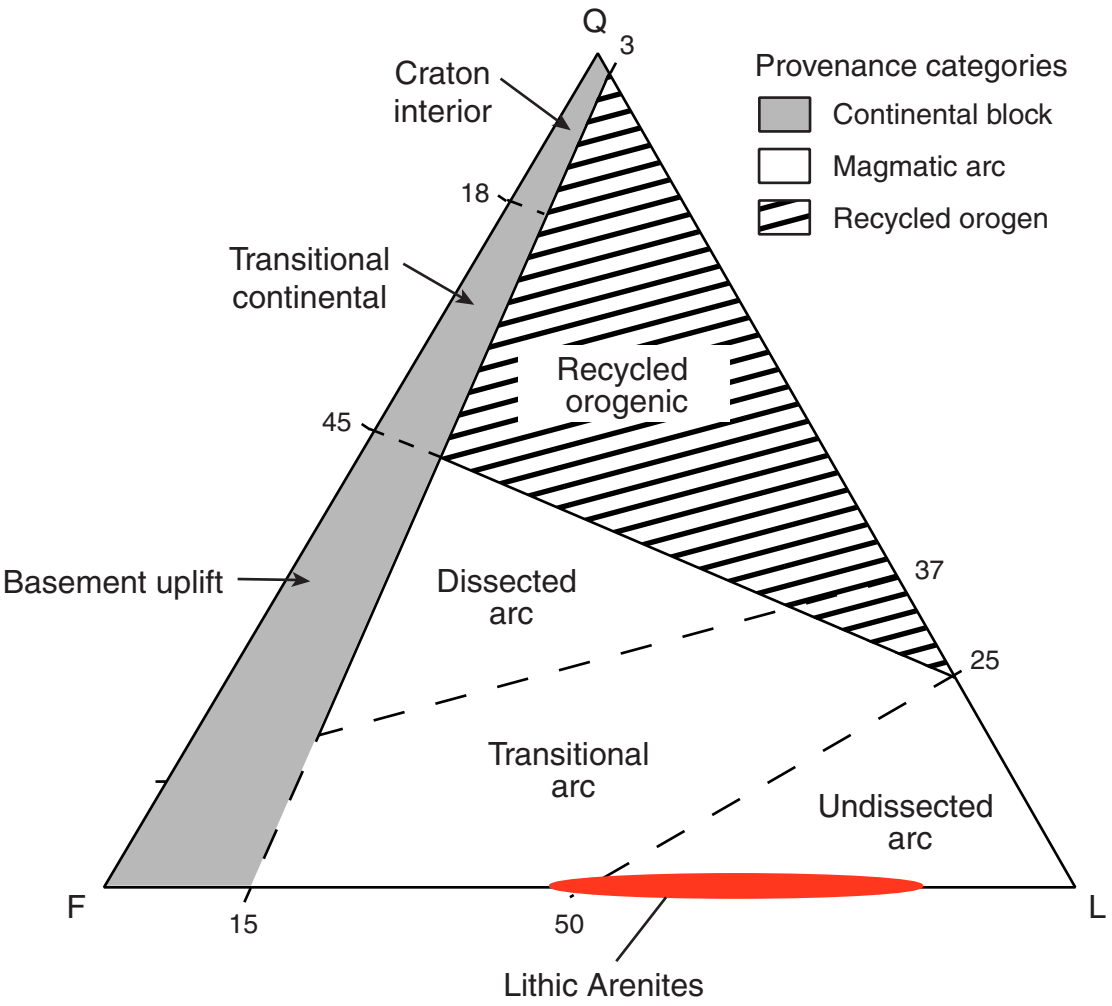

Figure F21. A. Photomicrograph of a zoned and twinned plagioclase grain in a sandstone from Unit II. The dusky inner part of the grain represents the slightly altered, calcic-rich core of the feldspar, whereas the fresh margin is sodium rich. Arrows point to incipient diagenetic feldspar overgrowth in optical continuity with the detrital grain (thin section from Sample **195-1201D-14R-1, 9–11 cm** [205.39 mbsf]) (cross-polarized light). **B.** Photomicrograph of authigenic prismatic lathes of phillipsite and pore-lining clay rim in a vitrophyre vesicle. The clay rim consists of small flakes of expandable clay minerals that grew perpendicular to the detrital substrate into the pore space (thin section from Sample **195-1201B-8X-2, 22–24 cm** [53.62 mbsf]) (plane-polarized light).

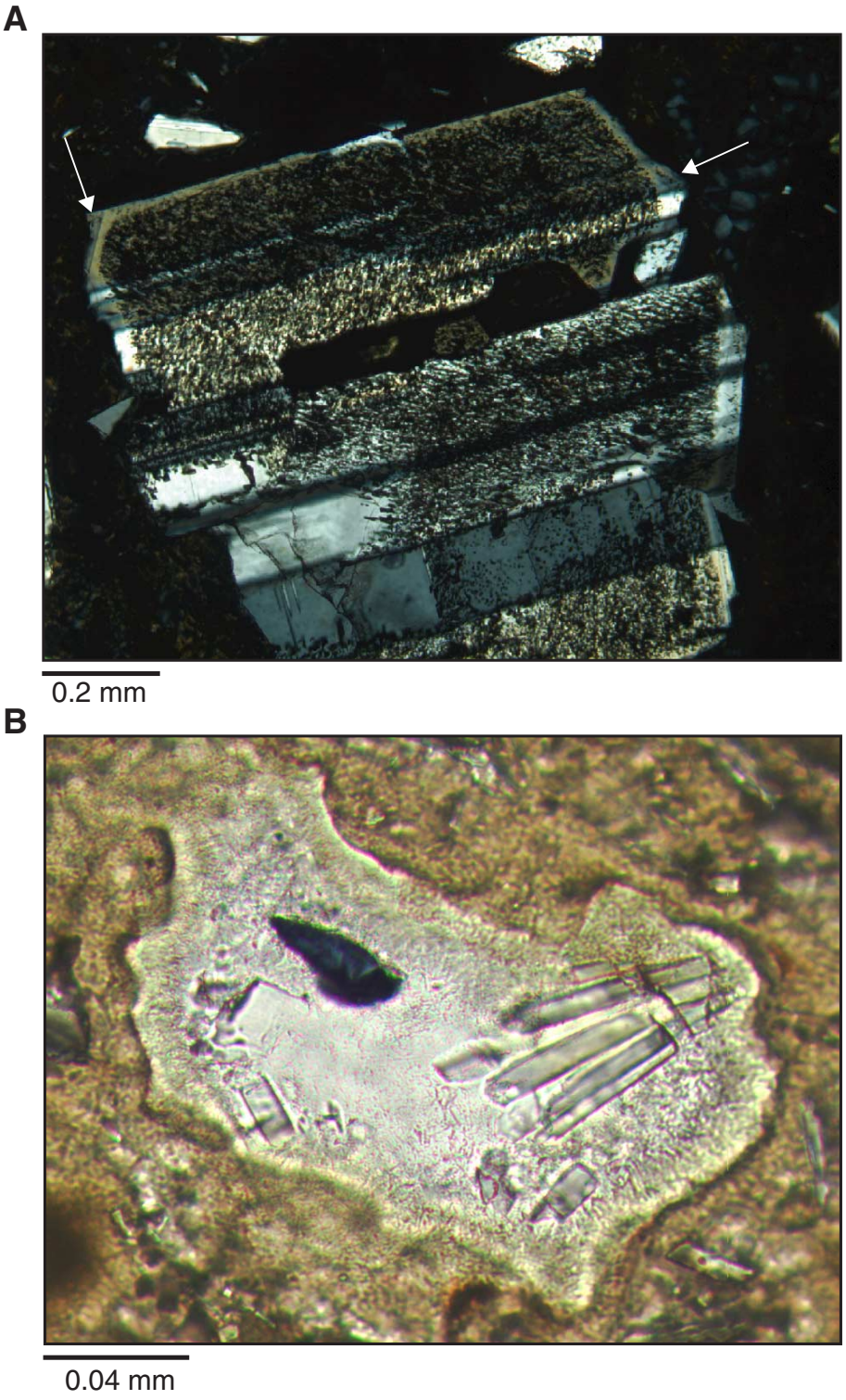

Figure F22. A. Photomicrograph of typical diagenetic features in sandstones from the middle of Unit II. The left-hand green grain possibly represents a devitrified glass shard made up of cryptocrystalline clay minerals. Together with the other framework grains, it is coated by clay rims. The pore-lining clay rims are overgrown by zeolite spherolites that occupy the intergranular pore space (thin section from Sample **195-1201D-14R-1, 9–11 cm** [205.39 mbsf]) (slightly cross-polarized light). **B.** Photomicrograph of detail of pore-filling zeolite spherolites, displaying fan-shaped outlines in cross section. The roots likely consist of fibrous analcime, overgrown along a sharp contact by radiating prisms of clinoptilolite (thin section from Sample **195-1201D-17R-3, 106–108 cm** [237.77 mbsf]) (plane-polarized light).

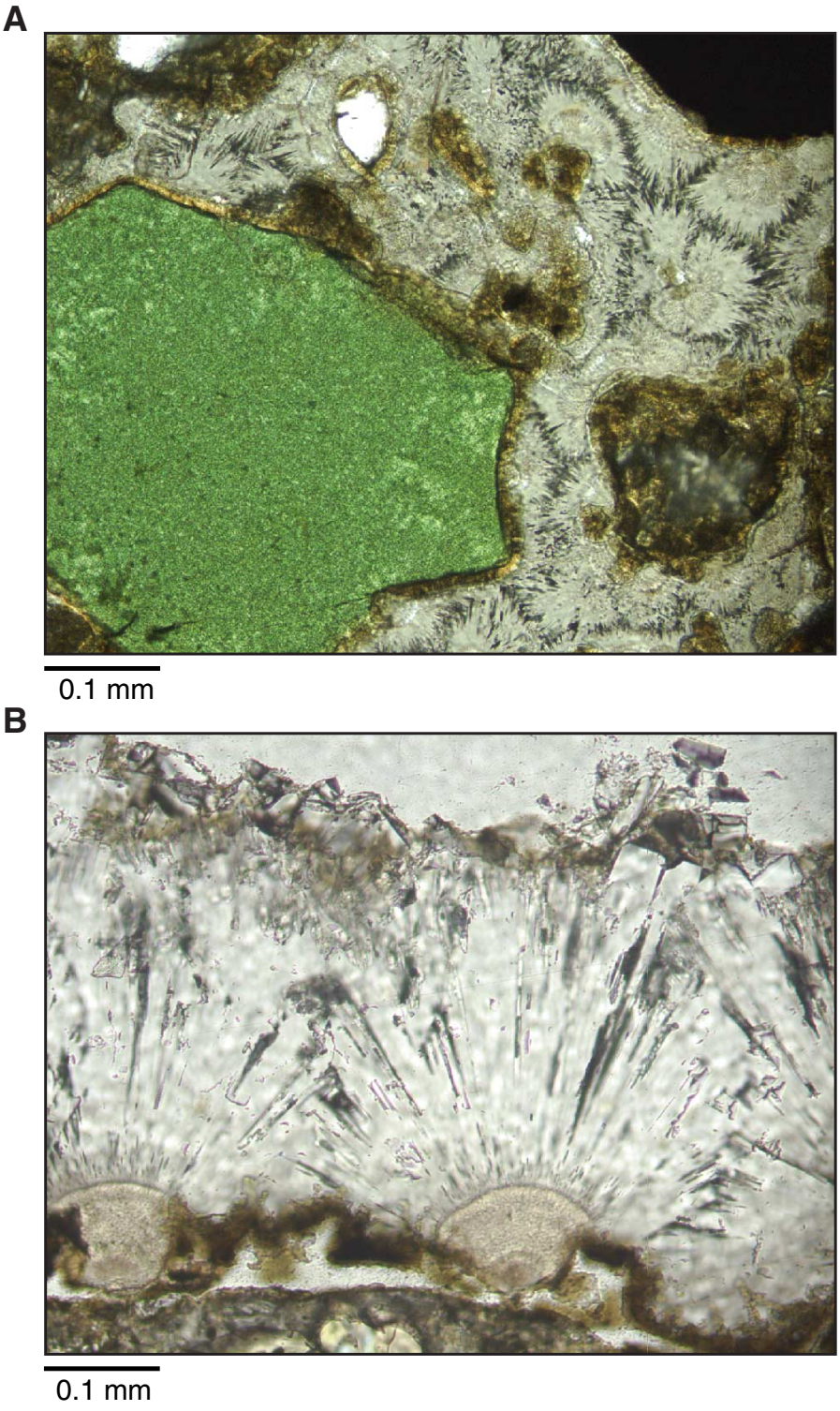

Figure F23. Photomicrographs of advanced stage of diagenesis in sandstones from the middle to lower part of Unit II. The sample exhibits vesicles in sideromelane with pore-lining clay rims from an earlier stage of diagenesis. Later, the vitric groundmass was completely replaced by sparry, partly poikilotopic zeolite, including needles of another zeolite generation. The zeolites might be members of the heulandite-clinoptilolite and analcime-wairakite solid solution series (thin section from Sample **195-1201D-30R-6, 114–116 cm** [367.74 mbsf]) **A.** Plane-polarized light. **B.** Cross-polarized light.

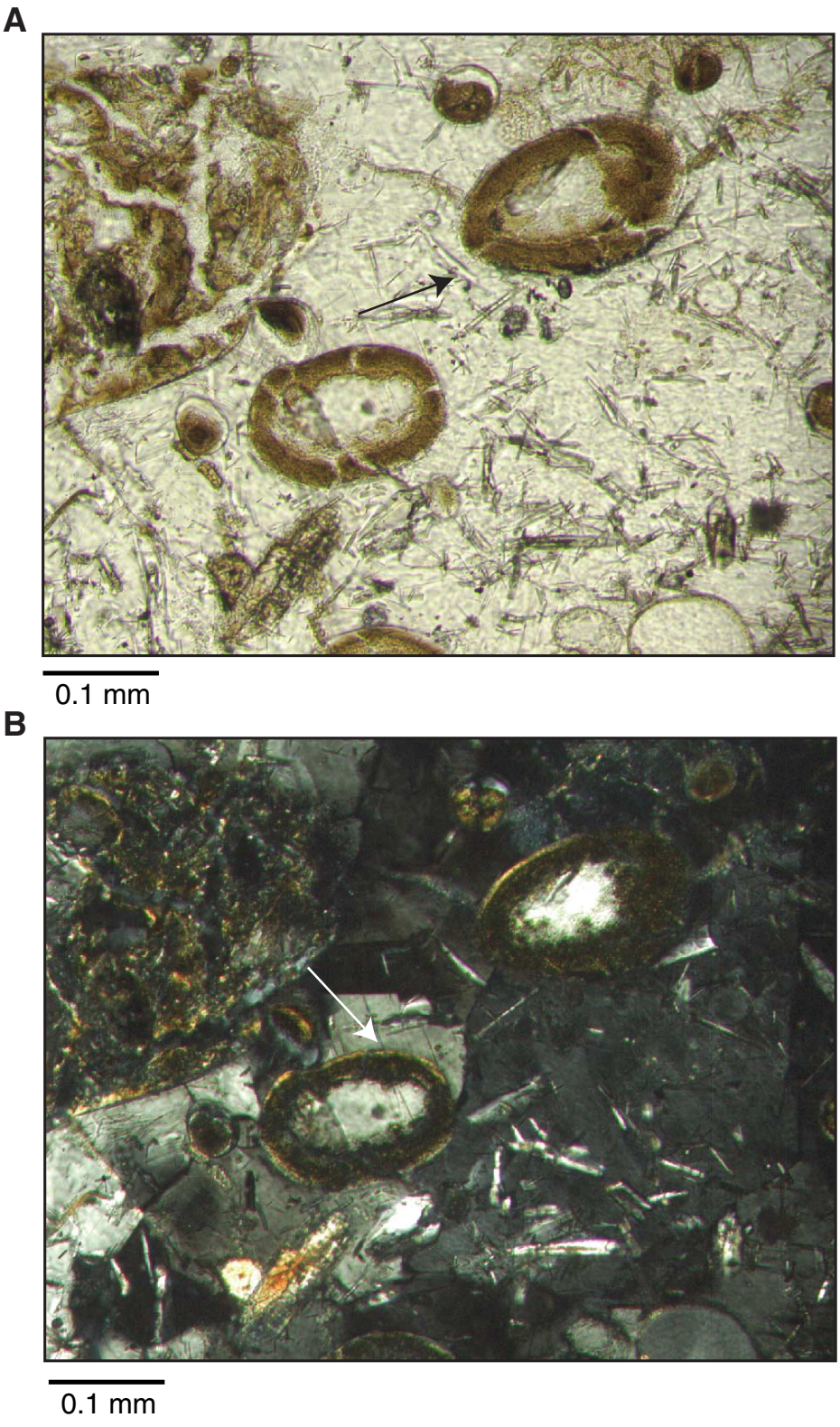

Figure F24. A. Photomicrograph of a strongly altered sandy siltstone from Unit II (thin section from Sample 195-1201D-17R-3, 106–108 cm [237.77 mbsf]) (plane-polarized light). The silty groundmass consists of devitrified (palagonitized) glass shards hosting "ghosts" of former detrital sand grains, which were pseudomorphically replaced by sparry zeolite. **B.** Photomicrograph showing details in a replaced sand grain (cross-polarized light).

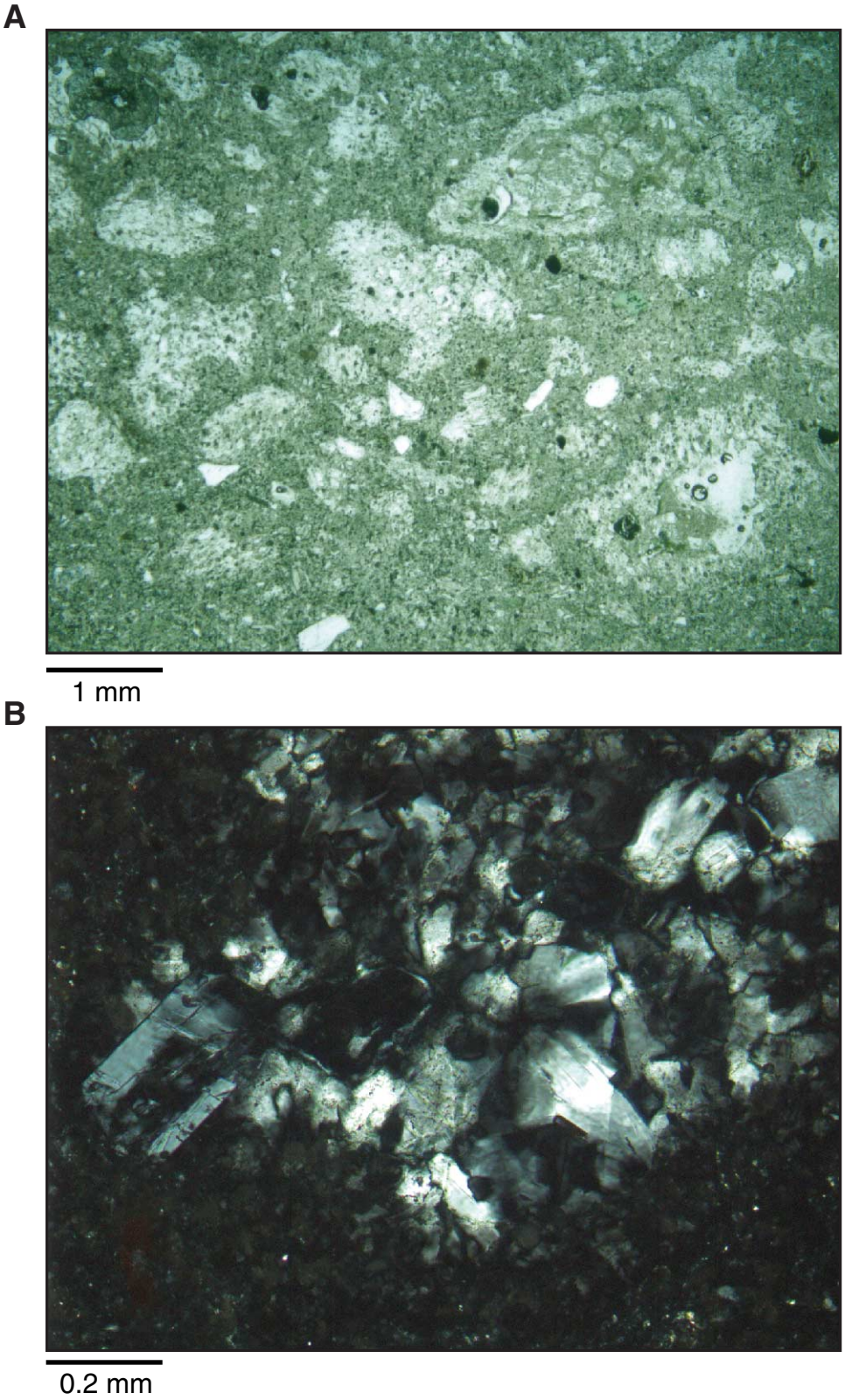

Figure F25. A. Photomicrograph of the highest degree of diagenesis in siltstones from the lower part of Unit II with abundant neoformation of secondary Ca-rich minerals. Gypsum (Gy) after the habit of anhydrite can be seen as the white mineral with pronounced cleavage traces, which grew in the greenish palagonitized silt groundmass. Other authigenic phases contain zeolites (chabazite and erionite) that are present as black patches of micro-gritty material (Z1) and as whitish wisps (Z2) (plane-polarized light). **B.** Gypsum shows anomalous brownish to bluish interference colors (thin section from Sample **195-1201D-38R-1, 29–32 cm** [436.29 mbsf]) (cross-polarized light).

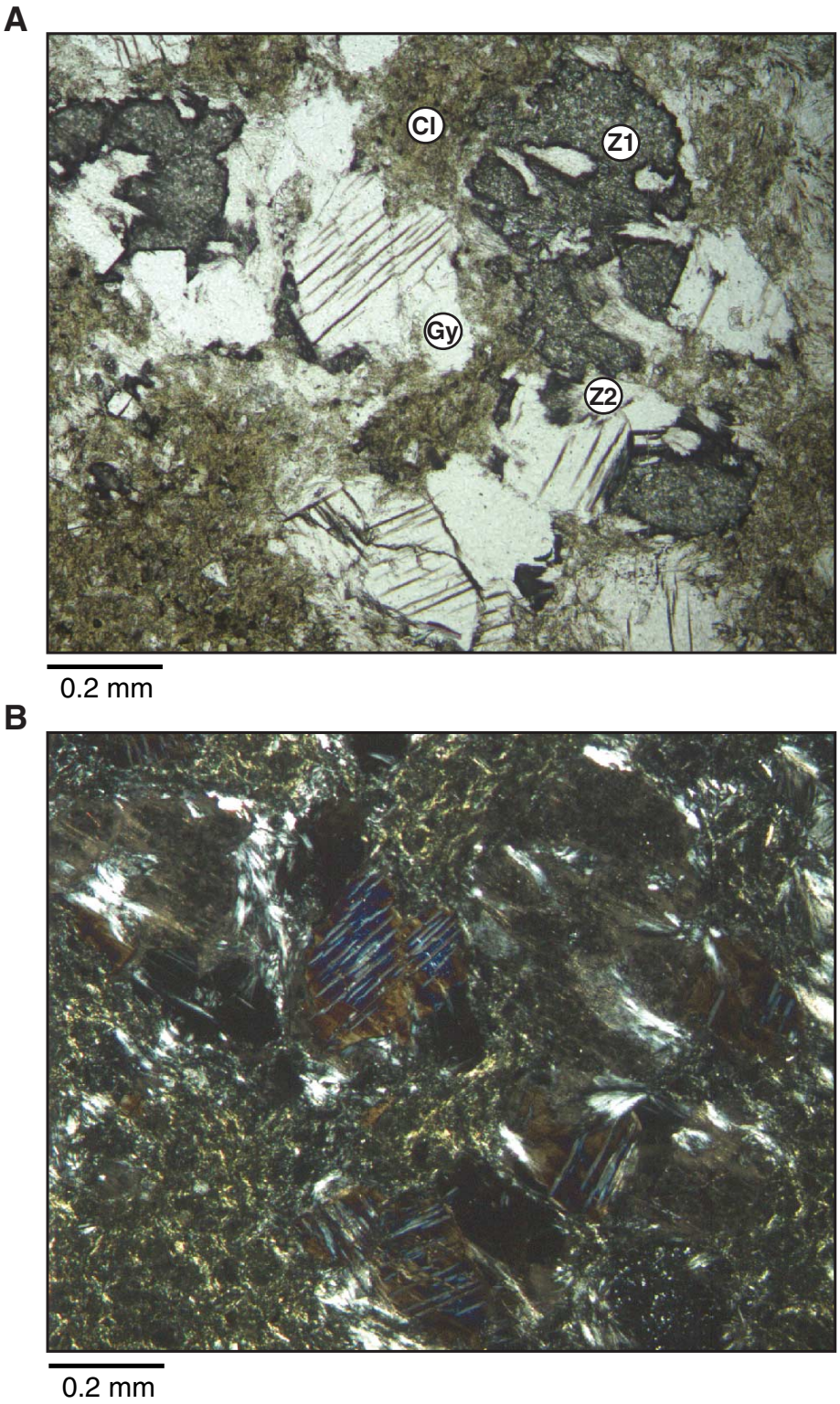

Figure F26. XRD patterns of major sediment and sedimentary rock types from Site 1201 measured on bulk powder mounts. Exp. CM = expandable clay minerals, Phil = phillipsite, Qz = quartz, Plag = plagioclase, Cpx = clinopyroxene, Clpt = clinoptilolite, Heu = heulandite, Anal = analcime, Chab = chabazite, Erio = erionite, Sm = well-crystallized smectite, Gyps = gypsum.

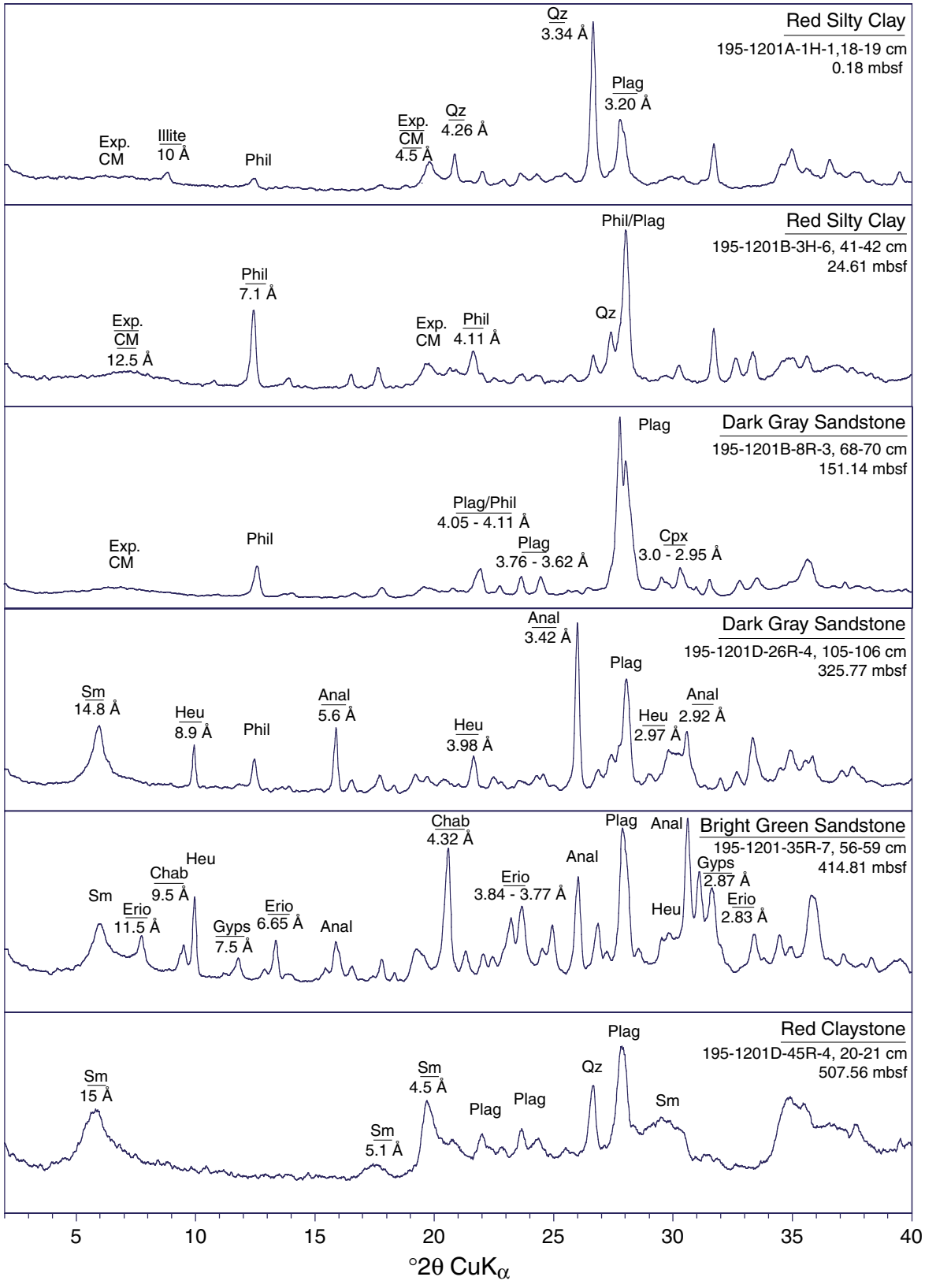

Figure F27. XRD patterns of clay minerals and zeolites in the ≤2-µm grain-size fraction measured on textured mounts in the air-dried state, after ethylene glycolation, and after heat treatment at 550°C. Samples from the uppermost red silty clays of Unit I include detrital illite and generally show broad low-angle peaks related to admixtures of various expandable clay minerals. Because chlorite is missing (no 14-Å peak after heat treatment,) the 7- and 4.77-Å peaks may indicate minor proportions of vermiculite as one of the expandable clay minerals besides poorly crystallized smectite. Below 240 mbsf, the expandable clay minerals consist of pure, well-crystallized smectite as indicated by the relatively sharp 17-Å peaks in the glycolated state. The sample of green sandstone displays a 8.9-Å peak of clinoptilolite/heulandite that disappears after heat treatment and thus provides a positive indication of clinoptilolite instead of heulandite, which would survive the heat treatment.

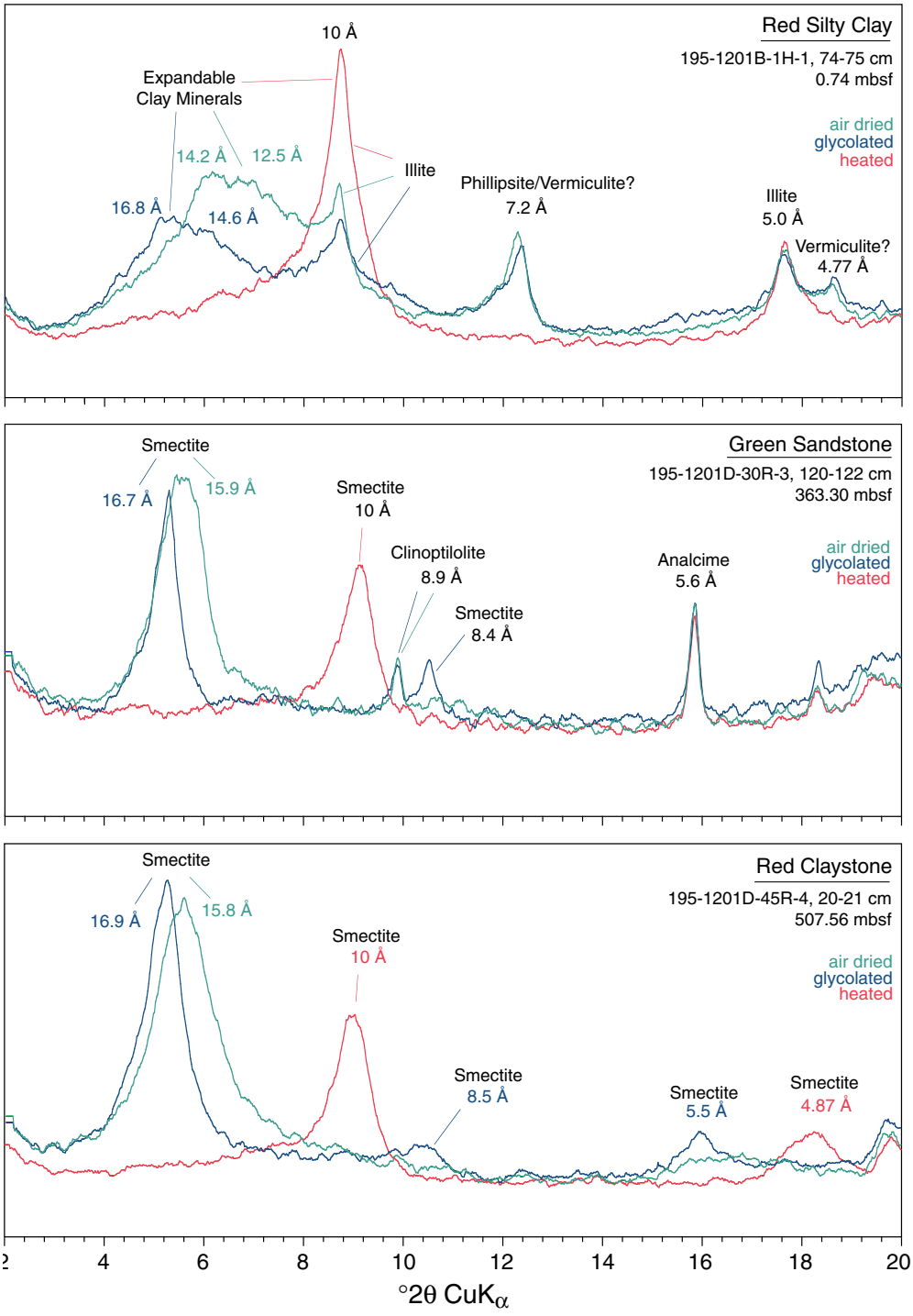

Figure F28. Possible environmental interpretations from the sedimentary succession at Site 1201. Schematic volcano symbolizes a magmatic arc setting. In Stage 2, the sediment composition suggests that subaqueous eruptions were more prevalent than in later stages of volcanic activity, which were dominated by subaerial volcanism. Several possible environmental boundary conditions that might have produced the sedimentary succession are indicated with a question mark.

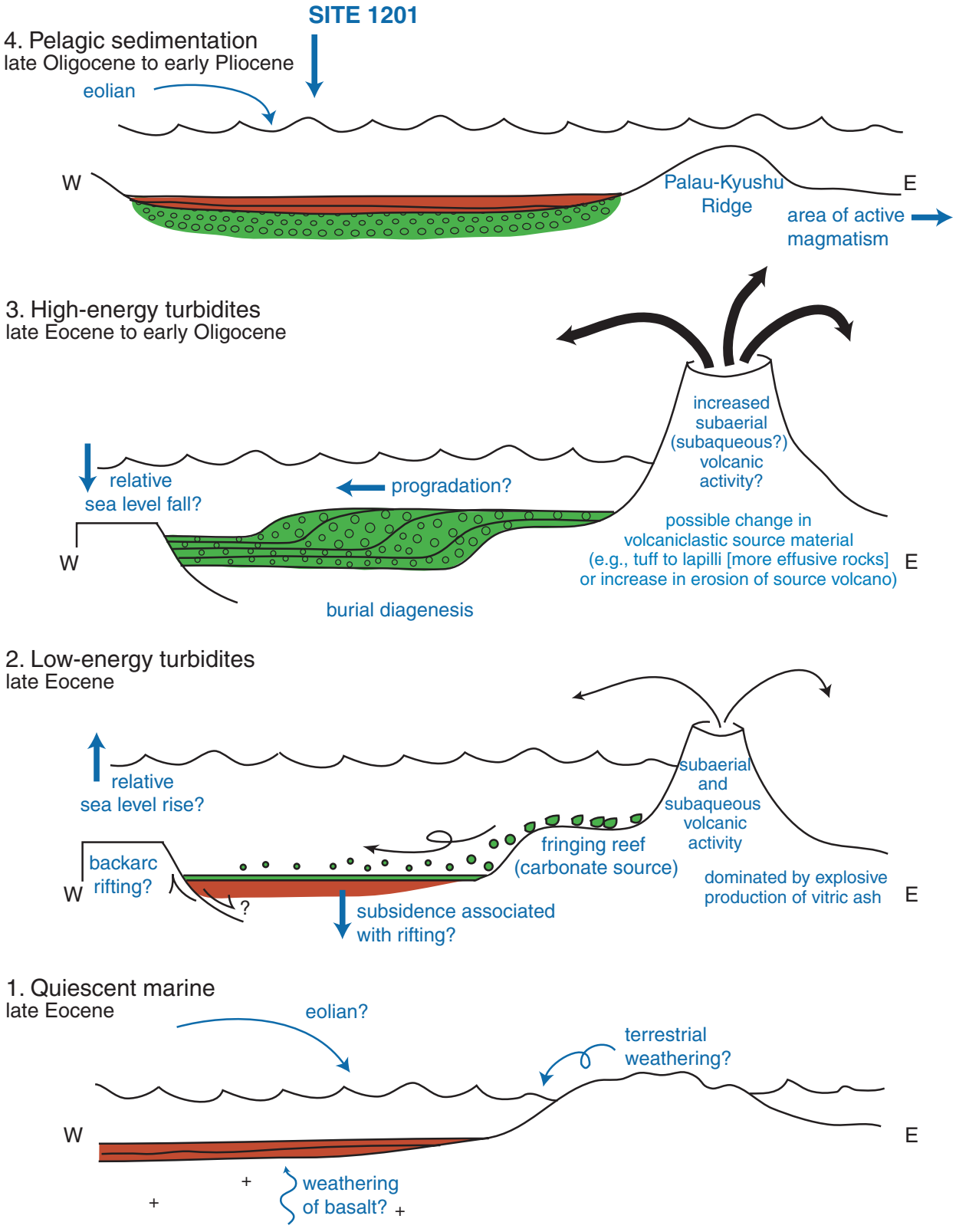

Figure F29. Aphyric basalt exhibiting radiating vesicles, possibly indicative of a pillow margin (interval 195-1201D-46R-4, 78–89 cm).

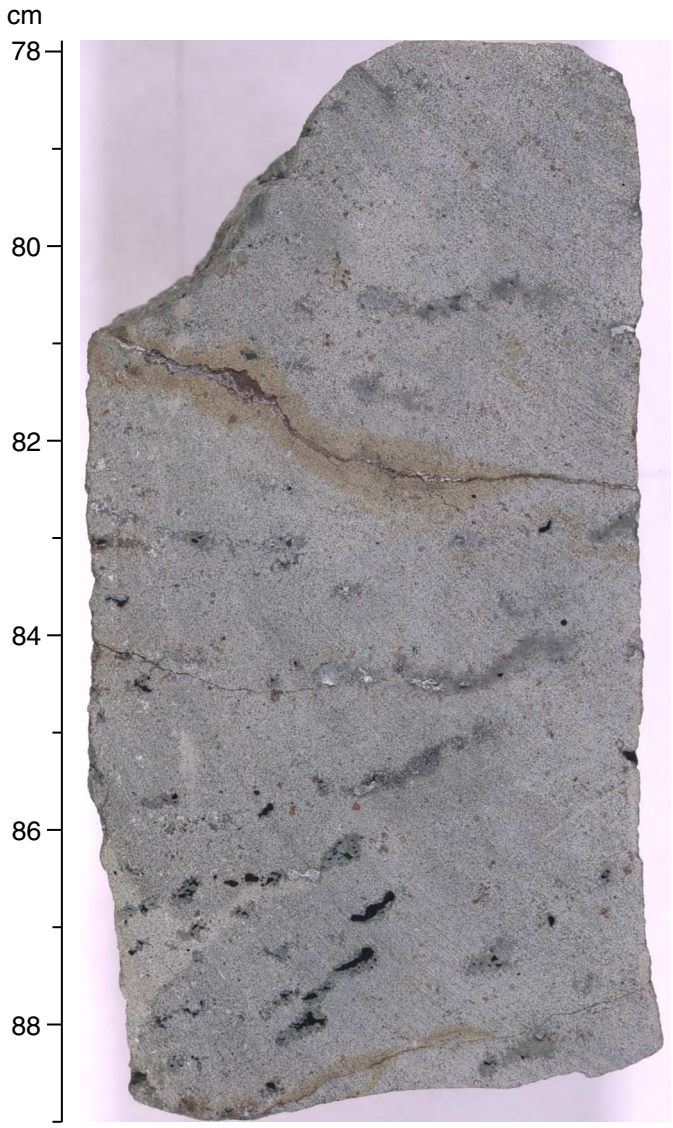

Figure F30. A. Reconstruction of small pillow based on three adjacent pieces. Note the glassy chilled margin on the top piece (green) covered by hyaloclastite containing angular green glass fragments (interval 195-1201D-48R-4, 12–26 cm). **B.** Long, relatively continuous piece of aphyric basalt exhibiting a glassy pillow margin on upper surface (interval 195-1201D-52R-1, 18–44 cm).

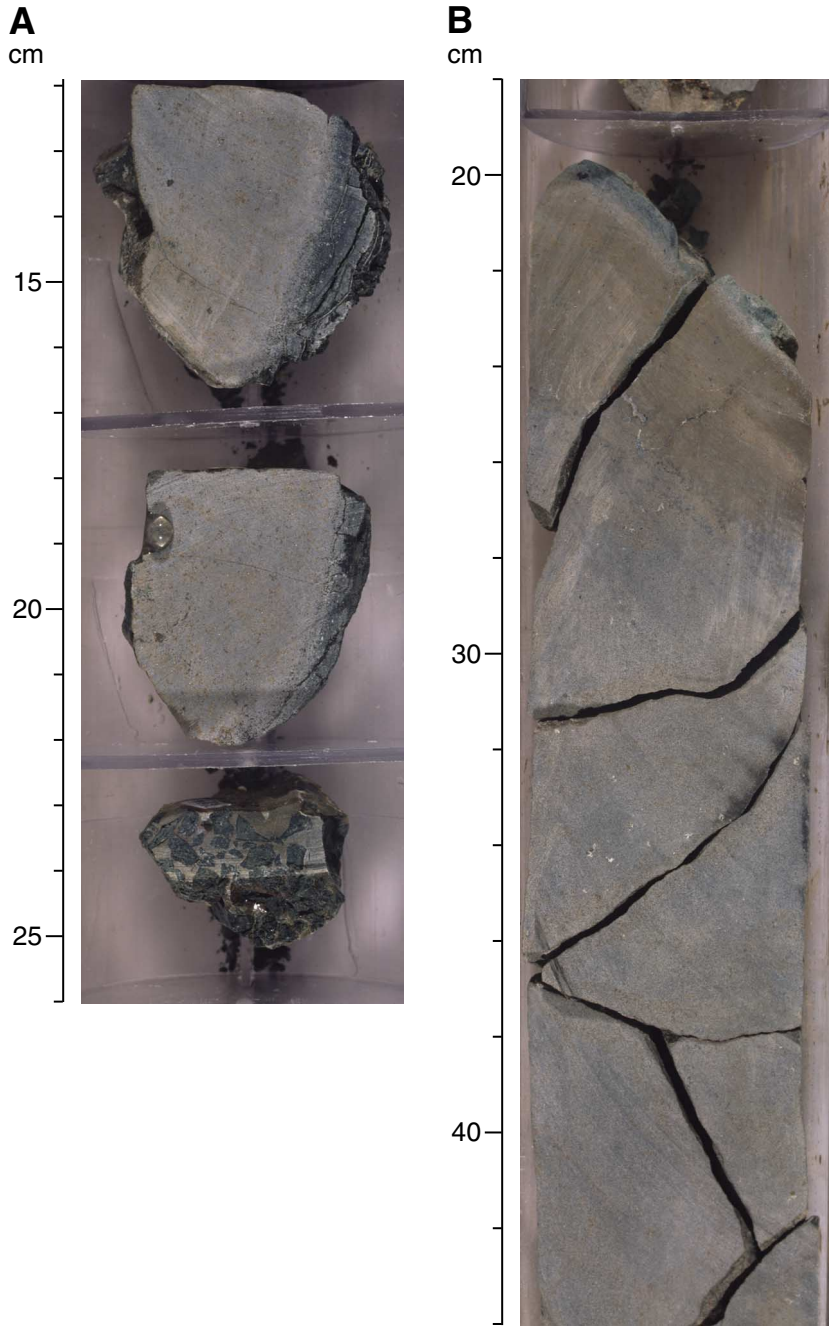

Figure F31. A. Several pieces of hyaloclastite (20–23, 27–29, and 29–33 cm) and one small pillow piece (23–27 cm) exhibiting radiating vesicles and glassy margin (interval 195-1201D-46R-4, 20–33 cm). (Continued on next page.)

Figure F31 (continued). B. Photomicrograph of biogenic clast found in the interpillow sedimentary material (Sample 195-1201D-46R-4, 24–27 cm) (cross-polarized light; conoscopic illumination).

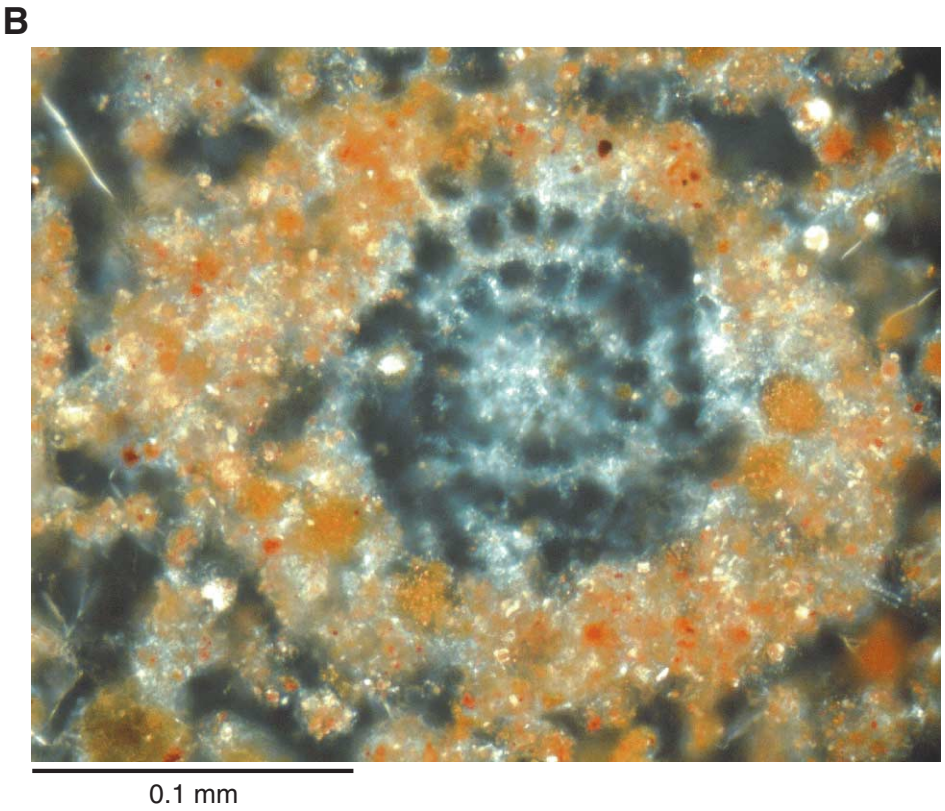

Figure F32. Pillow breccia consisting of angular fragments of aphyric basaltic glass cemented in brown sedimentary material. The top edge of the upper piece exhibits a glassy margin (interval 195-1201D-47R-3, 21–35 cm).

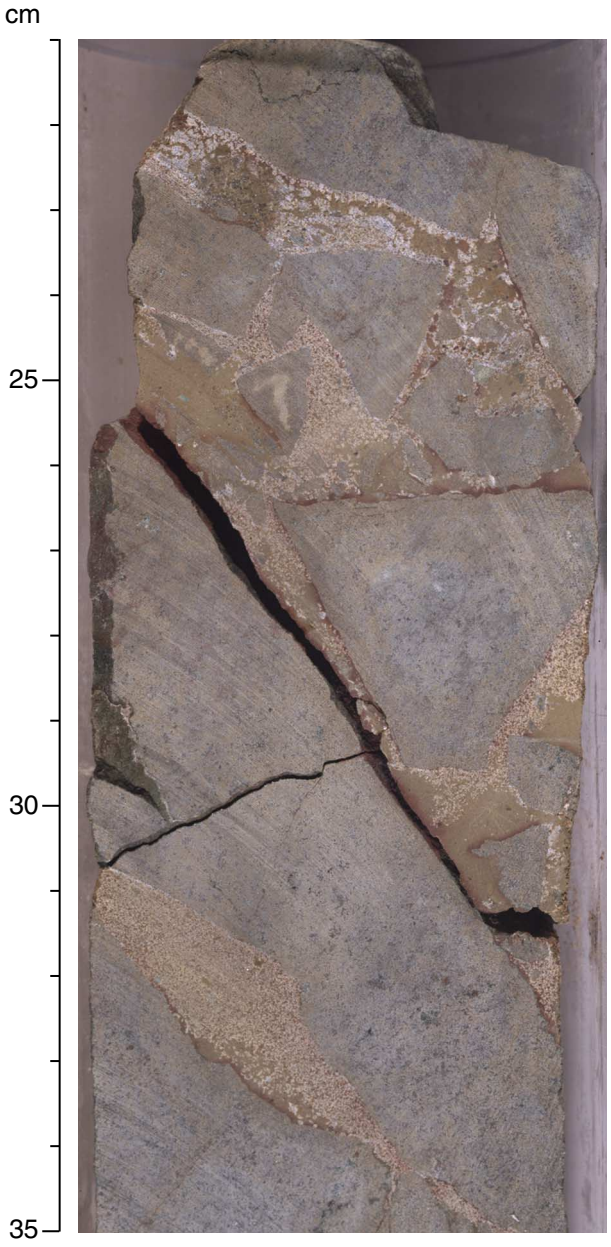

Figure F33. Sedimentary material and hyaloclastite consisting of angular brown fragments of aphyric basaltic glass (111–123 cm). The piece in 123–130 cm exhibits a pillow margin with radiating fractures, vesicles, and veins (interval 195-1201D-47R-1, 111–130 cm).

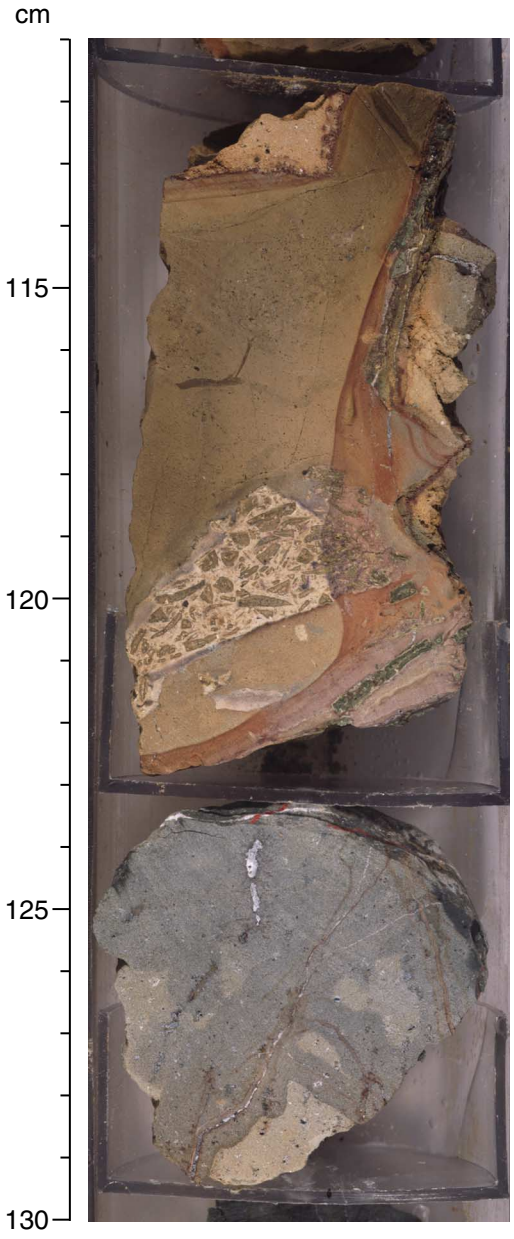

Figure F34. Vesicular, hydrothermally altered, aphyric basalt close to the contact with the sedimentary sequence overlaying the basement. The piece is crosscut by several large veins of sedimentary material, carbonate, and green angular fragments of glassy basalt (hyaloclastite). The veins are accompanied by large halos showing different colors. Thin veins of reddish iron oxyhydroxide are also visible (interval 195-1201D-46R-1, 24–66 cm).

Figure F35. Photomicrograph of hyalopilitic texture and completely replaced olivine. Olivine has been replaced by clay minerals and iron oxyhydroxide (Sample **195-1201D-47R-2, 124–127 cm**) (plane-polarized light).

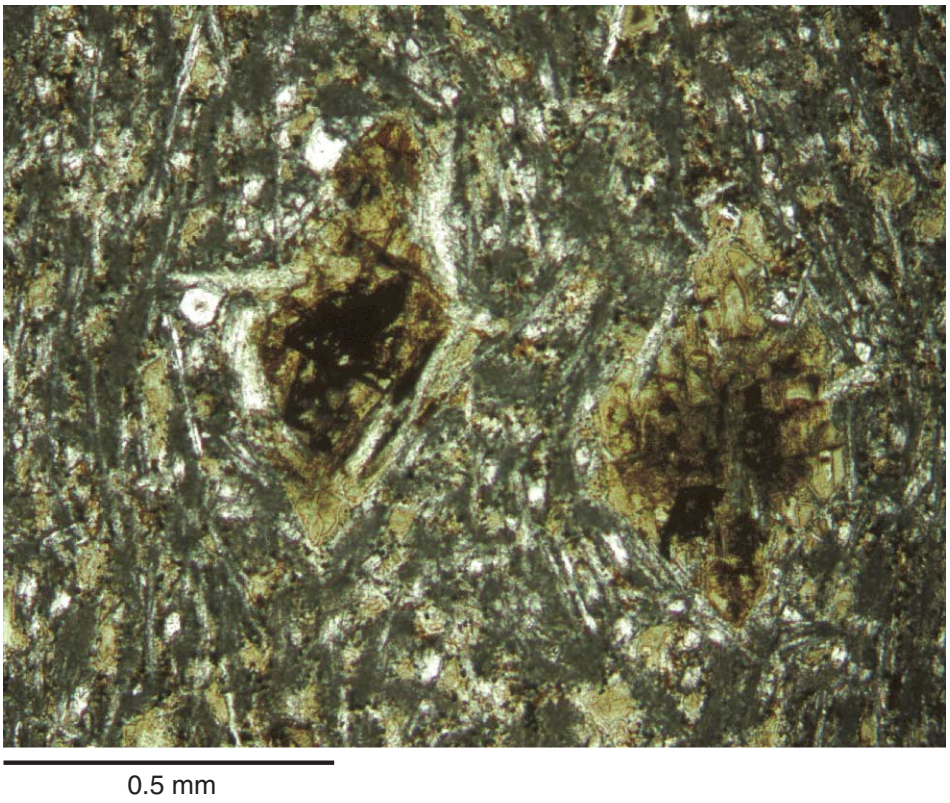

Figure F36. Photomicrograph of skeletal plagioclase, some exhibiting "swallow-tail" morphology. Branching textures are seen in the groundmass (Sample **195-1201D-48R-2, 135–138 cm**) (plane-polarized light).

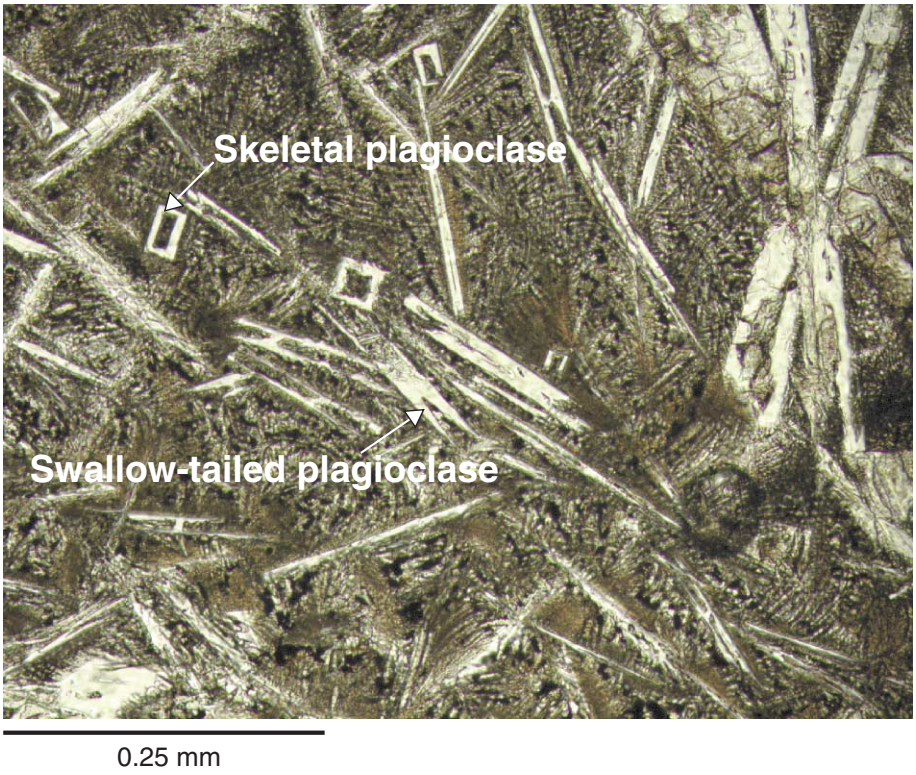

Figure F37. Photomicrograph showing a plagioclase lath, clinopyroxene, and amygdules. The plagioclase lath has been replaced by carbonate and zeolites. The amygdules are filled by zeolites (Sample **195-1201D-46R-5, 8–11 cm**) (cross-polarized light).

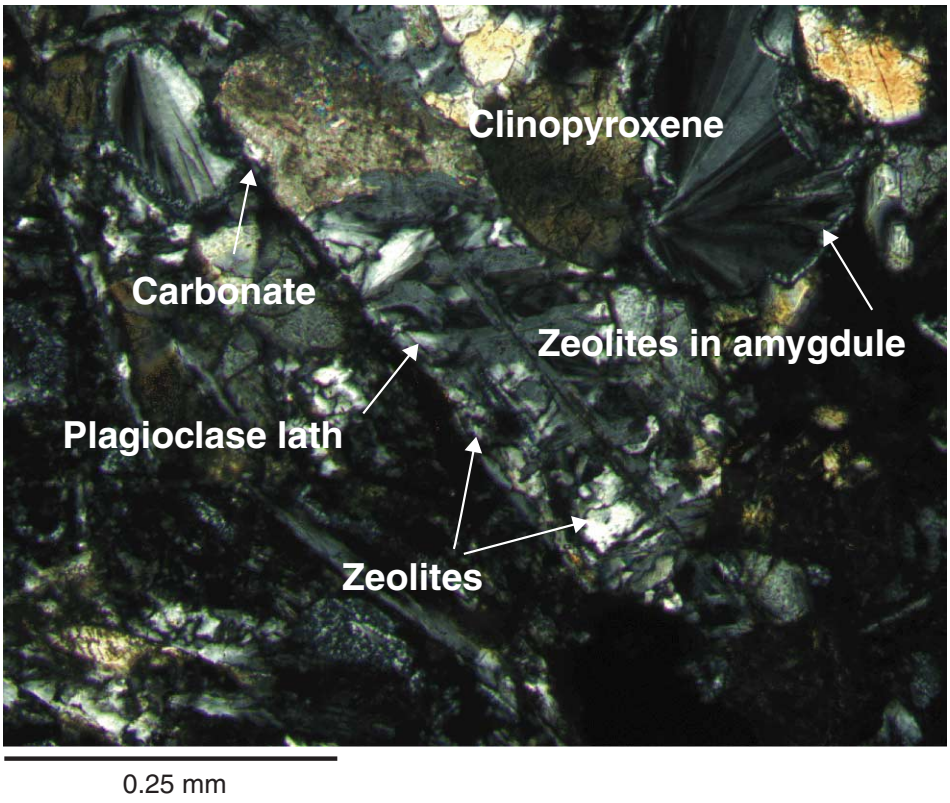

Figure F38. Photomicrograph of plagioclase lath replaced by secondary minerals in the interior with sodium-rich rims preserved (Sample **195-1201D-48R-2, 74–76 cm**) (plane-polarized light).

Figure F39. Photomicrograph showing a spherulite of clinopyroxene and plagioclase in a highly vesicular groundmass (Sample **195-1201D-46R-5, 8–11 cm**) (cross-polarized light).

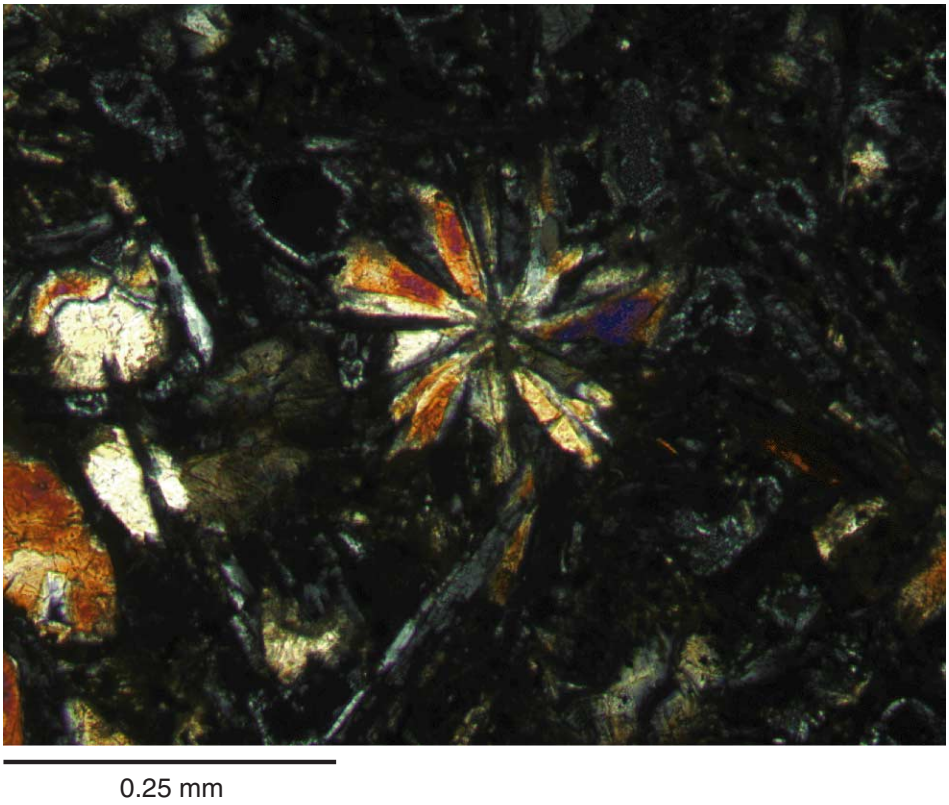

Figure F40. Photomicrograph of branching clinopyroxene and skeletal plagioclase in rapidly cooled basalt. A possible pseudomorph after olivine is seen in the upper right corner of the picture (Sample **195-1201D-48R-1, 47–50 cm**) (plane-polarized light).

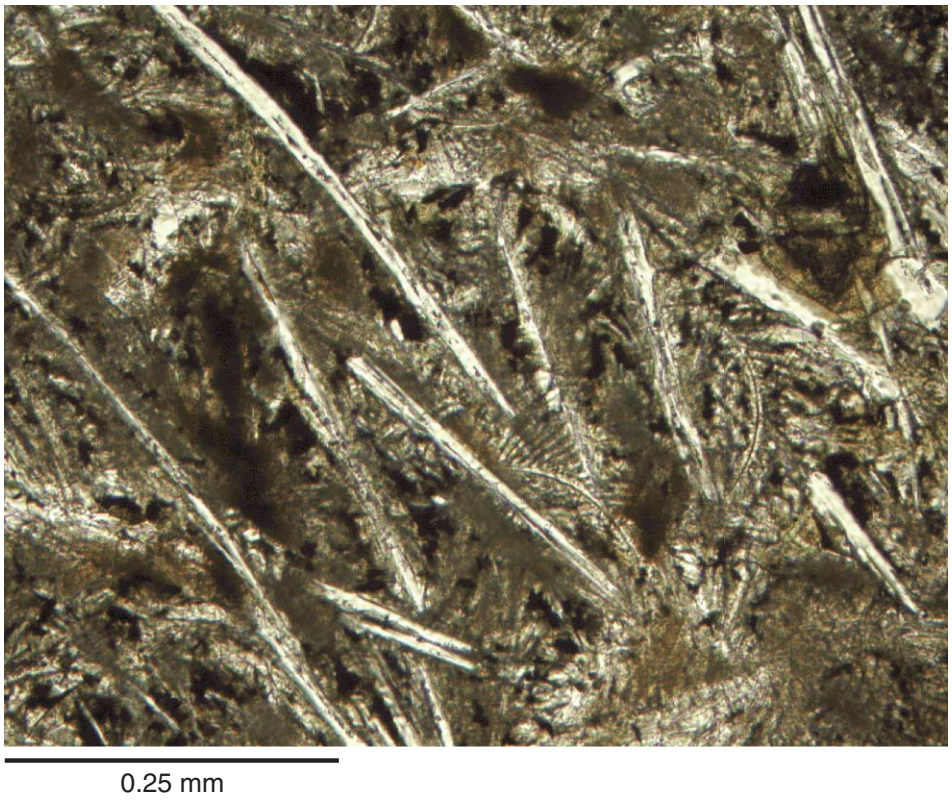

Figure F41. A. Photomicrograph of subophitic texture with plagioclase partially enclosed by clinopyroxene (Sample 195-1201D-55R-1, 103–106 cm) (cross-polarized light). **B.** Photomicrograph of subophitic texture with plagioclase enclosed by olivine (interval 195-1201D-47R-2, 109–111 cm) (plane-polarized light).

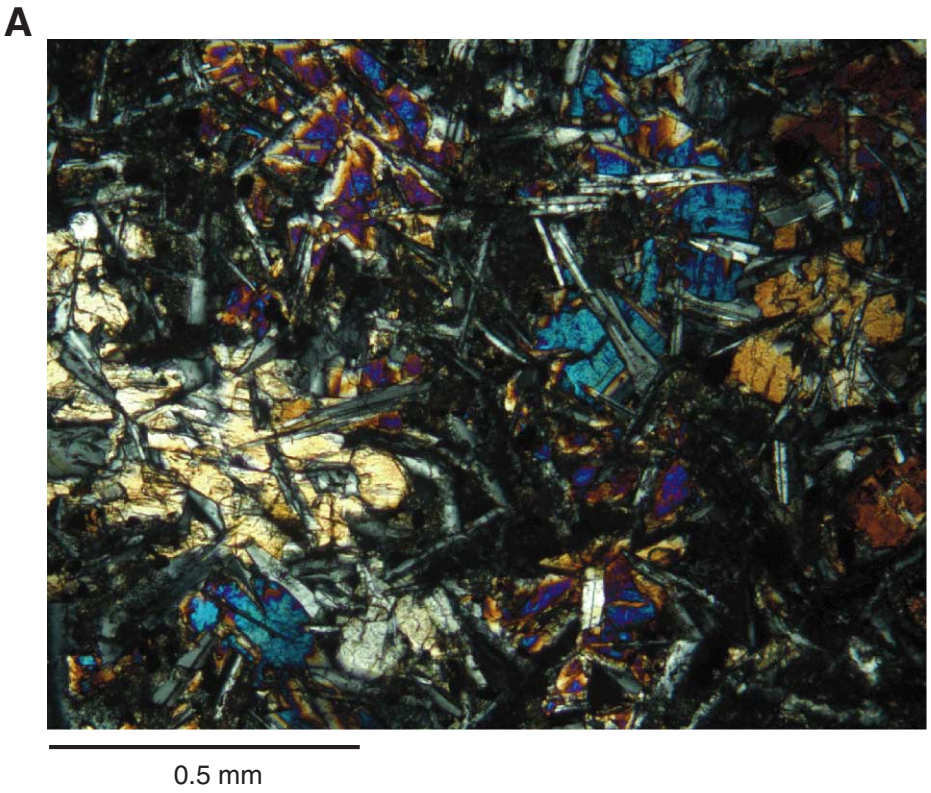

Figure F42. Plot of Sr (in parts per million) and CaO, K_2O, Na_2O, and LOI (in weight percent) in basalts vs. depth. Data are from Table T4, p. 195.

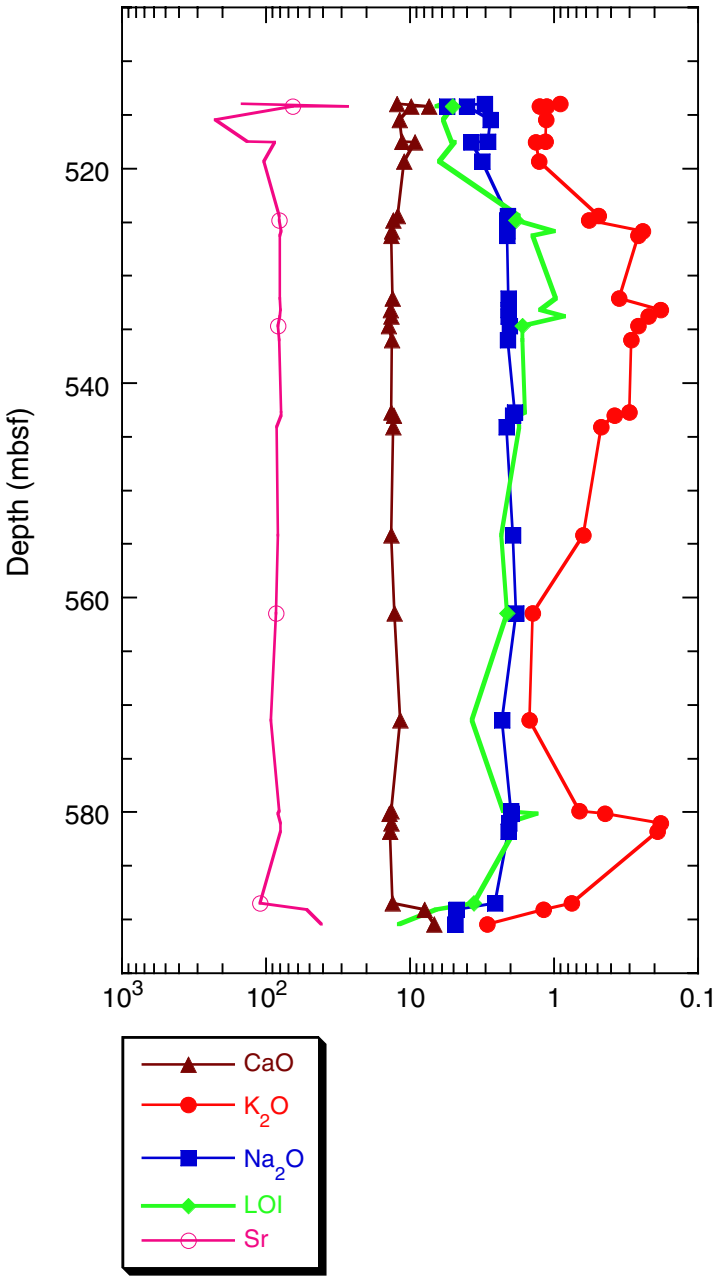

Figure F43. Total alkalis vs. silica classification diagram for volcanic rocks on a volatile-free basis (after Le Bas et al., 1986). Ol = olivine.

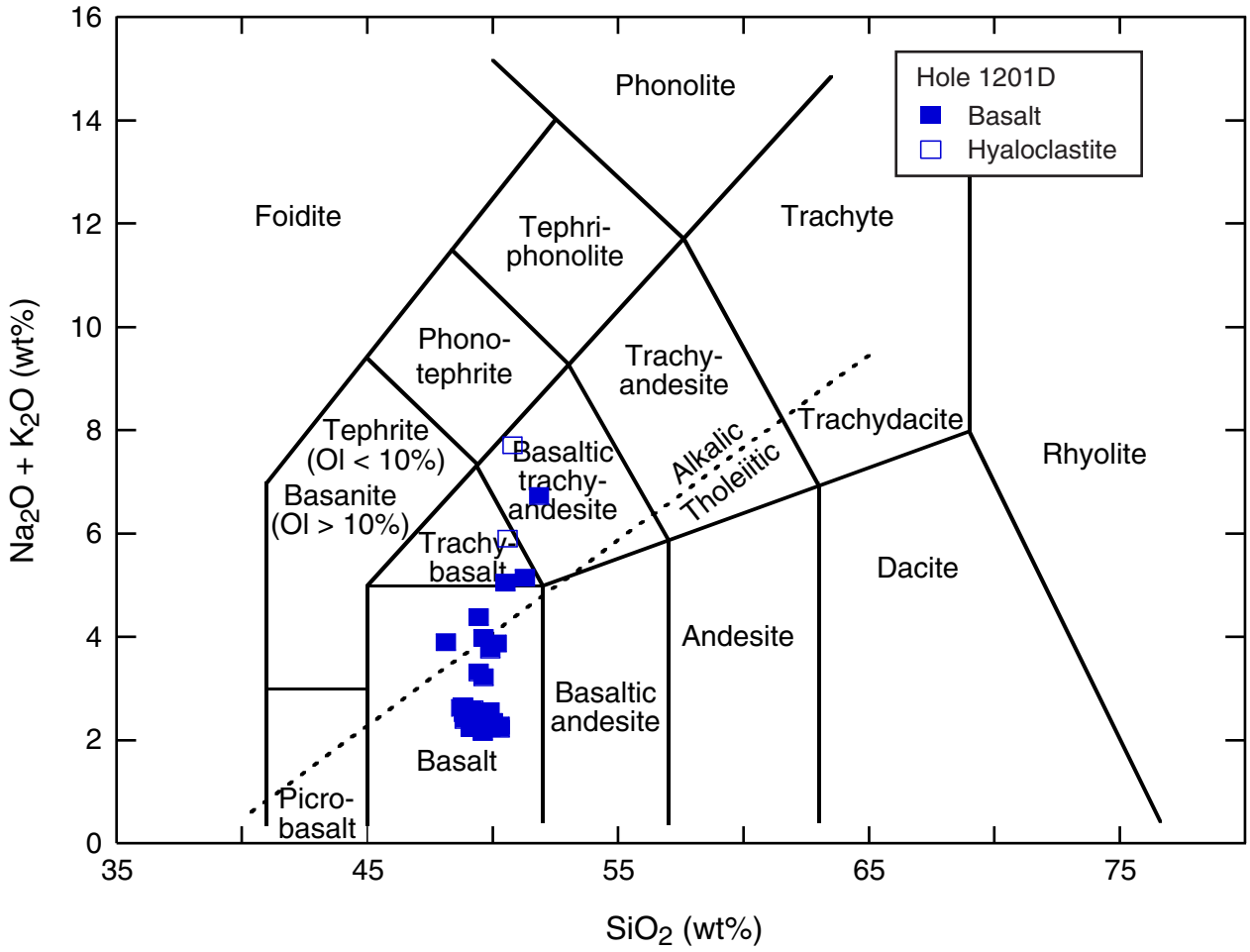

Figure F44. (Ti/100)-Zr-(Y+3) discrimination diagram (after Pearce and Cann, 1973). MORB = mid-ocean-ridge basalt, WPB = within-plate basalt, CAB = calc-alkaline basalt, IAT = island arc tholeiites.

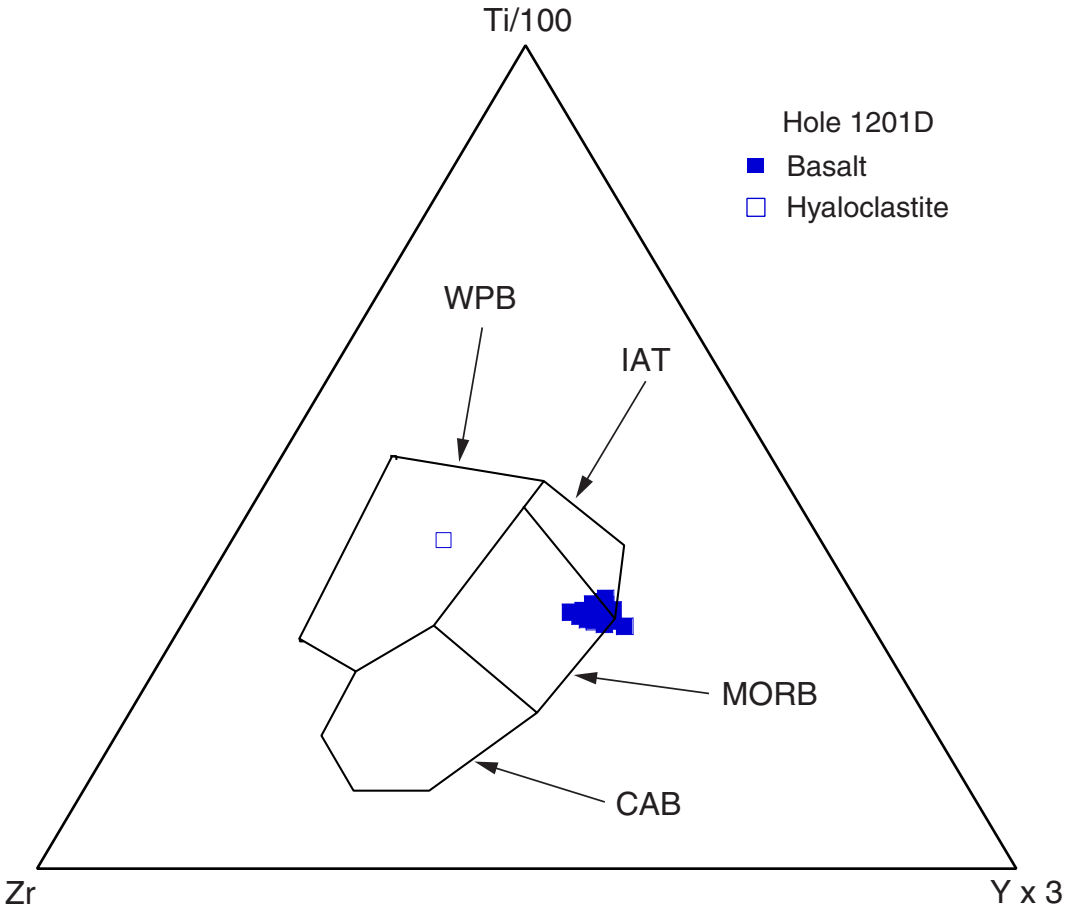

Figure F45. Ti/1000 vs. V discrimination diagram (after Shervais, 1982). MORB = mid-ocean ridge-basalt, BABB = backarc basin basalt, OIB = ocean island basalt.

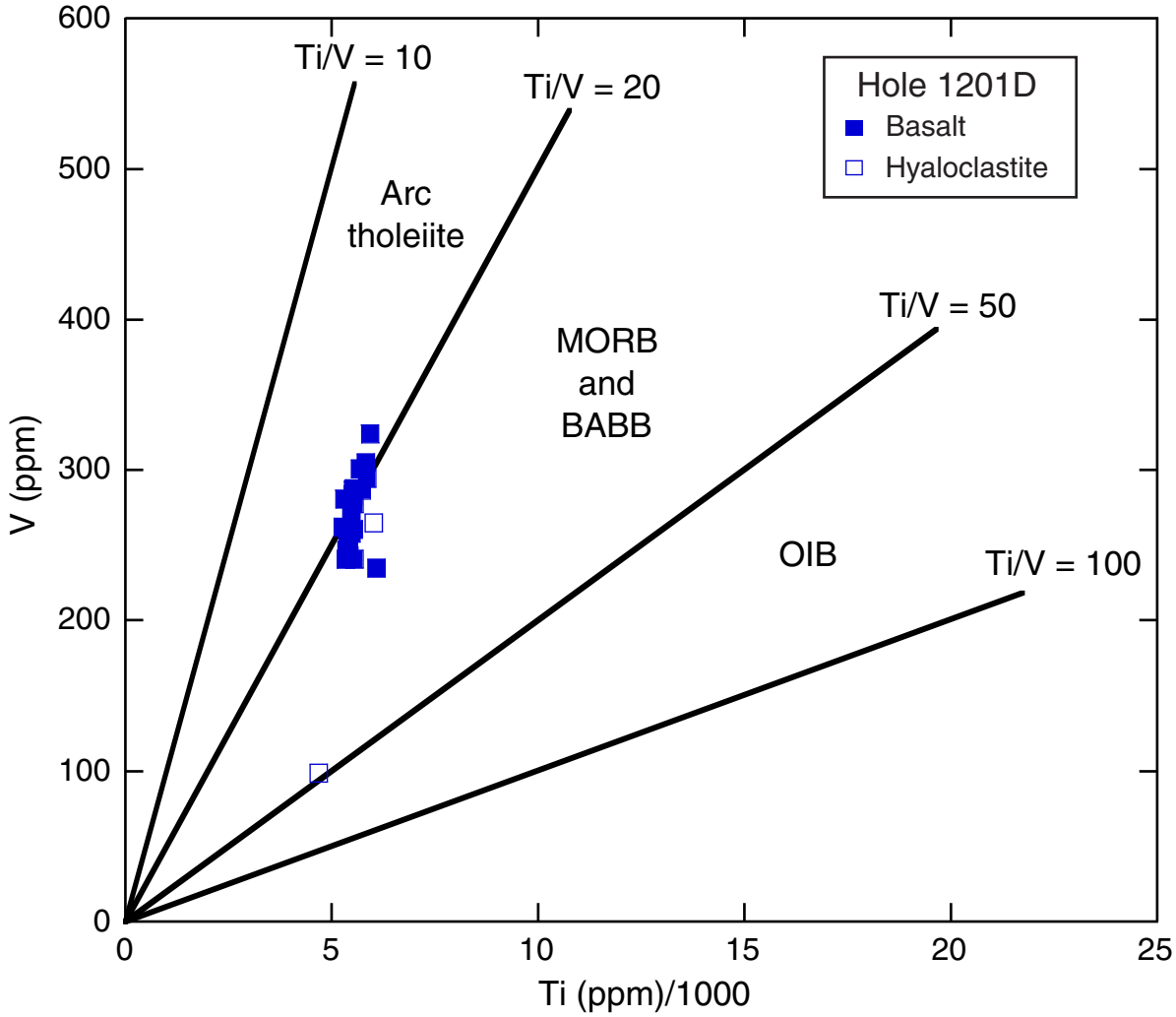

Figure F46. TiO_2-(MnO×10)-(P_2O_5×10) discrimination diagram (after Mullen, 1983). MORB = mid-ocean-ridge basalt, CAB = calc-alkaline basalt, OIT = ocean island tholeiites, OIA = ocean island alkaline basalt, IAT = island arc tholeiites, BON = boninites.

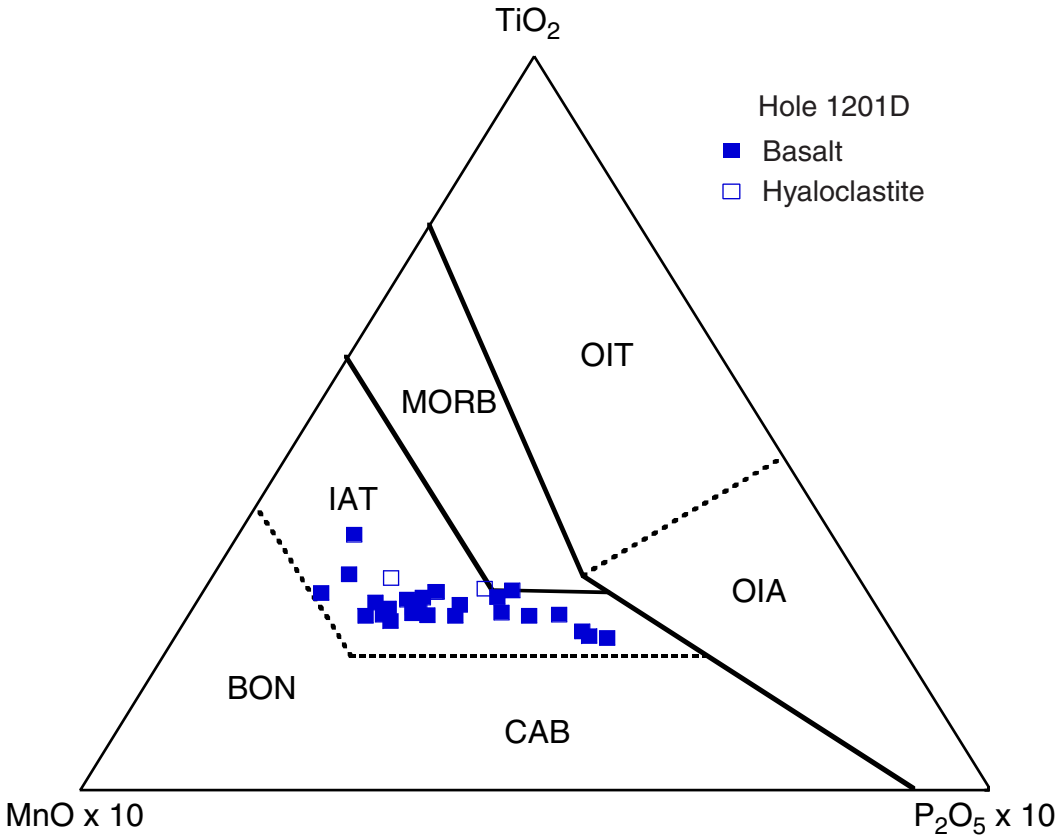

Figure F47. Cr vs. Y discrimination diagram (after Pearce, 1982). MORB = mid-ocean-ridge basalt, WPB = within-plate basalt, IAT = island arc tholeiites.

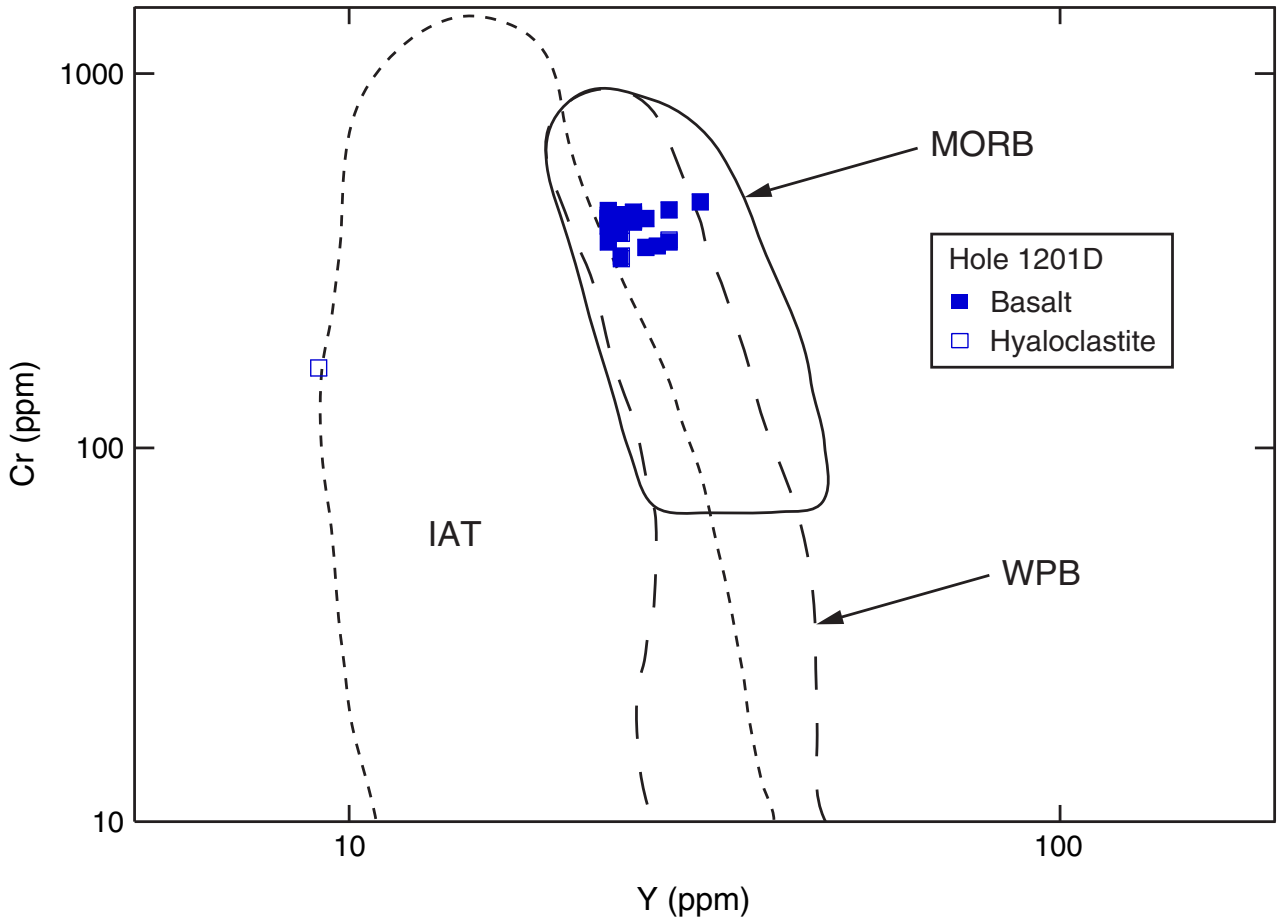

Figure F48. Preservation and abundance of calcareous nannofossils for Holes 1201B and 1201D plotted with the graphic lithology log. The scale representing the preservation state and nannofossil abundance is arbitrary, designed to enhance visualization of the patterns. In the graphic lithology column, c = clay, s = silt, s = sand, g = gravel.

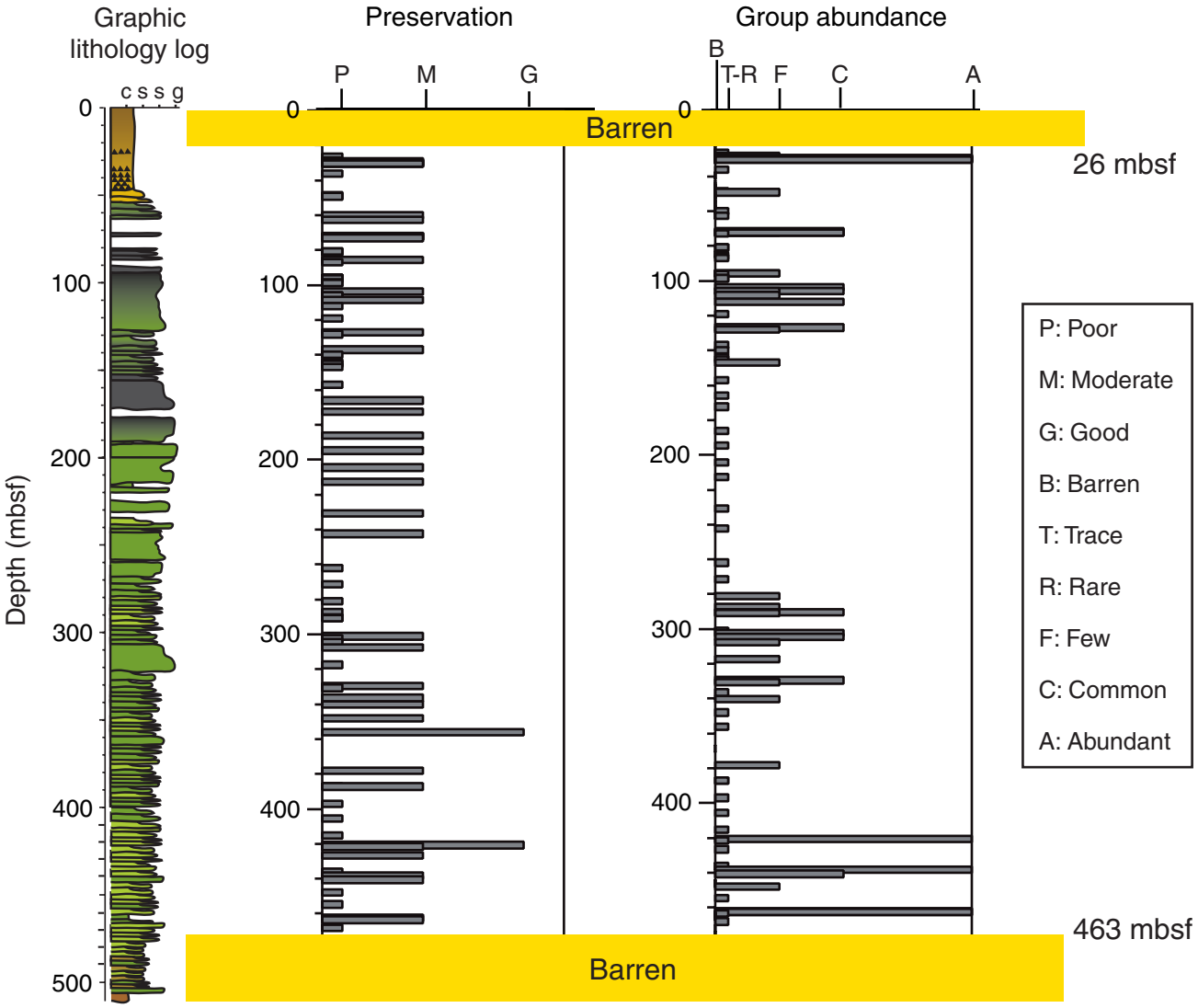

Figure F49. Occurrence of seven age-diagnostic calcareous nannofossils in the composite section from 0 to 500 mbsf (Holes 1201B and 1201D). The length of the horizontal bar at each depth level represents the abundance of nannofossils in four categories: rare, few, common, and abundant. The scale was set arbitrarily and is only meant to enhance visualization of the distribution patterns of the nannofossils in the succession. FO = first occurrence, LO = last occurrence. In the graphic lithology column, c = clay, s = silt, s = sand, g = gravel.

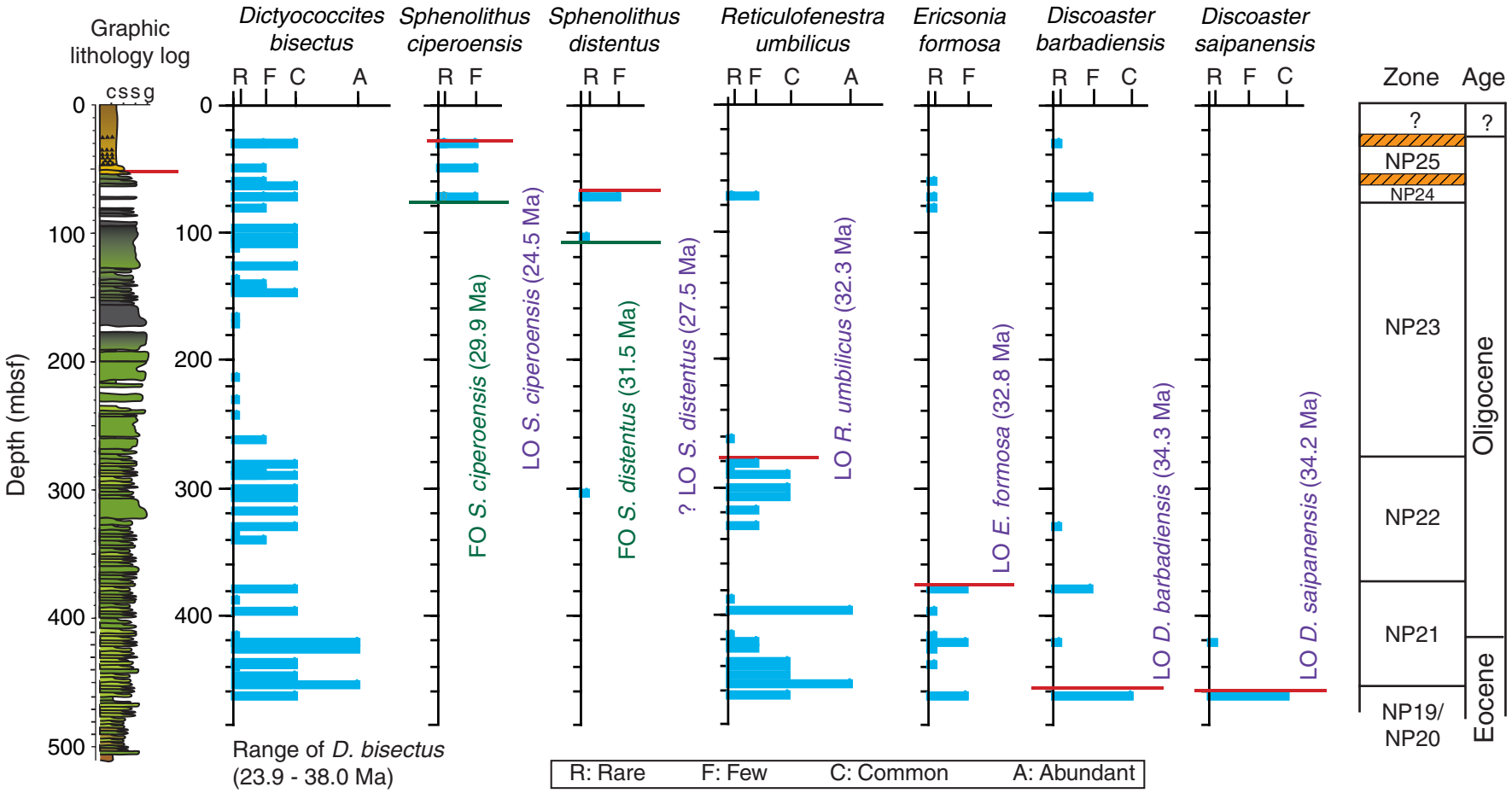

Figure F50. Ranges of selected age-diagnostic nannofossil species in a composite succession from Holes 1201B and 1201D. The solid lines represent our interpretation of the "true" ranges of species by interpolating their existence through samples. Upward extension of the occurrences caused by reworking was excluded. In the graphic lithology column, c = clay, s = silt, s = sand, g = gravel.

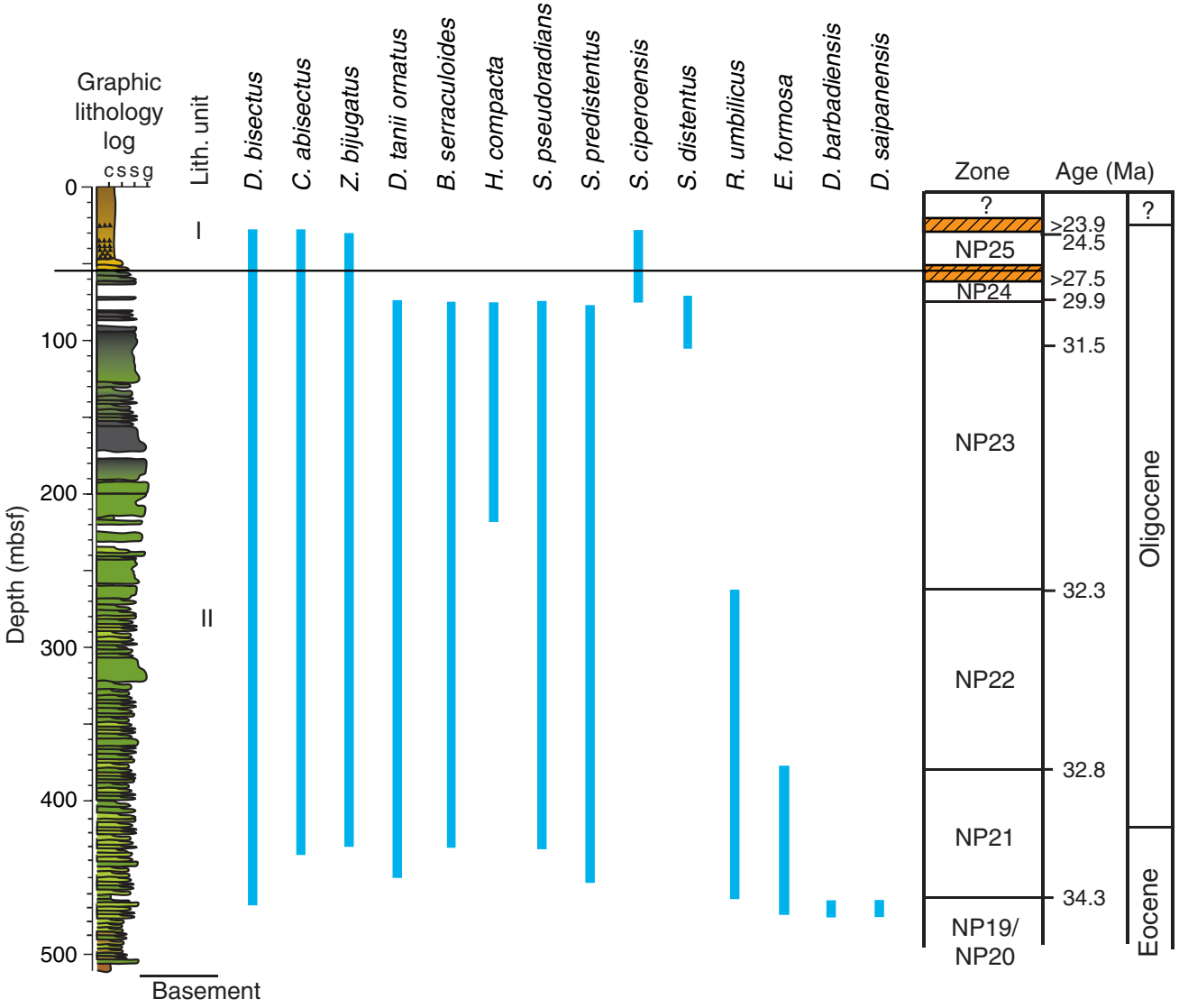

Figure F51. Downcore variations of concentration-dependent parameters (*k* and ARM) and relative magnetic grain-size proxy (ARM/*k*) at Site 1201.

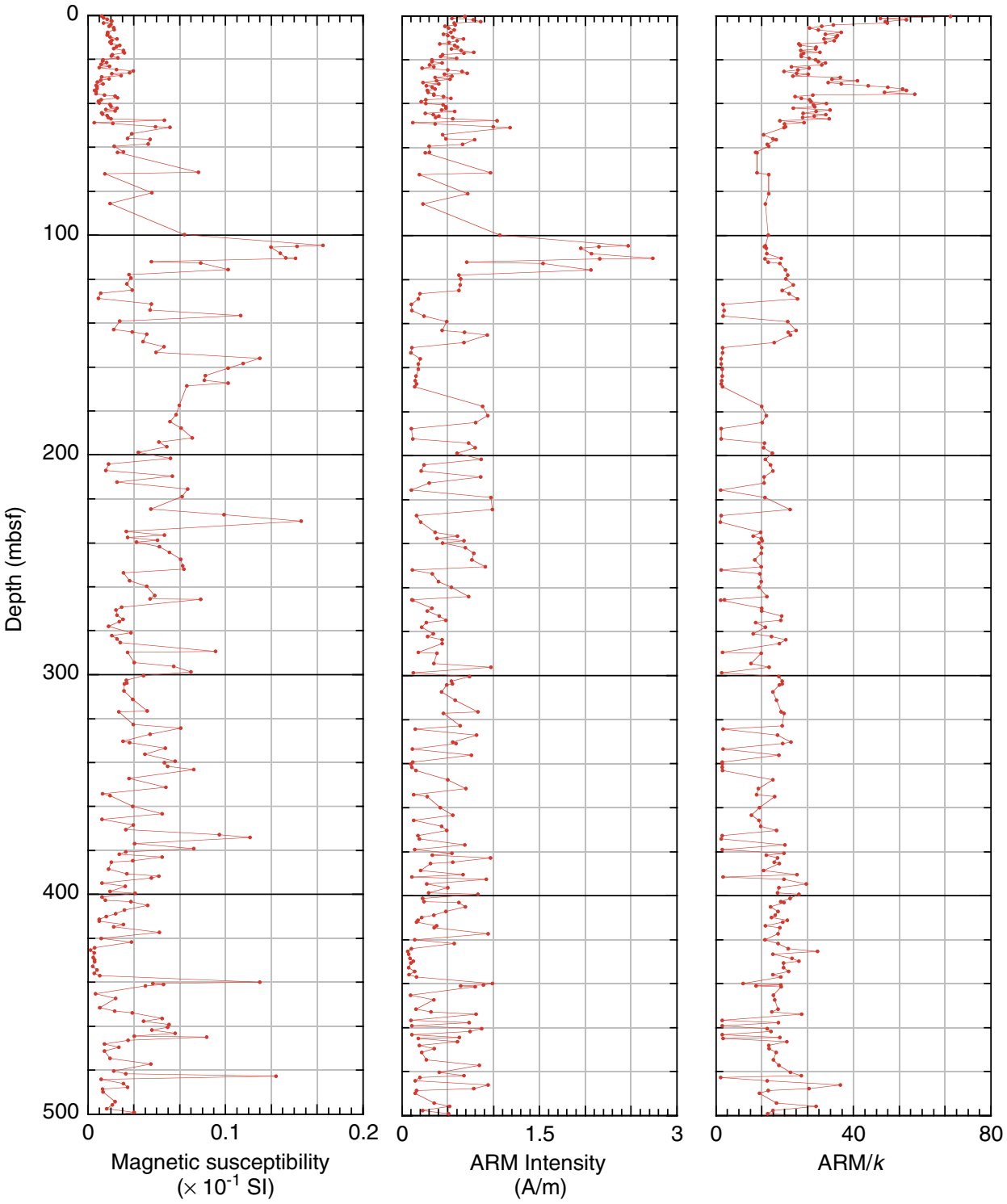

Figure F52. Isothermal remanent magnetization and backfield acquisition curves for representative discrete samples from Site 1201.

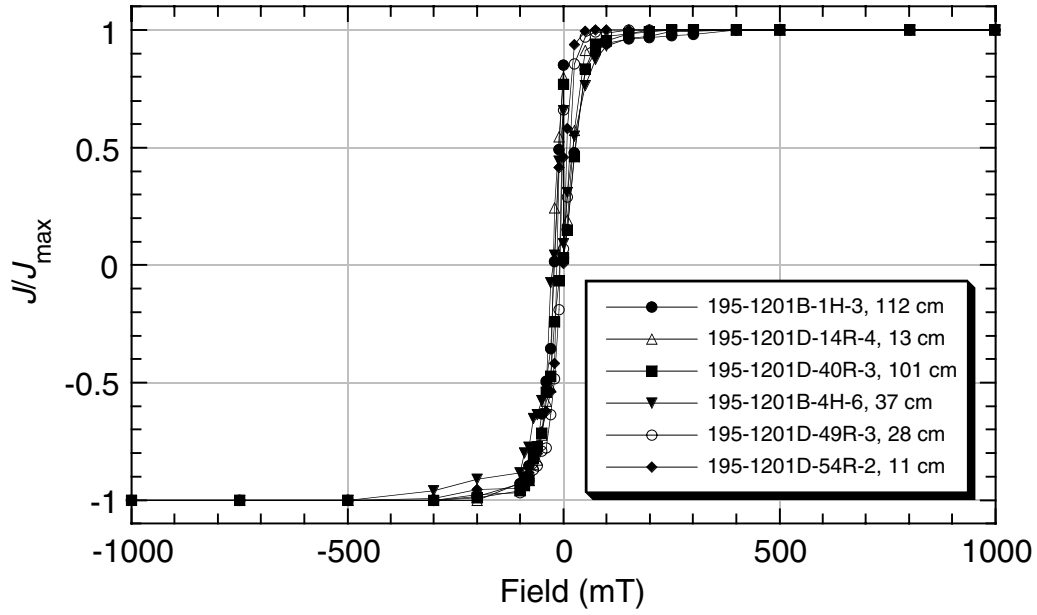

Figure F53. Magnetic intensity as a function of increasing AF field for (**A**) lithostratigraphic Unit I and (**B**) lithostratigraphic Unit II.

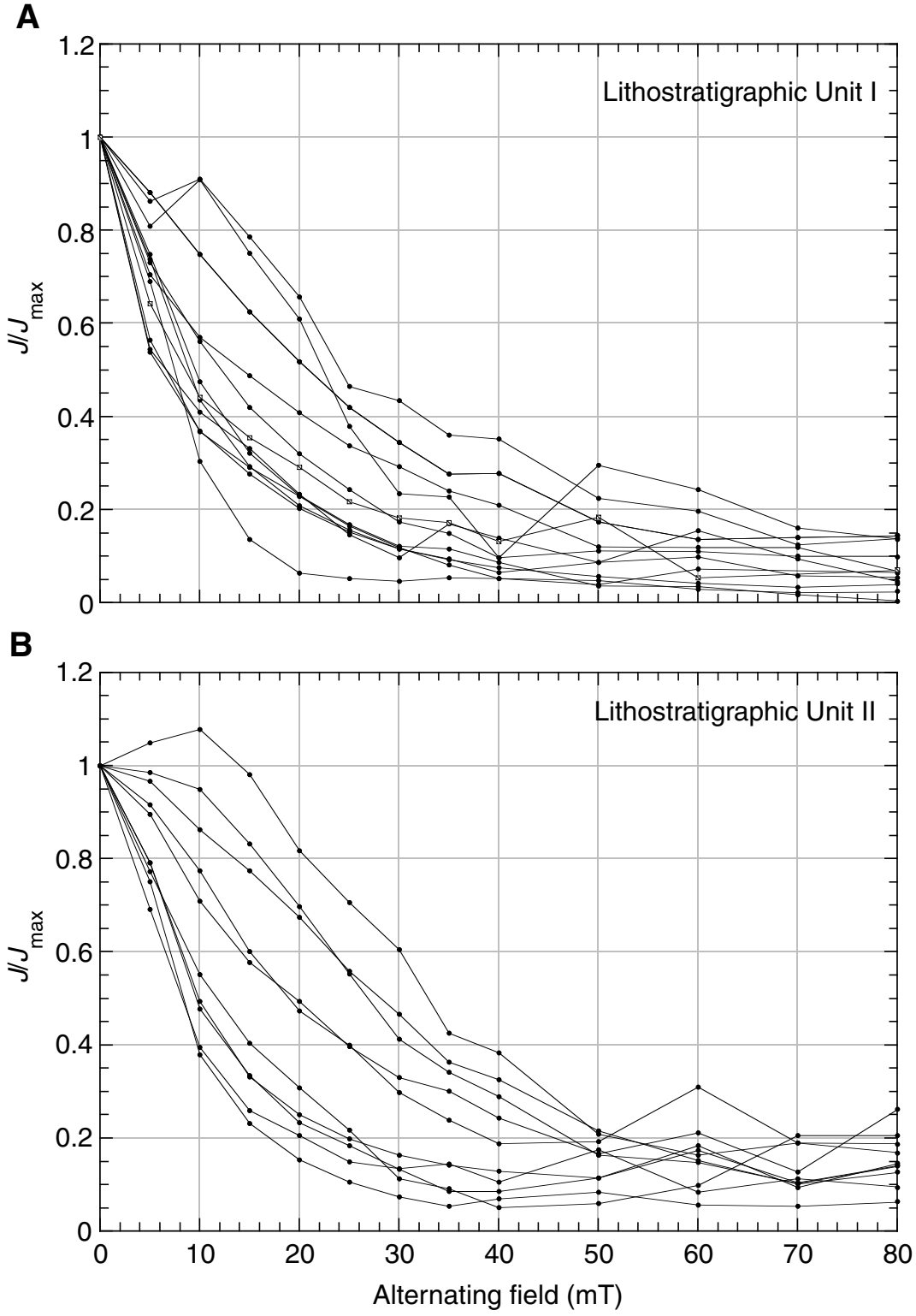

Figure F54. Thermal demagnetization data from (**A**) sediment and (**B**) basalt samples.

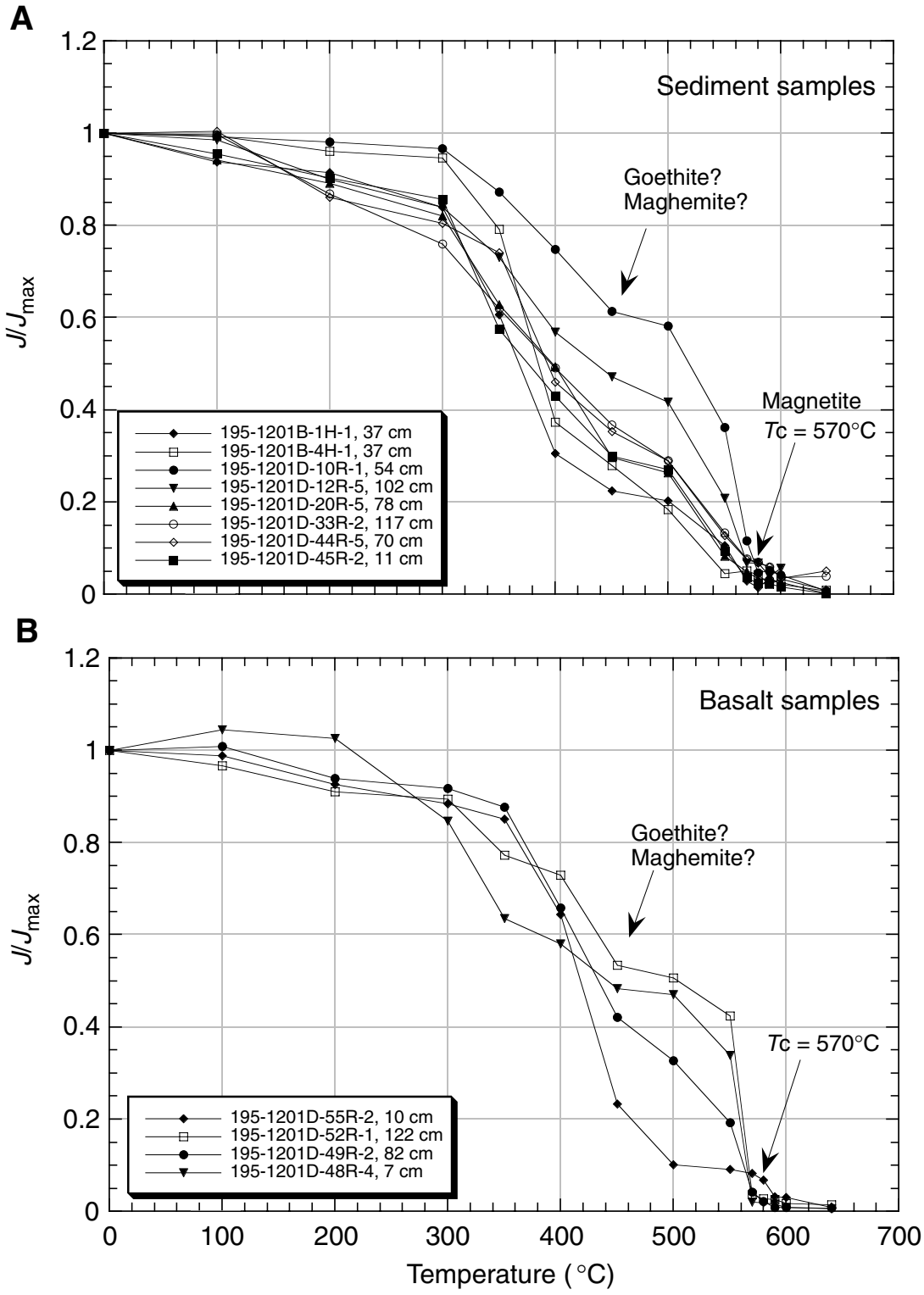

Figure F55. Magnetic susceptibility, intensity, and inclination of the composite record at Site 1201. Magnetic intensity is plotted before AF demagnetization. In the graphic lithology log, c = clay, s = silt, s = sand, g = gravel.

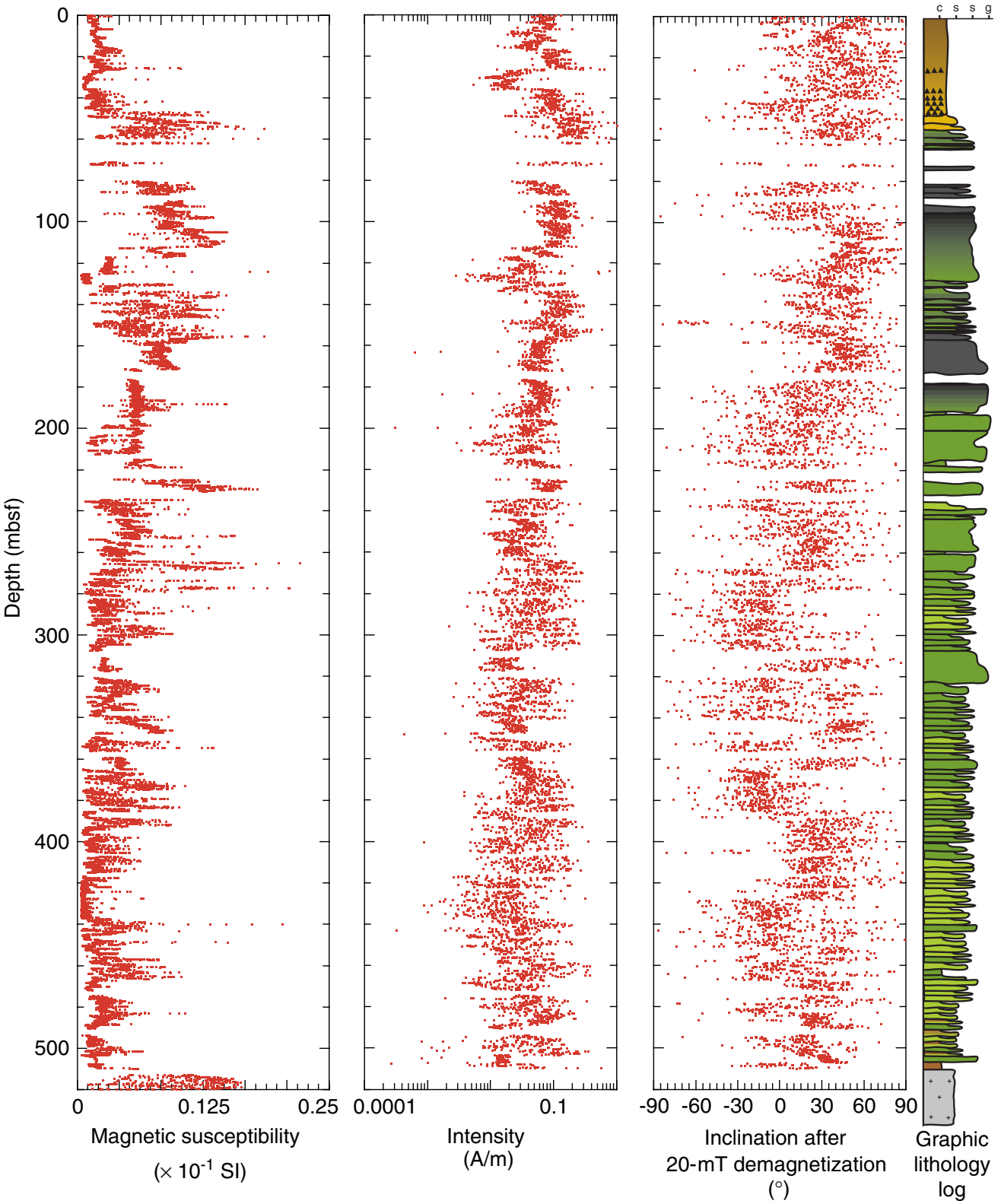

Figure F56. Vector component diagram with normalized intensity decay plots of demagnetization (AF) behavior for representative sediment samples from Site 1201. Open (solid) symbols represent projections onto the vertical (horizontal) plane. The core is not azimuthally oriented; therefore the declination values are not meaningful.

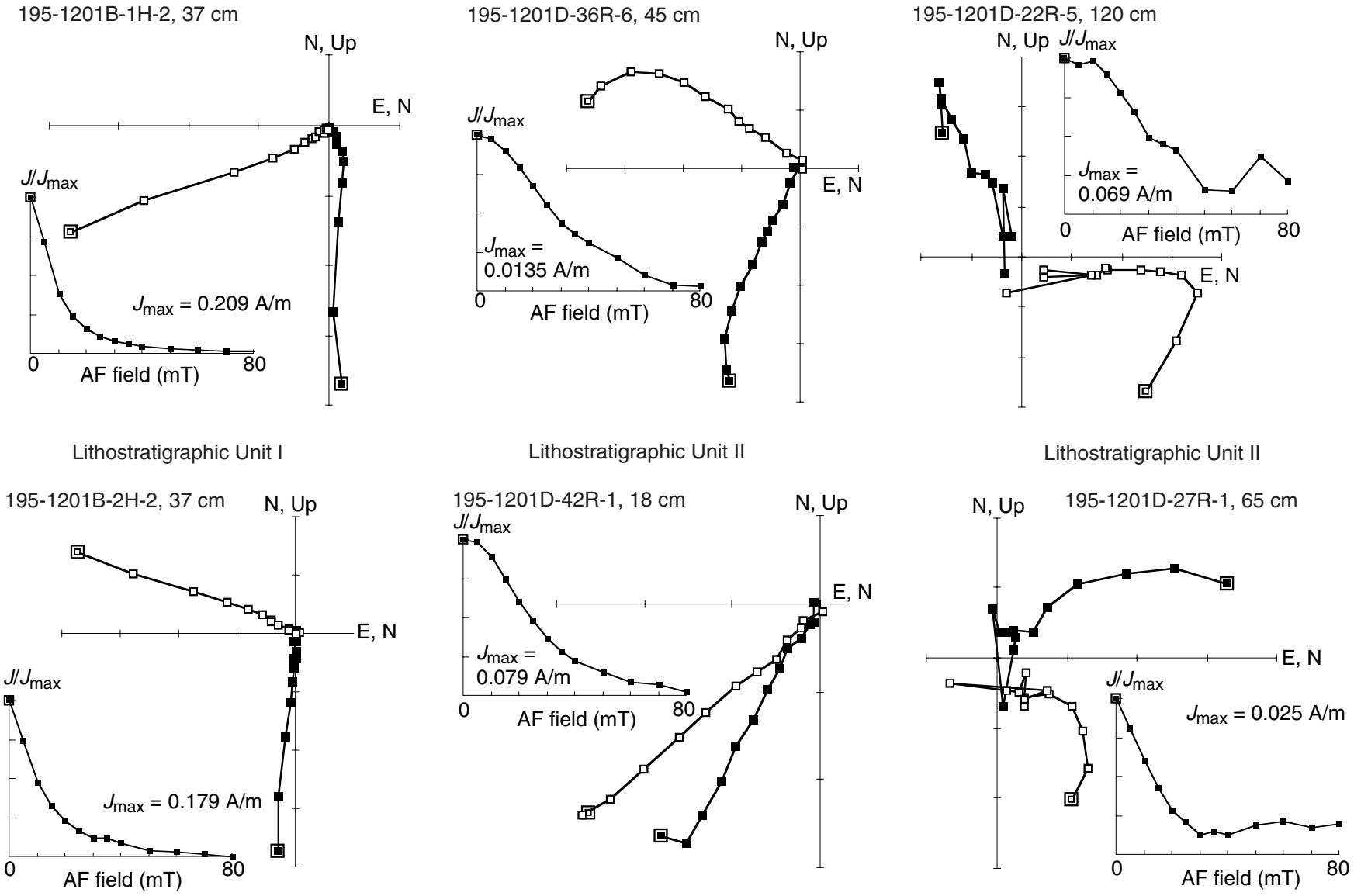

Figure F57. Magnetostratigraphic record from Site 1201 **A.** (0–50 mbsf) The plot of NRM inclination and declination is after demagnetization at 20 mT. Inclinations and declinations of discrete samples (solid circles) were determined by linear regression fits to multiple demagnetization steps. Polarity is shown on the log to the right: black = normal polarity, white = reversed polarity, hatched intervals = undetermined polarity, undulating line = hiatus. Chron ages for polarity reversal boundaries are from Berggren et al. (1995). PCA = principal component analysis. (Continued on next page.)

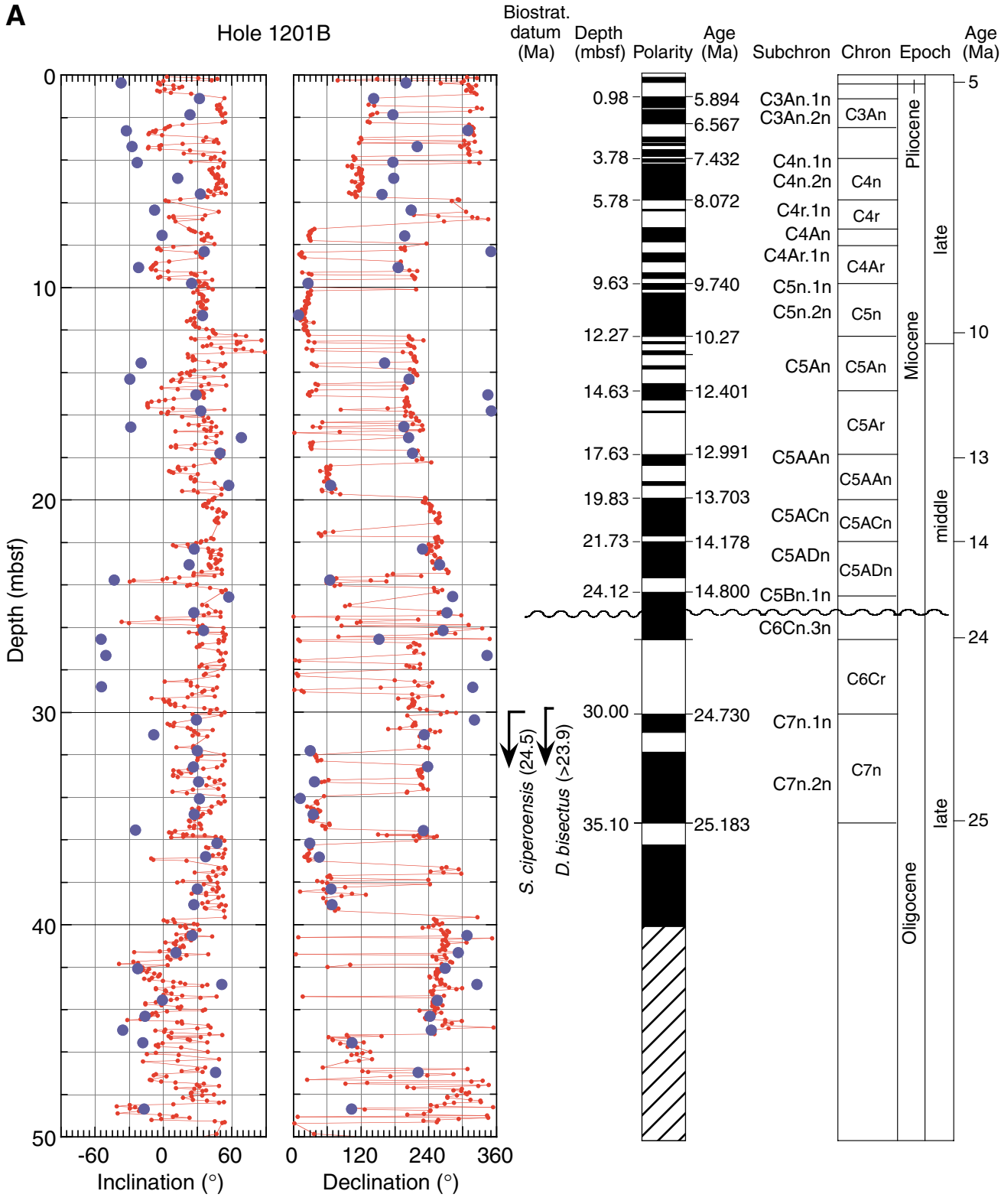

Figure F57 (continued). Magnetostratigraphic record from Site 1201 **B.** (50–509 mbsf).

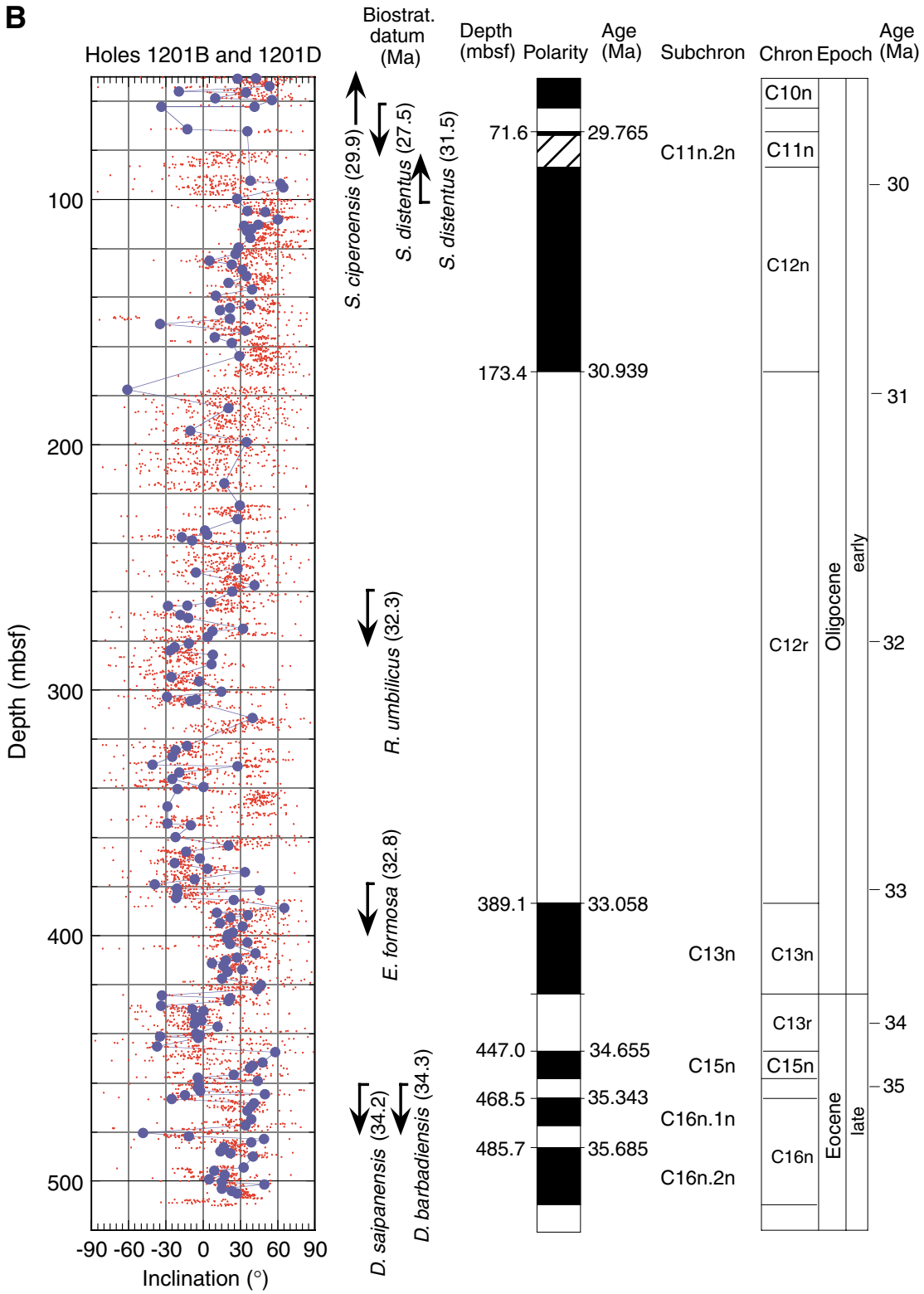

Figure F58. A. Age model and correlation of the composite magnetic polarity record for Site 1201. Magnetic polarity interpretations are given in Figure **F57,** p. 125, and individual reversal ages are from Berggren et al. (1995). Solid line = line of correlation, undulating line = hiatus. LO = last occurrence, FO = first occurrence. Lithostratigraphic summary is from **"Lithostratigraphy,"** p. 10, and biostratigraphic datums are from **"Biostratigraphy,"** p. 23. In the graphic lithology log, c = clay, s = silt, s = sand, g = gravel. (Continued on next page.)

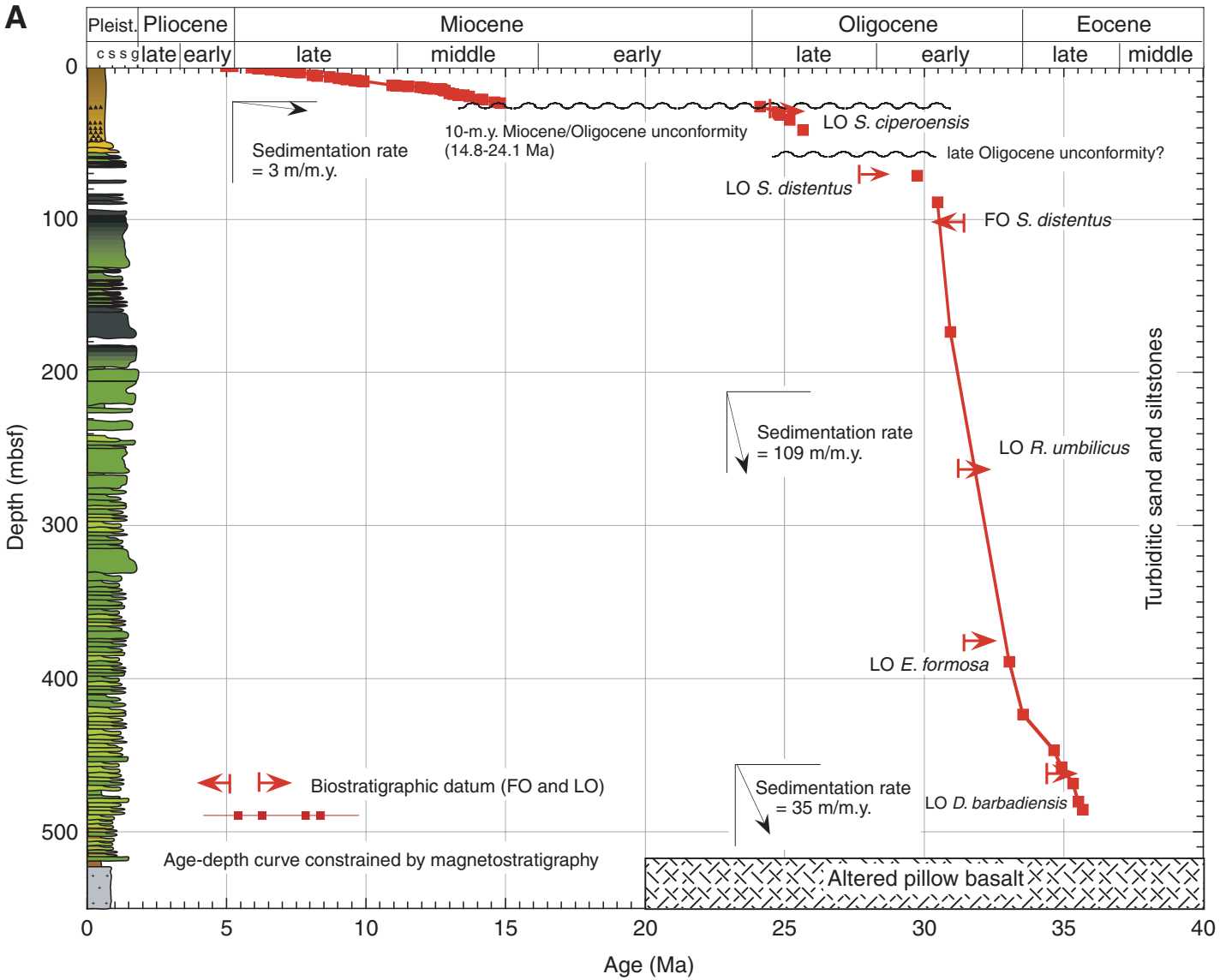

Figure F58 (continued). B. The 0–50 mbsf interval enlarged. The main features are discussed in "Sedimentation Rates," p. 32, in "Paleomagnetism."

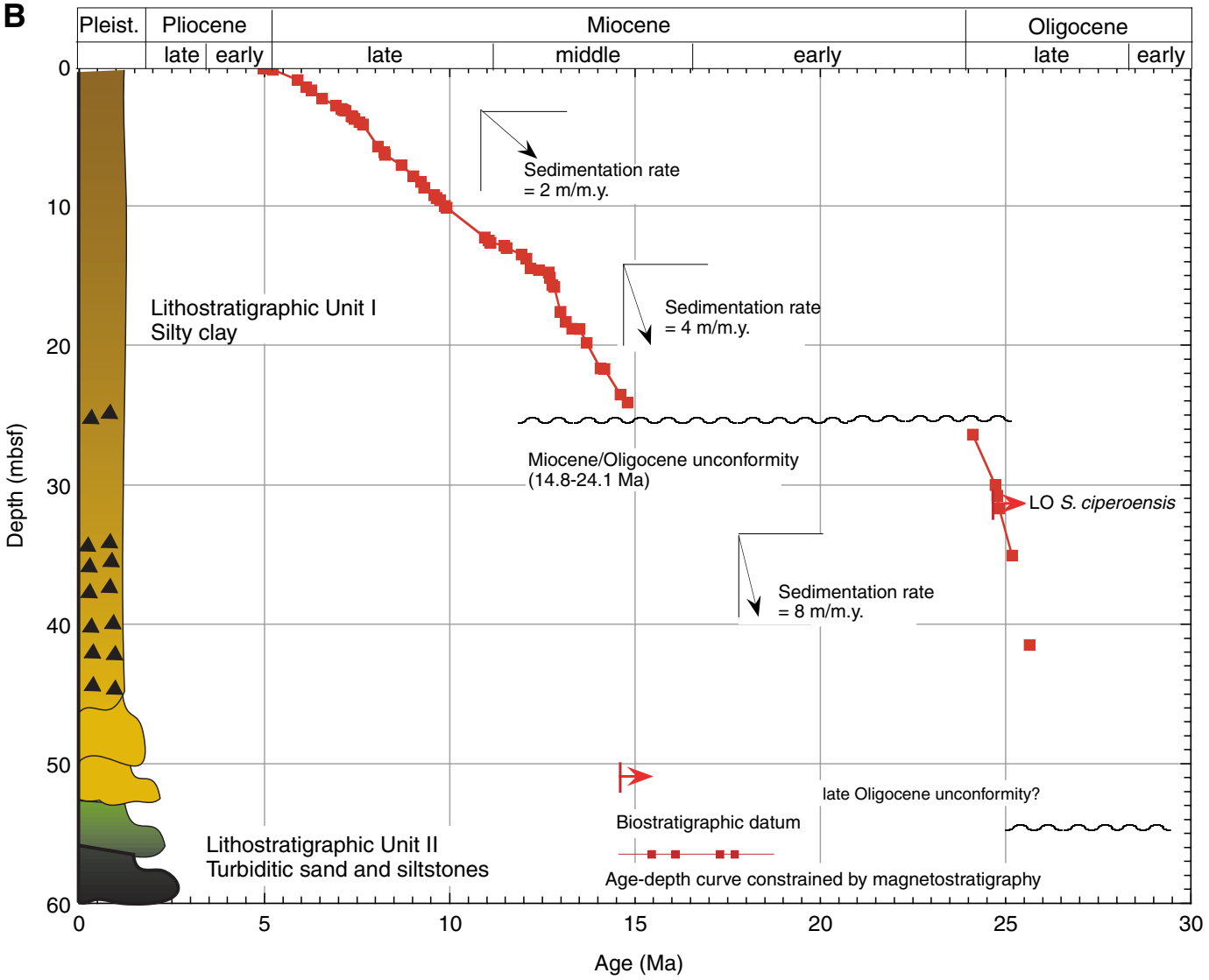

Figure F59. Vector component diagram with normalized intensity decay plots of demagnetization (AF) behavior of representative basalt samples for Site 1201. Open (closed) symbols represent projections onto the vertical (horizontal) plane. The declination values are not meaningful because the core is not azimuthally oriented.

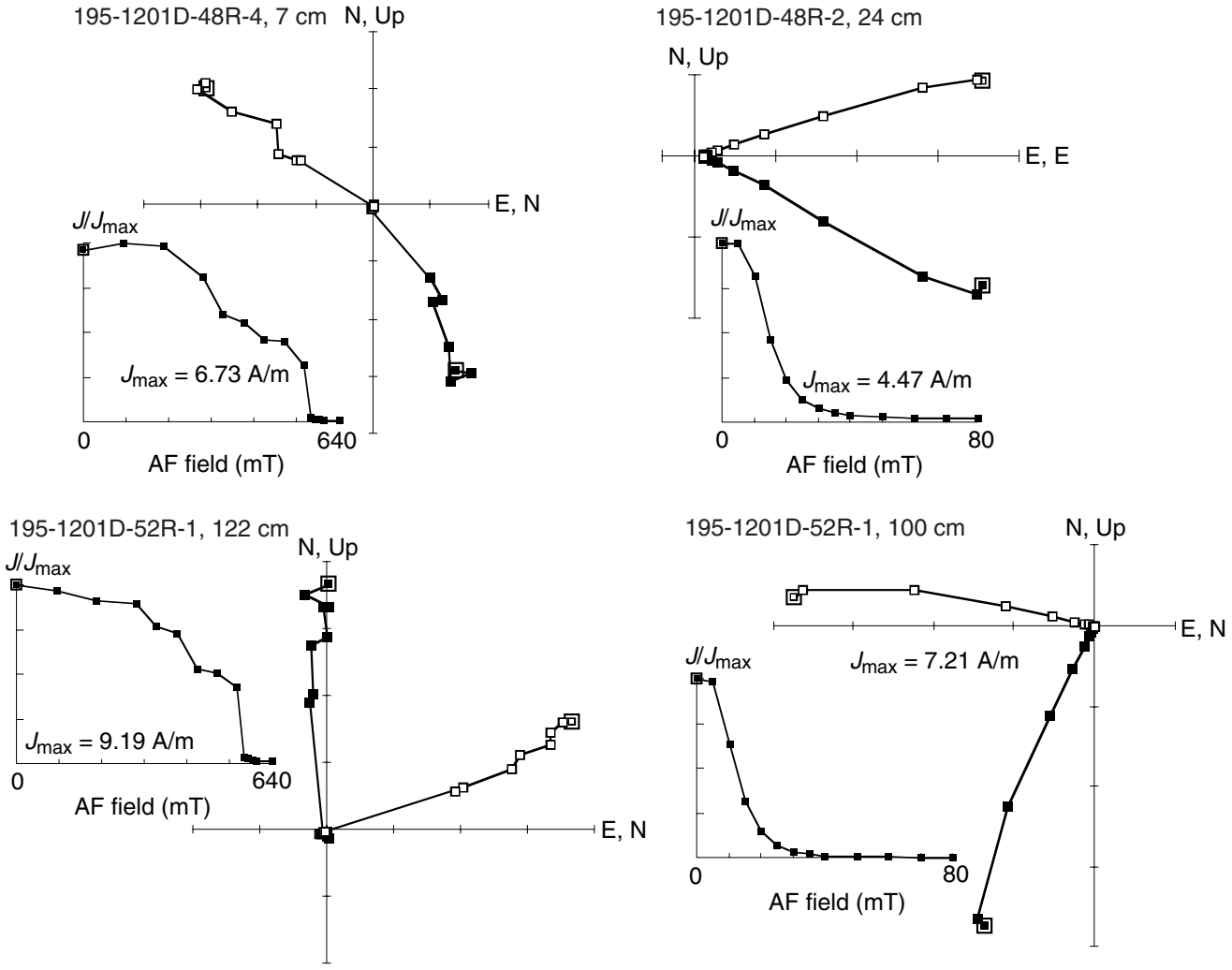

Figure F60. Plot of magnetic inclinations of discrete basalt samples from Hole 1201D. Inclinations were determined by linear regression fits to multiple demagnetization steps. Magnetic inclination is shallow, indicating an equatorial position of the Philippine plate during the time at which the basalts were formed.

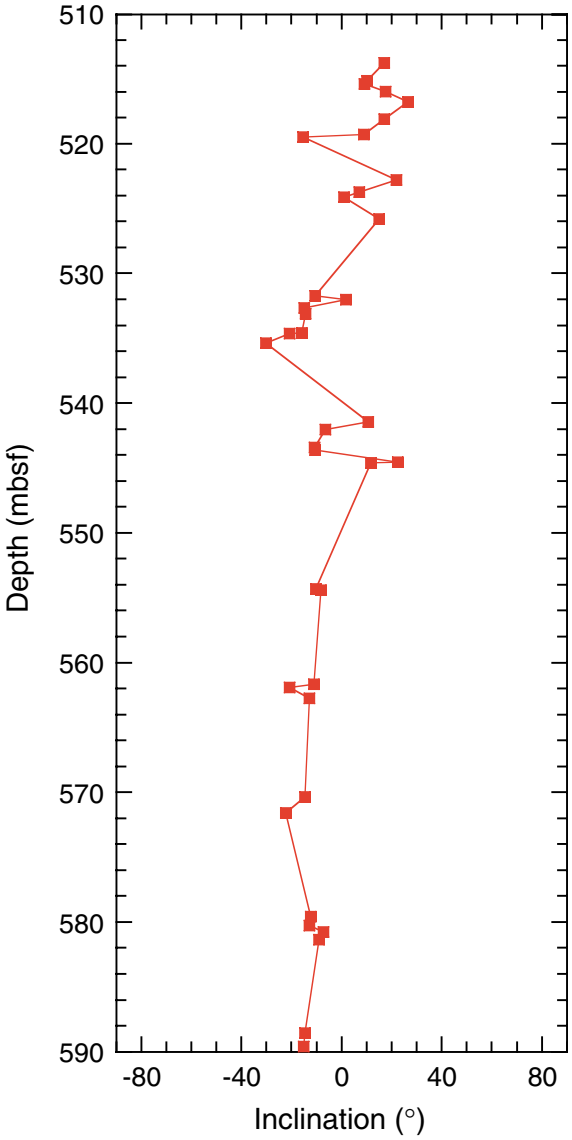

Figure F61. Percentage of total milliequivalents of major anions and cations in Site 1201 pore water compared with average seawater.

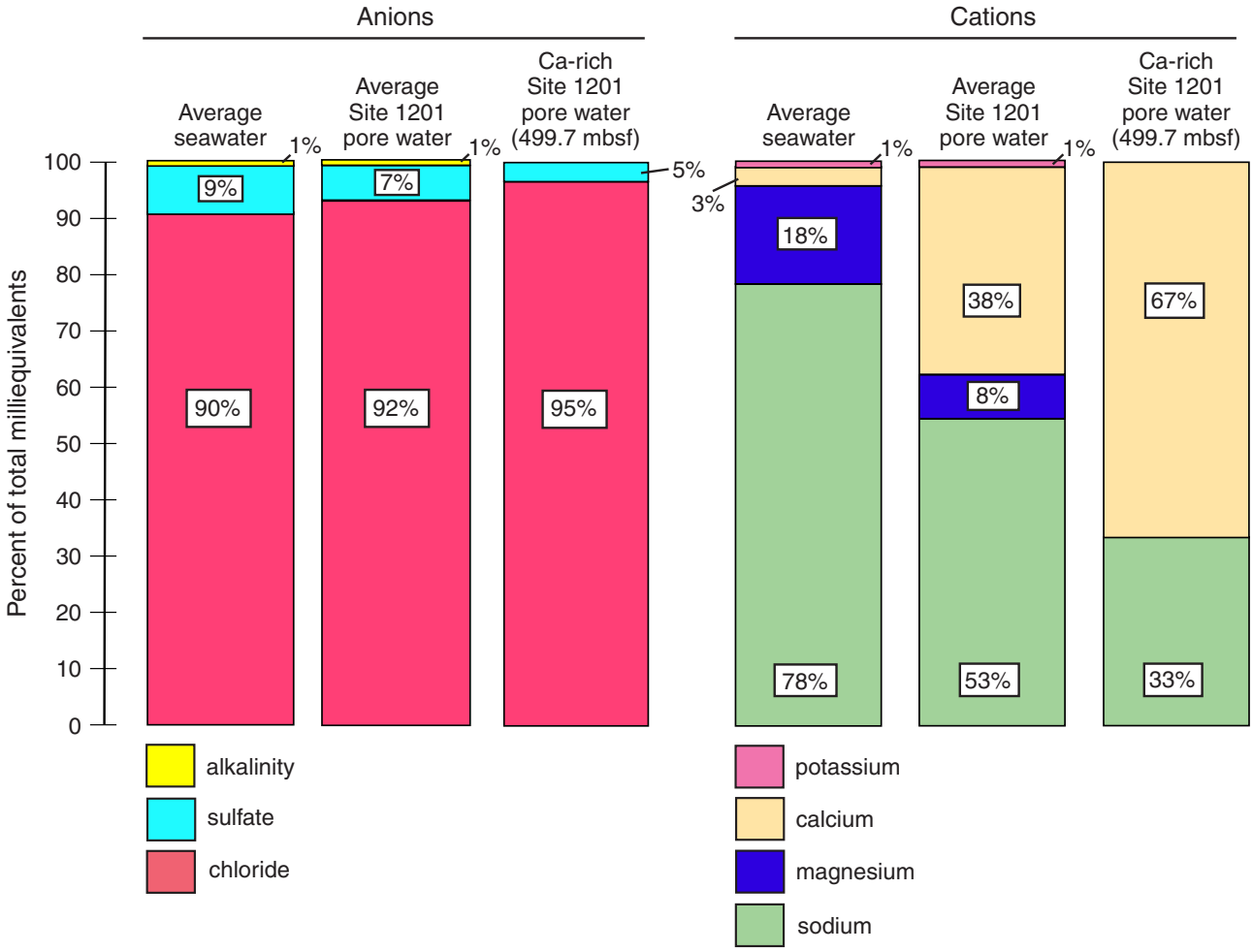

Figure F62. Composition of interstitial water from Site 1201. **A.** pH. **B.** Alkalinity. **C.** Ammonia. **D.** Sulfate. **E.** Chlorinity. Arrows = seawater values. In the graphic lithology log, c = clay, s = silt, s = sand, g = gravel.

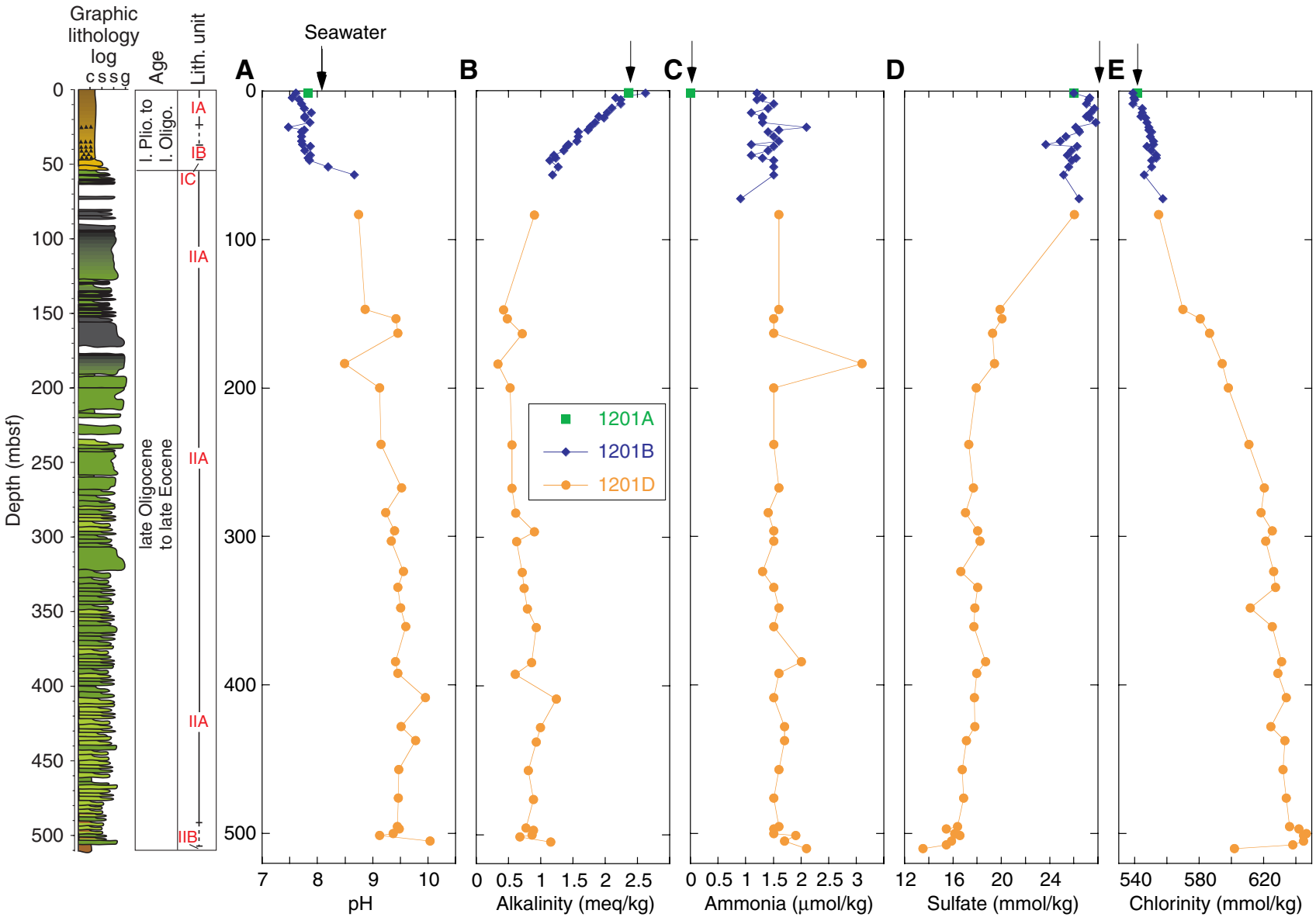

Figure F63. Cation composition of interstitial water from Site 1201. **A.** Magnesium. **B.** Calcium. **C.** Sodium. **D.** Potassium. Arrows = seawater values. In the graphic lithology log, c = clay, s = silt, s = sand, g = gravel.

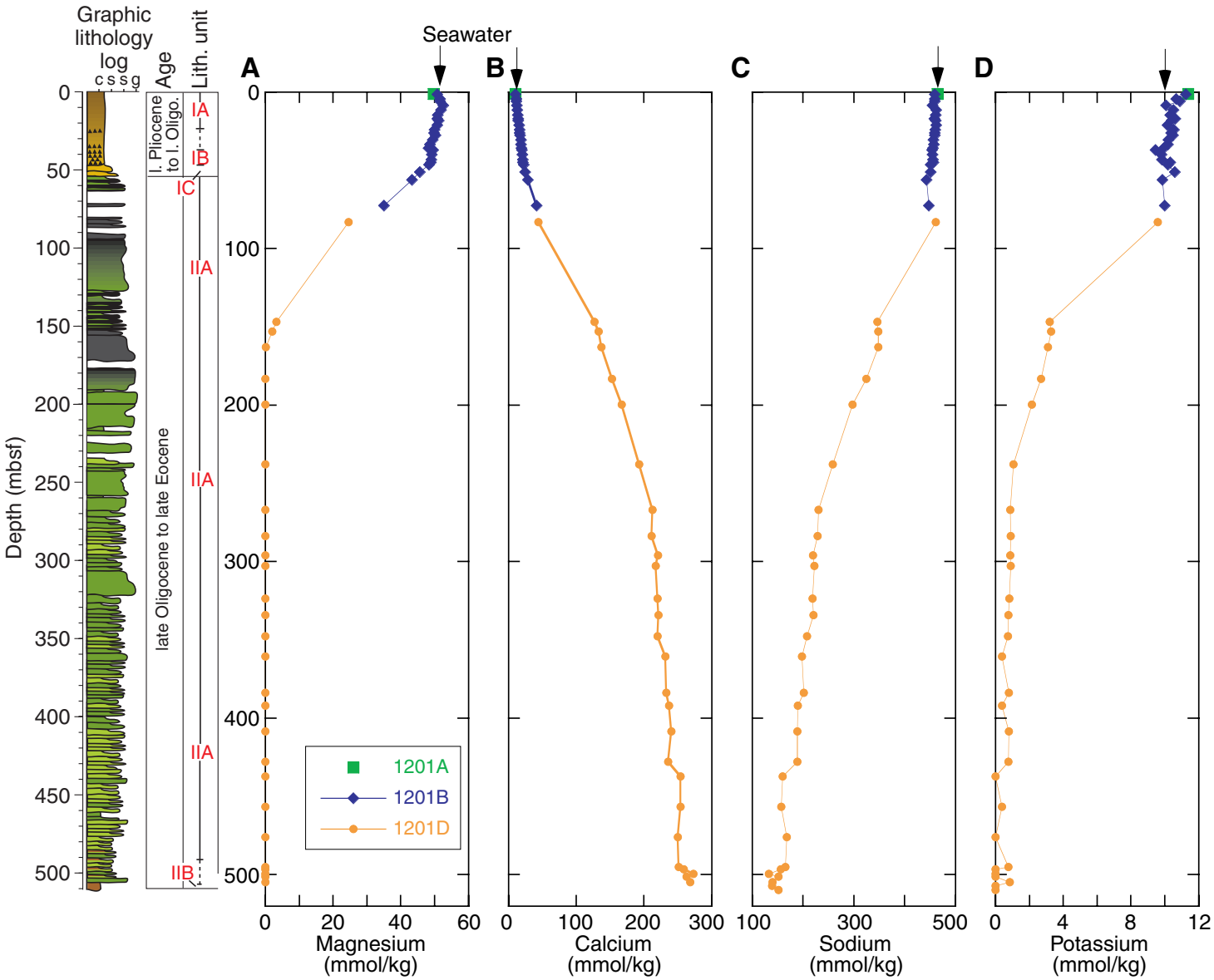

Figure F64. Composition of interstitial water from Site 1201. **A.** Silica. **B.** Strontium. **C.** Manganese. **D.** Fluoride. Arrows = seawater values. In the graphic lithology log, c = clay, s = silt, s = sand, g = gravel.

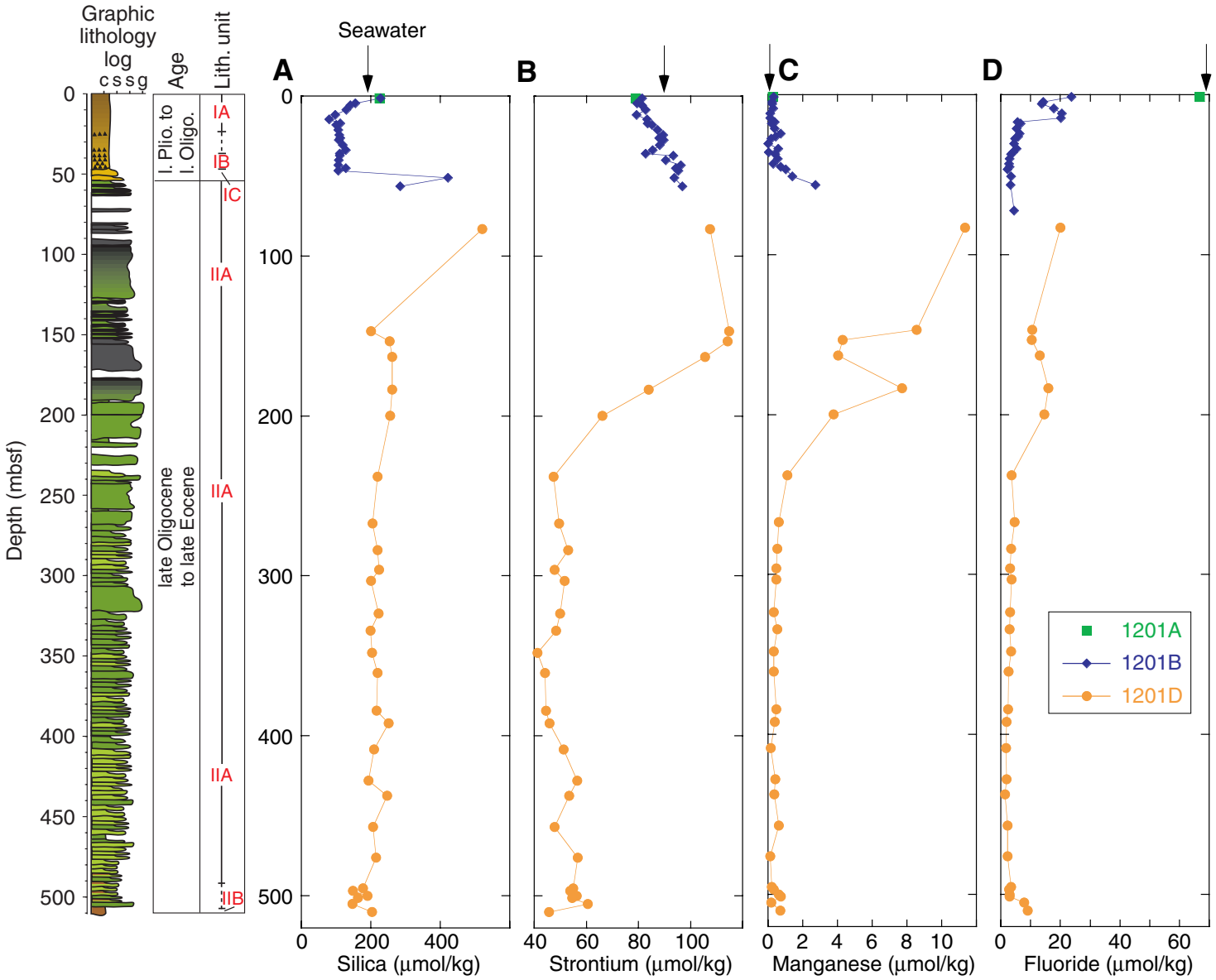

Figure F65. Composition of interstitial water from Site 1201. **A.** Lithium. **B.** Boron. **C.** Aluminum. Arrows = seawater values. In the graphic lithology log, c = clay, s = silt, s = sand, g = gravel.

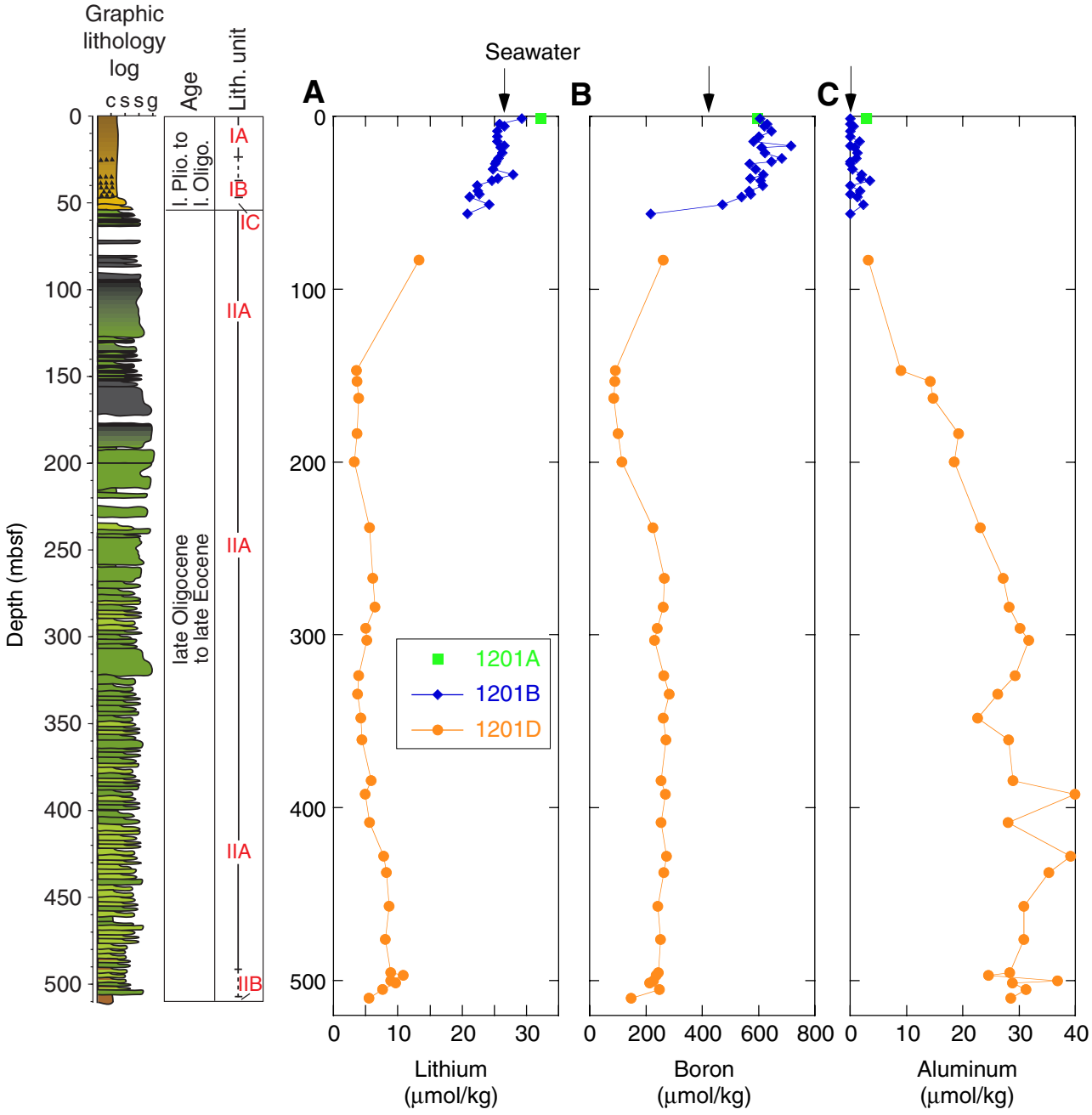

Figure F66. MST results in Holes 1201B (<72.5 mbsf) and 1201D (>80 mbsf). **A.** Volume magnetic susceptibility. **B.** Bulk density. **C.** Natural gamma radiation. **D.** Graphic lithology log, lithologic units, and approximate ages (see "Lithostratigraphy," p. 10). In the graphic lithology log, c = clay, s = silt, s = sand, g = gravel. Expanded 100-m sections are presented in Figures F67, p. 137, F68, p. 138, F69, p. 139, F70, p. 140, F71, p. 141, and F72, p. 142.

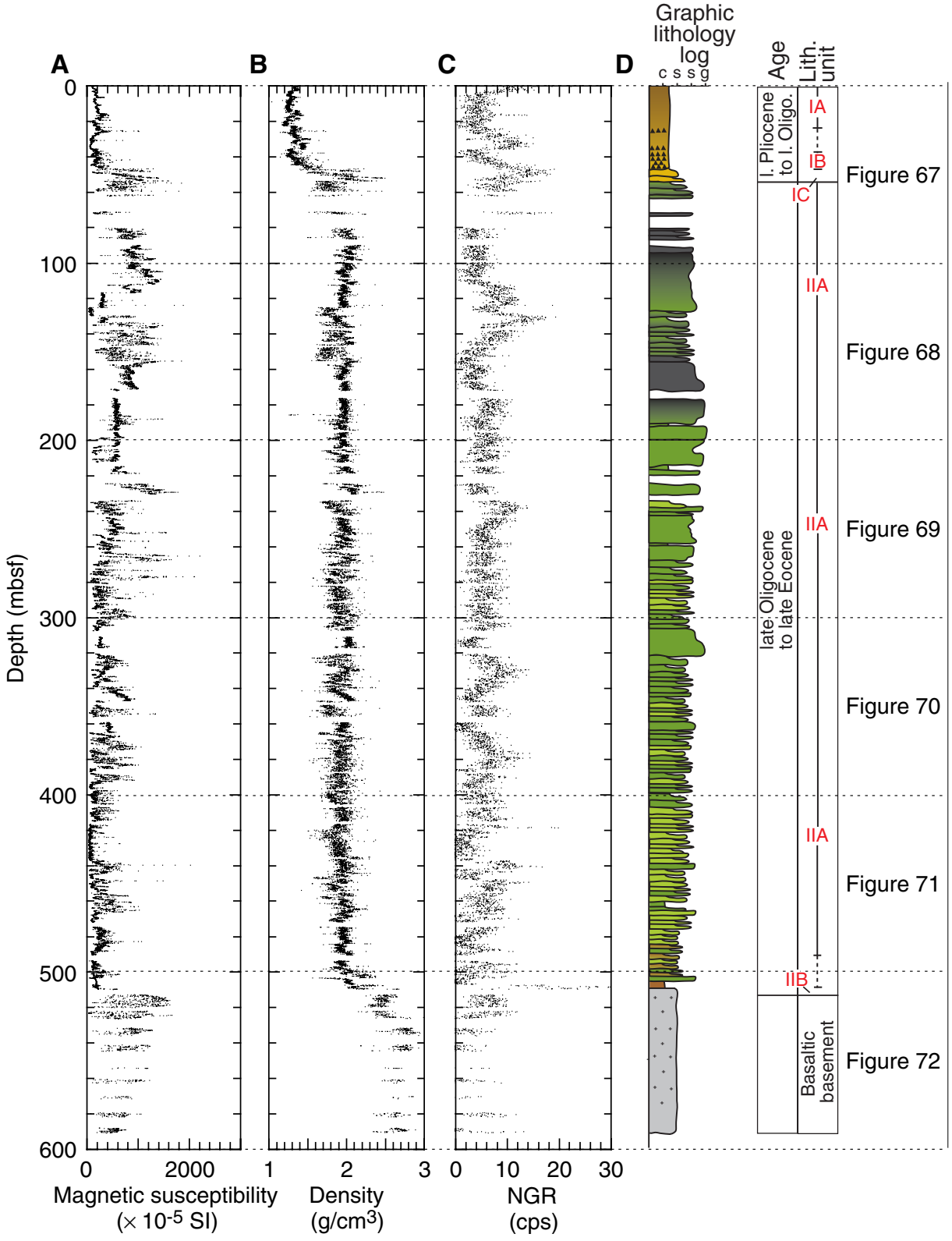

Figure F67. MST results in Holes 1201B (<72.5 mbsf) and 1201D (>80 mbsf) for the interval 0–100 mbsf. **A.** Volume magnetic susceptibility. **B.** Bulk density. Open circles represent index properties measurements derived from discrete samples. **C.** Natural gamma radiation. **D.** Graphic lithology log (see "Lithostratigraphy," p. 10).

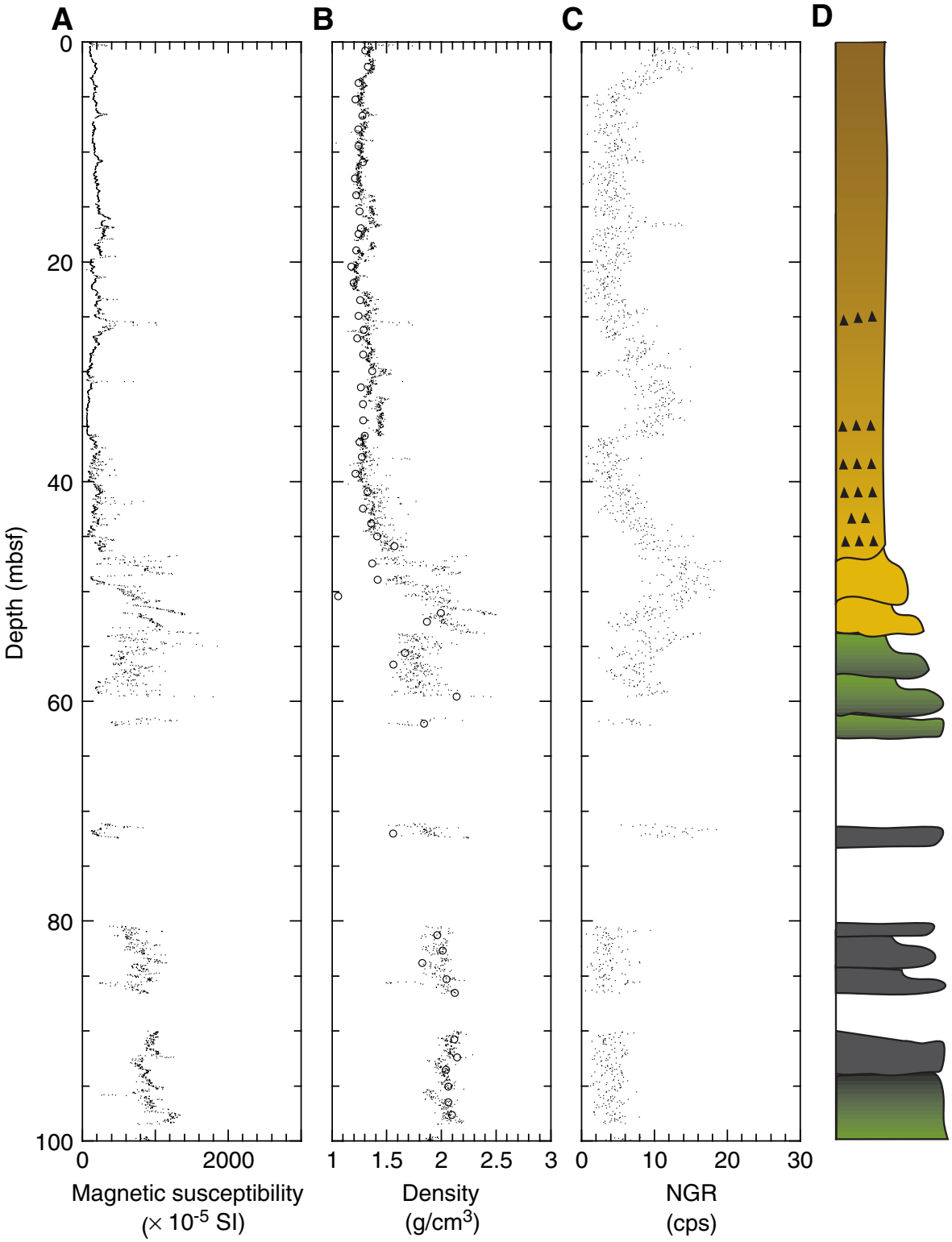

Figure F68. MST results in Hole 1201D for the interval from 100 to 200 mbsf. **A.** Volume magnetic susceptibility. **B.** Bulk density. Open circles represent index properties measurements derived from discrete samples. **C.** Natural gamma radiation. **D.** Graphic lithology log (see "Lithostratigraphy," p. 10).

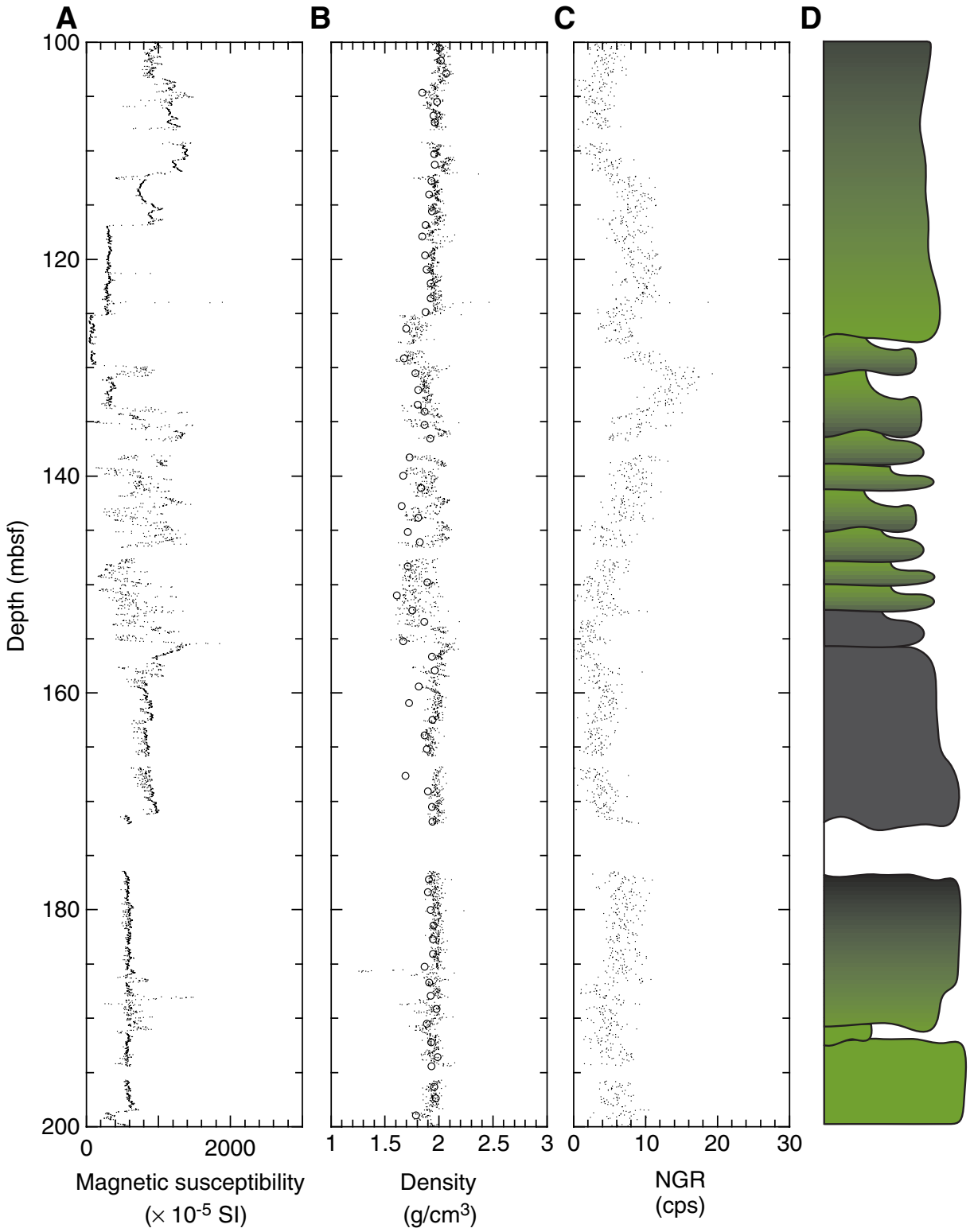

Figure F69. MST results in Hole 1201D for the interval from 200 to 300 mbsf. **A.** Volume magnetic susceptibility. **B.** Bulk density. Open circles represent index properties measurements derived from discrete samples. **C.** Natural gamma radiation. **D.** Graphic lithology log (see "Lithostratigraphy," p. 10).

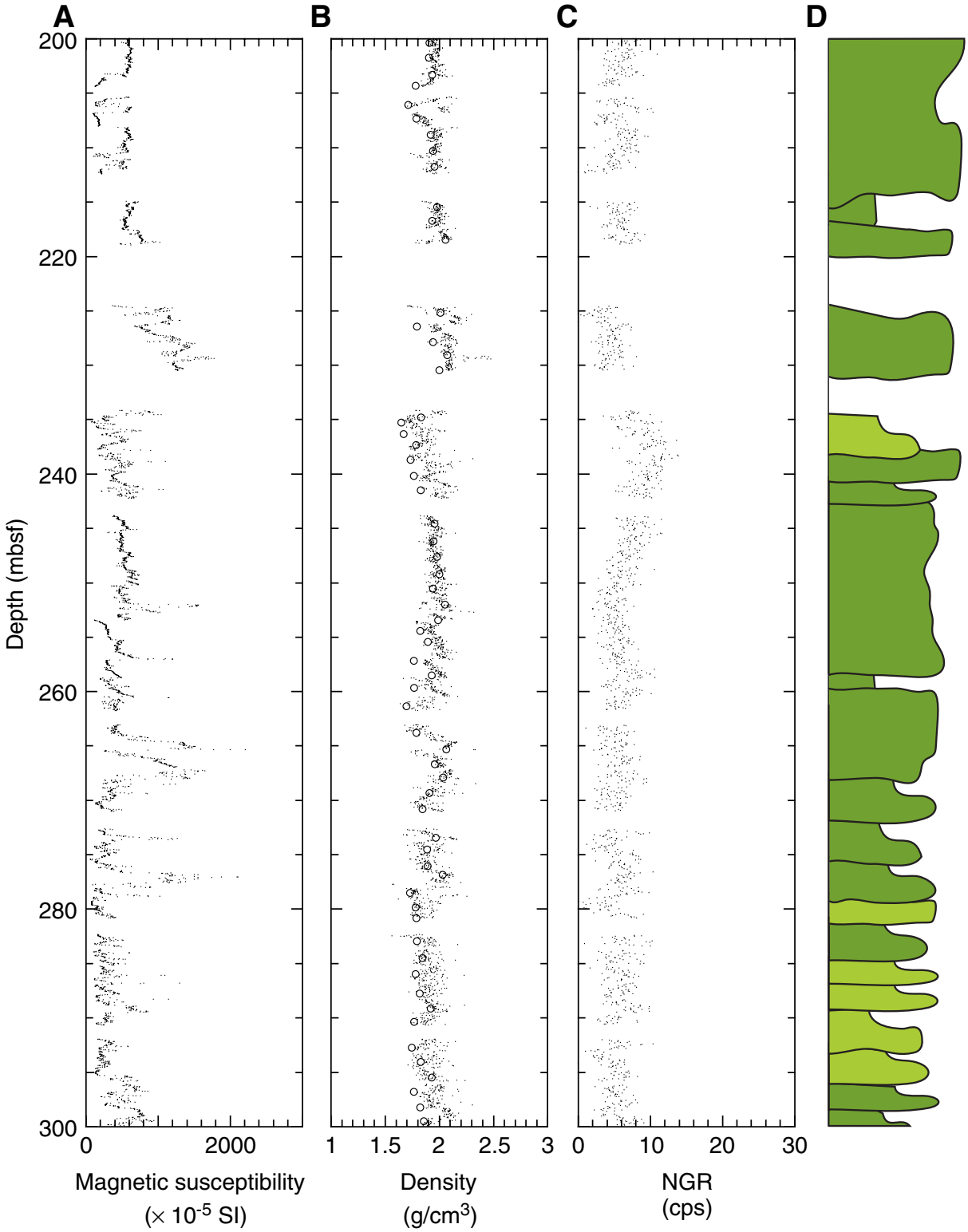

Figure F70. MST results in Hole 1201D for the interval from 300 to 400 mbsf. **A.** Volume magnetic susceptibility. **B.** Bulk density. Open circles represent index properties measurements derived from discrete samples. **C.** Natural gamma radiation. **D.** Graphic lithology log (see "Lithostratigraphy," p. 10).

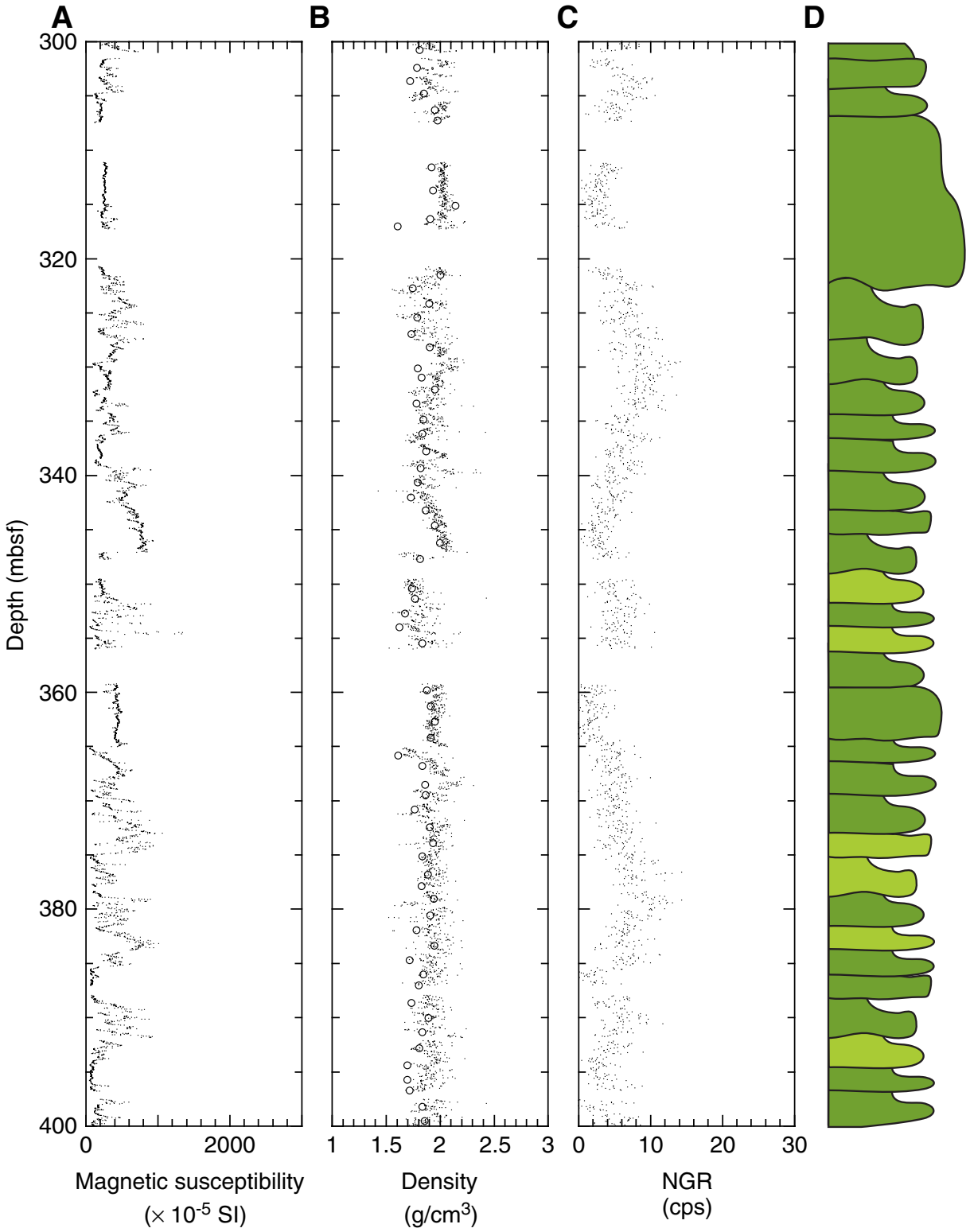

Figure F71. MST results in Hole 1201D for the interval from 400 to 500 mbsf. **A.** Volume magnetic susceptibility. **B.** Bulk density. Open circles represent index properties measurements derived from discrete samples. **C.** Natural gamma radiation. **D.** Graphic lithology log (see "Lithostratigraphy," p. 10).

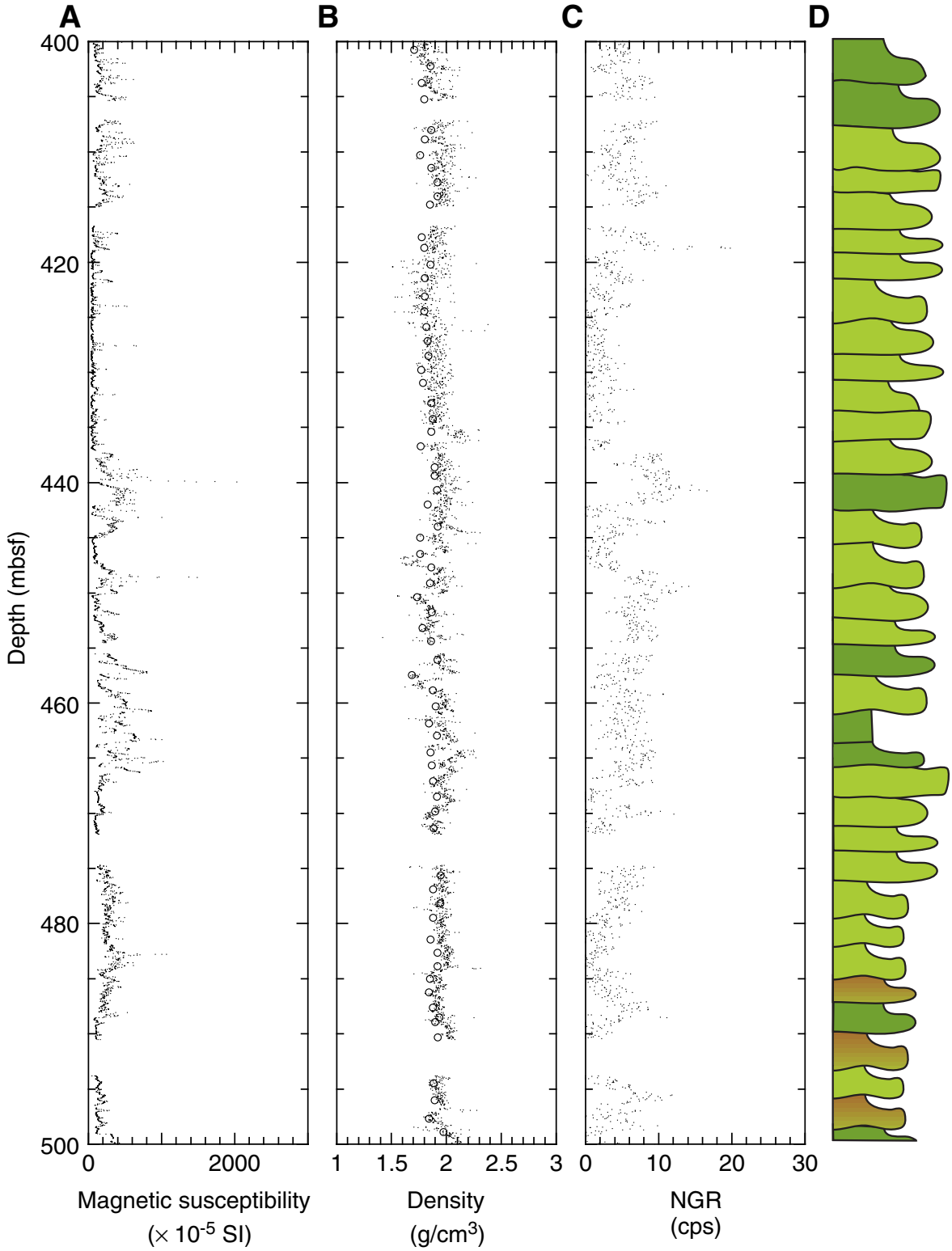

Figure F72. MST results in Hole 1201D for the interval from 500 to 591 mbsf. **A.** Volume magnetic susceptibility. **B.** Bulk density. Open circles represent index properties measurements derived from discrete samples. **C.** Natural gamma radiation. **D.** Graphic lithology log (see "Lithostratigraphy," p. 10).

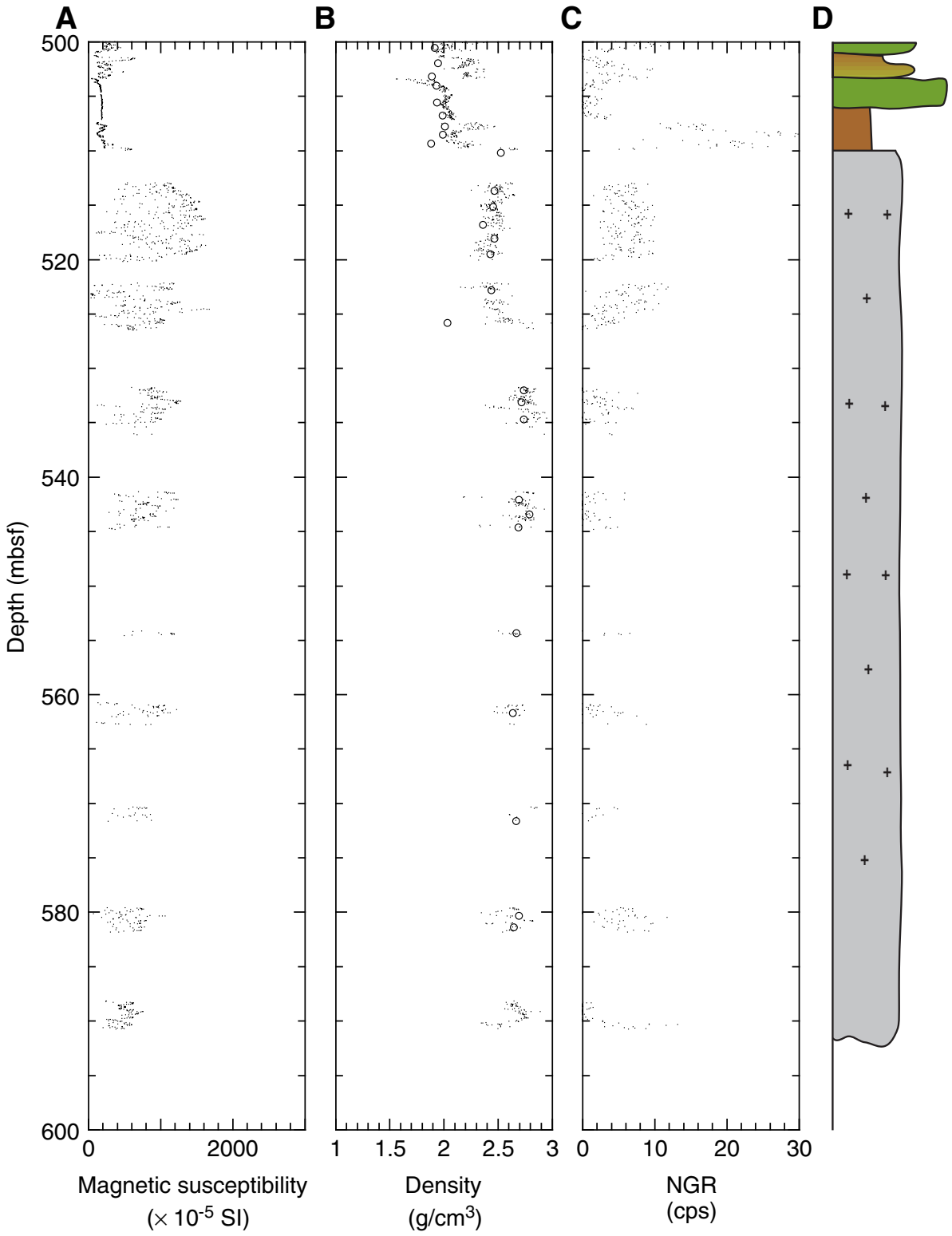

Figure F73. MST results for Holes 1201B and 1201C. **A.** Volume magnetic susceptibility. **B.** Bulk density. **C.** Natural gamma radiation. Arrows indicate anomalies that are identified to be the same event but occur ~1 m deeper in Hole 1201B.

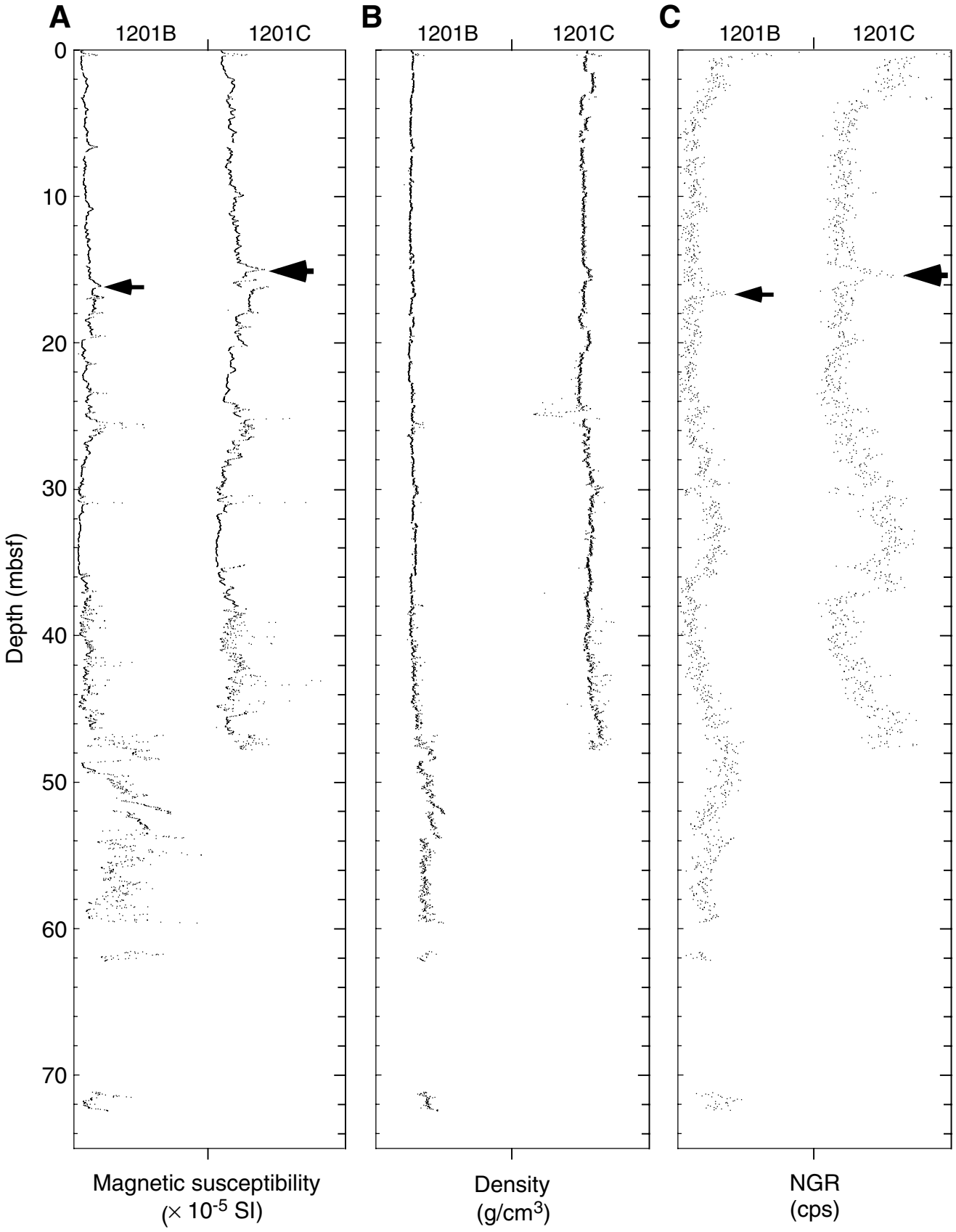

Figure F74. Magnetic susceptibility in Hole 1202D for the depth interval from 340 to 348 mbsf showing sequences on three different scales: 341.5–347.0, 342.5–344.0, and 343.3–343.5 mbsf.

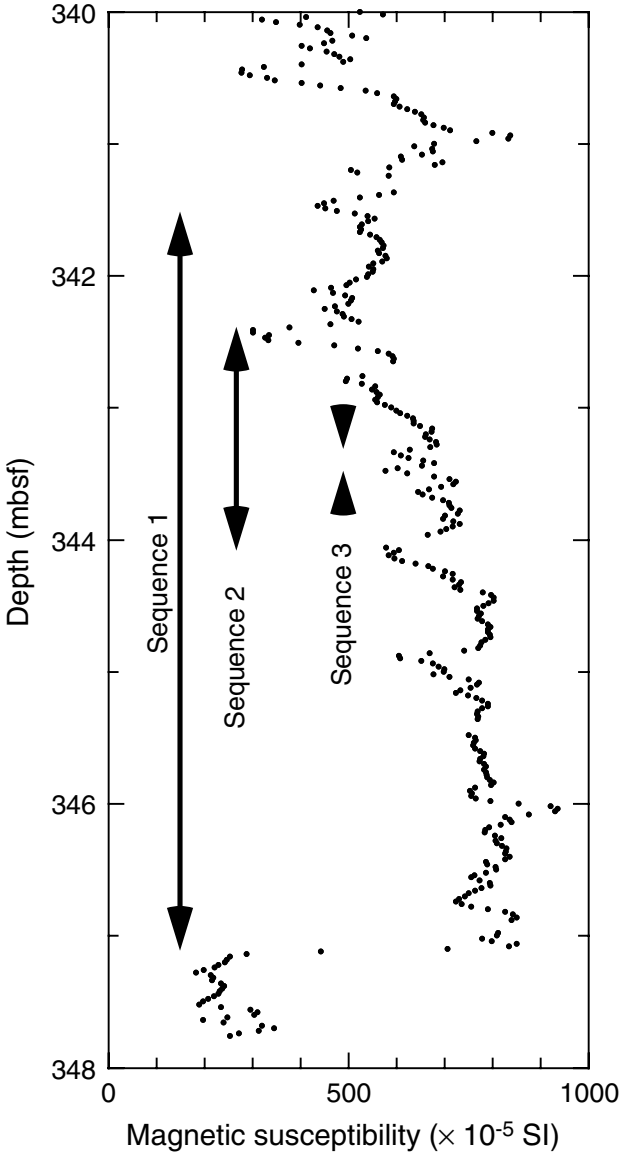

Figure F75. **A.** Grain density from index properties measurements. **B.** Bulk density from index properties measurements. **C.** Porosity from index properties measurements. **D.** Velocity measurements; includes x-, y-, and z-axis measurements. **E.** Acoustic impedance calculated for index properties samples using **Equation 2,** p. 39. Arrows indicate changes in lithologic units, where the reflection coefficient, *R,* has been calculated using **Equation 3,** p. 39.

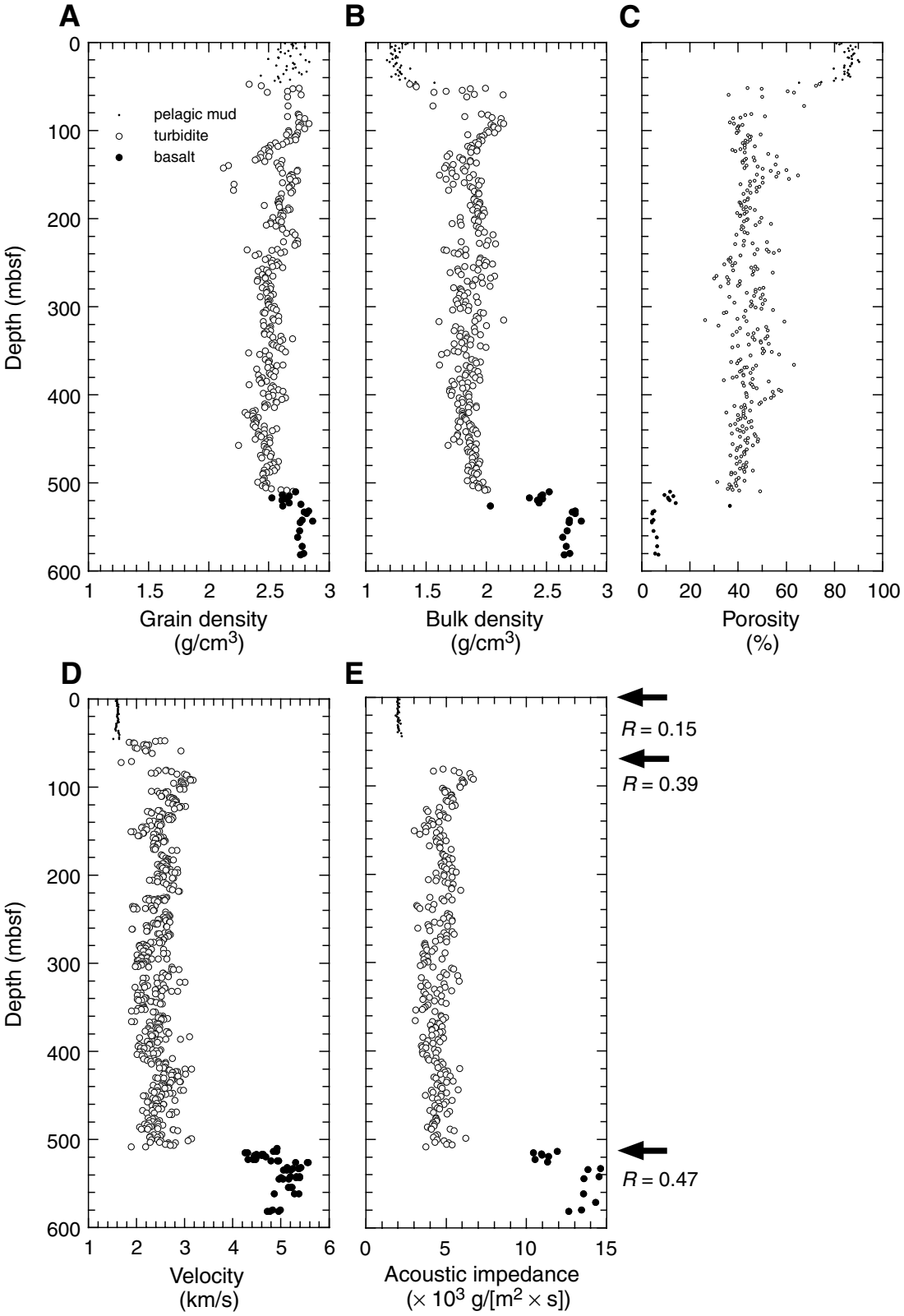

Figure F76. Comparison of the seismic record at Site 1201 to a synthetic trace.

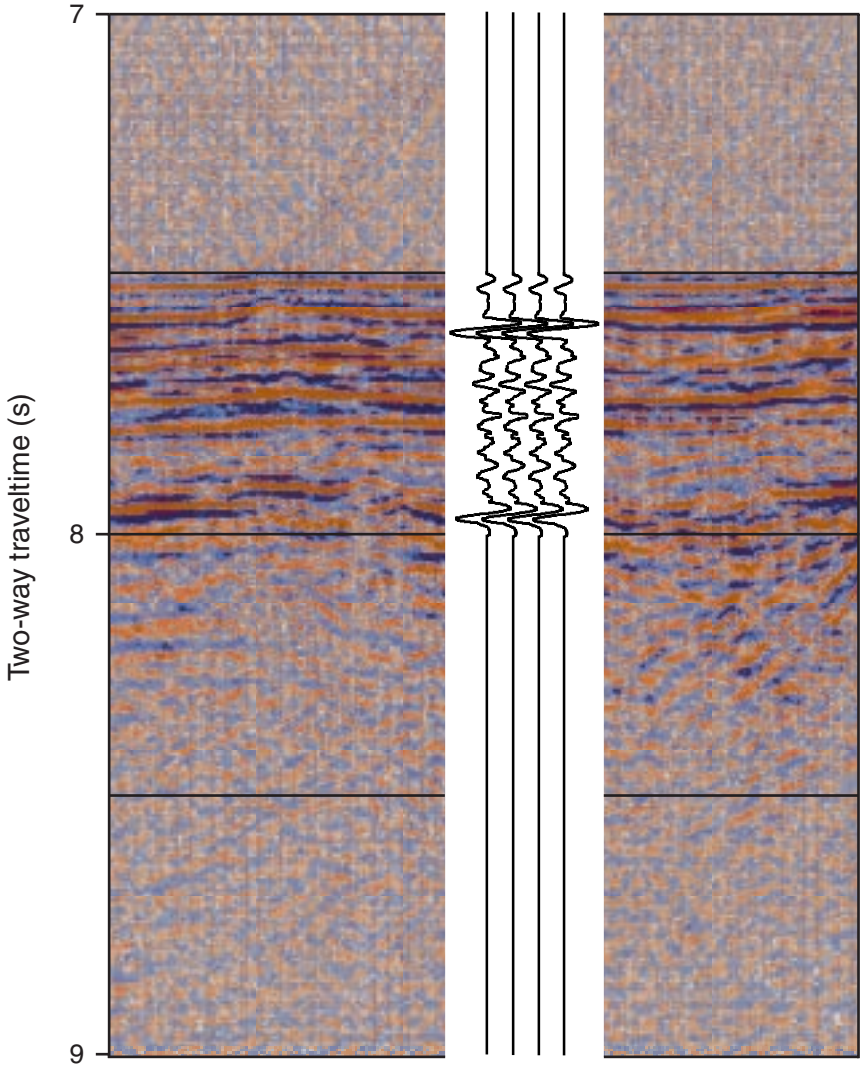

Figure F77. Seismic velocity anisotropy calculated from velocity measurements parallel to the core axis (V_z) and perpendicular to the core axis (V_h). The vertical line corresponds to no anisotropy.

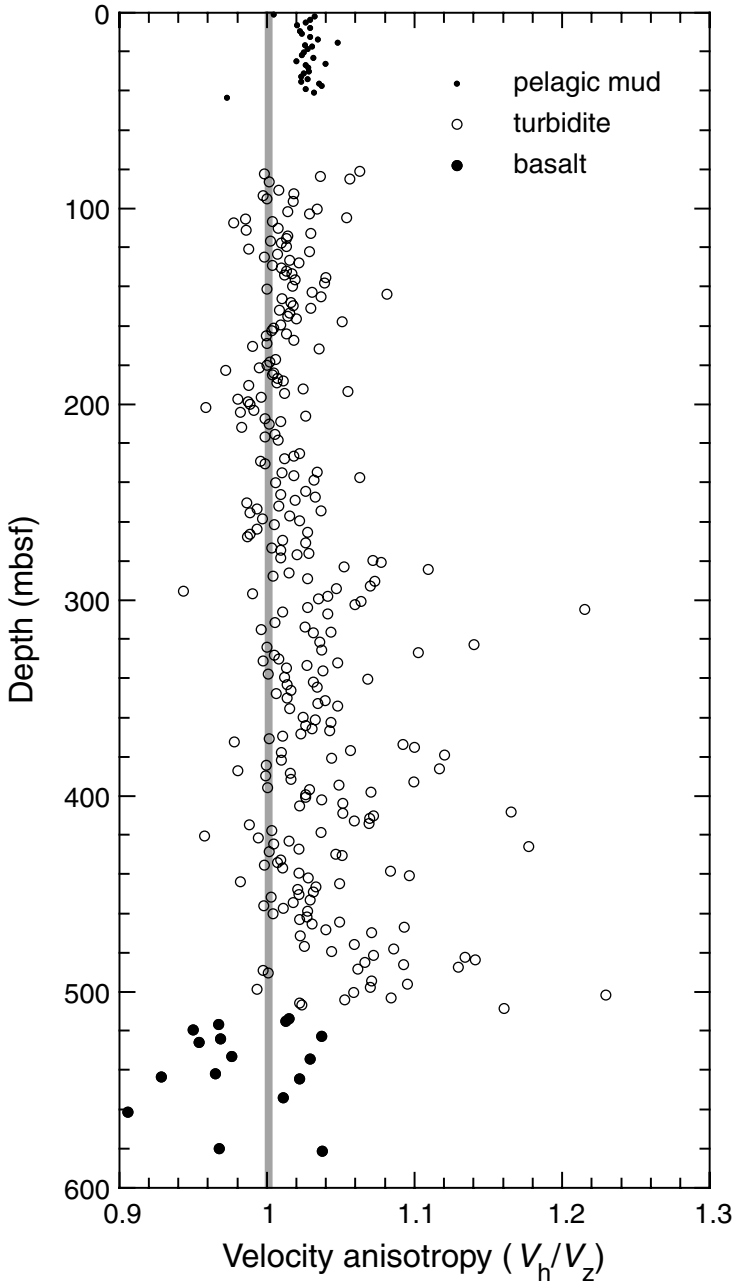

Figure F78. Peak shear strength measured in the pelagic muds for Holes 1201A and 1201B using the vane shear apparatus.

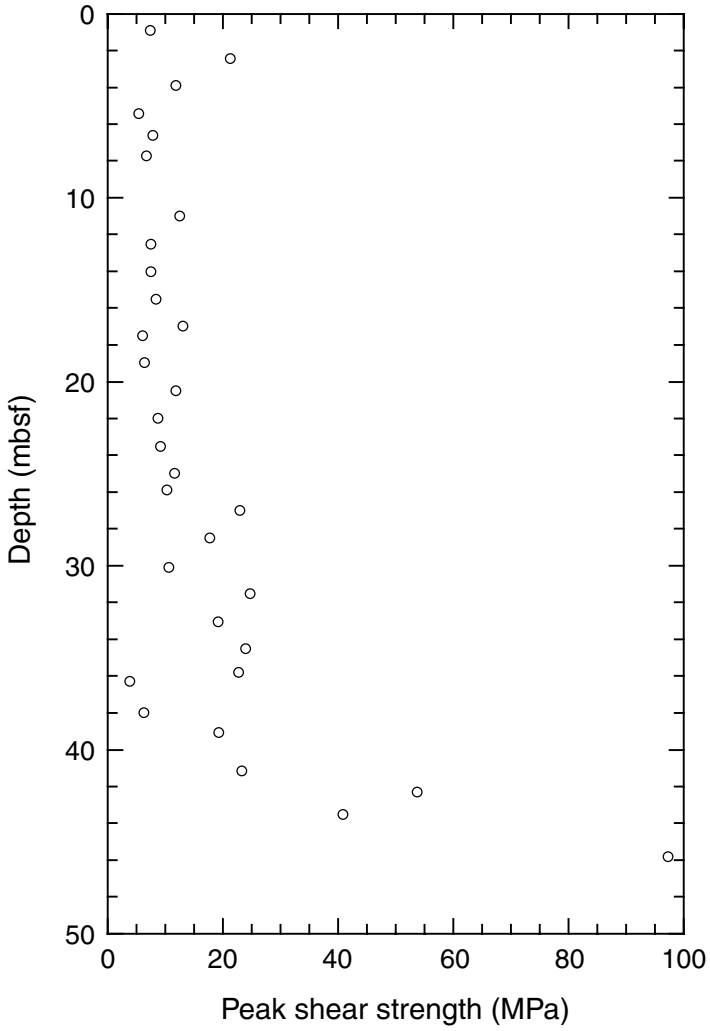

Figure F79. A. Formation factor for Holes 1201A and 1201B, determined from apparent resistivity measurements, assuming seawater as the pore fluid. **B.** Histogram of calculated formation factors. These values exhibit significant scatter, especially at depths greater than ~20 mbsf, about a mean of 2.62.

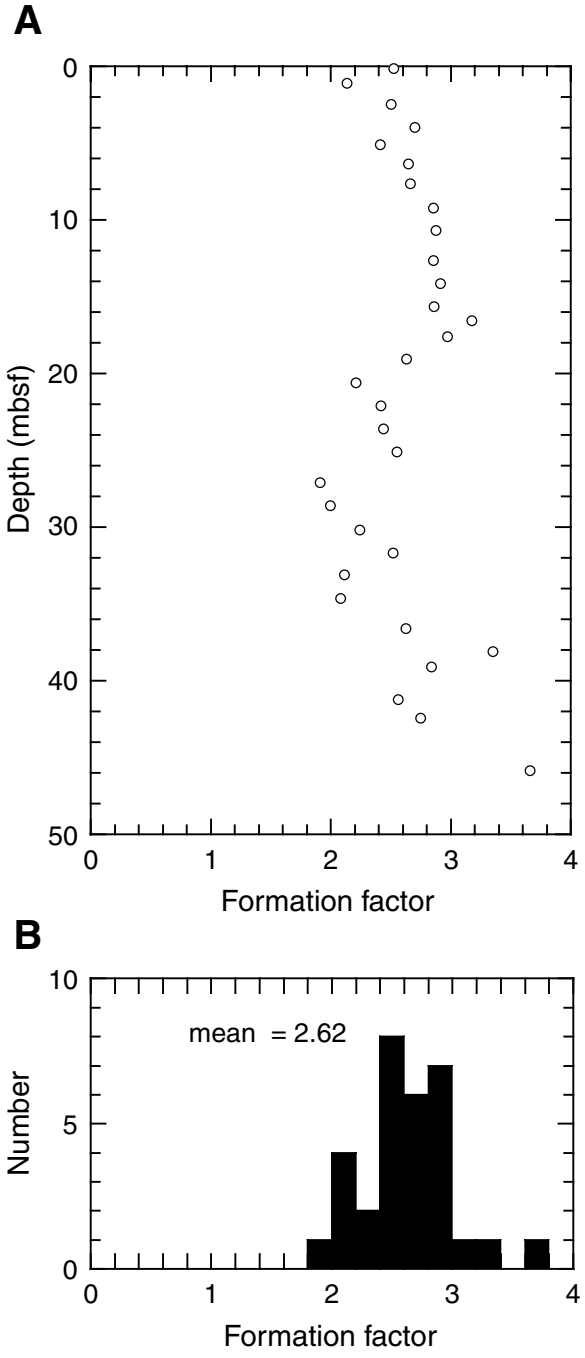

Figure F80. Thermal conductivities measured at Site 1201. The mean value measured in the muds = 0.79 W/(m·K), turbidites = 1.06 W/(m·K), and basalt = 1.58 W/(m·K).

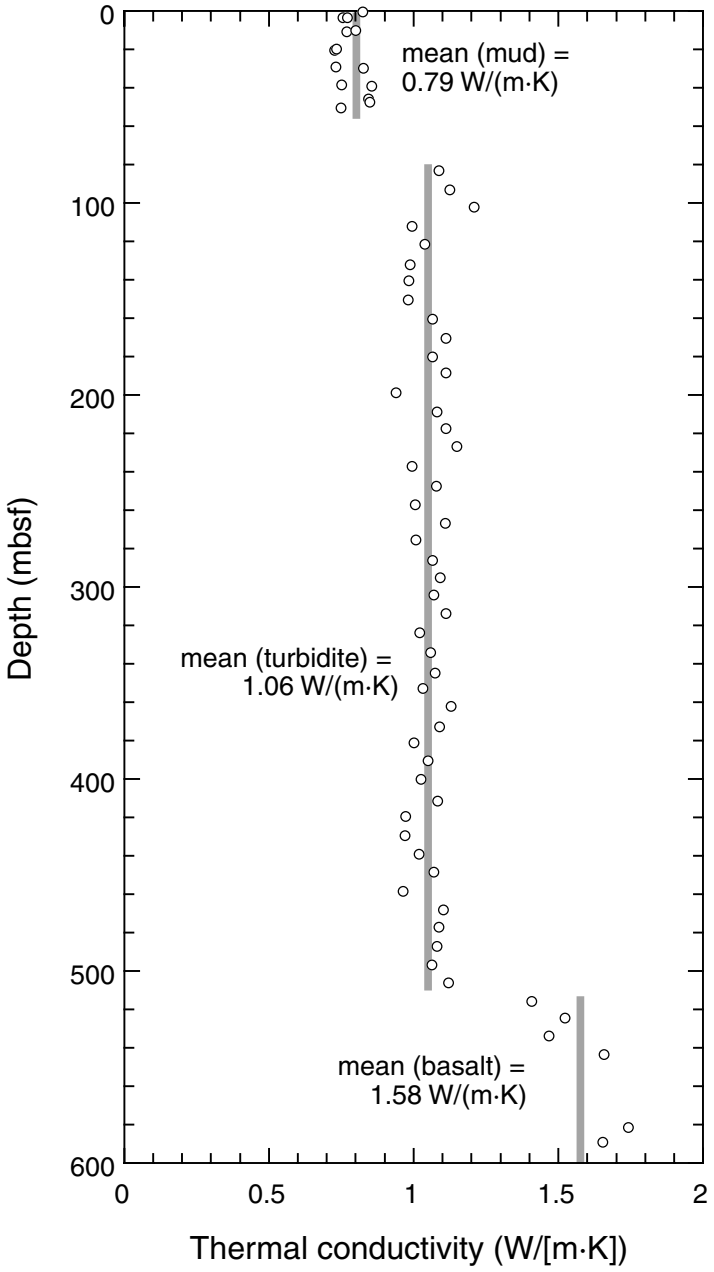

Figure F81. Temperature measurement in Hole 1201C at 44.6 mbsf. T_{ml} = mudline temperature, T_{sed} = sediment temperature.

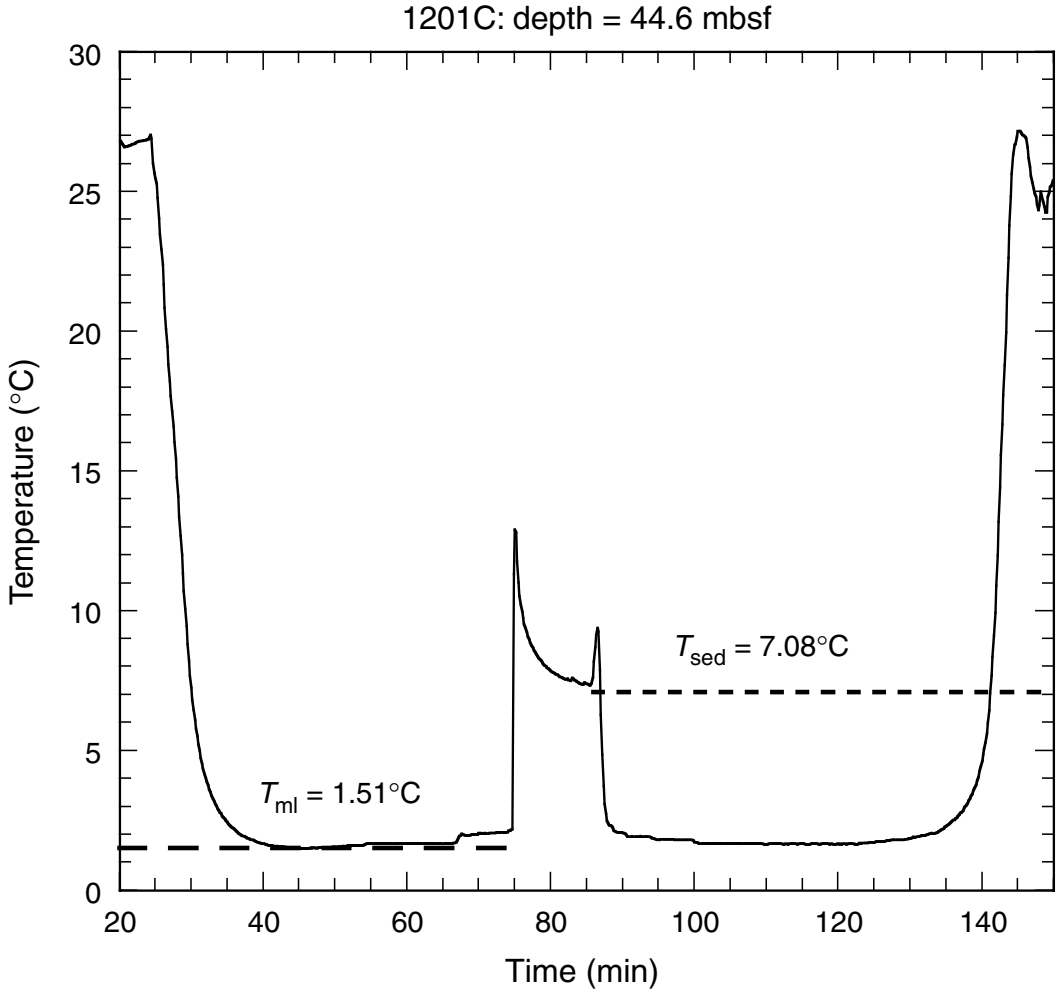

Figure F82. Logging operations summary diagram showing the intervals logged in Hole 1201D with the triple combo and FMS/sonic tool strings and the pipe and seafloor depths.

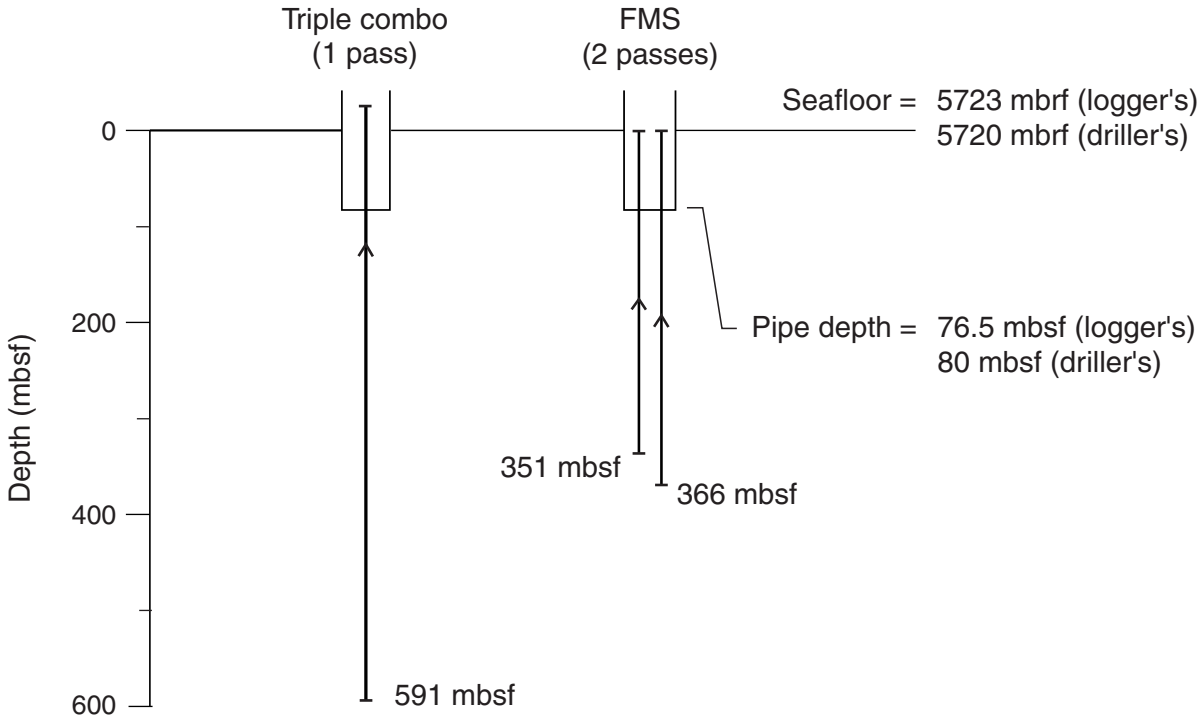

Figure F83. Summary of downhole logging results in Hole 1201D; caliper, total gamma ray emission, density, porosity, resistivity, and sonic velocity logs are shown. The depths of the pipe and the splice between the two uplogs are marked. * = spurious data or spikes (see **"Data Quality,"** p. 41, in "Downhole Measurements" and Table **T14,** p. 224, for further information). The logging units are marked, and coarser turbiditic beds a–d are highlighted. Laboratory physical properties measurements of the density, porosity, and sonic velocity of core material are also plotted along with the graphic lithology log based on core descriptions. In the graphic lithology log, c = clay, s = silt, s = sand, g = gravel.

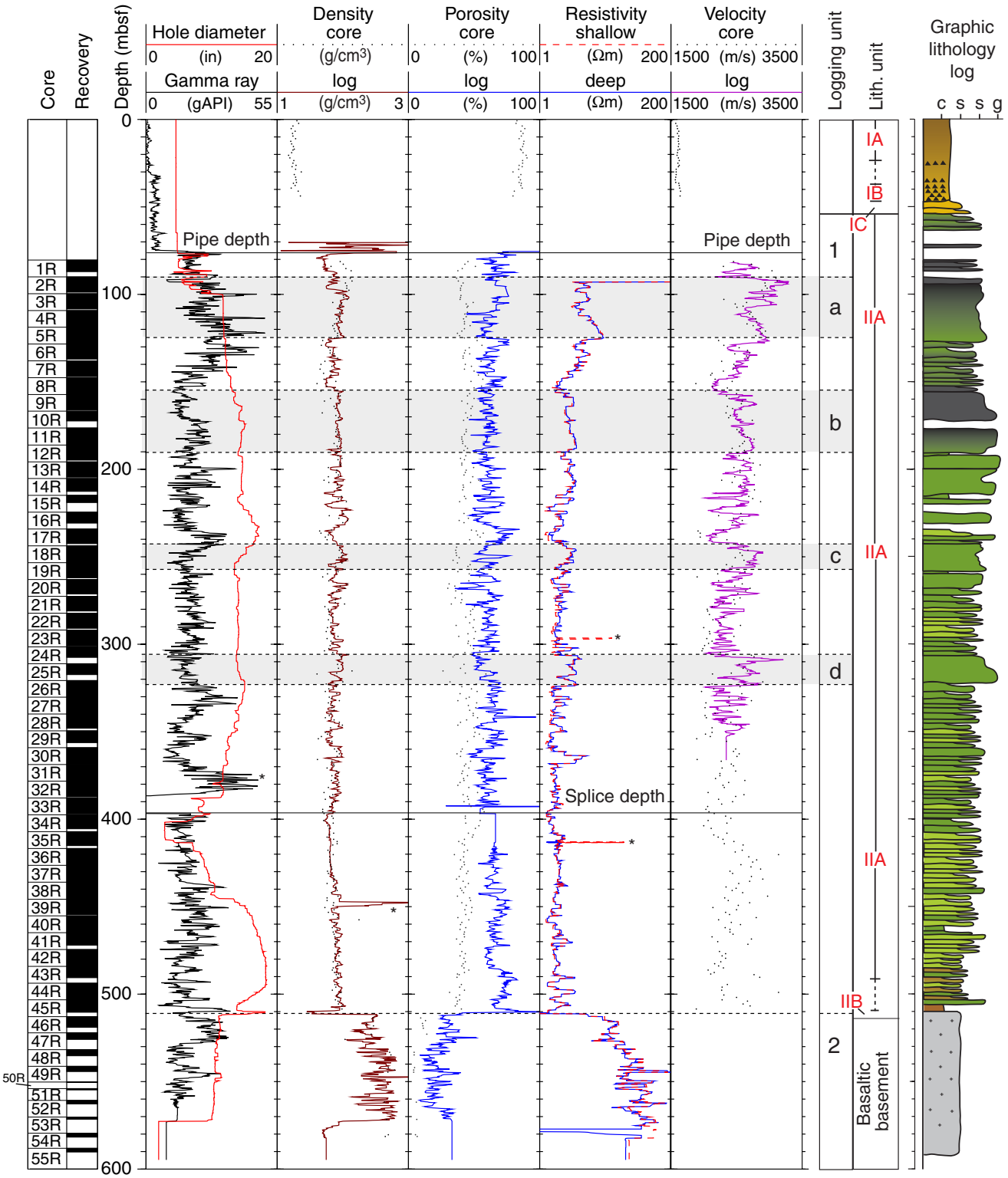

Figure F84. Summary of natural gamma ray logs in Hole 1201D; total gamma ray emission, potassium, thorium, uranium, and photoelectric effect (PEF) curves are displayed along with the graphic lithology log. The depths of the pipe and the splice between the two uplogs are marked. Logging units are marked, and coarser turbiditic beds a–d are highlighted. In the graphic lithology log, c = clay, s = silt, s = sand, g = gravel.

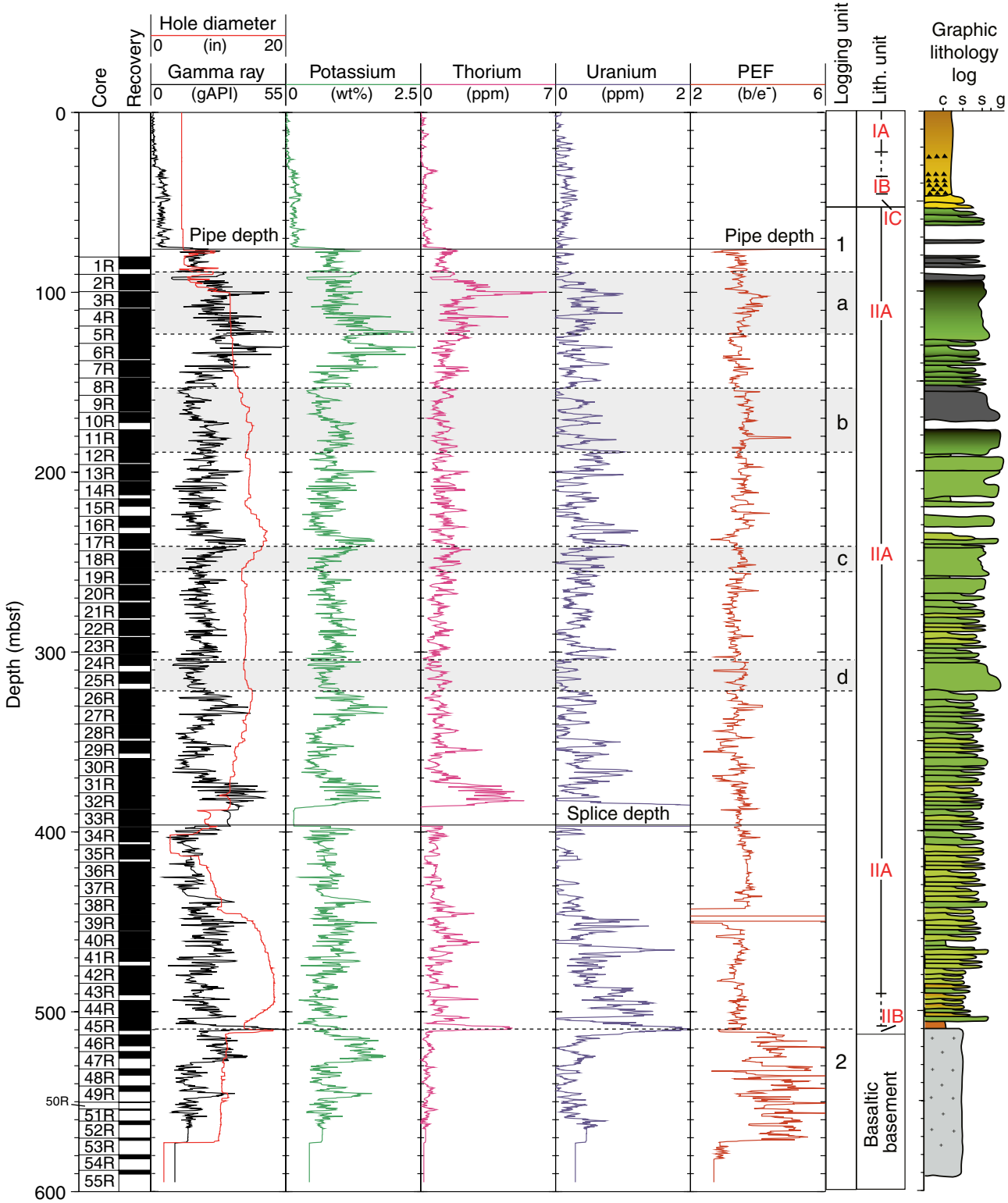

Figure F85. Static-normalized FMS images from a coarse turbidite-laminated claystone interval between 240 and 320 mbsf in Hole 1201D. The "spiky" and blocky features observed on the gamma ray curve are an artifact of the malfunctioning speed correction; c and d correspond to turbiditic intervals highlighted in Figure F84, p. 154.

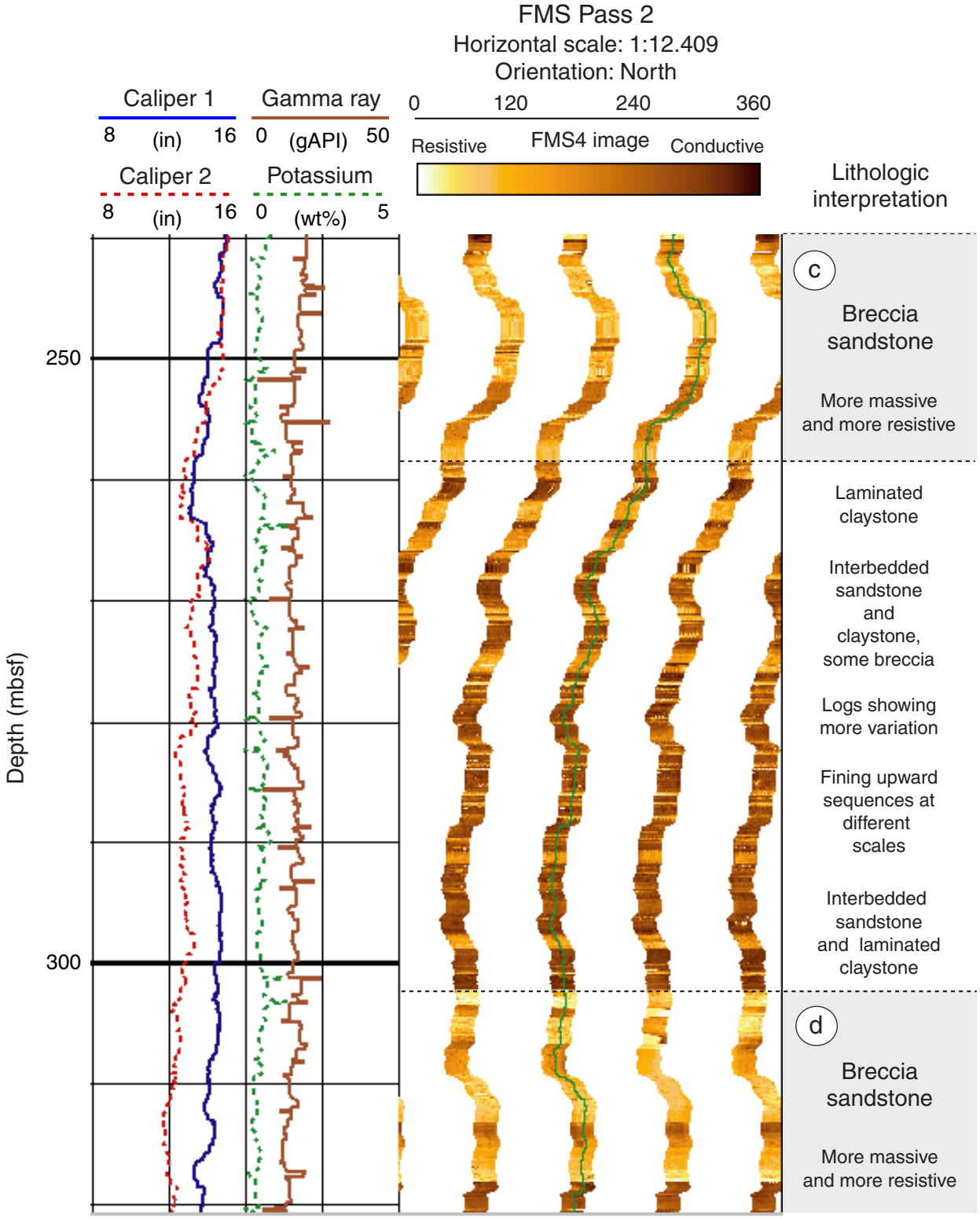

Figure F86. Pressure and temperature data obtained from the TAP tool in Hole 1201D plotted against elapsed time. The temperature and pressure variations reflect the different stages of lowering and raising of the tool within the hole (see "Temperature Log," p. 44, in "Downhole Measurements" for explanation).

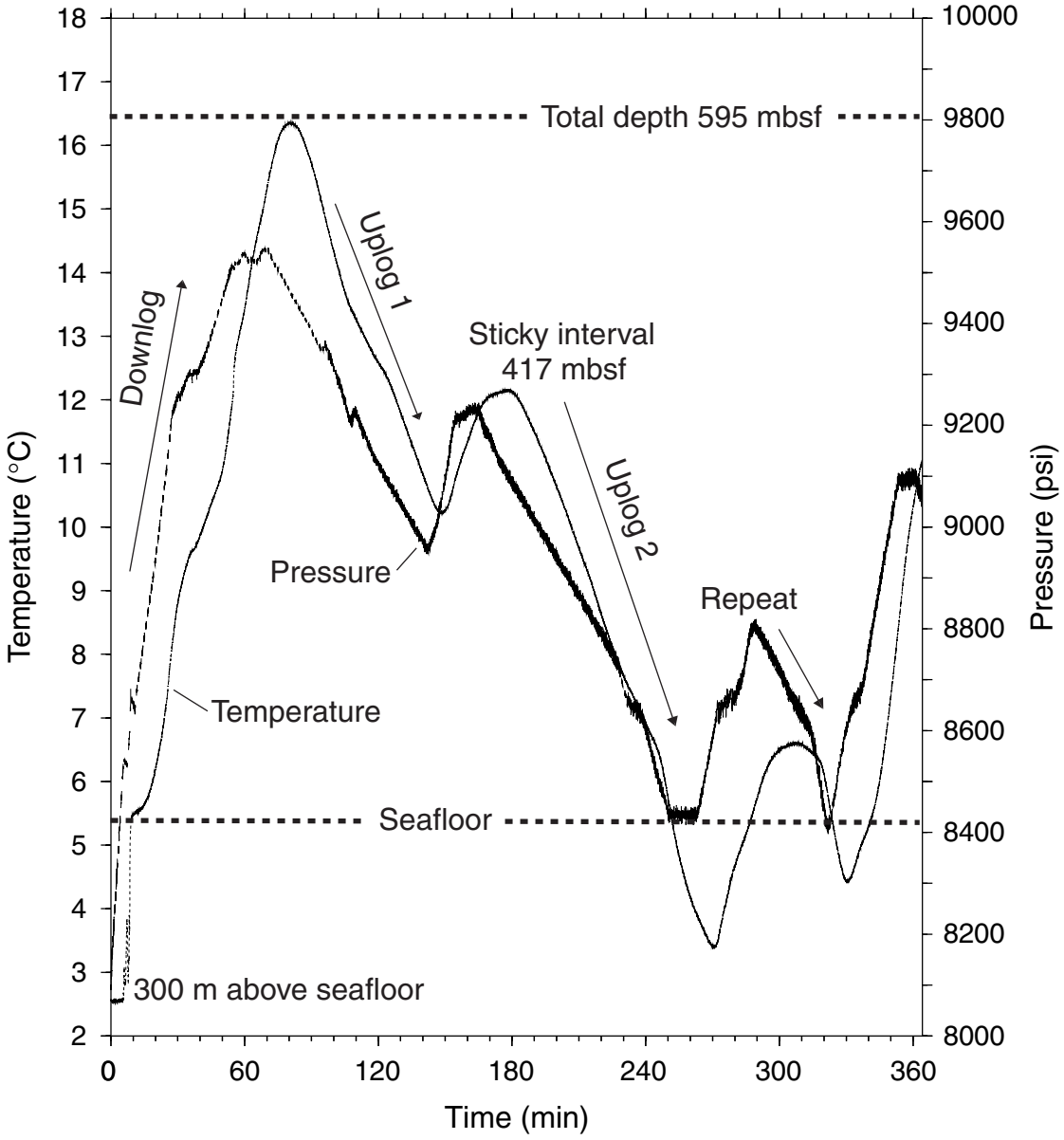

Figure F87. Location map of seismic station coverage in the Philippine Sea. Yellow circles = nearby land seismic stations, orange circles = current and proposed seafloor borehole observatories. INU = Inuyama, Japan; TJN = Taejon, Korea; ISG = Ishigakijima, Japan; BAG = Baguio, Philippines; DAV= Davao City, Philippines; JAY= Jayapura, Indonesia, GUMO = Guam, USA, MCSJ = Minami Torishima, Japan; OGS = Chichijima, Japan.

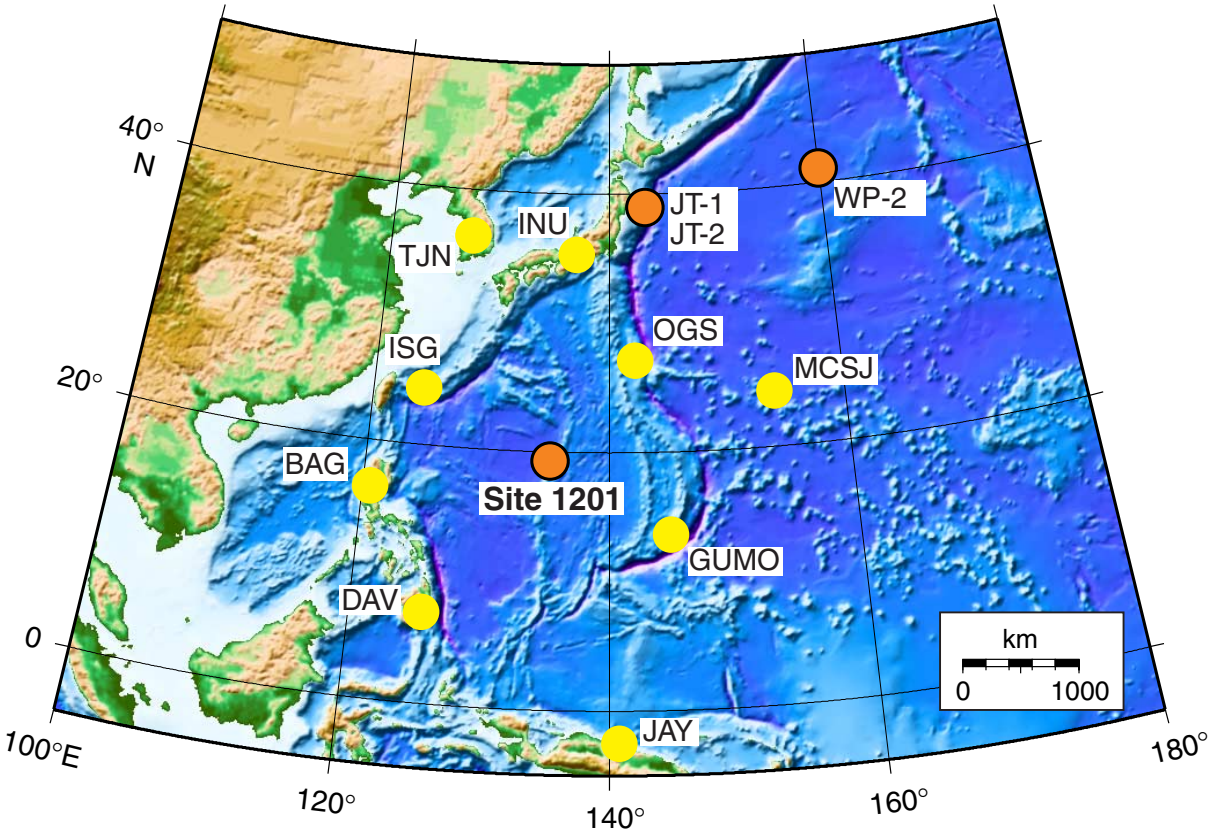

Figure F88. Location of the WP-1 seafloor borehole seismic observatory in relation to global seismicity. M = magnitude of earthquakes. A total of 1334 earthquakes that occurred from 1992 to 1996 with a magnitude of >5.5 are plotted. Hypocenters are located by the International Seismological Centre (ISC). Concentric circles indicate epicentral distances of 45°, 90°, and 135° from the WP-1 observatory. Because earthquakes with magnitudes >5.5 can be generally observed by many seismic stations in the world, >1000 earthquakes are expected to be observed by the WP-1 seafloor borehole seismic station in a 5-yr period.

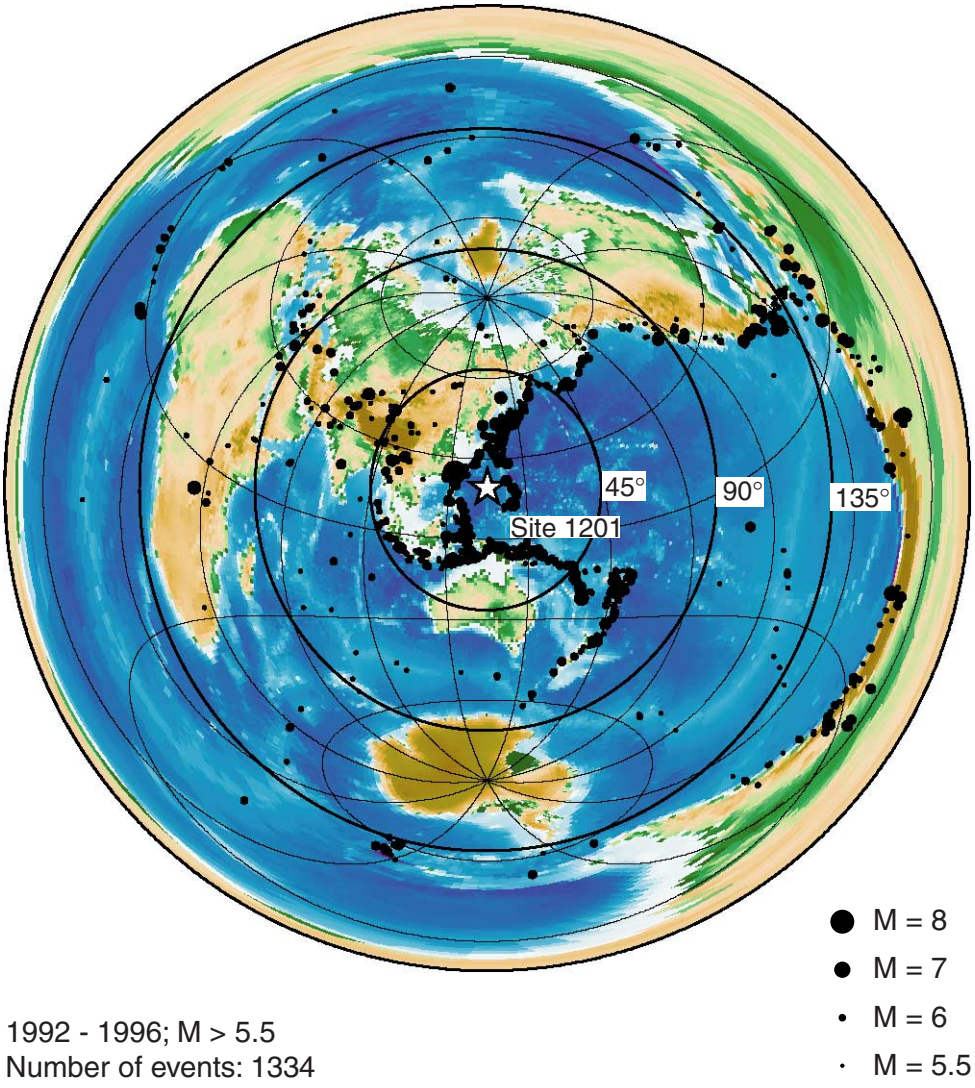

Figure F89. Schematic view of the NEREID-195 system of the WP-1 seafloor borehole seismological observatory. Two seismometers are cemented in the borehole, and the signals from seismometers are sent to the seafloor by separate cables. The data control unit (MEG-195) combines the data to one stream and sends it to the data recording unit (SAM-195). The power is supplied from lithium batteries housed in titanium spheres (LBU). The WP-1 observatory has two LBUs. ROV = remotely operated vehicle, SAM = storage acquisition module, PAT = power access terminal, MEG = multiple-access expandable gateway, BIA = borehole instrument assembly, HD = hard drive.

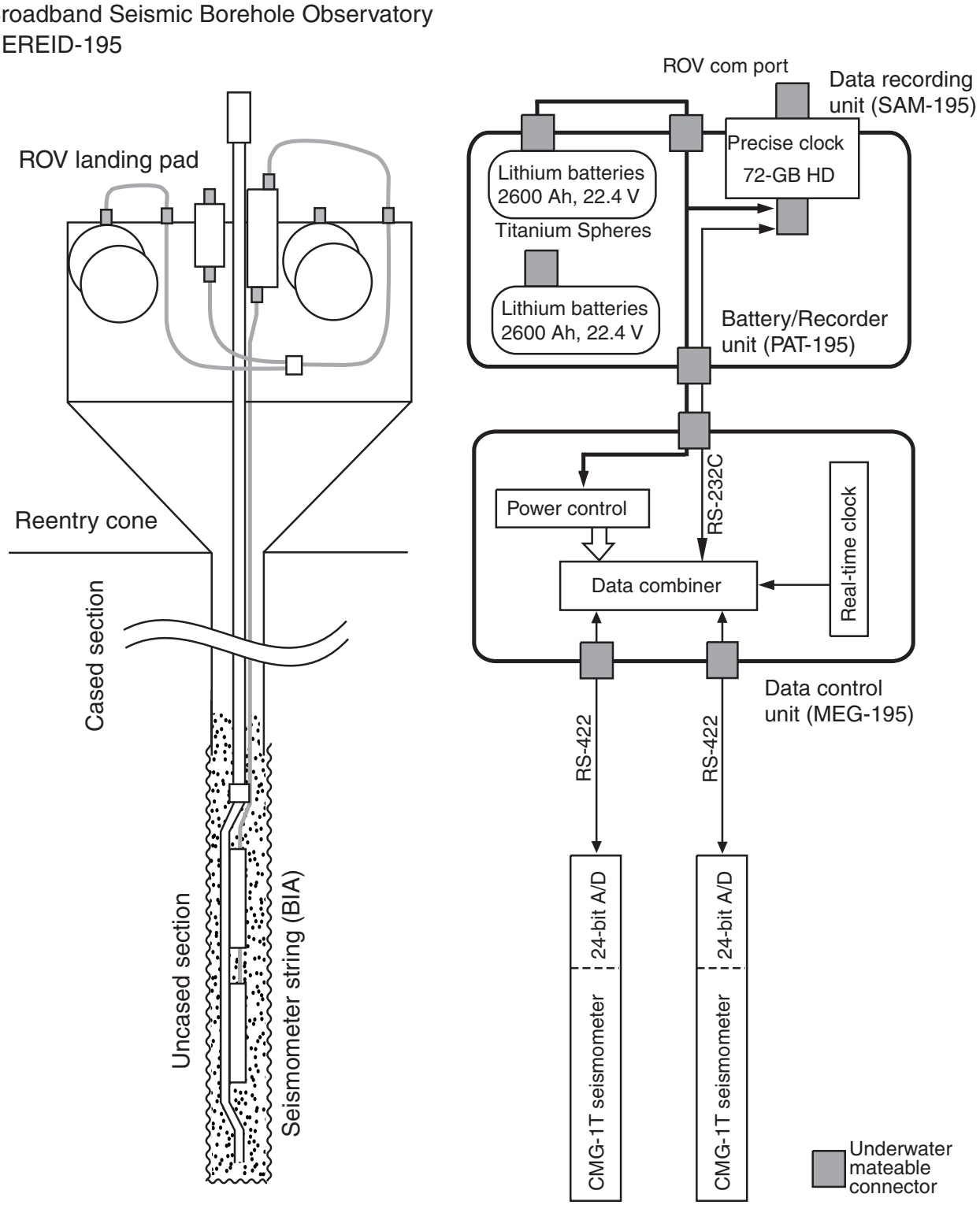

Figure F90. Borehole instrument assembly (BIA) installation schematic. The BIA hangs on a 4.5-in casing pipe, which in turn hangs on the riser hanger support just below the reentry cone. The cables from the sensors are strapped to the casing pipe with tie wraps and duct tape and protected by centralizers. Cement is pumped through the 4.5-in casing pipe and the BIA and out the bottom of the stinger. Cement is pumped to completely fill the open borehole and to extend into a lower part of the 10.75-in casing. The sensors are thus strongly coupled to the bare rock. PAT = power access terminal. MEG = multiple-access expandable gateway, ROV = remotely operated vehicle.

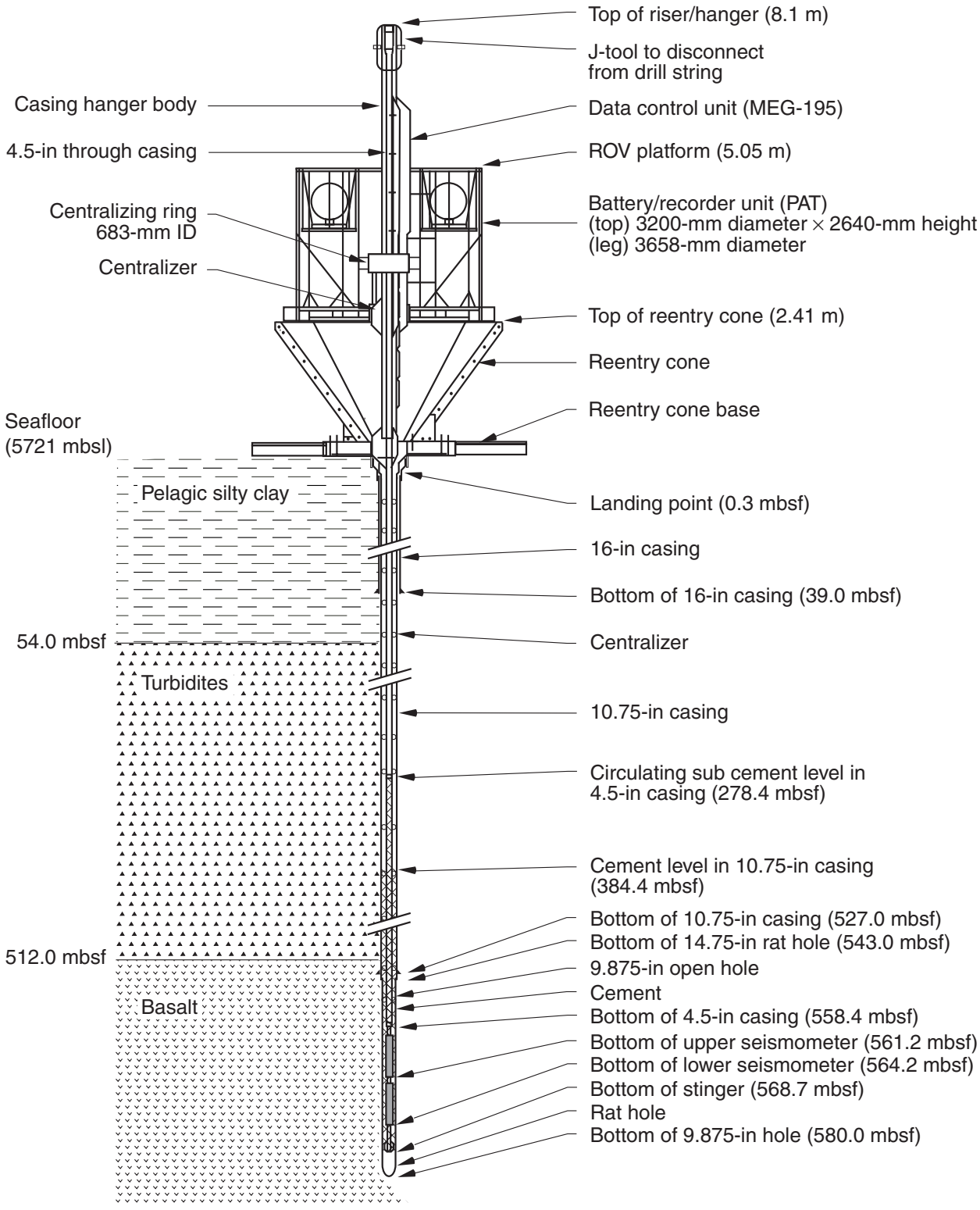

Figure F91. Cable strappings and centralizer.

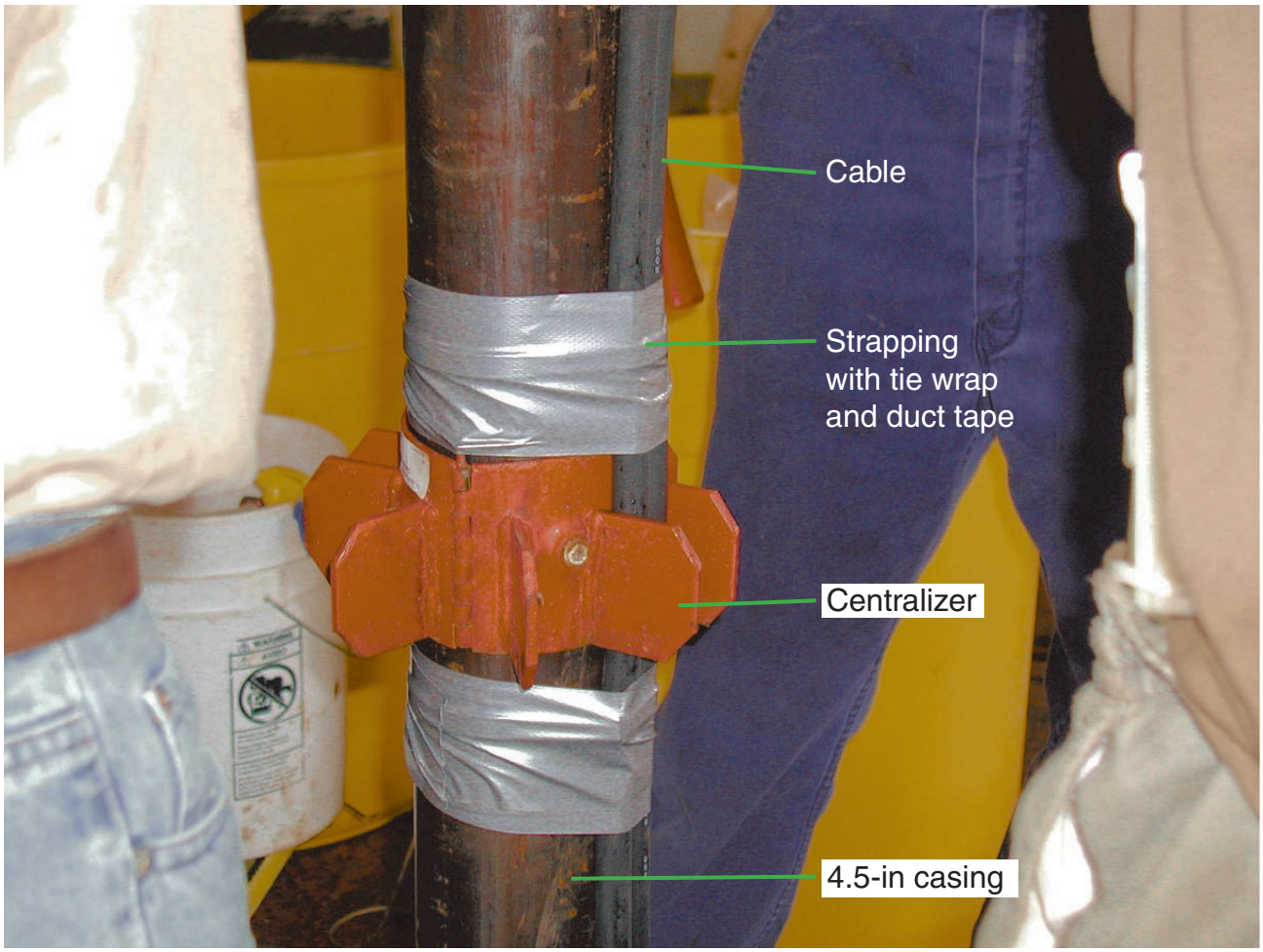

Figure F92. Borehole instrument assembly (BIA) with two ocean borehole seismometers (OBHs).

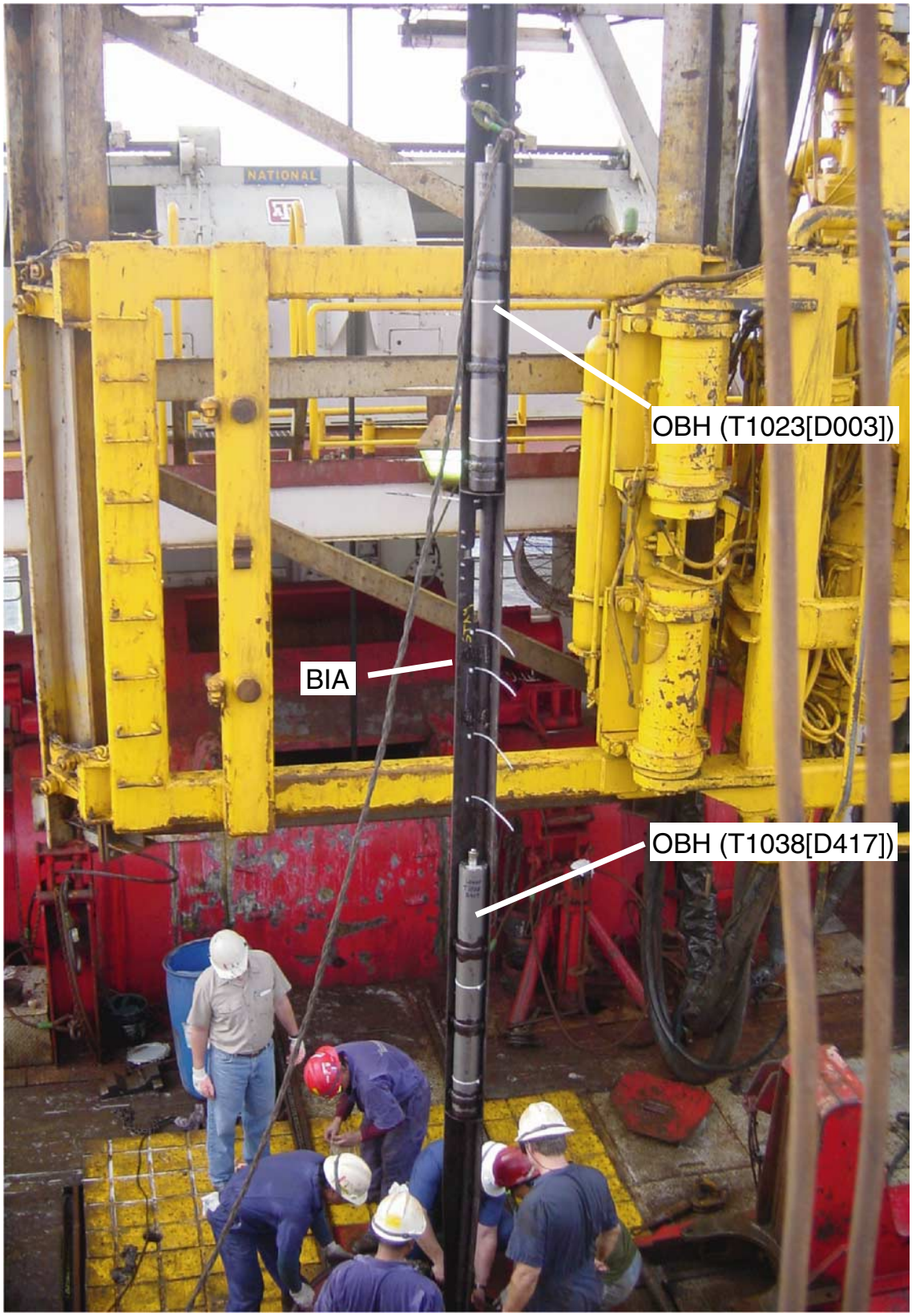

Figure F93. An ocean borehole seismometer (OBH) sensor was emplaced on the borehole instrument assembly (BIA) within the area enclosed by two blades. Note that the OBH is not electrically in contact with the BIA.

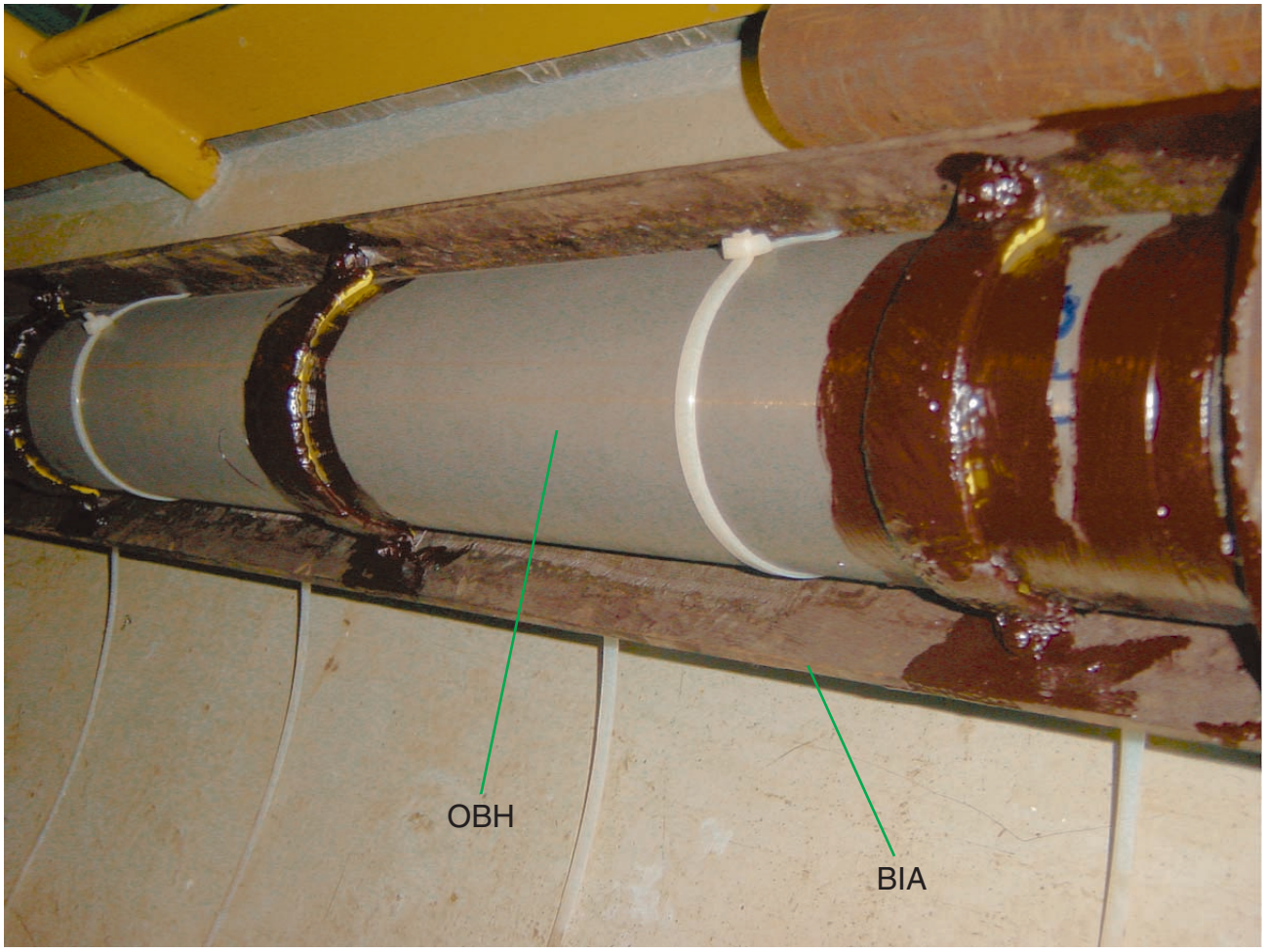

Figure F94. Borehole instrument assembly (BIA) with two ocean borehole seismometers (OBHs) is lowered to the sea.

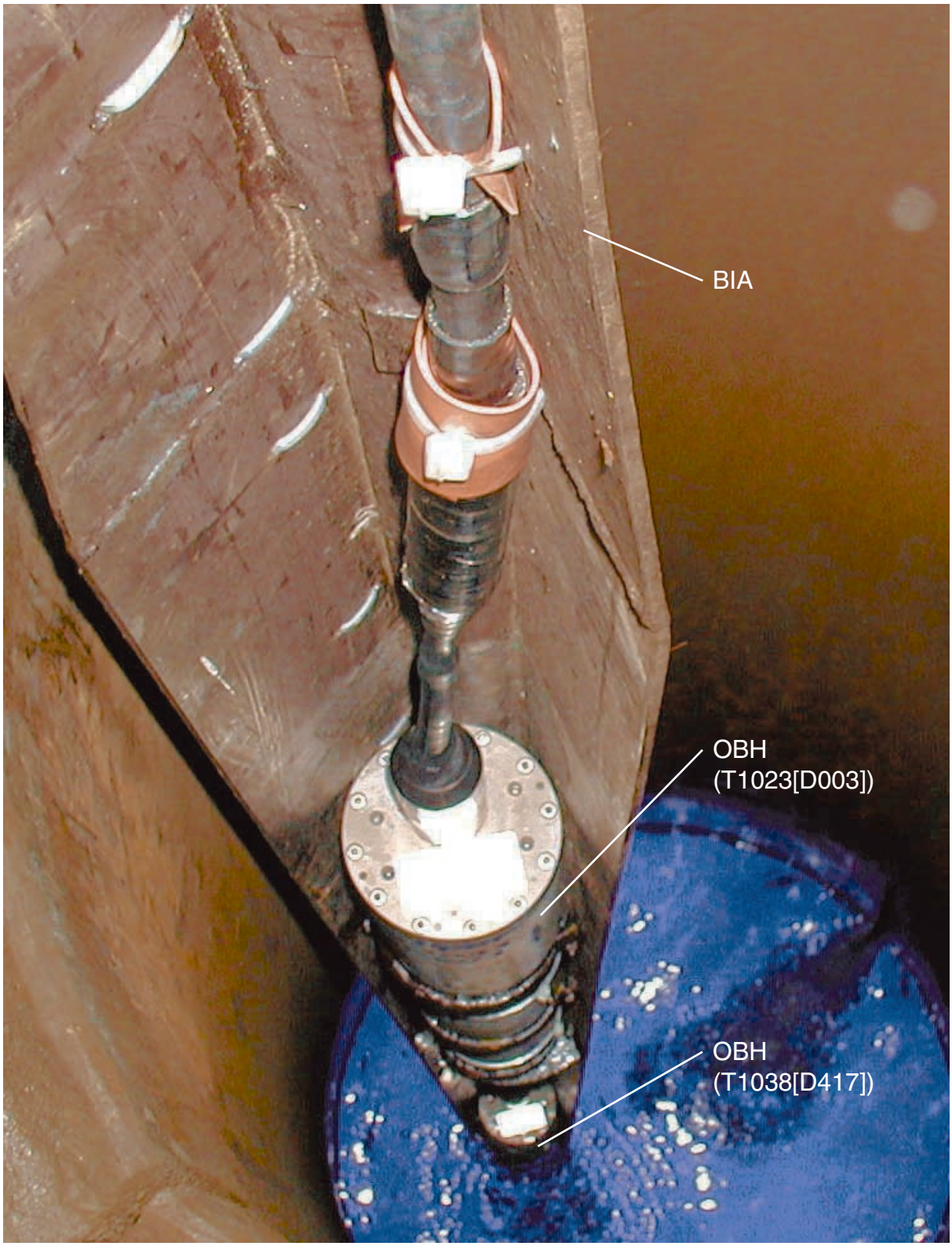

Figure F95. Drawing showing the components of the ocean borehole seismometer used for Leg 195 installation. The undersea connector on the top bulkhead is an eight-way SEACON titanium base connector. The digitizer electronics and sensor stack are connected by a cable to the miniature 26-way D-type connector on the top of the sensor stack. (Modified from Kanazawa, Sager, Escutia, et al., 2001.)

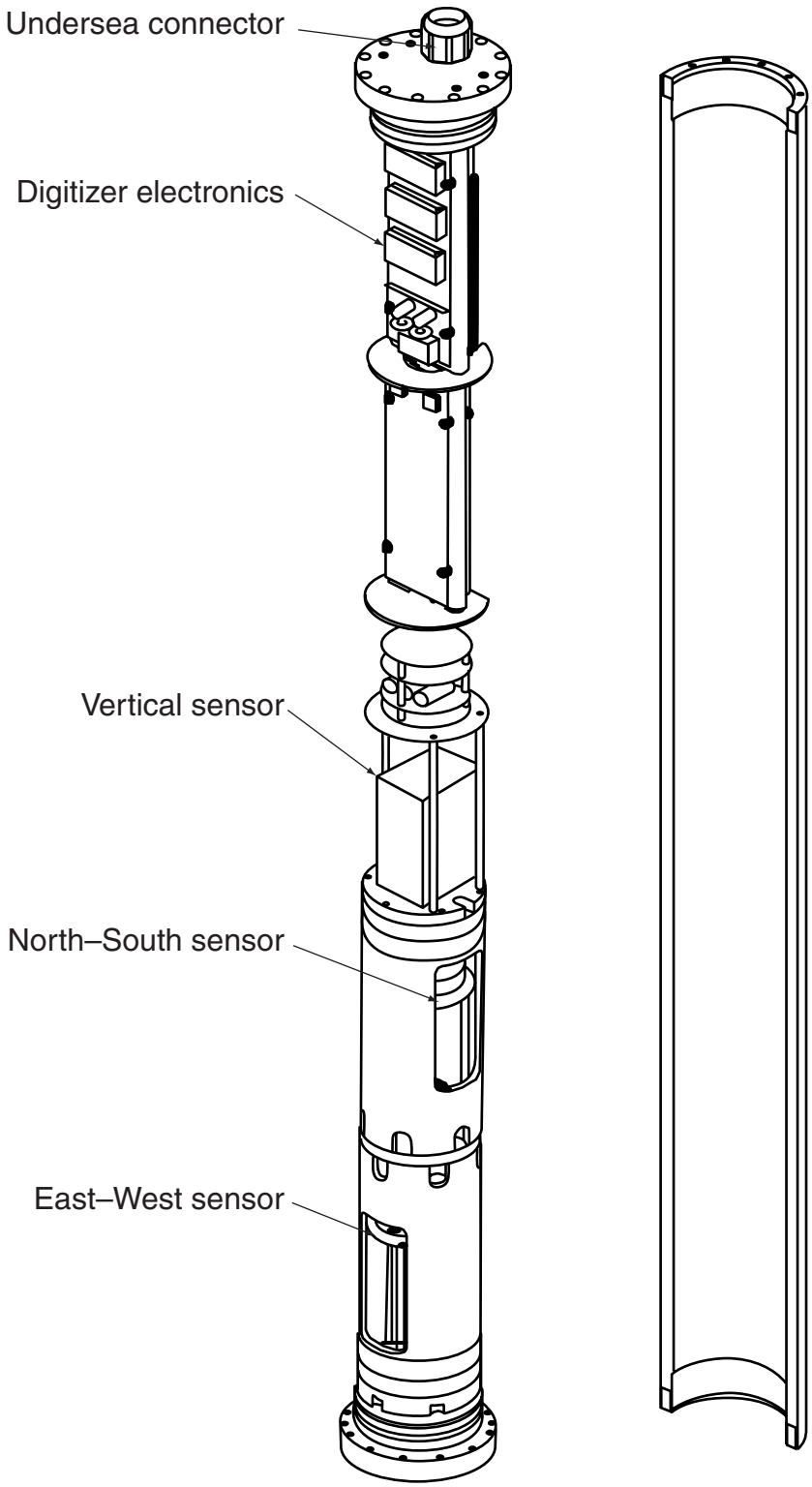

Figure F96. Spectra of the instrument ground and self-noise for the vertical and two horizontal components of each OBH deployed during Leg 195. The OBH self-noise curves were estimated by taking the incoherent power spectrum for ground-noise records of two adjacent OBHs deployed at Nokogiriyama vault in Chiba prefecture, Japan, on 30 January 2001. The increase of the 2-s period noise level is due to insufficient reduction of the large ground noise.

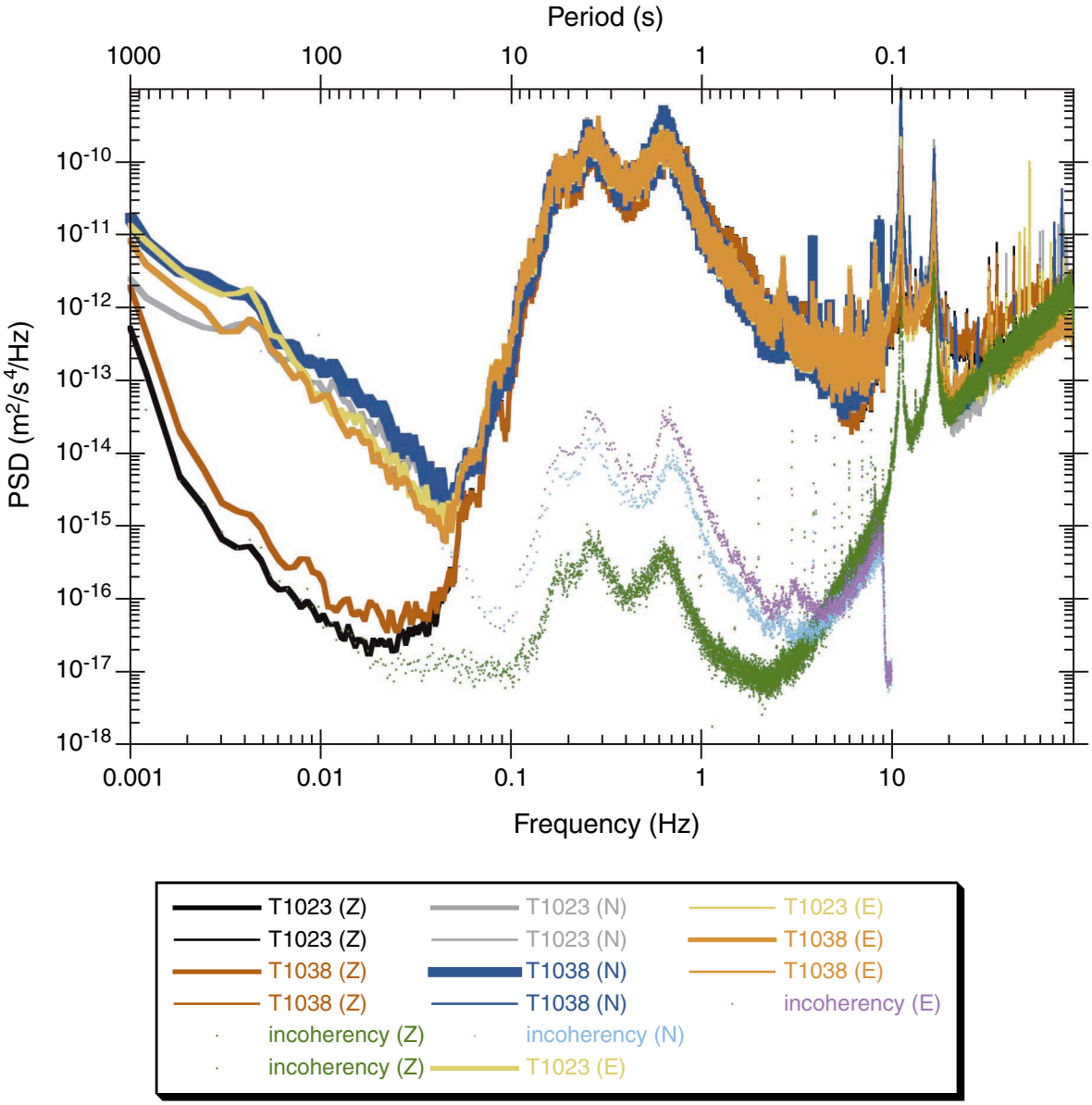

Figure F97. Cutaway drawing of the CMG-1T vertical sensor. The unit that appears in the drawing is mounted on a brass base, which holds the electronics circuit boards as well. (Modified from Kanazawa, Sager, Escutia, et al., 2001.)

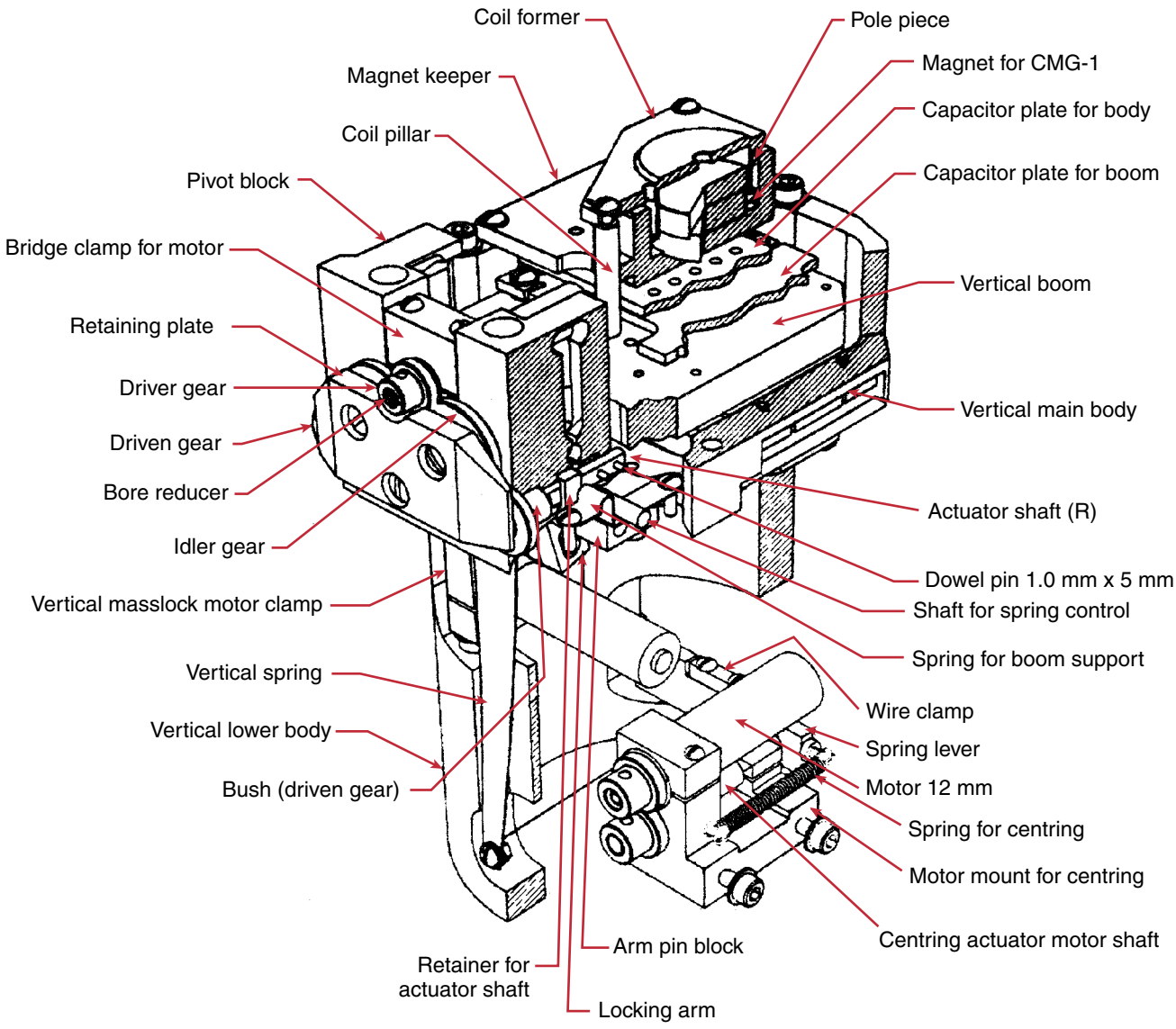

Figure F98. Schematic diagram for the electronic circuits of the CMG-1T sensors. The seismometer power and the state of health (SOH) circuitry are common for all sensors, whereas the other parts consist of separate units for each sensor. (Modified from Kanazawa, Sager, Escutia, et al., 2001.)

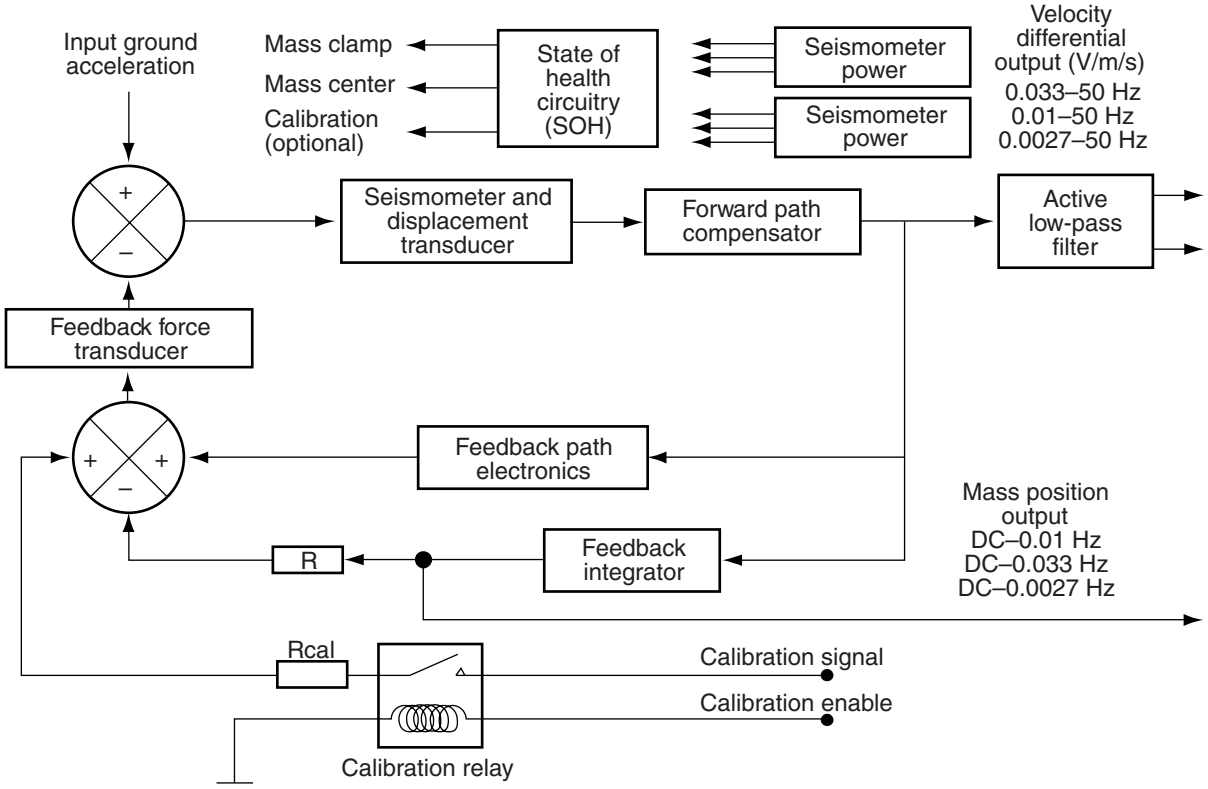

Figure F99. Ocean borehole seismometer (OBH) clock offset and drift to the MEG-195. Bold lines = offset, narrow lines = drift time. Broken lines = OBH (T1023), others = OBH (T1038). MEG = multiple-access expandable gateway, UTC = universal time coordinated.

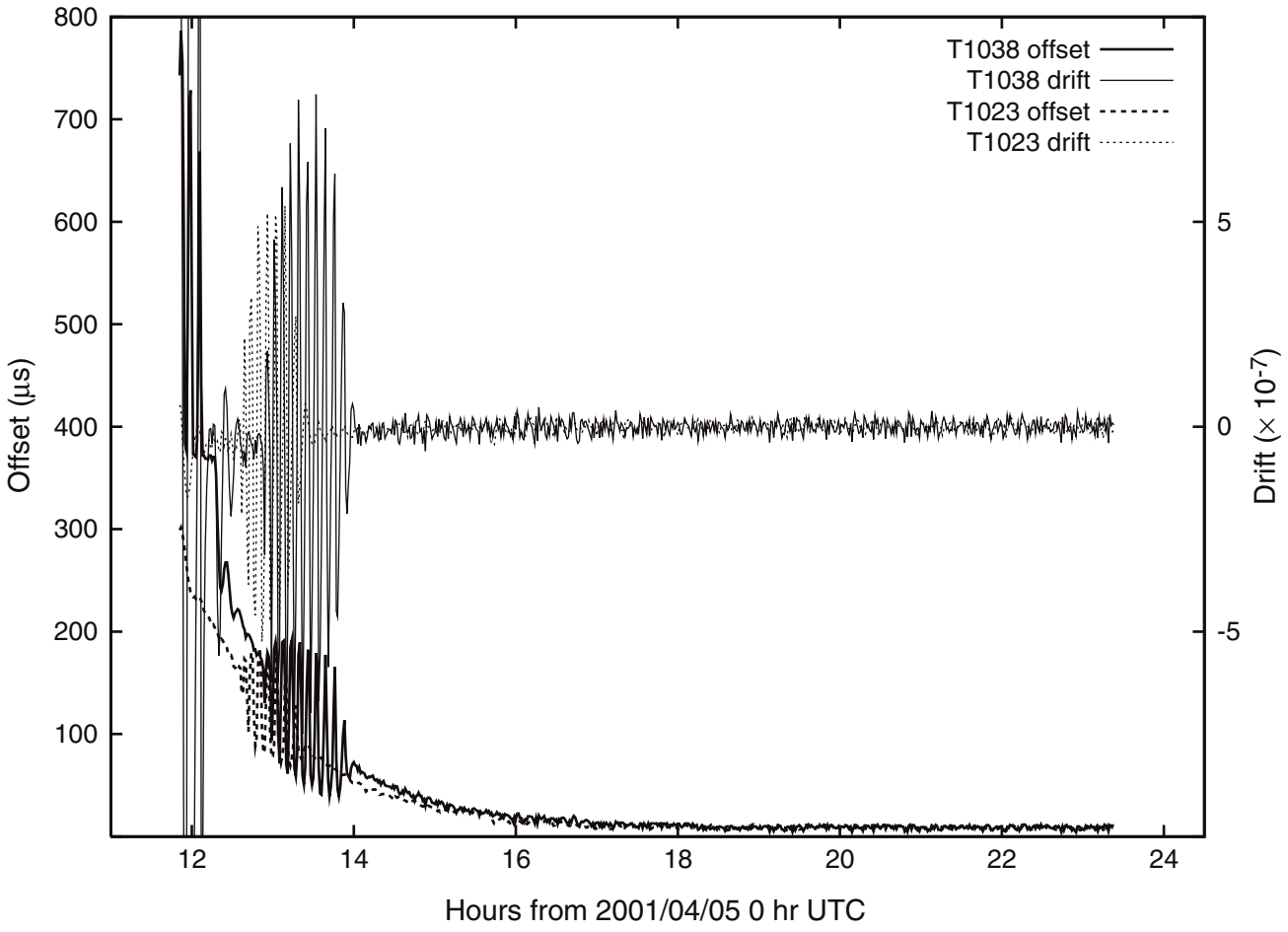

Figure F100. Schematic diagram of the DM24 digitizer. FPGA = field programmable gate array, DSP = digital signal processor, RAM = random access memory, GPS = Global Positioning System, UARTS = universal asynchronous receiver transmitters. (Modified from Kanazawa, Sager, Escutia, et al., 2001.)

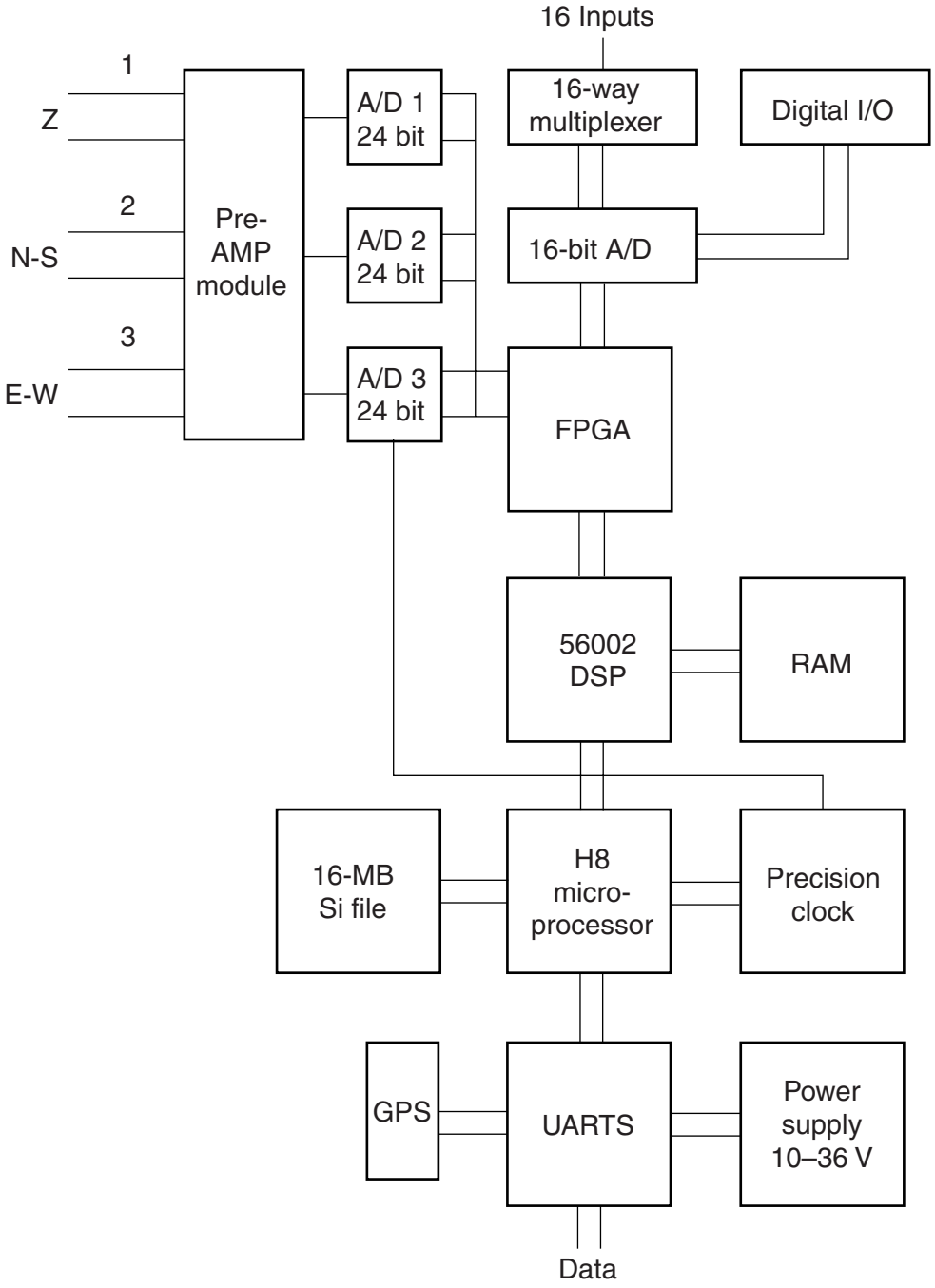

Figure F101. MEG-195 system block diagram. PDM = power distribution module, SAM = storage acquisition module, DC = direct current, LBU = lithium battery unit, MOS = metal oxide semiconductor, FET = field-effect transistor, CRM = combiner/repeater module, TTL = transistor-transistor logic, OBH = ocean borehole seismometer.

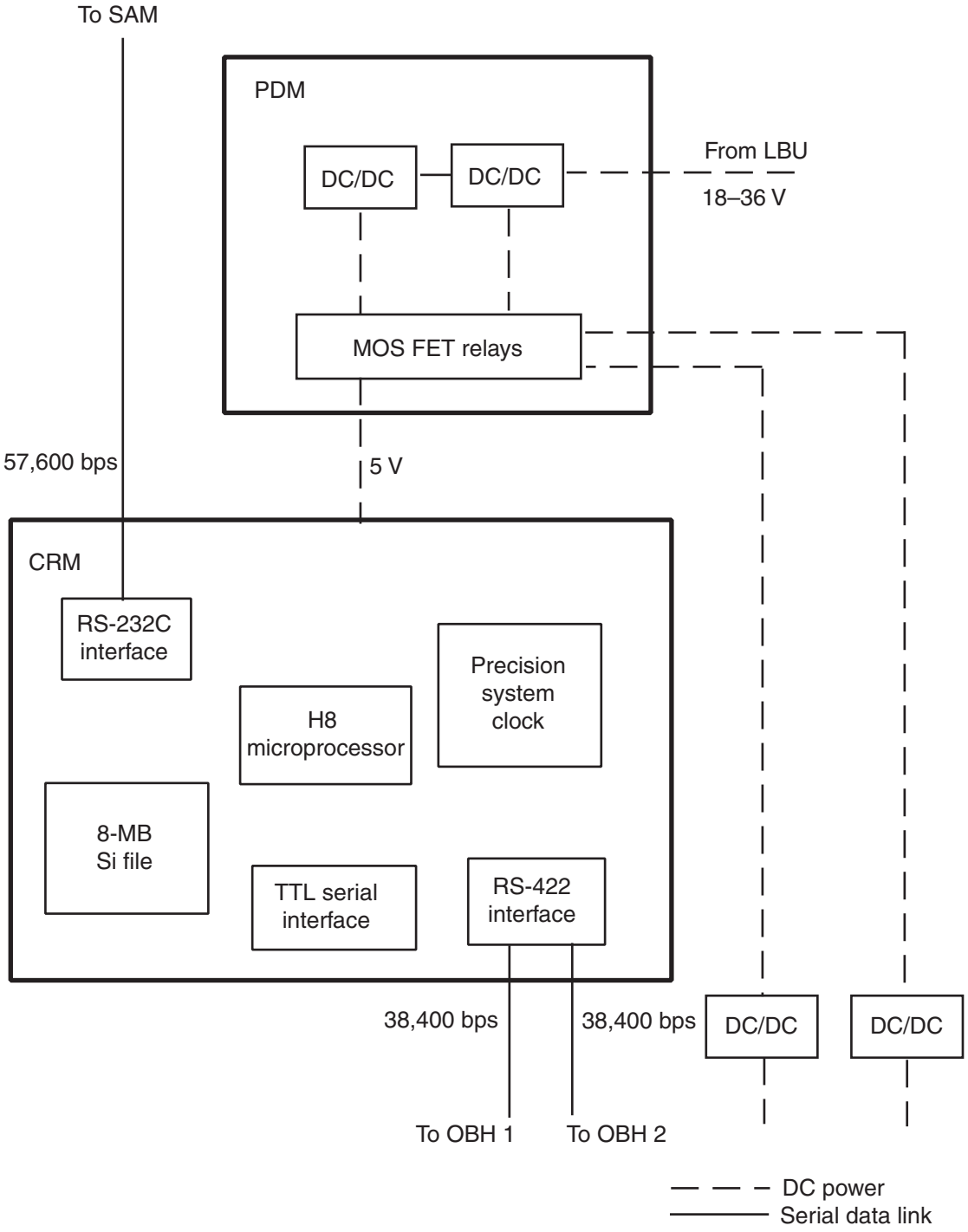

Figure F102. Photograph showing the MEG-195 vessel installed in the multiple-access expandable gateway (MEG) frame and the installation team (top left to right: M. Shinohara, T. Yamada, and K. Nakahigashi; bottom: E. Araki). UMC = underwater mateable connector.

Figure F103. Allocation of the underwater mateable connectors at the bottom of the multiple-access expandable gateway (MEG) vessel.

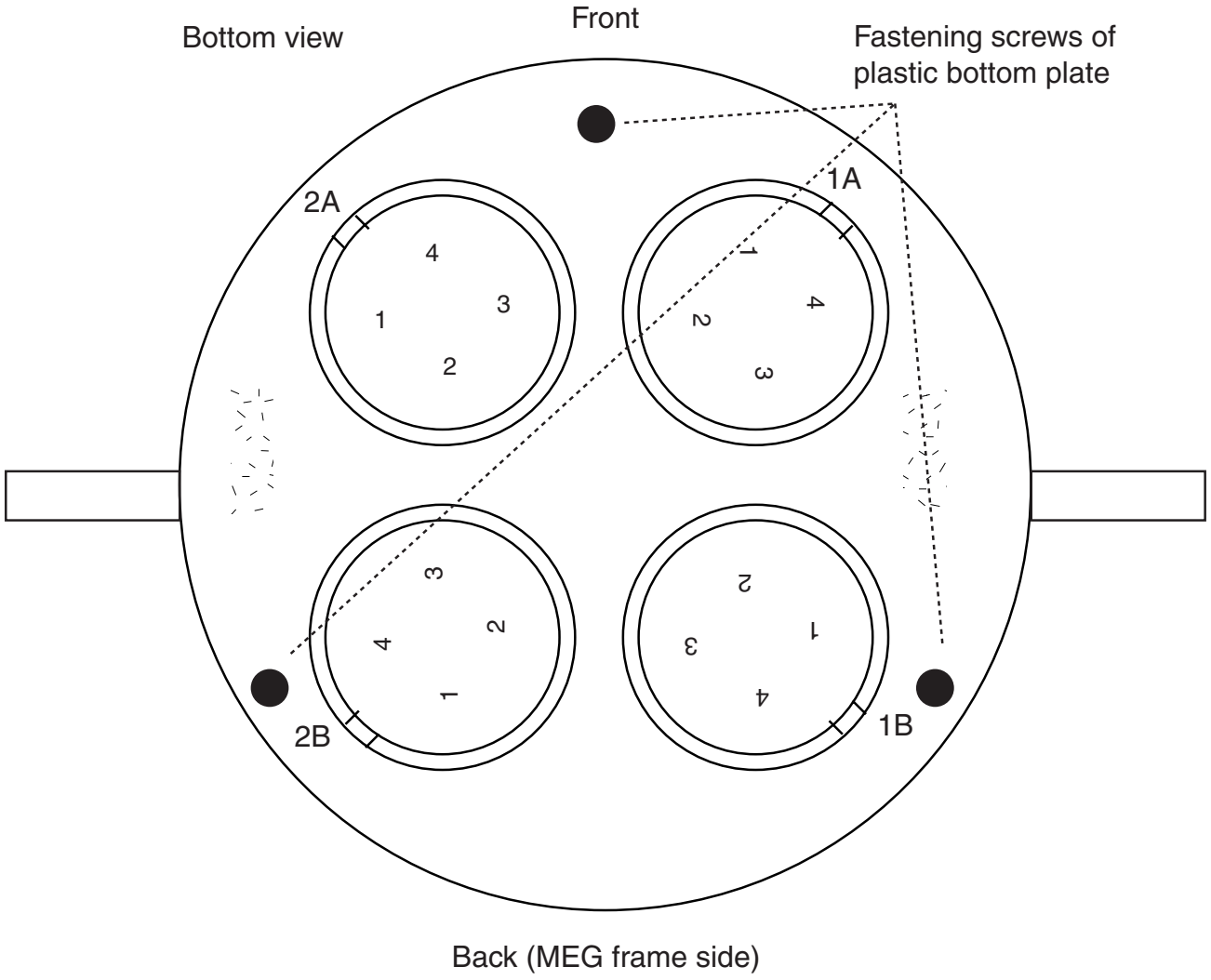

Figure F104. Example showing the results of the time difference measurement between the MEG-195 and the SAM-195. MEG = multiple-access expandable gateway, SAM = storage acquisition module, UTC = universal time coordinated.

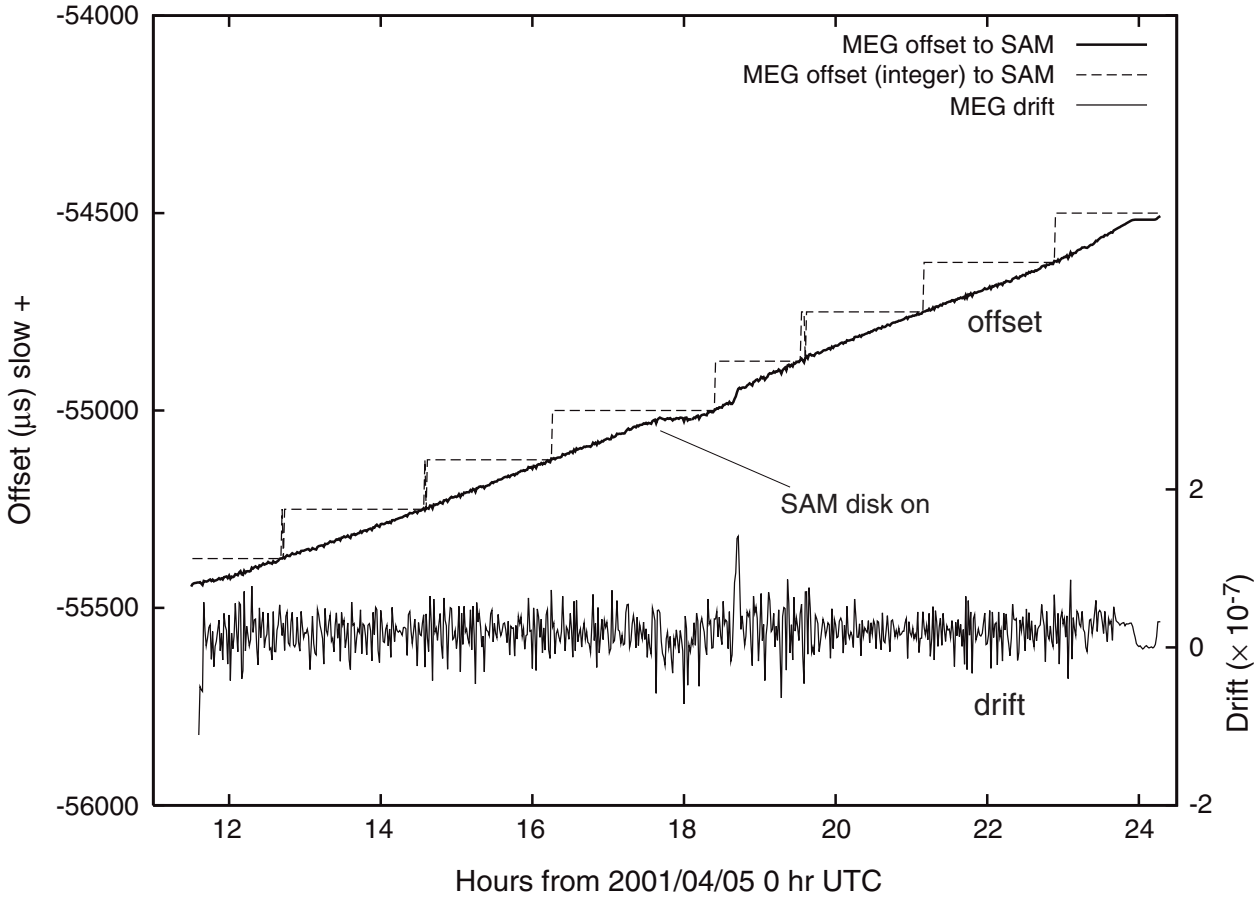

Figure F105. Diagram showing the usage of the flash memory in the SAM-195. UTC = universal time coordinated.

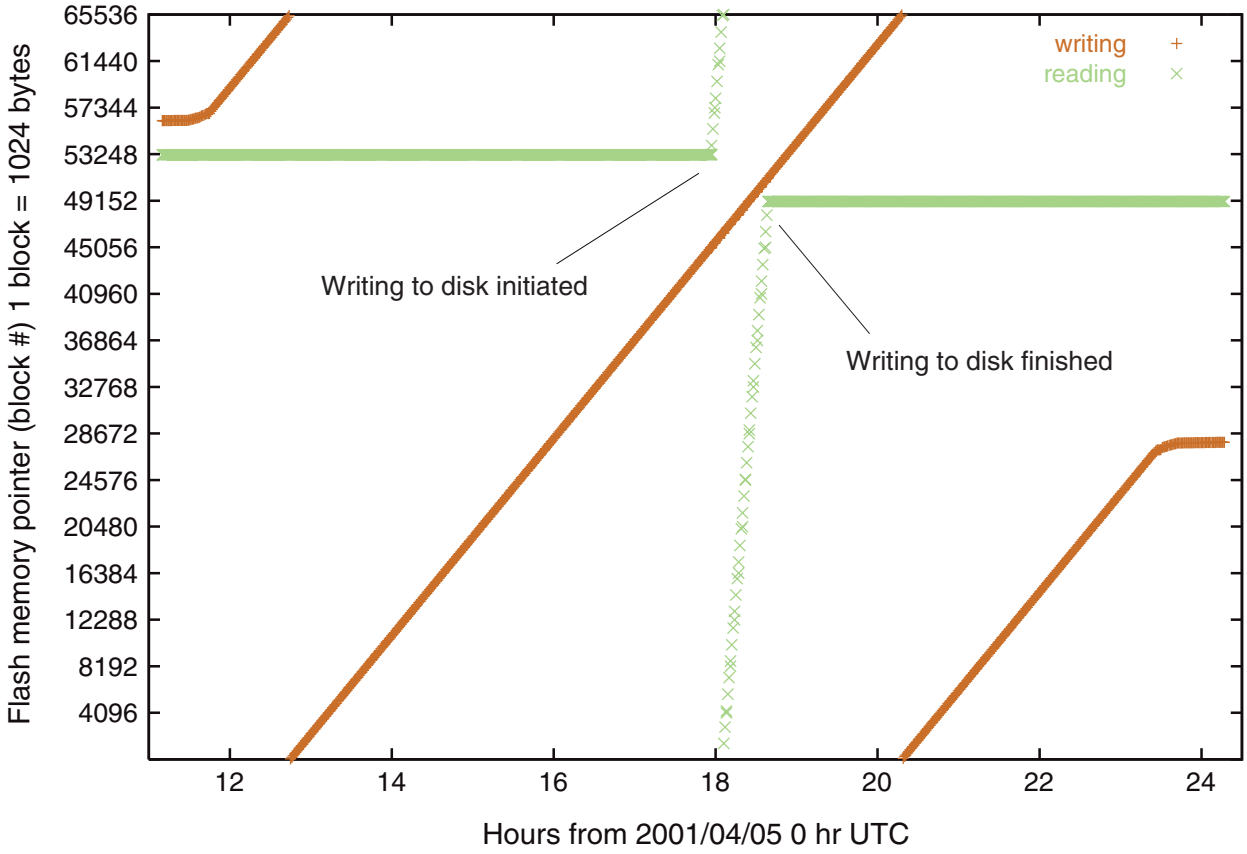

Figure F106. Temperature in the SAM-195 and the MEG-195 pressure vessels, measured in a ground temperature environment. SAM = storage acquisition module, MEG = multiple-access expandable gateway, UTC = universal time coordinated.

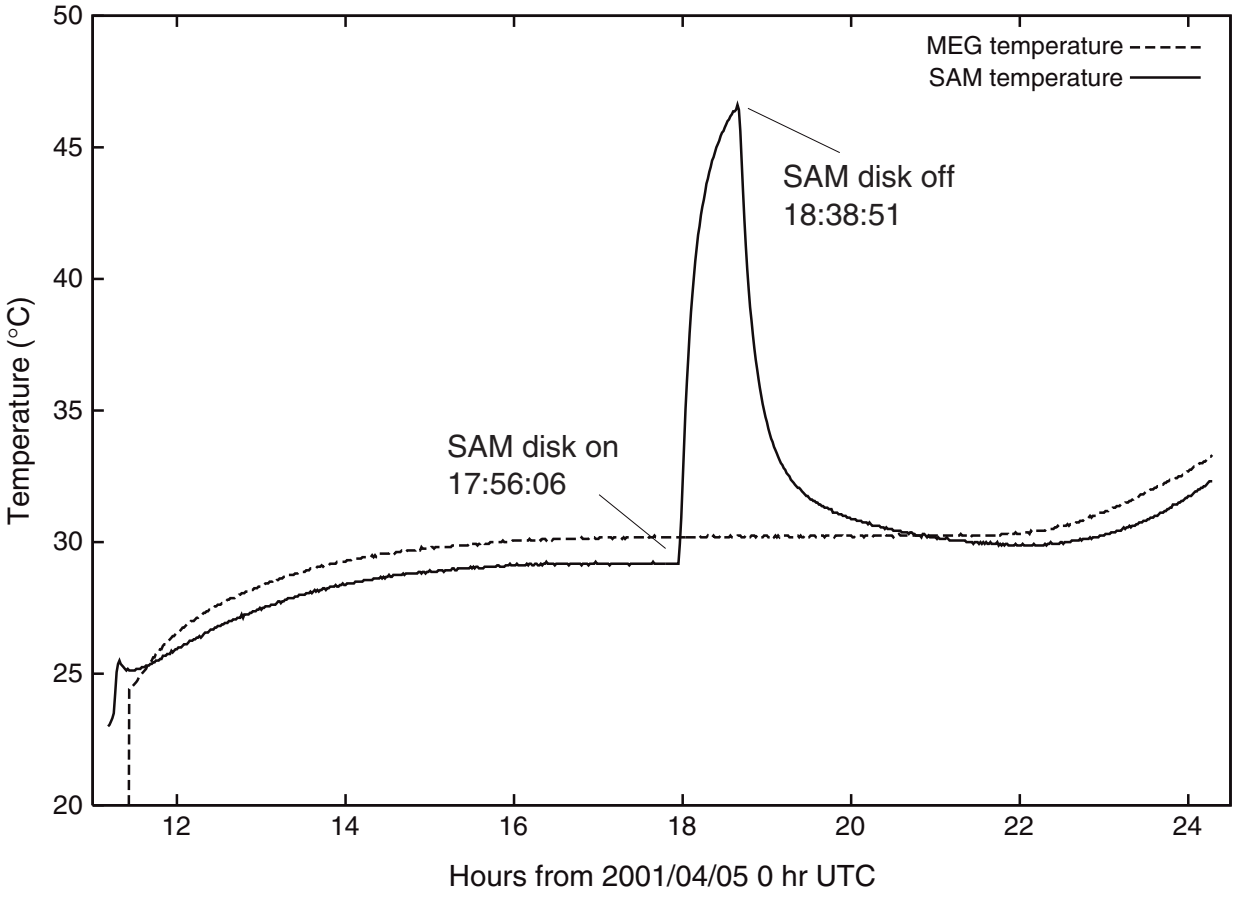

Figure F107. Supply voltage measured at the MEG-195 and the SAM-195. MEG = multiple-access expandable gateway, SAM = storage acquisition module, UTC = universal time coordinated.

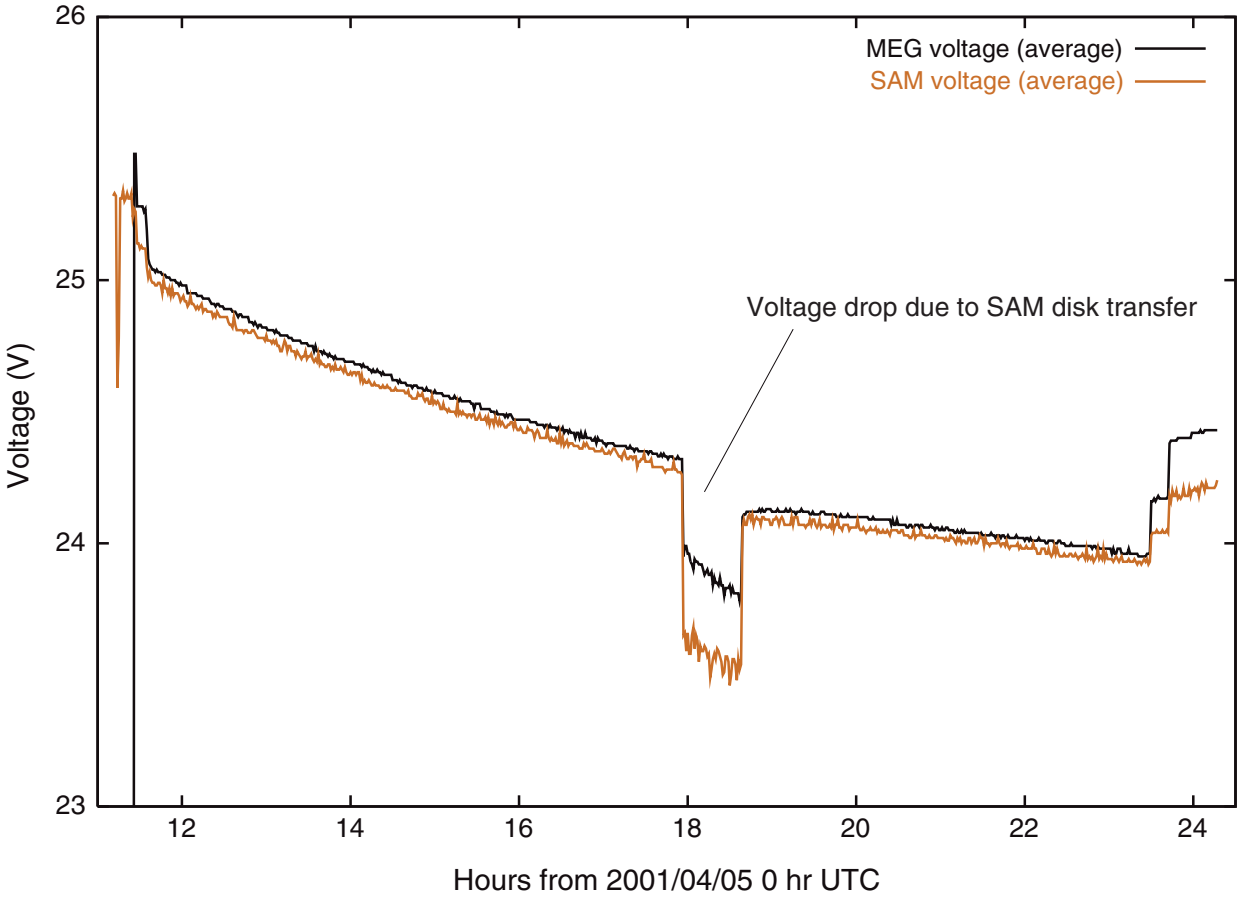

Figure F108. Inside structure of a manganese dioxide/lithium primary battery, Yuasa CL-1300L. Manganese dioxide and lithium are used as anode and cathode, respectively. Contents of the battery are hermetically sealed in a stainless steel canister.

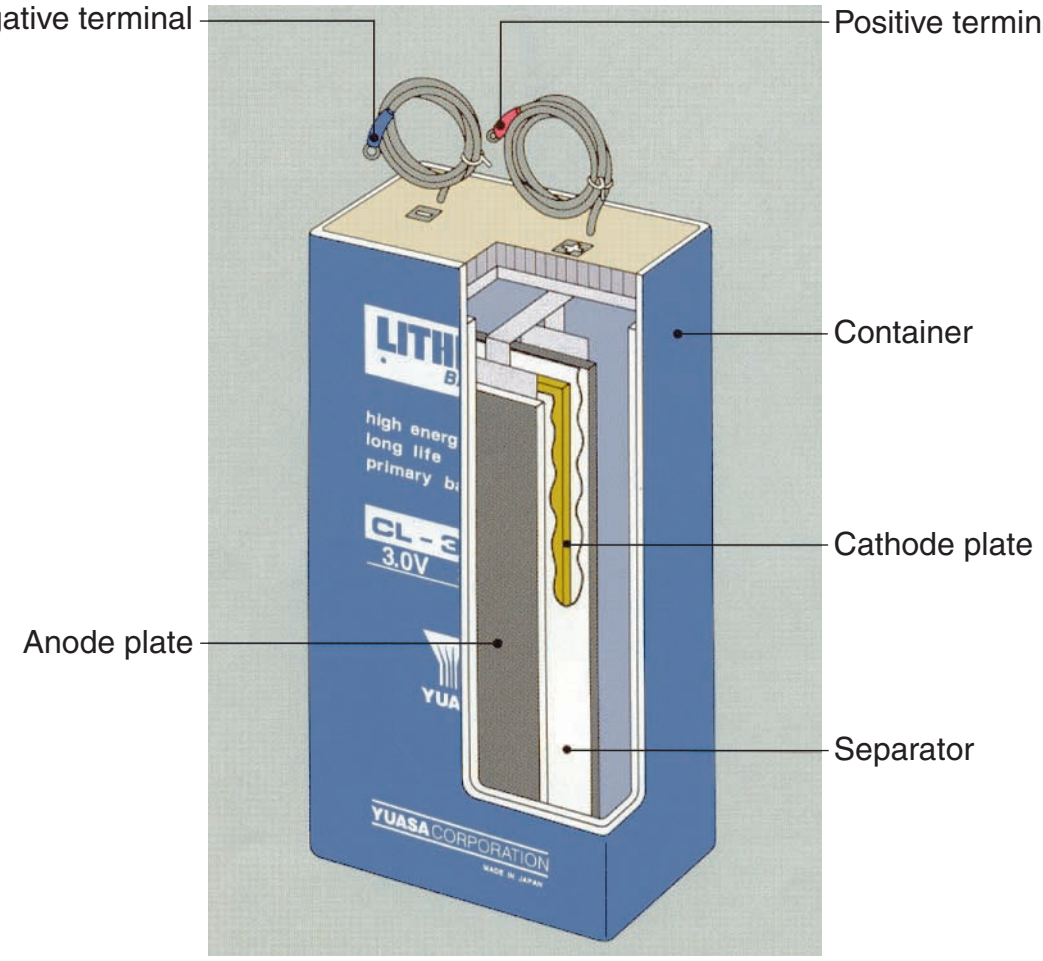

Figure F109. Variation of the voltage of the CL-1300L cell. The cell was discharged with a load of a constant current (0.26 A) at 0°C. The CL-1300L has a dominant voltage of 2.8 V. At the end of discharge, voltage of cell rapidly drops to 2.0 V.

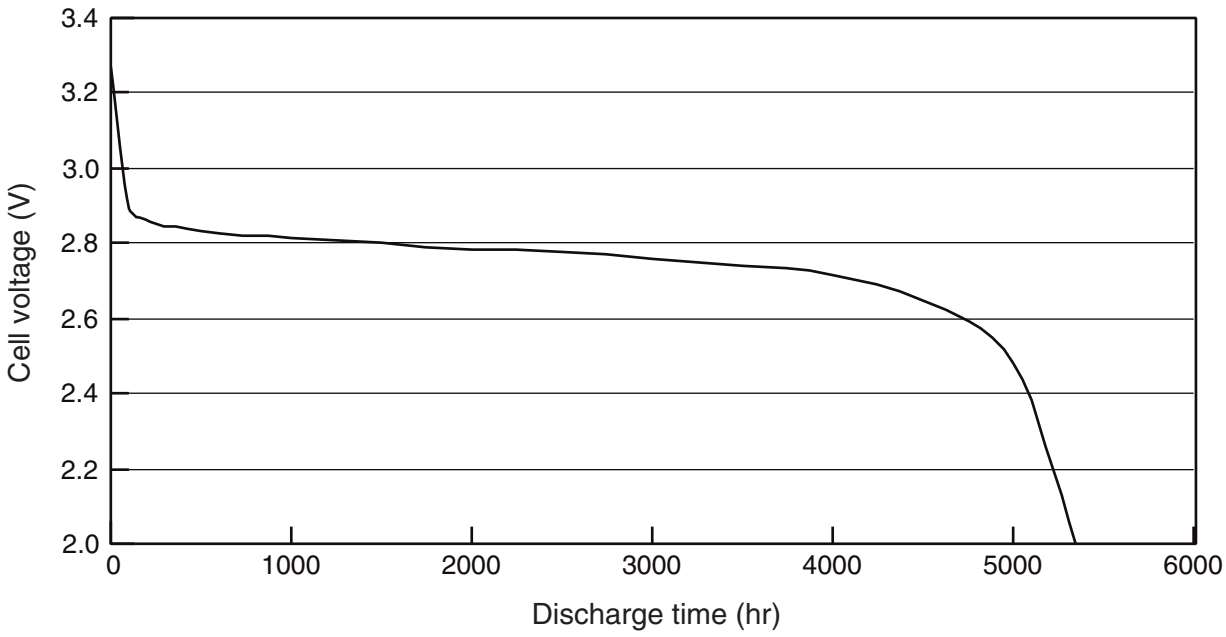

Figure F110. Variation of the voltage of the CL-1300L cell at constant loads of 5, 20, and 36 W. A larger load corresponds to a lower dominant voltage. The capacity of cell is independent of the amount of load. The voltage of the cell drops rapidly beyond 1100 Ah.

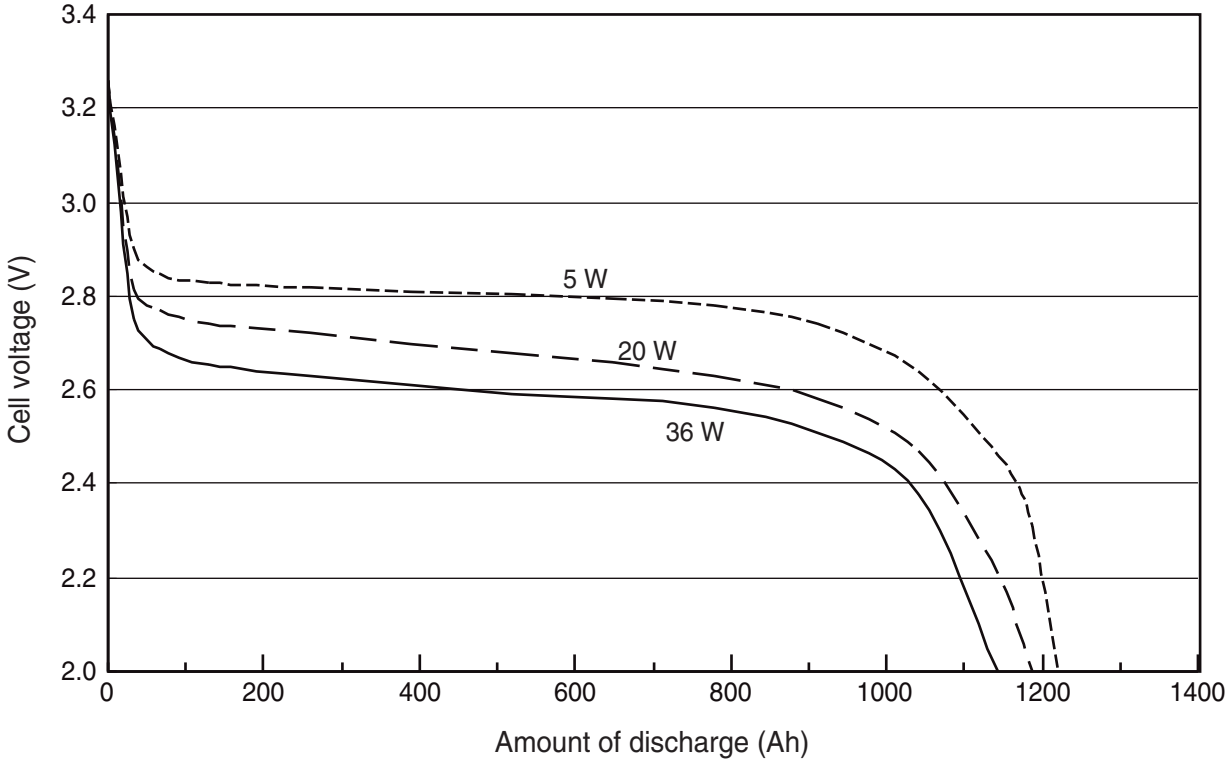

Figure F111. Schematic of the inside of the titanium sphere. Eight lithium battery cells are housed in a spherical pressure vessel made with titanium alloy. A rack made by Bakelite is used for emplacement of battery cells.

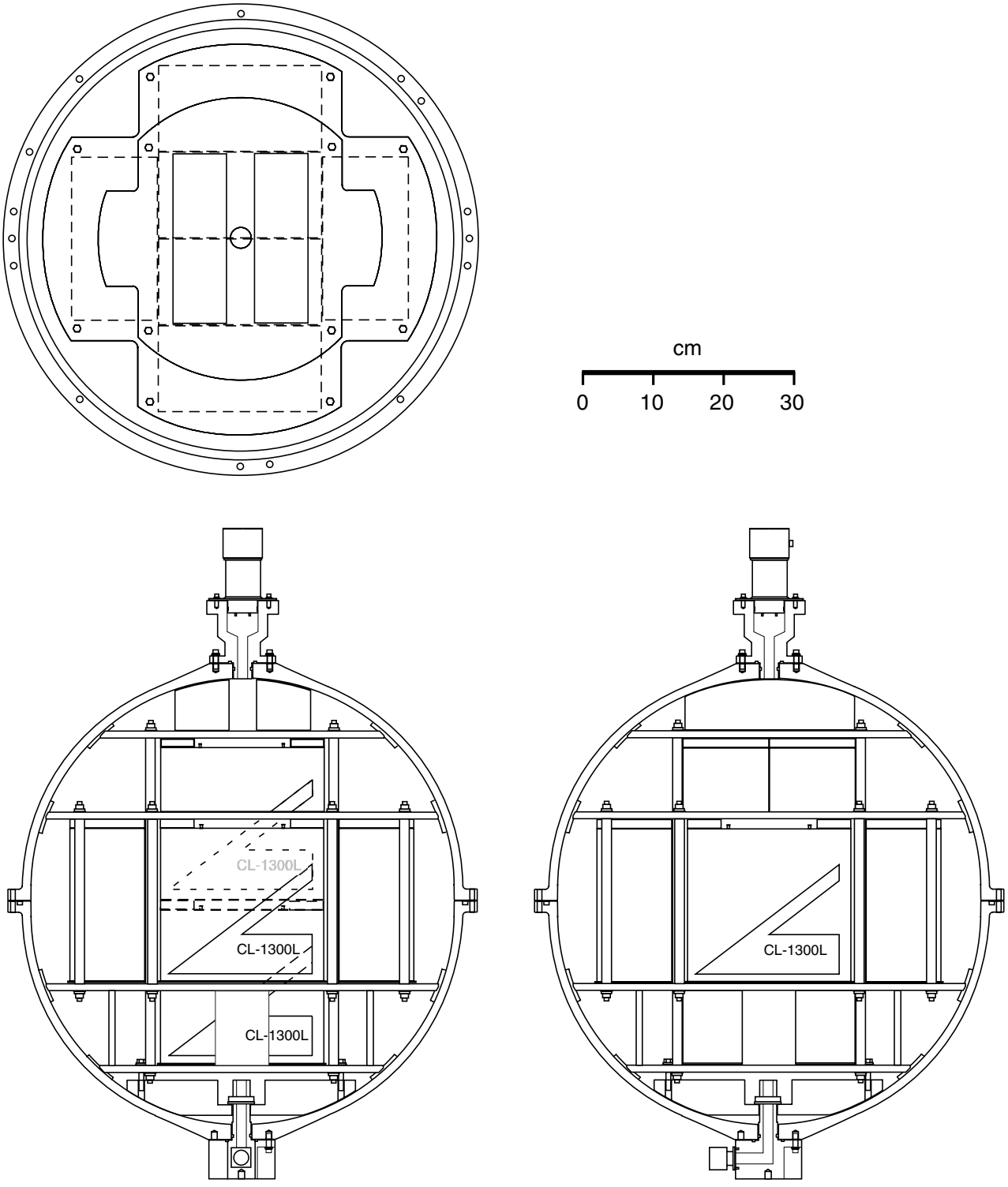

Figure F112. Perspective view of lithium cells and rack. The rack is designed for effective emplacement of batteries.

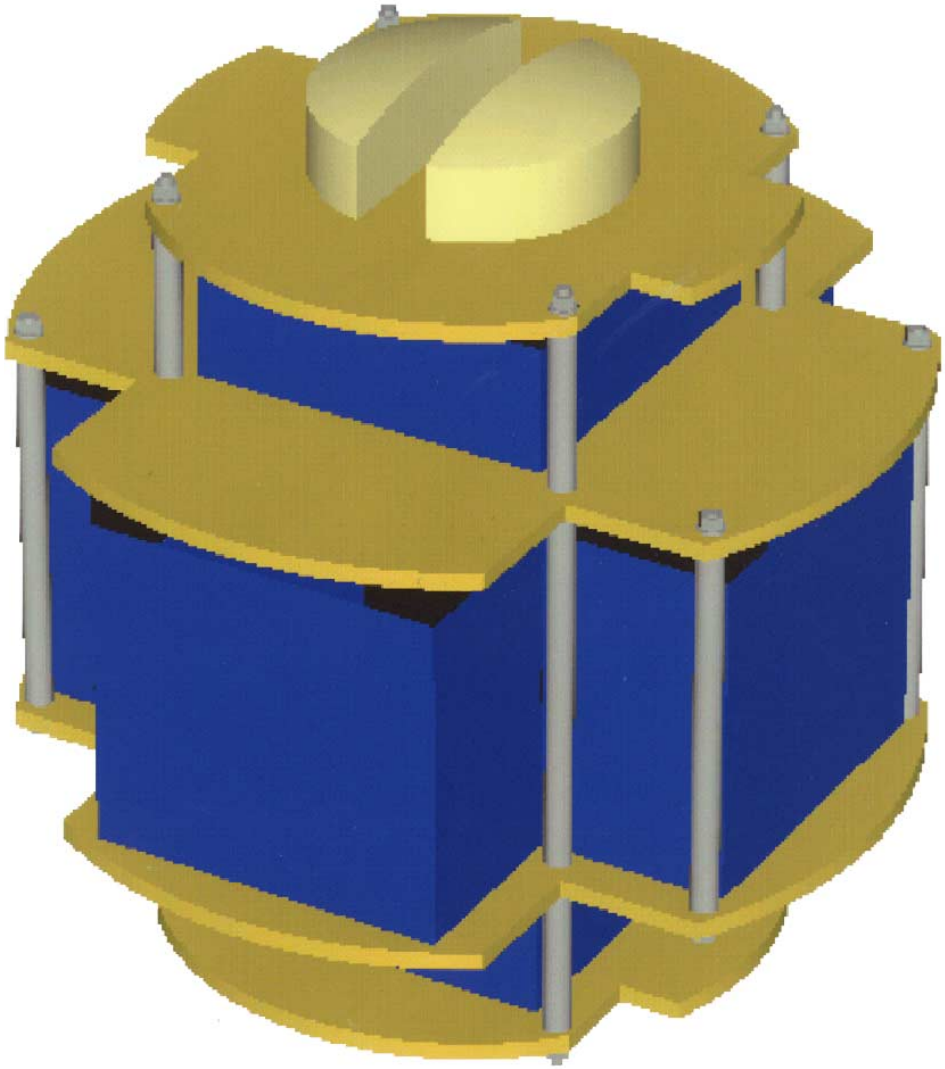

Figure F113. Electric block diagram of a lithium battery system unit. Eight cells in one sphere are connected in series, and two series are connected in parallel by underwater cable with dry-mate connectors. For parallel connection, a diode is connected in series for each series for safety reasons.

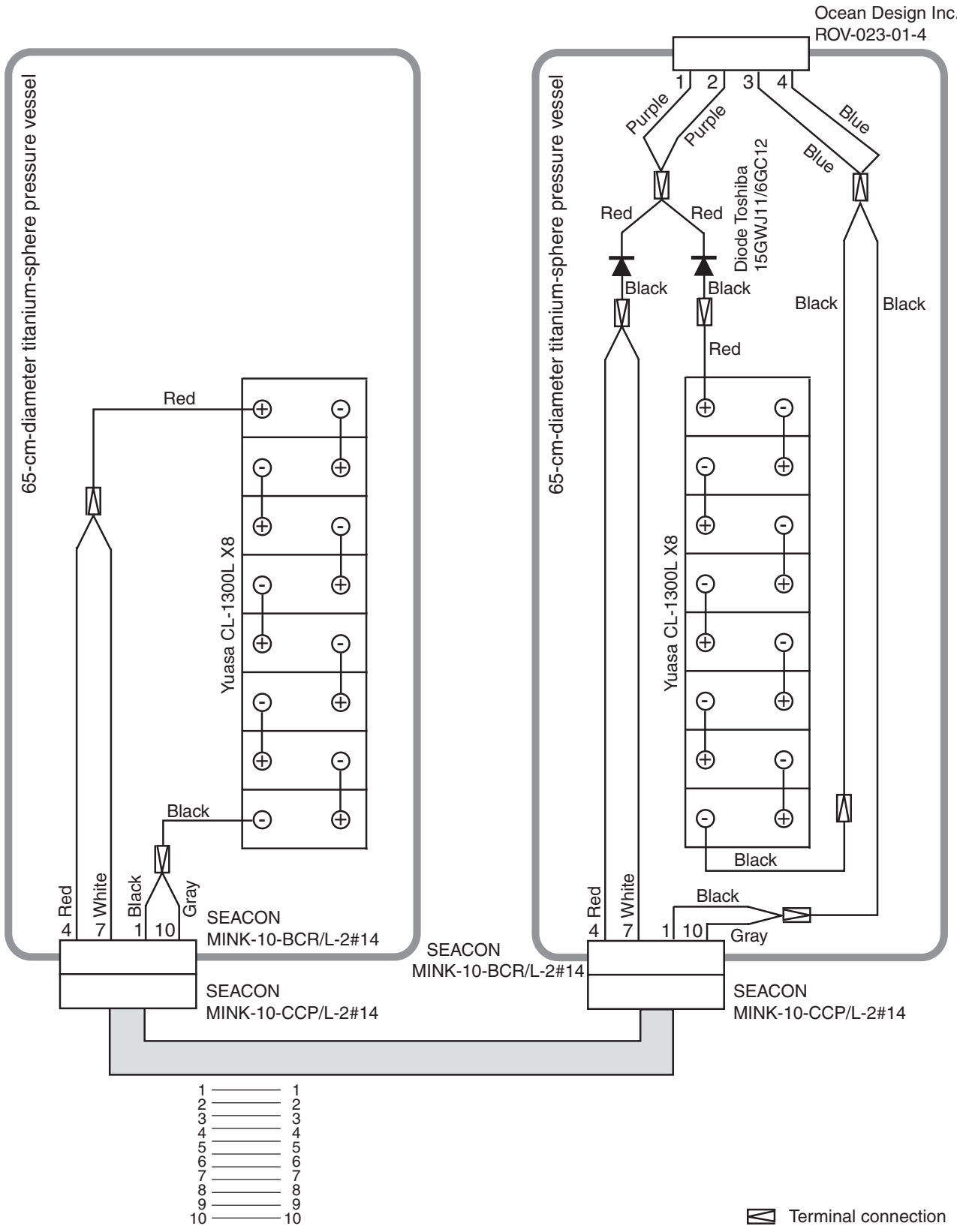

Figure F114. Photograph of the lithium battery unit (LBU) during assembly. Two titanium spheres are mounted on a frame made of titanium. The bottom of the LBU is a gray, flat panel made of fiber-reinforced plastic drainboard.

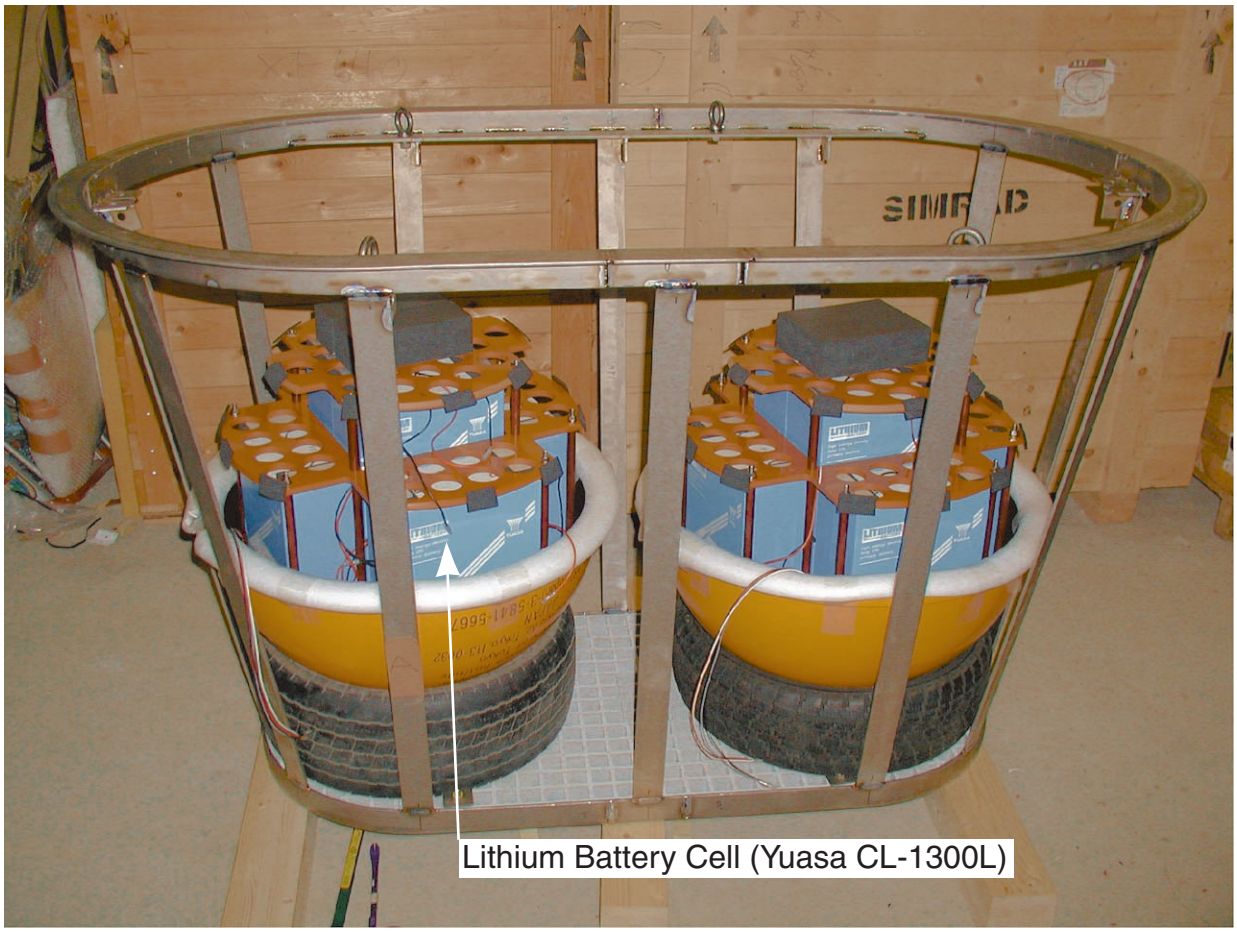

Figure F115. Photograph of the lithium battery unit (LBU). One sphere has an underwater mateable connector (UMC) on the top for supplying power to the whole system. The top of the LBU is the same drainboard as the power access terminal and has an access hole for the UMC.

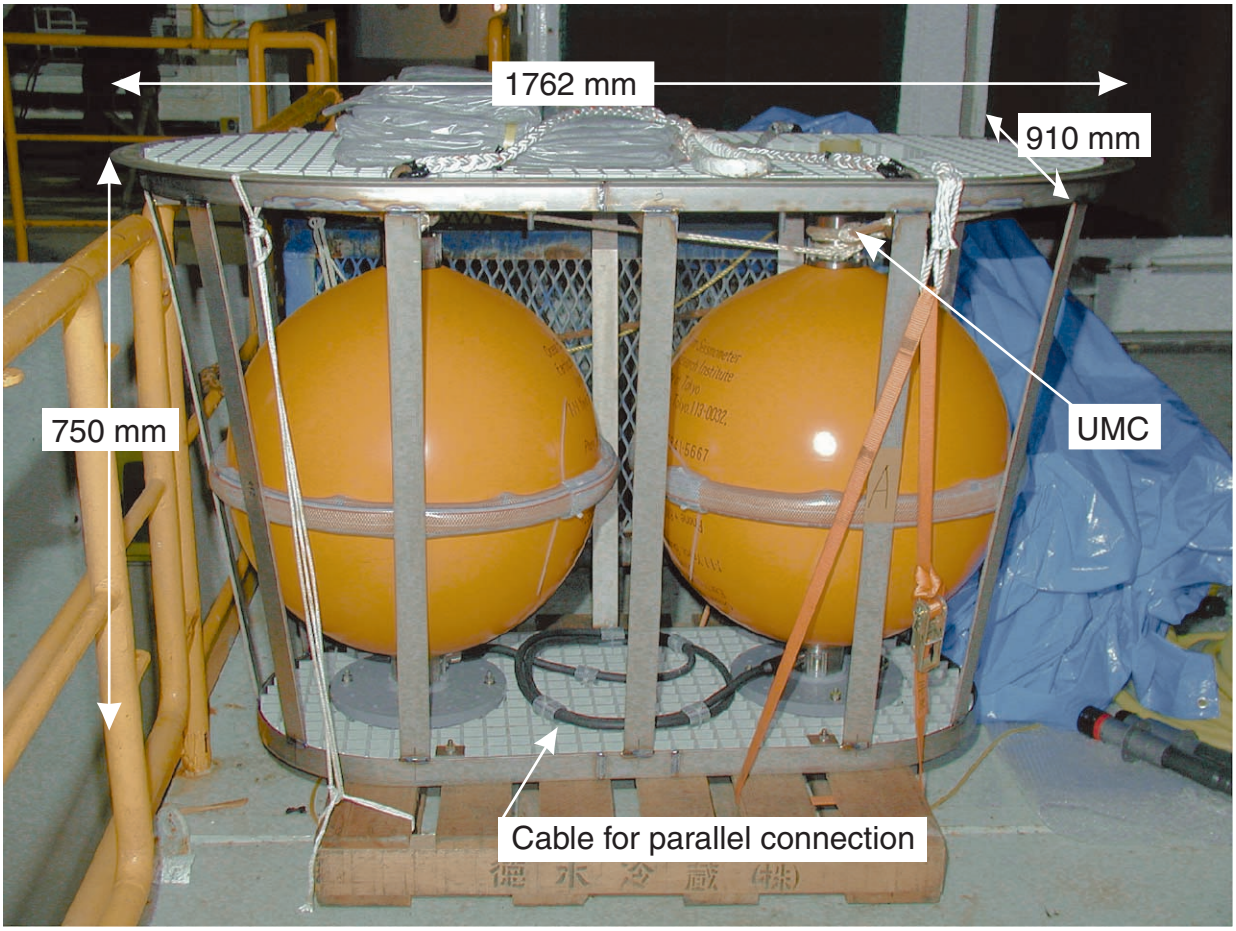

Figure F116. Photograph of the power access terminal (PAT) in the moonpool area just before deployment. The PAT has two lithium battery units (LBU) and a storage acquisition module (SAM) holder. Two cables with underwater mateable connectors (UMCs) are held on top of the PAT by a temporary fastener, which is easily released by a remotely operated vehicle (ROV). One cable has already been connected to LBU 2, and another cable will be connected to the MEG-195 by an ROV.

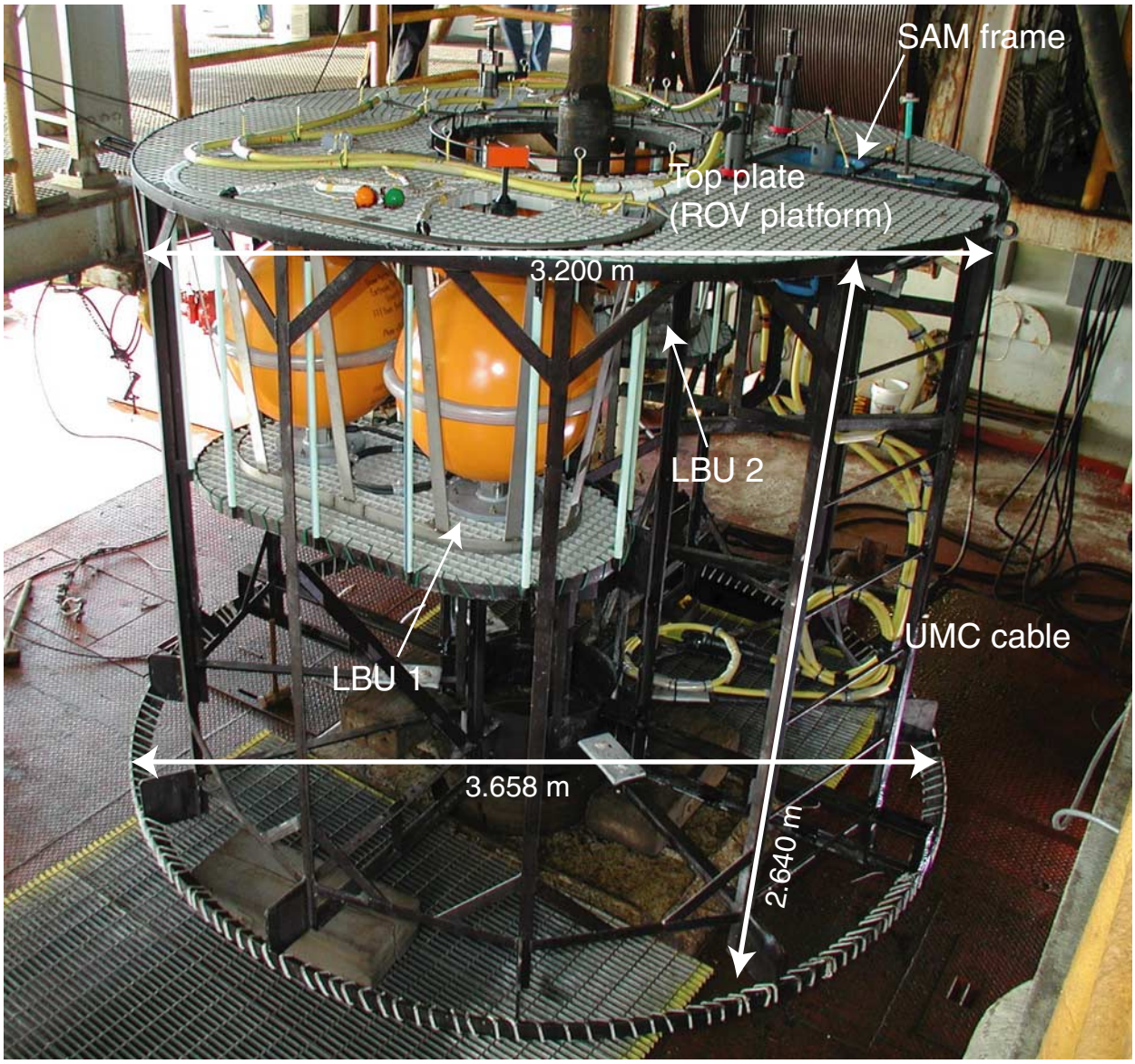

Figure F117. A. Photograph of the top of the PAT-195 around the recorder frame of the SAM-195. The recorder frame has a mechanism that will allow a remotely operated vehicle (ROV) to eject the SAM-195. Two underwater mateable connectors (UMCs) for the lithium battery unit (LBU) and MEG-195 are also seen. MEG = multiple-access expandable gateway, SAM = storage acquisition module. **B.** Photograph of the recorder frame, viewed from the bottom. The SAM frame has a guide wedge, or key, inside the SAM hole because the connector on the bottom of the SAM-195 canister must be correctly positioned to mate. The SAM-195 can be set and ejected by an ROV-operated lever mechanism in the recorder frame.

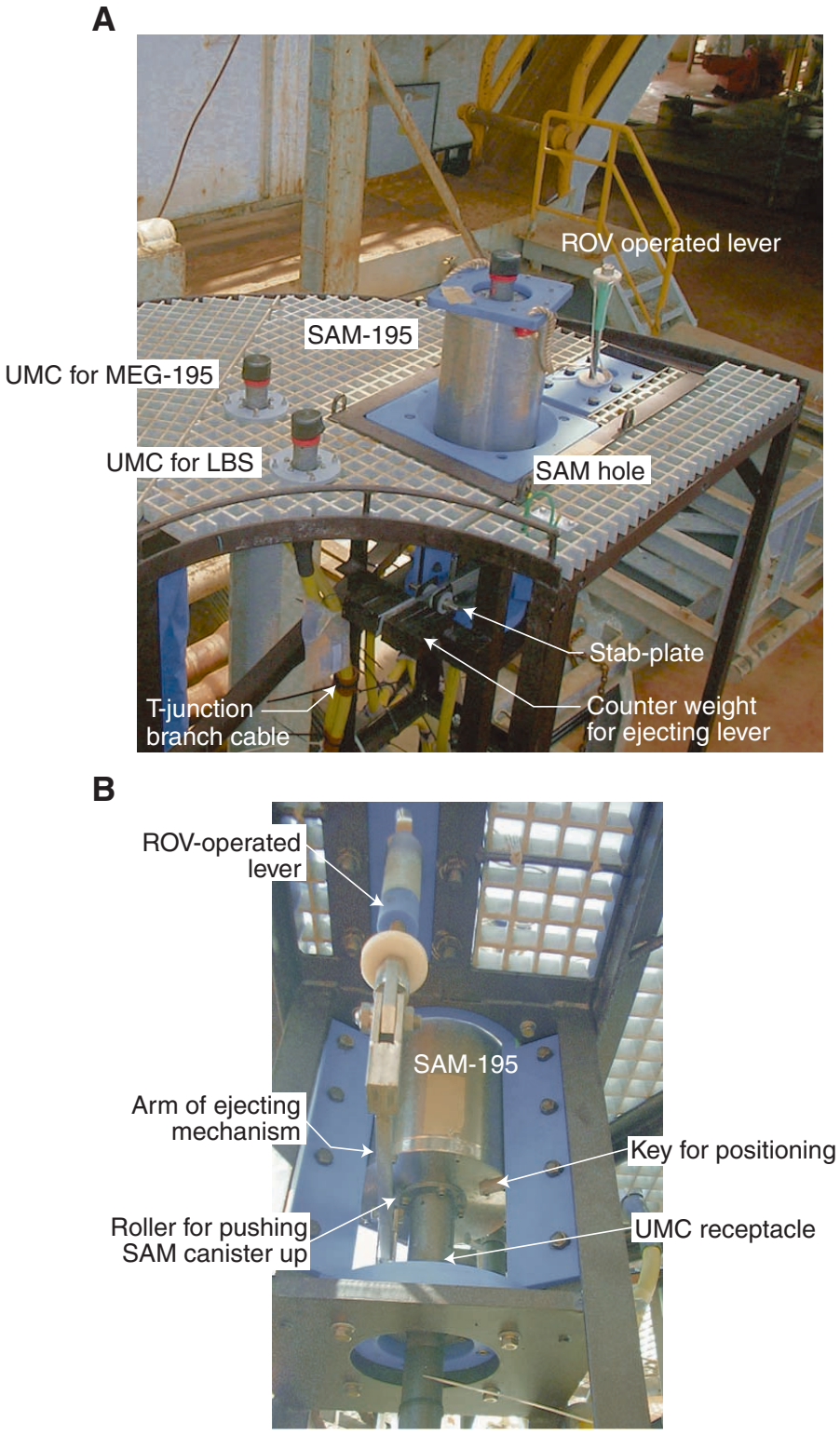

Figure F118. Photograph of the Japan Marine Science and Technology Center's (JAMSTEC) ROV, the *Kaiko*. All seafloor assembly electrical connections, the data storage unit, and the control unit can be removed and replaced by such an ROV. The *Kaiko* is scheduled to visit Site 1201 in November 2001 to activate the borehole observatory.

Table T1. Coring summary, Site 1201. (See table notes. Continued on next two pages.)

Hole 1201A
Latitude: 19°17.8830′N
Longitude: 135°5.9501′E
Time on site (hr): 557.00 (1600 hr, 31 Mar–1715 hr, 3 Apr 2001; 0715 hr, 5 Apr–1100 hr, 25 Apr 2001)
Time on hole (hr): 23.75 (1600 hr, 31 Mar–1545 hr, 1 Apr 2001)
Seafloor (drill pipe measurement from rig floor, mbrf): 5721.0
Distance between rig floor and sea level (m): 11.1
Water depth (drill pipe measurement from sea level, m): 5709.9
Total depth (drill pipe measurement from rig floor, mbrf): 5722.6
Total penetration (meters below seafloor, mbsf): 1.60
Total length of cored section (m): 1.6
Total core recovered (m): 1.49
Core recovery (%): 93.1
Total number of cores: 1

Hole 1201B
Latitude: 19°17.8788′N
Longitude: 135°5.9506′E
Time on hole (hr): 26.5 (1545 hr, 1 Apr–1815 hr, 2 Apr 2001)
Seafloor (drill pipe measurement from rig floor, mbrf): 5721.3
Distance between rig floor and sea level (m): 11.1
Water depth (drill pipe measurement from sea level, m): 5710.2
Total depth (drill pipe measurement from rig floor, mbrf): 5811.6
Total penetration (meters below seafloor, mbsf): 90.30
Total length of cored section (m): 90.3
Total core recovered (m): 65.91
Core recovery (%): 73.0
Total number of cores: 11

Hole 1201C
Latitude: 19°17.8829′N
Longitude: 135°5.9408′E
Time on hole (hr): 23.0 (1815 hr, 2 Apr–1715 hr, 3 Apr 2001)
Seafloor (drill pipe measurement from rig floor, mbrf): 5720.9
Distance between rig floor and sea level (m): 11.1
Water depth (drill pipe measurement from sea level, m): 5709.8
Total depth (drill pipe measurement from rig floor, mbrf): 5769.0
Total penetration (meters below seafloor, mbsf): 48.1
Total length of cored section (m): 48.1
Total core recovered (m): 49.51
Core recovery (%): 102.9
Total number of cores: 6

Hole 1201D
Latitude: 19°17.8165′N
Longitude: 135°5.9519′E
Time on hole (hr): 210.25 (0715 hr, 5 Apr–0130 hr, 14 Apr 2001 hr)
Seafloor (drill pipe measurement from rig floor, mbrf): 5720.0
Distance between rig floor and sea level (m): 11.3
Water depth (drill pipe measurement from sea level, m): 5708.7
Total depth (drill pipe measurement from rig floor, mbrf): 6320.0
Total penetration (meters below seafloor, mbsf): 600.0
Total length of cored section (m): 519.6
Total length of drilled intervals (m): 80.4
Total core recovered (m): 406.79
Core recovery (%): 78.3
Total number of cores: 55
Total number of drilled intervals: 1

Hole 1201E
Latitude: 19°17.8542′N
Longitude: 135°5.9491′E
Time on hole (hr): 273.50 (0130 hr, 14 Apr–1100 hr, 25 Apr 2001)
Seafloor (drill pipe measurement from rig floor, mbrf): 5721.0
Distance between rig floor and sea level (m): 11.0
Water depth (drill pipe measurement from sea level, m): 5710.0
Total depth (drill pipe measurement from rig floor, mbrf): 6301.0
Total penetration (meters below seafloor, mbsf): 580.0
Total core recovered (m): 0
Total length of drilled intervals (m): 580.0
Comment: Hole 1201E was drilled and cased to install the ION instrumentation.

Table T1 (continued).

Core	Date (April 2001)	Time (local)	Depth (mbsf) Top	Depth (mbsf) Bottom	Length (m) Cored	Length (m) Recovered	Recovery (%)	Comments
195-1201A-								
1H	1	1540	0.0	1.6	1.6	1.49	93.1	
				Totals:	1.6	1.49	93.1	
195-1201B-								
1H	1	2000	0.0	7.2	7.2	7.12	98.9	
2H	1	2250	7.2	16.7	9.5	10.10	106.3	
3H	2	0020	16.7	26.2	9.5	9.80	103.2	Oriented
4H	2	0155	26.2	35.7	9.5	10.03	105.6	Oriented
5H	2	0325	35.7	45.2	9.5	9.67	101.8	Oriented
6H	2	0500	45.2	46.7	1.5	1.63	108.7	Oriented
7X	2	0700	46.7	51.9	5.2	5.82	111.9	
8X	2	0850	51.9	61.5	9.6	8.14	84.8	
9X	2	1145	61.5	71.1	9.6	1.30	13.5	AHC
10X	2	1410	71.1	80.7	9.6	1.93	20.1	AHC
11X	2	1715	80.7	90.3	9.6	0.37	3.9	AHC
				Totals:	90.3	65.91	73.0	
195-1201C-								
1H	1	2020	0.0	6.6	6.6	6.51	98.6	
2H	1	2200	6.6	16.1	9.5	9.85	103.7	
3H	3	0035	16.1	25.6	9.5	9.83	103.5	Oriented; Adara
4H	3	0225	25.6	35.1	9.5	10.04	105.7	Oriented
5H	3	0435	35.1	44.6	9.5	9.78	102.9	Oriented; Adara
6H	3	0635	44.6	48.1	3.5	3.50	100.0	Oriented
				Totals:	48.1	49.51	102.9	
195-1201D-								
			*****Drilled from 0.0 to 80.4 mbsf*****					AHC; drilled interval
1R	6	0030	80.4	90.0	9.6	6.58	68.5	AHC
2R	6	0340	90.0	99.6	9.6	8.74	91.0	AHC
3R	6	0715	99.6	109.2	9.6	8.73	90.9	AHC
4R	6	1030	109.2	118.8	9.6	9.82	102.3	AHC
5R	6	1325	118.8	128.4	9.6	9.41	98.0	AHC
6R	6	1530	128.4	138.0	9.6	8.66	90.2	AHC
7R	6	1740	138.0	147.6	9.6	8.98	93.5	AHC
8R	6	1910	147.6	157.2	9.6	9.48	98.8	AHC
9R	6	2035	157.2	166.8	9.6	8.90	92.7	AHC
10R	6	2205	166.8	176.4	9.6	5.54	57.7	AHC
11R	6	2350	176.4	186.1	9.7	9.94	102.5	AHC
12R	7	0135	186.1	195.7	9.6	8.66	90.2	AHC
13R	7	0335	195.7	205.3	9.6	8.82	91.9	AHC
14R	7	0525	205.3	214.9	9.6	7.37	76.8	AHC
15R	7	0700	214.9	224.5	9.6	4.10	42.7	AHC
16R	7	0835	224.5	234.1	9.6	6.28	65.4	AHC
17R	7	1005	234.1	243.8	9.7	8.36	86.2	AHC
18R	7	1200	243.8	253.4	9.6	9.87	102.8	AHC
19R	7	1325	253.4	263.0	9.6	8.60	89.6	AHC
20R	7	1450	263.0	272.6	9.6	8.30	86.5	AHC
21R	7	1620	272.6	282.3	9.7	8.38	86.4	AHC
22R	7	1745	282.3	291.9	9.6	8.58	89.4	AHC
23R	7	1910	291.9	301.5	9.6	9.15	95.3	AHC
24R	7	2040	301.5	311.1	9.6	6.05	63.0	AHC
25R	7	2220	311.1	320.7	9.6	6.29	65.5	AHC
26R	7	2355	320.7	330.3	9.6	9.92	103.3	AHC
27R	8	0200	330.3	339.9	9.6	9.94	103.5	AHC
28R	8	0645	339.9	349.5	9.6	8.10	84.4	AHC
29R	8	0845	349.5	359.1	9.6	6.78	70.6	AHC
30R	8	1035	359.1	368.7	9.6	9.75	101.6	AHC
31R	8	1205	368.7	378.3	9.6	9.53	99.3	AHC
32R	8	1340	378.3	387.9	9.6	8.93	93.0	AHC
33R	8	1510	387.9	397.5	9.6	9.16	95.4	AHC
34R	8	1645	397.5	407.1	9.6	8.02	83.5	AHC
35R	8	1815	407.1	416.7	9.6	8.07	84.1	AHC
36R	8	2020	416.7	426.4	9.7	9.91	102.2	AHC
37R	8	2210	426.4	436.0	9.6	9.88	102.9	AHC
38R	8	2350	436.0	445.7	9.7	9.89	102.0	AHC
39R	9	0115	445.7	455.3	9.6	8.95	93.2	AHC
40R	9	0255	455.3	464.9	9.6	10.02	104.4	AHC
41R	9	0420	464.9	474.5	9.6	7.16	74.6	AHC

Table T1 (continued).

Core	Date (April 2001)	Time (local)	Depth (mbsf) Top	Depth (mbsf) Bottom	Length (m) Cored	Length (m) Recovered	Recovery (%)	Comments
42R	9	0600	474.5	484.1	9.6	10.03	104.5	AHC
43R	9	0800	484.1	493.7	9.6	6.52	67.9	AHC
44R	9	0935	493.7	503.3	9.6	9.88	102.9	AHC
45R	9	1200	503.3	512.9	9.6	7.06	73.5	AHC
46R	9	1700	512.9	522.1	9.2	6.10	66.3	AHC
47R	9	2240	522.1	531.7	9.6	3.77	39.3	AHC
48R	10	0450	531.7	541.3	9.6	3.51	36.6	AHC
49R	10	1140	541.3	550.3	9.0	2.91	32.3	AHC on first 5 m
50R	10	1630	550.3	554.0	3.7	0.10	2.7	AHC; core catcher jammed
51R	10	2045	554.0	560.7	6.7	0.72	10.8	AHC
52R	11	0340	560.7	570.3	9.6	2.03	21.2	AHC
53R	11	0910	570.3	579.5	9.2	1.16	12.6	AHC
54R	11	1555	579.5	588.1	8.6	2.20	25.6	AHC
55R	11	0000	588.1	600.0	11.9	3.20	26.9	AHC
				Cored totals:	519.6	406.79	78.3	
				Drilled totals:	80.4			
				Total:	600.0			

Notes: ION = International Ocean Network. AHC = advanced hydraulic piston coring.

Table T2. XRD data for soft sediments and sedimentary rocks from bulk powder mounts, Site 1201. (**See table notes.** Continued on next page.)

Core, section, interval (cm)	Depth (mbsf)	Lithology	Mineral											
			Quartz	Plagioclase	Expandable clay minerals	Illite	Well-crystallized smectite	Calcite	Phillipsite	Clinoptilolite/Heulandite	Analcime/Wairakite	Erionite	Chabazite	Gypsum
195-1201A-														
1H-1, 0–1	0.00	Red silty clay	A	C	C	C								
1H-1, 9–10	0.09	Red silty clay	P	A	C	C								
1H-1, 18–19	0.18	Red silty clay	D	A	C	C								
1H-1, 31–32	0.31	Red silty clay	A	A	C	P			P					
1H-1, 66–67	0.66	Red silty clay	C	A	C	C			P					
1H-1, 81–82	0.81	Red silty clay	C	A	C	C			P					
1H-1, 105–106	1.05	Red silty clay	D	A	C	C			P					
195-1201B-														
1H-1, 5–6	0.05	Red silty clay	C	C	C	C			P					
1H-1, 74–75	0.74	Red silty clay	D	P	C	P			P					
1H-2, 74–75	2.24	Red silty clay	A	A	C	P			P					
1H-3, 74–75	3.74	Red silty clay	A	A	P	P			P					
1H-4, 74–75	5.24	Red silty clay	A	A	A	P			P					
1H-5, 74–75	6.74	Red silty clay	A	D	A				P					
2H-1, 74–75	7.94	Red silty clay	A	A	A				P					
2H-2, 74–75	9.44	Red silty clay	A	A	A				P					
2H-3, 74–75	10.94	Red silty clay	A	A	A				P					
2H-4, 74–75	12.44	Red silty clay	A	A	A				P					
2H-5, 74–75	13.94	Red silty clay	A	A	A				C					
2H-6, 74–75	15.44	Red silty clay	A	A	A				C					
2H-7, 74–75	16.94	Red silty clay	C	D	A				P					
3H-1, 74–75	17.44	Red silty clay	C	D	A				C					
3H-2, 74–75	18.94	Red silty clay	A	A	A				C					
3H-3, 74–75	20.44	Red silty clay	A	A	A									
3H-4, 20–21	21.40	Red silty clay	C	A	C				D					
3H-4, 74–75	21.94	Concretion	C	A	A				C					
3H-5, 74–75	23.44	Brown silty clay	A	P	A				C					
3H-5, 121–122	23.91	Brown silty clay	P	P	A				C					
3H-6, 41–42	24.61	Brown silty clay	C	A	C				A					
3H-6, 56–57	24.76	Brown silty clay	C	D	A				C					
3H-7, 8–9	25.78	Chert	C	D	A									
3H-7, 50–51	26.20	Brown silty clay	C	A	A				C					
4H-1, 74–75	26.94	Dark brown silty clay	C	A	A				C					
4H-2, 48–49	28.18	Dark brown silty clay	C	A	C				C					
4H-3, 74–75	29.94	Dark brown silty clay	P	P	P			D	P					
4H-4, 41–42	31.11	Dark brown silty clay	A	A	C				C					
4H-5, 74–75	32.94	Dark brown silty clay	P	A	C				P					
4H-5, 117–118	33.37	White silty clay layer			A				D					
4H-6, 41–42	34.11	Very dark brown silty clay	P	A	C				A					
4H-7, 41–42	35.61	Very dark brown silty clay	A	A	C				A					
5H-1, 74–75	36.44	Dark brown silty clay	C	A	A				P					
5H-2, 21–22	37.41	Brown silty clay	C	A	A				A					
5H-3, 14–15	38.84	Brown silty clay	C	A	A				A					
5H-3, 74–75	39.44	Brown silty clay	C	A	A				A					
5H-4, 45–46	40.65	Chert	P	A	A				C					
5H-4, 49–50	40.69	Tan silty clay	P	P	A				A					
5H-4, 69–70	40.89	Tan silty clay	P	A	C				A					
5H-5, 74–75	42.44	Tan silty clay	C	A	C				P					
5H-6, 29–30	43.49	Tan silty clay	C	A	C				A					
6H-1, 74–75	45.94	Tan silty clay	C	D	C				A					
7X-1, 74–75	47.44	Tan silty clay	C	D	C				A					
7X-2, 74–76	48.94	Tan silty clay	C	A	C				A					
7X-3, 20–22	49.90	Tan laminated silty sand	C	D	C				A					
7X-3, 74–75	50.44	Tan silty sand	C	D	C				C					
8X-1, 40–42	52.30	Tan grit	C	D	C				C					
8X-2, 80–82	54.20	Dark siltstone	C	D	C				C					
8X-4, 59–61	56.99	Dark siltstone	C	D	C				C					
8X-6, 4–6	58.94	Laminated sand	C	D	C									

Table T2 (continued).

Core, section, interval (cm)	Depth (mbsf)	Lithology	Mineral											
			Quartz	Plagioclase	Expandable clay minerals	Illite	Well-crystallized smectite	Calcite	Phillipsite	Clinoptilolite/Heulandite	Analcime/Wairakite	Erionite	Chabazite	Gypsum
10X-1, 30–32	71.40	Dark siltstone	C	D	C				C					
10X-1, 88–90	71.98	Calcareous mudstone	C	D	P				C					
10X-CC, 19–20	72.79	Dark sandstone	C	D	P				P					
195-1201D-														
1R-1, 81–82	81.21	Sandstone	C	D	C				P					
1R-4, 83–84	85.53	Siltstone	C	D	P				C					
5R-7, 44–45	127.33	Sandy mudstone	C	A	A				C					
6R-4, 70–71	133.34	Sandstone			A				D					
6R-6, 49–50	135.39	Siltstone	P	D	A				C					
8R-1, 76–77	148.36	Siltstone	P	A	A				C					
8R-3, 68–70	150.99	Sandstone		D	C									
8R-3, 83–84	151.14	Sandstone		A	A				A					
12R-1, 16–17	186.26	Dark coarse sandstone			A				A	C				
12R-4, 101–102	190.86	Dark siltstone	P	C	C				P					
14R-5, 18–19	211.20	Dark silt clast	P	D	A									
17R-3, 100–101	237.71	Dark siltstone		D	P		C			P		P		
19R-6, 50–51	261.16	Dark sandy siltstone	P	A			C		C	P	A			
22R-2, 103–104	284.74	Green siltstone	P	A							D			
26R-4, 105–106	325.77	Dark sandstone	P	A			A		C	P	C			
26R-5, 111–112	327.33	Dark siltstone	P	P			C		P	P	A			
28R-CC, 0–2	347.97	Dark sandstone		A			C			D				
29R-2, 101–102	351.60	Green siltstone								D				C
30R-3, 120–122	363.30	Dark sandstone		A			C			A	A			
30R-6, 147–148	368.07	Green concretion								P				
30R-7, 55–56	368.65	Dark siltstone	P	C			C		P	C	C			
31R-4, 99–100	374.09	Green sandstone		A			P			D	C	P		
31R-6, 77–79	376.87	Altered green sandstone		A			A			P	A			
33R-4, 29–30	392.37	Zeolite concretion								D		P		
35R-5, 128–129	413.20	Dark siltstone	P	P			P			P	A			
35R-7, 56–59	414.81	Altered green sandstone	P	P			C			P	A	C	A	P
36R-2, 15–18	418.13	Silty sandstone		A			P			C	P	C	C	P
37R-3, 72–73	429.79	Dark siltstone		A			C			P		C	A	P
38R-1, 29–32	436.29	Sandstone with white veins		C			P			P	P		C	A
42R-5, 23–25	480.73	Dark sandstone		A	C		A				C		A	
42R-7, 70–71	484.12	Dark siltstone		A			A			C	A			
43R-2, 50–52	485.99	Red siltstone		D			A			C				
43R-4, 36–38	488.52	Red fine sandstone		A			C			C	P		C	
43R-CC, 0–1	490.59	Red sandstone		A	C		C			A				
44R-3, 1–2	496.71	Green siltstone		A	C		A			P	P		A	
44R-7, 0–1	502.70	Red mudstone	C	A	C		P			C	P		C	
45R-4, 20–21	507.56	Reddish brown claystone	A	A			A							
45R-5, 63–64	509.49	Sand stringer		P	D		C							
45R-5, 90–91	509.76	Dark brown claystone	C	P	A		C							

Notes: Clay mineralogy was verified by XRD results from textured clay mounts. Semiquantitative estimation of mineral abundance is based on major XRD peak intensities displayed by the various minerals: D = dominant (50%–100%), A = abundant (20%–50%), C = common (5%–20%), P = present (1%–5%).

Table T3. XRD data on selected basement samples, Site 1201.

Core, section, interval (cm)	Depth (mbsf)	Rock type	Mineral							
			Plagioclase	K-feldspar	Augite	Quartz	Analcime	Natrolite/Thomsomite	12-Å clay mineral	15-Å clay mineral
195-1201D-										
45R-5, 91–92	509.77	Basalt	A		A		C		P	
46R-1, 35–36	513.25	Basalt with vein	A		C		D	C	P	
46R-2, 70–73	515.10	Rim of hyaloclastite	A		A		A	P	P	
46R-2, 108–110	515.48	Basalt	D		A		C	P	P	P
46R-4, 31–33	517.57	Hyaloclastite			D		D		C	C
47R-1, 24–27	522.34	Hyaloclastite	P		P		D		P	
47R-1, 117–120	523.27	Basalt with sediment	C		C	P	D		P	
47R-3, 121–124	526.29	Basalt	D		A				P	C
52R-2, 34–36	562.47	Altered basalt		D	A				P	P
54R-1, 106–108	580.56	Interpillow sediment	P				A			D
54R-2, 39–41	581.07	Reddish purple basalt	D		A				P	P
55R-1, 43–45	588.53	Basalt	D		C					P
55R-1, 103–106	589.13	Basalt	D		C					P

Note: D = dominant, A = abundant, C = common, P = present.

Table T4. Elemental content, mineral composition, LOI, and Mg# of representative basement rocks, Hole 1201D. (Continued on next page.)

Core, section:	45R-5	46R-1	46R-1	46R-1	46R-2	46R-4	46R-4	46R-5	47R-2	47R-2	47R-3	47R-3	48R-1	48R-2	48R-2
Interval (cm):	104–107	108–110	134–136	138–140	108–110	24–27	31–33	58–60	85–87	124–126	83–86	121–124	48–50	74–76	135–138
Piece:	1	8	10	10	5B	6A	7	4B	10	16	7	13	2C	1D	5C
Depth (mbsf):	509.90	513.98	514.24	514.28	515.48	517.50	517.57	519.34	524.45	524.84	525.91	526.29	532.18	533.18	533.79
Rock type:	Basalt	Basalt	Basalt	Basalt	Basalt	Hyaloclastite	Hyaloclastite	Basalt	Basalt	Basalt	Basalt	Basalt	Basalt	Basalt	Basalt
Major element oxides (wt%):															
SiO_2	51.38	47.66	51.76	50.74	50.42	50.76	49.70	49.38	49.78	49.60	49.20	49.45	49.37	49.85	49.35
TiO_2	0.90	0.97	1.02	0.90	0.91	1.01	0.77	0.89	0.91	0.89	0.96	0.94	0.92	0.92	0.92
Al_2O_3	16.27	17.17	16.23	16.19	16.80	17.02	17.29	17.18	16.03	16.36	16.28	16.07	15.62	15.96	15.70
Fe_2O_3T	9.15	9.51	9.76	8.83	8.80	10.08	10.53	8.72	9.16	9.10	9.29	10.48	8.99	9.92	10.65
MnO	0.16	0.16	0.15	0.15	0.14	0.16	0.14	0.15	0.14	0.14	0.20	0.20	0.17	0.20	0.22
MgO	6.08	7.38	6.76	7.18	7.68	7.39	5.22	7.87	8.40	8.64	8.08	8.23	8.18	8.52	8.38
CaO	14.05	12.13	7.35	9.69	11.86	7.92	6.67	11.27	9.05	11.01	12.03	13.16	13.15	13.70	13.26
Na_2O	2.83	2.98	5.48	4.00	2.77	4.75	4.73	2.83	3.68	3.15	2.06	2.13	2.09	2.13	2.08
K_2O	0.65	0.89	1.25	1.11	1.13	1.18	2.84	1.14	1.31	1.26	0.48	0.57	0.24	0.26	0.35
P_2O_5	0.19	0.21	0.13	0.20	0.04	0.12	0.06	0.15	0.16	0.22	0.13	0.10	0.09	0.07	0.09
Total:	101.65	99.07	99.90	99.00	100.56	100.39	97.95	99.58	98.61	100.37	98.70	101.34	98.82	101.54	100.99
Trace elements (ppm):															
Sc	41.88	47.63	48.34	42.57	45.74	46.09	36.02	43.68	46.85	46.37	46.39	41.96	45.14	42.48	41.65
V	237.61	293.88	234.03	242.17	252.86	263.78	98.31	239.87	283.50	279.92	303.60	260.17	277.37	249.63	259.40
Cr	342.37	348.12	359.72	330.21	397.81	363.86	165.05	360.39	351.20	324.20	414.40	409.93	379.50	397.24	407.38
Ni	71.22	—	72.16	73.05	142.42	88.78	—	106.27	—	—	—	—	—	—	—
Sr	109.43	145.67	26.58	64.69	223.28	51.86	41.14	134.39	86.83	102.95	80.87	80.75	77.71	80.06	80.04
Y	26.58	25.81	28.37	23.84	22.69	28.11	8.95	22.95	26.82	24.22	25.69	24.95	23.90	23.20	24.57
Ba	14.48	21.32	26.18	19.73	22.34	24.54	16.69	23.50	25.99	26.01	14.94	12.51	11.50	10.86	10.44
Zr	50.46	50.71	56.74	51.93	52.23	56.44	46.79	48.77	50.60	47.07	47.18	48.17	44.58	45.98	47.10
LOI:	3.32	5.87	6.47	5.02	5.87	6.55	11.85	5.14	4.87	6.2	1.76	1.83	1	1.4	0.97
CIPW-normative minerals (wt%):															
or	3.82	5.27	7.39	6.56	6.69	6.99	16.77	6.72	7.72	7.46	2.86	3.40	1.42	1.54	2.06
ab	23.84	17.33	33.49	29.09	22.54	30.33	22.39	22.09	26.47	20.85	17.45	17.99	17.66	18.02	17.57
an	29.78	30.83	15.99	22.96	30.05	21.61	17.58	30.80	23.38	26.77	33.72	32.61	32.55	33.23	32.48
ne	0.07	4.28	6.98	2.57	0.49	5.35	9.55	1.02	2.52	3.15	0.00	0.00	0.00	0.00	0.00
di	31.70	22.81	16.04	19.35	23.19	13.79	12.53	19.61	16.58	21.42	20.41	26.14	26.05	27.83	26.66
hy	0.00	0.00	0.00	0.00	0.00	0.00	0.00	0.00	0.00	0.00	14.76	4.83	11.84	6.86	7.49
ol	7.92	13.74	15.22	13.99	13.49	17.48	14.80	15.04	17.46	16.16	4.95	11.64	5.00	9.56	10.00
mt	1.58	1.64	1.68	1.52	1.52	1.74	1.82	1.50	1.58	1.57	1.60	1.81	1.55	1.71	1.84
il	1.70	1.85	1.94	1.71	1.73	1.92	1.46	1.69	1.73	1.70	1.83	1.78	1.75	1.75	1.74
ap	0.45	0.49	0.32	0.49	0.08	0.28	0.13	0.35	0.39	0.51	0.30	0.23	0.22	0.18	0.22
Total:	100.86	98.24	99.05	98.23	99.79	99.51	97.03	98.83	97.82	99.58	97.89	100.42	98.04	100.67	100.06
Mg#:	59.89	63.55	60.91	64.62	66.23	62.23	52.71	66.96	67.33	68.09	66.15	63.84	67.18	65.89	63.88

Notes: Element compositions were determined by inductively coupled plasma–atomic emission spectroscopy. LOI = loss on ignition. Mg# = $100 \times Mg^{2+}/(Mg^{2+}+Fe^{2+})$. Calculated CIPW-normative compositions: or = norm orthoclase, ab = norm albite, an = norm anorthite, ne = norm nepheline, di = norm diopside, hy = norm hyperthene, ol = norm olivine, mt = norm magnetite, il = norm ilmenite, ap = norm apatite.

Table T4 (continued).

Core, section:	48R-3	48R-4	49R-1	49R-2	49R-2	51R-1	52R-1	53R-1	54R-1	54R-1	54R-2	54R-2	55R-1	55R-1	55R-2
Interval:	77–79	70–72	144–147	28–30	131–133	22–23	78–80	116–118	43–45	69–71	39–41	118–120	43–45	103–106	95–97
Piece:	7C	13	14C	6	14	4	7A	17A	4	9	4C	9	5G	5R	8
Depth (mbsf):	534.71	536.04	542.74	543.08	544.11	554.22	561.48	571.46	579.93	580.19	581.07	581.86	588.53	589.13	590.51
Rock type:	Basalt	Basalt	Basalt	Basalt	Basalt	Basalt	Basalt	Basalt	Basalt	Basalt	Basalt	Basalt	Basalt	Basalt	Basalt
Major element oxides (wt%):															
SiO_2	50.01	50.79	49.76	50.53	48.35	47.49	50.14	50.01	50.07	50.51	49.54	50.01	50.30	50.32	49.65
TiO_2	0.92	0.91	0.92	0.93	0.88	0.88	0.94	0.95	0.97	1.01	0.94	0.94	0.90	0.91	0.96
Al_2O_3	15.87	15.97	15.97	16.15	15.45	15.38	16.29	16.39	16.61	17.24	16.32	16.44	15.45	15.72	16.43
Fe_2O_3T	10.03	10.24	8.66	9.51	8.83	8.29	10.03	10.42	10.64	10.81	10.54	9.62	9.23	9.40	9.95
MnO	0.21	0.21	0.17	0.22	0.19	0.17	0.21	0.22	0.17	0.16	0.23	0.18	0.18	0.18	0.18
MgO	8.71	8.90	8.07	8.81	8.43	7.93	8.31	7.91	6.14	5.83	7.69	7.44	8.34	8.15	6.64
CaO	13.81	13.89	14.06	13.65	13.19	12.16	13.25	13.84	12.95	11.79	13.66	14.11	13.39	13.84	13.17
Na_2O	2.11	2.14	2.02	2.13	1.83	1.82	2.18	1.96	1.85	2.32	2.02	1.98	2.06	2.08	2.58
K_2O	0.18	0.23	0.26	0.30	0.29	0.36	0.48	0.64	1.41	1.49	0.67	0.45	0.18	0.19	0.75
P_2O_5	0.05	0.08	0.09	0.09	0.10	0.05	0.10	0.09	0.14	0.13	0.08	0.09	0.09	0.08	0.12
Total:	101.90	103.38	99.97	102.32	97.54	94.53	101.93	102.43	100.97	101.29	101.70	101.26	100.13	100.88	100.44
Trace elements (ppm):															
Sc	39.46	42.31	41.64	43.70	42.29	43.03	43.63	45.01	45.73	46.00	43.90	43.89	41.63	41.66	48.13
V	246.46	261.18	257.09	259.83	243.91	239.52	270.05	285.75	286.13	323.18	286.67	281.78	247.92	260.40	300.44
Cr	416.84	420.80	426.10	431.81	411.17	398.62	409.55	425.17	437.53	460.29	410.97	435.95	415.39	423.66	420.87
Ni	—	—	130.22	—	—	—	—	—	74.03	90.10	—	94.71	166.75	124.23	88.36
Sr	79.41	79.71	82.14	80.52	78.35	77.66	83.71	81.52	84.56	91.97	81.47	82.14	79.31	79.07	108.70
Y	23.32	24.32	24.01	24.91	23.42	23.63	24.93	25.10	27.89	30.56	24.00	23.44	23.29	23.42	25.27
Ba	10.79	11.61	9.54	10.98	11.38	11.89	11.25	13.50	21.00	21.14	15.15	11.79	11.26	8.17	15.99
Zr	44.46	47.91	47.70	43.93	45.69	43.22	50.09	52.39	50.00	50.90	44.47	46.83	44.77	44.30	48.53
LOI:	1.24	0.85	1.65	1.65	1.58	1.78	1.73	2.31	2.109	3.71	2.25	1.32	2.14	1.89	3.58
CIPW-normative minerals (wt%):															
or	1.07	1.37	1.53	1.78	1.73	2.13	2.85	3.78	8.35	8.82	3.99	2.66	1.06	1.11	4.45
ab	17.89	18.11	17.08	18.01	15.46	15.38	18.46	16.62	15.66	19.64	17.05	16.77	17.41	17.62	21.27
an	33.28	33.29	33.74	33.63	33.10	32.73	33.23	34.01	32.83	32.21	33.50	34.64	32.39	33.00	31.01
ne	0.00	0.00	0.00	0.00	0.00	0.00	0.00	0.00	0.00	0.00	0.00	0.00	0.00	0.00	0.31
di	28.40	28.50	28.70	27.20	25.67	22.11	25.92	27.81	25.07	20.96	27.56	28.32	27.14	28.53	27.51
hy	7.32	7.98	9.37	8.62	11.95	15.80	7.03	5.76	8.54	6.73	4.11	8.48	14.69	11.54	0.00
ol	9.49	9.53	5.33	8.65	5.43	2.44	9.83	9.74	5.56	7.91	10.77	5.89	3.10	4.71	11.20
mt	1.73	1.77	1.49	1.64	1.52	1.43	1.73	1.80	1.84	1.86	1.82	1.66	1.59	1.62	1.72
il	1.74	1.73	1.74	1.76	1.67	1.67	1.78	1.80	1.84	1.91	1.79	1.78	1.72	1.72	1.82
ap	0.11	0.20	0.22	0.21	0.24	0.11	0.24	0.21	0.34	0.31	0.19	0.22	0.21	0.20	0.28
Total:	101.02	102.48	99.22	101.49	96.77	93.80	101.05	101.52	100.04	100.35	100.78	100.42	99.32	100.06	99.57
Mg#:	66.14	66.15	67.68	67.56	68.21	68.25	65.07	63.03	56.48	54.79	62.14	63.50	67.01	66.10	60.00

Table T5. Distribution of calcareous nannofossils, Holes 1201A, 1201B, 1201C, and 1201D. (**See table notes.** Continued on next five pages.)

Core, section, interval (cm)	Depth (mbsf)	Zone	Preservation	Group abundance	*Bicolumnus ovatus*	*Bramletteius serraculoides*	*Chiasmolithus* spp.	*Clausicoccus fenestratus*	*Coccoliths* spp. (dissolved)	*Coccolithus pelagicus*	*Coronocyclus nitescens*	*Cyclicargolithus abisectus*	*Cyclicargolithus* cf. *abisectus*	*Cyclicargolithus floridanus*	*Cyclicargolithus* spp. (dissolved)	*Dictyococcites bisectus*	*Dictyococcites hesslandii*	*Discoaster barbadiensis*	*Discoaster deflandrei*	*Discoaster saipanensis*	*Discoaster* spp.	*Discoaster tanii ornatus*	*Ericsonia formosa*	*Ericsonia subdisticha*	*Helicosphaera compacta*	*Helicosphaera euphratis*	*Helicosphaera* spp.	*Reticulofenestra circus*	*Reticulofenestra daviesii*
195-1201B-																													
1H-CC, 8–13	7.07			B																									
2H-3, 130–130	11.50			B																									
2H-5, 57–57	13.77			B																									
2H-CC, 13–19	17.24			B																									
3H-1, 50–50	17.20			B																									
3H-6, 65–65	24.85			B																									
3H-7, 50–50	26.20			B																									
3H-CC, 13–18	26.45			B																									
4H-1, 37–37	26.57		P	T					R				R																
4H-2, 78.5–78.5	28.49		P	F						R									D		R								
4H-3, 18.5–18.5	29.39	NN25	M	T									R		R				C										
4H-3, 50–50	29.70	NN25	M	A					R		F				A	F													
4H-3, 68–68	29.88	NN25	M	A				A	A	F	F	F			A	C			A							R			
4H-3, 95–95	30.15	NN25	M	A				A	A	C	F	A			A	C		R	F							R			
4H-3, 113–113	30.33	NN25	M	A								C			R	C		R	C										
4H-3, 127–127	30.47	NN25	M	A				A	A	C	F	C			A	C		R	C		C					F			
4H-3, 139–139	30.59	NN25		B																									
4H-CC, 21–26	36.18	NN25	P	T					R																				
5H-3, 73–73	39.43	NN25		B																									
5H-3, 104–104	39.74	NN25		B																									
5H-6, 80–80	44.00	NN25		B																									
5H-CC, 7–12	45.32	NN25		B																									
6H-1, 112–112	46.32	NN25		B																									
6H-CC, 28–33	46.78	NN25		B																									
7X-1, 27–29	46.97	NN25		B																									
7X-1, 96–98	47.66	NN25		B																									
7X-2, 49–51	48.69	NN25	P	T										R															
7X-2, 103–105	49.23	NN25	P	F				F	C	C		C		C	C	F					R								R
7X-3, 85–87	50.55	NN25		B																									
7X-3, 116–118	50.86	NN25		B																									
7X-CC, 21–31	52.42	NN25		B																									
8X-2, 56–58	53.96	NN25		B																									
8X-3, 105–107	55.95	NN25		B																									
8X-4, 3–5	56.43	NN25		B																									
8X-5, 45–45	58.35	NN25		B																									
8X-6, 5–5	58.95	NN25		B																									
8X-CC, 30–36	59.98	NN25	M	R					R				F		F	F			R				R						
9X-CC, 30–30	62.59	NN25		B																									
9X-CC, 47–51	62.76	NN25	M	T						R			C			C													
10X-1, 68–68	71.78	NN24	M	C		R		C		C		C	C			C			R			F			F	F			
10X-1, 93–93	72.03	NN24	M	C		R		C		C		C	C	C		C			R			F			R	R			
10X-1, 100–100	72.10	NN24	M	F		R		C		C		F		C	C	F			F		F			F	R				
10X-1, 117–117	72.27	NN24	M	C			R	C		C		F		A	C	F		F	F		F	F		R	R		F		
10X-CC, 38–43	72.98	NN24	M	R					C	C			C	C	C	F			F		R		R			R			
11X-CC, 32–37	81.02	NN24	P	R						C		C	C	C		F							R						
195-1201D-																													
1R-1, 43–43	80.83	NN24	P	T									R						R										
1R-4, 2–2	84.72	NN24		B																									
1R-4, 95–95	85.65	NN24	M	T									R																
1R-CC, 28–30	86.96	NN24	P	T																									
2R-4, 129–129	95.63	NN24		B																									
2R-5, 5–5	95.81	NN24	P	F					C	F		C																	
2R-5, 10–10	95.86	NN24	P	F					C	F		D																	
2R-5, 57–57	96.33	NN24	P	R									C			C													
2R-6, 126–126	98.48	NN24	P	R									C																
2R-CC, 13–15	98.72	NN24	P	R						R			A																
3R-4, 42–42	103.75	NP23	M	C	R		R	R	C	F		C	C	C		C									R				
3R-5, 112.5–112.5	105.89	NP23	P	C				R	C	C		C	F			F	F				R								

Table T5 (continued).

Core, section, interval (cm)	Depth (mbsf)	Zone	Preservation	Group abundance	*Reticulofenestra pseudoumbilicus*	*Reticulofenestra samodurovii*	*Reticulofenestra* sp.	*Reticulofenestra umbilicus*	*Sphenolithus ciperoensis*	*Sphenolithus conicus*	*Sphenolithus distentus*	*Sphenolithus intercalaris*	*Sphenolithus moriformis*	*Sphenolithus predistentus*	*Sphenolithus pseudoradians*	*Sphenolithus radians*	*Sphenolithus* spp.	*Zygrhablithus bijugatus*	Comments
195-1201B-																			
1H-CC, 8–13	7.07			B															
2H-3, 130–130	11.50			B															
2H-5, 57–57	13.77			B															
2H-CC, 13–19	17.24			B															
3H-1, 50–50	17.20			B															
3H-6, 65–65	24.85			B															
3H-7, 50–50	26.20			B															
3H-CC, 13–18	26.45			B															
4H-1, 37–37	26.57		P	T			R												
4H-2, 78.5–78.5	28.49		P	F									F						
4H-3, 18.5–18.5	29.39	NN25	M	T															
4H-3, 50–50	29.70	NN25	M	A			R		R				C						
4H-3, 68–68	29.88	NN25	M	A					R	F			C	R					
4H-3, 95–95	30.15	NN25	M	A					F	F			C	R					
4H-3, 113–113	30.33	NN25	M	A					F	F				F				R	
4H-3, 127–127	30.47	NN25	M	A		C			R	R			C	F					
4H-3, 139–139	30.59	NN25		B															
4H-CC, 21–26	36.18	NN25	P	T															
5H-3, 73–73	39.43	NN25		B															
5H-3, 104–104	39.74	NN25		B															
5H-6, 80–80	44.00	NN25		B															
5H-CC, 7–12	45.32	NN25		B															
6H-1, 112–112	46.32	NN25		B															
6H-CC, 28–33	46.78	NN25		B															
7X-1, 27–29	46.97	NN25		B															
7X-1, 96–98	47.66	NN25		B															
7X-2, 49–51	48.69	NN25	P	T			R						R						
7X-2, 103–105	49.23	NN25	P	F		R	C		F				C	F				R	Dissolution and then overgrown
7X-3, 85–87	50.55	NN25		B															
7X-3, 116–118	50.86	NN25		B															
7X-CC, 21–31	52.42	NN25		B															
8X-2, 56–58	53.96	NN25		B															
8X-3, 105–107	55.95	NN25		B															
8X-4, 3–5	56.43	NN25		B															
8X-5, 45–45	58.35	NN25		B															
8X-6, 5–5	58.95	NN25		B															
8X-CC, 30–36	59.98	NN25	M	R		R							R	R					
9X-CC, 30–30	62.59	NN25		B															
9X-CC, 47–51	62.76	NN25	M	T															
10X-1, 68–68	71.78	NN24	M	C		C		R	F		R		F	C	R			F	
10X-1, 93–93	72.03	NN24	M	C		C		F	R		R		R	C				R	
10X-1, 100–100	72.10	NN24	M	F		R		R	R		F		A	C	R			R	
10X-1, 117–117	72.27	NN24	M	C		F		R	R		F		C	C	R			F	
10X-CC, 38–43	72.98	NN24	M	R		F	C		R		R		F	F	R			R	
11X-CC, 32–37	81.02	NN24	P	R		R								C					
195-1201D-																			
1R-1, 43–43	80.83	NN24	P	T															
1R-4, 2–2	84.72	NN24		B															
1R-4, 95–95	85.65	NN24	M	T															
1R-CC, 28–30	86.96	NN24	P	T		F													
2R-4, 129–129	95.63	NN24		B															
2R-5, 5–5	95.81	NN24	P	F									F	F					
2R-5, 10–10	95.86	NN24	P	F									R	R					Dissolution and then overgrown
2R-5, 57–57	96.33	NN24	P	R															Dissolution and then overgrown
2R-6, 126–126	98.48	NN24	P	R															Dissolution and then overgrown
2R-CC, 13–15	98.72	NN24	P	R									R	F					Overgrown
3R-4, 42–42	103.75	NP23	M	C							R		F	R					Overgrown
3R-5, 112.5–112.5	105.89	NP23	P	C		F						F	F	C					Overgrown

Table T5 (continued).

Core, section, interval (cm)	Depth (mbsf)	Zone	Preservation	Group abundance	*Bicolumnus ovatus*	*Bramletteius serraculoides*	*Chiasmolithus* spp.	*Clausicoccus fenestratus*	*Coccoliths* spp. (dissolved)	*Coccolithus pelagicus*	*Coronocyclus nitescens*	*Cyclicargolithus abisectus*	*Cyclicargolithus* cf. *abisectus*	*Cyclicargolithus floridanus*	*Cyclicargolithus* spp. (dissolved)	*Dictyococcites bisectus*	*Dictyococcites hesslandii*	*Discoaster barbadiensis*	*Discoaster deflandrei*	*Discoaster saipanensis*	*Discoaster* spp.	*Discoaster tanii ornatus*	*Ericsonia formosa*	*Ericsonia subdisticha*	*Helicosphaera compacta*	*Helicosphaera euphratis*	*Helicosphaera* spp.	*Reticulofenestra circus*	*Reticulofenestra daviesii*
3R-5, 117–117	105.93	NP23	P	F				R	R	F		F				R	R				R								
3R-CC, 17–19	108.31	NP23	M	F					C	C		C				C					R								
4R-3, 8–8	112.07	NP23	P	C				F		F		D				R					R			R					
4R-CC, 31–34	118.99	NP23	P	T									R																
5R-7, 4–4	126.93	NP23	M	C				F		F		A				C					R								R
5R-CC, 26–30	128.17	NP23	P	F						R			D						R		R								
6R-CC, 17–22	137.01	NP23	M	T					C	C	R		C			R					R	R			C				
7R-2, 53.5–53.5	139.72	NP23	P	R						F		C				F			F										
7R-5, 93–93	144.07	NP23	P	R						F		C				F			F								R		
7R-6, 72–72	145.15	NP23	P	R						R		F				R			R										
7R-CC, 28–33	146.93	NP23	P	F					C	C		C				C			F		R	F							
8R-CC, 0–5	157.03	NP23	P	T								R																	
9R-CC, 14–19	166.05	NP23	M	T						C		C				R													
10R-CC, 16–20	172.30	NP23	M	R						C		C				R			R										
11R-CC, 10–24	186.20	NP23	M	R						C		C																	
12R-CC, 24–26	194.74	NP23	M	R						C		C																	
13R-CC, 4–6	204.50	NP23	M	R								C																	
14R-CC, 16–19	212.64	NP23	M	R				R		F	R	A				R			R			R		F	R				F
16R-CC, 20–22	230.76	NP23	M	R								F				R													
17R-CC, 9–14	242.41	NP23	M	T								C				R													
19R-CC, 13–17	261.96	NP22	P	R					C			C				F						R							
20R-CC, 18–22	271.26	NP22	P	T								R																	
21R-CC, 0–6	280.92	NP22	P	F					C			C				C			F										
22R-4, 56–56	287.28	NP22	P	F						F		R		R		F			R		F								
22R-6, 78–78	290.47	NP22	P	C						C		F				C													
22R-CC, 13–15	290.86	NP22	P	F							F	C				F			R			R							
23R-CC, 0–3	301.02	NP22	M	R								C				C			F								F		
24R-1, 94–94	302.44	NP22	P	C						C			C	F		C					F								
24R-3, 38–38	304.42	NP22	P	C						F			C	C		C					C						F		
24R-CC, 0–6	307.49	NP22	M	F						C						C			R			R							F
25R-CC, 0–3	317.36	NP22	P	F						C			C			C			F			R							
26R-7, 31–31	329.44	NP22	M	C						C		R																	
26R-CC, 17–21	330.58	NP22	P	F						C		C				C		R	F			F							
27R-5, 87–87	336.43	NP22	M	R												R													
27R-CC, 20–23	340.21	NP22	M	F						R		C				F			C		F								
28R-CC, 0–3	347.97	NP22	M	T								R							R										
29R-CC, 16–20	356.24	NP22	G	T																									
30R-CC, 0–4	368.81	NP22		B																									
31R-CC, 20–24	378.19	NP21	M	F						C						C		F				R	F						
32R-7, 52.5–52.5	386.99	NP21	P	R												R													
32R-CC, 8–13	387.18	NP21	M	T								R																	
33R-CC, 17–20	397.03	NP21	P	R									R			C							R						
34R-CC, 6–9	405.49	NP21	P	T																									
35R-CC, 11–14	415.14	NP21	P	R												R							R						
36R-4, 2–2	420.75	NP21	G	A	C	F	R	F		C	R	A				A		R	C	R	F		F			F			F
36R-4, 85–85	421.58	NP21	M	R	C					A		C				A					F								
36R-CC, 18–22	426.57	NP21	M	R	F					C		C				A			R				R						
37R-CC, 20–24	436.24	NP21		B																									
38R-1, 12–12	436.12	NP21	P	R												C			R										
38R-2, 83–83	438.10	NP21	M	A	R					C	R					C			R			R	R						
38R-4, 53.5–53.5	440.55	NP21	M	C												R			R										
38R-CC, 17–22	445.84	NP21		B																									
39R-1, 70–70	446.40	NP21		B																									
39R-2, 77.5–77.5	447.82	NP21	P	F												C													
39R-CC, 0–4	454.61	NP21	P	R												A													
40R-6, 10–10	462.36	NP19/20	M	A	F					C						C		C	R	C	F		F						
40R-6, 25–25	462.51	NP19/20	M	A	F					C						C		C	R	C	F		F						
40R-6, 120–120	463.46		M	T																									
40R-7, 14–14	463.79			B																									
40R-7, 103–103	464.68			B																									

Table T5 (continued).

Core, section, interval (cm)	Depth (mbsf)	Zone	Preservation	Group abundance	*Reticulofenestra pseudoumbilicus*	*Reticulofenestra samodurovii*	*Reticulofenestra* sp.	*Reticulofenestra umbilicus*	*Sphenolithus ciperoensis*	*Sphenolithus conicus*	*Sphenolithus distentus*	*Sphenolithus intercalaris*	*Sphenolithus moriformis*	*Sphenolithus predistentus*	*Sphenolithus pseudoradians*	*Sphenolithus radians*	*Sphenolithus* spp.	*Zygrhablithus bijugatus*	Comments
3R-5, 117–117	105.93	NP23	P	F		R						R	R	R					
3R-CC, 17–19	108.31	NP23	M	F								R		F					Dissolution and then overgrown
4R-3, 8–8	112.07	NP23	P	C		C							F	F					
4R-CC, 31–34	118.99	NP23	P	T															Dissolution and then overgrown
5R-7, 4–4	126.93	NP23	M	C									F	F					
5R-CC, 26–30	128.17	NP23	P	F		F								R					Strong dissolution
6R-CC, 17–22	137.01	NP23	M	T															Trace
7R-2, 53.5–53.5	139.72	NP23	P	R									F	F					Dissolution
7R-5, 93–93	144.07	NP23	P	R		R							R	R					Dissolution
7R-6, 72–72	145.15	NP23	P	R									R	R					Strong dissolution (<5% identifiable)
7R-CC, 28–33	146.93	NP23	P	F										R					Dissolution
8R-CC, 0–5	157.03	NP23	P	T															
9R-CC, 14–19	166.05	NP23	M	T															
10R-CC, 16–20	172.30	NP23	M	R															
11R-CC, 10–24	186.20	NP23	M	R															
12R-CC, 24–26	194.74	NP23	M	R															
13R-CC, 4–6	204.50	NP23	M	R															
14R-CC, 16–19	212.64	NP23	M	R		C							C	C	R				
16R-CC, 20–22	230.76	NP23	M	R		R													
17R-CC, 9–14	242.41	NP23	M	T															
19R-CC, 13–17	261.96	NP22	P	R		F		R					F	C					Strong dissolution
20R-CC, 18–22	271.26	NP22	P	T															Strong dissolution
21R-CC, 0–6	280.92	NP22	P	F		F		F				R	C	C					Strong dissolution
22R-4, 56–56	287.28	NP22	P	F		F		R				R	F						Strong dissolution (<5% identifiable)
22R-6, 78–78	290.47	NP22	P	C		R							C	C					Strong dissolution (10% identifiable)
22R-CC, 13–15	290.86	NP22	P	F		F		C				R	C	C					Strong dissolution
23R-CC, 0–3	301.02	NP22	M	R			A	C					C	C					Dissolution
24R-1, 94–94	302.44	NP22	P	C										C					Fragmental and overgrown
24R-3, 38–38	304.42	NP22	P	C		F				R			F	C					Strong dissolution
24R-CC, 0–6	307.49	NP22	M	F			C	C						F					
25R-CC, 0–3	317.36	NP22	P	F		F		F					R	R					Strong-moderate dissolution
26R-7, 31–31	329.44	NP22	M	C										C					Strong-moderate dissolution
26R-CC, 17–21	330.58	NP22	P	F				F					F	C					Strong-moderate dissolution
27R-5, 87–87	336.43	NP22	M	R															
27R-CC, 20–23	340.21	NP22	M	F									F	C					
28R-CC, 0–3	347.97	NP22	M	T										F					
29R-CC, 16–20	356.24	NP22	G	T		R													
30R-CC, 0–4	368.81	NP22		B															
31R-CC, 20–24	378.19	NP21	M	F													F		
32R-7, 52.5–52.5	386.99	NP21	P	R				R											
32R-CC, 8–13	387.18	NP21	M	T															
33R-CC, 17–20	397.03	NP21	P	R				A											
34R-CC, 6–9	405.49	NP21	P	T															
35R-CC, 11–14	415.14	NP21	P	R				R											
36R-4, 2–2	420.75	NP21	G	A		C		F					R	F	R	R	R	R	
36R-4, 85–85	421.58	NP21	M	R															
36R-CC, 18–22	426.57	NP21	M	R				F					F	F			F		
37R-CC, 20–24	436.24	NP21		B															
38R-1, 12–12	436.12	NP21	P	R				C											Dissolution and then overgrown
38R-2, 83–83	438.10	NP21	M	A				C						R		R			
38R-4, 53.5–53.5	440.55	NP21	M	C				C											
38R-CC, 17–22	445.84	NP21		B															
39R-1, 70–70	446.40	NP21		B															
39R-2, 77.5–77.5	447.82	NP21	P	F				C											
39R-CC, 0–4	454.61	NP21	P	R				A											
40R-6, 10–10	462.36	NP19/20	M	A				C											
40R-6, 25–25	462.51	NP19/20	M	A				C											
40R-6, 120–120	463.46		M	T			R												
40R-7, 14–14	463.79			B															
40R-7, 103–103	464.68			B															

Table T5 (continued).

Core, section, interval (cm)	Depth (mbsf)	Zone	Preservation	Group abundance	*Bicolumnus ovatus*	*Bramletteius serraculoides*	*Chiasmolithus* spp.	*Clausicoccus fenestratus*	*Coccoliths* spp. (dissolved)	*Coccolithus pelagicus*	*Coronocyclus nitescens*	*Cyclicargolithus abisectus*	*Cyclicargolithus* cf. *abisectus*	*Cyclicargolithus floridanus*	*Cyclicargolithus* spp. (dissolved)	*Dictyococcites bisectus*	*Dictyococcites hesslandii*	*Discoaster barbadiensis*	*Discoaster deflandrei*	*Discoaster saipanensis*	*Discoaster* spp.	*Discoaster tanii ornatus*	*Ericsonia formosa*	*Ericsonia subdisticha*	*Helicosphaera compacta*	*Helicosphaera euphratis*	*Helicosphaera* spp.	*Reticulofenestra circus*	*Reticulofenestra daviesii*
40R-CC, 23–27	465.28			B																									
41R-3, 32–32	468.00		P	T													R												
41R-CC, 0–5	472.01			B																									
42R-1, 84–84	475.34			B																									
42R-1, 89–89	475.39			B																									
42R-CC, 16–21	484.48			B																									
43R-CC, 0–3	490.59			B																									
44R-6, 80–80	502.00			B																									
44R-CC, 14–19	503.53			B																									
45R-1, 9–9	503.39			B																									
45R-1, 10.5–10.5	503.41			B																									
45R-1, 38–41	503.68			B																									
45R-2, 12–12	504.92			B																									
45R-2, 73–73	505.53			B																									
45R-3, 88–88	507.18			B																									
45R-4, 1–1	507.37			B																									
45R-4, 5–5	507.41			B																									
45R-4, 10–10	507.46			B																									
45R-4, 14–14	507.50			B																									
45R-4, 19–19	507.55			B																									
45R-4, 55–55	507.91			B																									
45R-4, 129–129	508.65			B																									
45R-5, 15–15	509.01			B																									
45R-5, 26–26	509.12			B																									
45R-5, 27–27	509.13			B																									
45R-5, 56–56	509.42			B																									
45R-5, 60–60	509.46			B																									
45R-5, 63–63	509.49			B																									
45R-5, 74.5–74.5	509.61			B																									
45R-5, 83–83	509.69			B																									
45R-5, 85–85	509.71			B																									
45R-5, 86–86	509.72			B																									
45R-5, 87–87	509.73			B																									
45R-5, 88–88	509.74			B																									
45R-5, 89–89	509.75			B																									
45R-5, 90–90	509.76			B																									
45R-5, 91–91	509.77			B																									
45R-CC, 16–20	510.17			B																									
46R-5, 88–88	519.64			B																									
47R-1, 102–102	523.12			B																									
47R-1, 106–106	523.16			B																									
47R-1, 110–110	523.20			B																									
47R-1, 118–118	523.28			B																									
195-1201A-																													
1H-CC, 11–18	1.42			B																									
195-1201C-																													
1H-CC, 12–16	6.47			B																									
2H-CC, 17–22	16.40			B																									
3H-1, 149–149	17.59		P	T									C																
3H-2, 128–128	18.88		P	T											C														
3H-3, 110–110	20.20			B																									
3H-6, 95–95	24.55		P	T									C																
3H-7, 2–2	25.12		M	T		R									F				R										
3H-CC, 11–16	25.88		M	T																									
4H-CC, 23–29	35.58			B																									
5H-CC, 26–32	44.82			B																									

Notes: The nannofossils in the long and continuous Holes 1201B and 1201D are used for zonation of this site. Preservation: G = good, M = moderate, P = poor. Abundance: D = dominant, A = abundant, C = common, F = few, R = rare, T = trace, B = barren. Categories for abundance and preservation are defined in "Biostratigraphy," p. 14, in the "Explanatory Notes" chapter.

Table T5 (continued).

Core, section, interval (cm)	Depth (mbsf)	Zone	Preservation	Group abundance	*Reticulofenestra pseudoumbilicus*	*Reticulofenestra samodurovii*	*Reticulofenestra* sp.	*Reticulofenestra umbilicus*	*Sphenolithus ciperoensis*	*Sphenolithus conicus*	*Sphenolithus distentus*	*Sphenolithus intercalaris*	*Sphenolithus moriformis*	*Sphenolithus predistentus*	*Sphenolithus pseudoradians*	*Sphenolithus radians*	*Sphenolithus* spp.	*Zygrhablithus bijugatus*	Comments
40R-CC, 23–27	465.28			B															
41R-3, 32–32	468.00		P	T															
41R-CC, 0–5	472.01			B															
42R-1, 84–84	475.34			B															
42R-1, 89–89	475.39			B															
42R-CC, 16–21	484.48			B															
43R-CC, 0–3	490.59			B															
44R-6, 80–80	502.00			B															
44R-CC, 14–19	503.53			B															
45R-1, 9–9	503.39			B															
45R-1, 10.5–10.5	503.41			B															
45R-1, 38–41	503.68			B															
45R-2, 12–12	504.92			B															
45R-2, 73–73	505.53			B															
45R-3, 88–88	507.18			B															
45R-4, 1–1	507.37			B															
45R-4, 5–5	507.41			B															
45R-4, 10–10	507.46			B															
45R-4, 14–14	507.50			B															
45R-4, 19–19	507.55			B															
45R-4, 55–55	507.91			B															
45R-4, 129–129	508.65			B															
45R-5, 15–15	509.01			B															
45R-5, 26–26	509.12			B															
45R-5, 27–27	509.13			B															
45R-5, 56–56	509.42			B															
45R-5, 60–60	509.46			B															
45R-5, 63–63	509.49			B															
45R-5, 74.5–74.5	509.61			B															
45R-5, 83–83	509.69			B															
45R-5, 85–85	509.71			B															
45R-5, 86–86	509.72			B															
45R-5, 87–87	509.73			B															
45R-5, 88–88	509.74			B															
45R-5, 89–89	509.75			B															
45R-5, 90–90	509.76			B															
45R-5, 91–91	509.77			B															
45R-CC, 16–20	510.17			B															
46R-5, 88–88	519.64			B															
47R-1, 102–102	523.12			B															
47R-1, 106–106	523.16			B															
47R-1, 110–110	523.20			B															
47R-1, 118–118	523.28			B															
195-1201A-																			
1H-CC, 11–18	1.42			B															
195-1201C-																			
1H-CC, 12–16	6.47			B															
2H-CC, 17–22	16.40			B															
3H-1, 149–149	17.59		P	T															
3H-2, 128–128	18.88		P	T															
3H-3, 110–110	20.20			B															
3H-6, 95–95	24.55		P	T															
3H-7, 2–2	25.12		M	T									R						
3H-CC, 11–16	25.88		M	T	R														
4H-CC, 23–29	35.58			B															
5H-CC, 26–32	44.82			B															

Table T6. Estimated ages of nannofossil datum levels, Site 1201.

Event	Core, section, interval (cm)	Depth (mbsf)	Age (Ma)
195-1201B-			
LO? *Dictyococcites bisectus*	4H-3, 50	29.70	>23.9
LO *Sphenolithus ciperoensis*	4H-3, 68	29.88	24.5
LO? *Sphenolithus distentus*	10X-1, 68	71.78	>27.5
FO *Sphenolithus ciperoensis*	10X-CC, 38–43	72.98	29.9
195-1201D-			
FO *Sphenolithus distentus*	3R-4, 42	103.75	31.5
LO *Reticulofenestra umbilicus*	19R-CC,13–17	261.96	32.3
LO *Ericsonia formosa*	31R-CC, 20–24	378.19	32.8
LO *Discoaster saipanensis*	40R-6, 10	462.36	34.2
LO *Discoaster barbadiensis*	40R-6, 10	462.36	34.3

Note: LO = last occurrence, FO = first occurrence, ? = possible last occurrence.

Table T7. Composite record compilation of magnetostratigraphic chron, age determination, and depth, Site 1201.

Chron	Age (Ma)	Depth (mbsf)
C3n.4n (t)	4.980	0.17
C3n.4n (o)	5.230	0.27
C3An.1n (t)	5.894	0.98
C3An.1n (o)	6.137	1.51
C3An.2n (t)	6.269	1.73
C3An.2n (o)	6.567	2.32
C3Bn (t)	6.935	2.85
C3Bn (o)	7.091	3.07
C3Br.1n (t)	7.135	3.17
C3Br.1n (o)	7.170	3.22
C3Br.2n (t)	7.341	3.56
C3Br.2n (o)	7.375	3.63
C4n.1n (t)	7.432	3.78
C4n.1n (o)	7.562	4.02
C4n.2n (t)	7.650	4.17
C4n.2n (o)	8.072	5.78
C4r.1n (t)	8.225	6.17
C4r.1n (o)	8.257	6.37
C4An (t)	8.699	7.10
C4An (o)	9.025	7.88
C4Ar.1n (t)	9.230	8.32
C4Ar.1n (o)	9.308	8.71
C4Ar.2n (t)	9.580	9.27
C4Ar.2n (o)	9.642	9.44
C5n.1n (t)	9.740	9.63
C5n.1n (o)	9.880	10.02
C5n.2n (t)	9.920	10.12
C5n.2n (o)	10.949	12.27
C5r.1n (t)	11.052	12.51
C5r.1n (o)	11.099	12.63
C5r.2n (t)	11.476	12.88
C5r.2n (o)	11.531	13.02
C5An.1n (t)	11.935	13.51
C5An.1n (o)	12.078	13.80
C5An.2n (t)	12.184	14.49
C5An.2n (o)	12.401	14.63
C5Ar.1n (t)	12.678	14.80
C5Ar.1n (o)	12.708	15.17
C5Ar.2n (t)	12.775	15.71
C5Ar.2n (o)	12.819	15.83
C5AAn (t)	12.991	17.63
C5AAn (o)	13.139	18.32
C5ABn (t)	13.302	18.83
C5ABn (o)	13.510	18.87
C5ACn (t)	13.703	19.83
C5ACn (o)	14.076	21.70
C5ADn (t)	14.178	21.73
C5ADn (o)	14.612	23.53
C5Bn.1n (t)	14.800	24.12
Hiatus		
C6Cn.3n (o)	24.118	26.40
C7n.1n (t)	24.730	30.00
C7n.1n (o)	24.781	30.80
C7n.2n (t)	24.835	31.70
C7n.2n (o)	25.183	35.10
Undetermined		
C11n.2n (t)	29.765	71.56
Undetermined		
C12n (t)	30.479	88.60
C12n (o)	30.939	173.40
C13n (t)	33.058	389.10
C13n (o)	33.545	423.40
C15n (t)	34.655	447.00
C15n (o)	34.940	457.80
C16n.1n	35.343	468.50
C16n.1n	35.526	480.30
C16n.2n	35.685	485.70

Note: t = termination, o = onset.

Table T8. Composition of interstitial water, Site 1201. (Continued on next page.)

Core, section, interval (cm)				Temperature		pH	Alkalinity (meq/kg)	Chlorinity (mmol/kg)	Sulfate (mmol/kg)	Na (mmol/kg)	K (mmol/kg)	Mg (mmol/kg)	Ca (mmol/kg)
Method:	IW#	Depth (mbsf)	Volume (mL)	In situ* (°C)	Squeeze (°C)	ISE	ET	ET	IC	Calculated†	IC	CT	ET
195-1201A-													
1H-1, 126–131	1	1.26	45	1.7	3.0	7.83	2.36	541.2	26.00	465.0	11.40	49.65	9.94
195-1201B-													
1H-1, 145–150	1	1.50	42	1.7	3.1	7.61	2.62	538.8	25.99	459.9	11.25	50.85	10.29
1H-3, 145–150	2	4.50	42	2.1	1.5	7.54	2.16	539.3	27.30	460.0	10.67	51.60	11.08
1H-4, 145–150	3	6.00	42	2.3	1.8	7.67	2.24	539.8	27.21	459.9	10.89	51.57	11.27
2H-1, 145–150	4	8.70	22	2.6	1.8	7.71	2.24	538.8	27.04	455.6	10.09	52.57	12.12
2H-3, 145–150	5	11.70	42	3.0	0.0	7.76	2.10	544.6	27.67	462.5	10.50	51.91	12.62
2H-5, 145–150	6	14.70	42	3.3	3.0	7.89	2.03	544.6	27.36	461.7	10.31	51.02	13.66
2H-7, 86–91	7	17.11	59	3.6	3.2	7.77	1.90	543.6	27.02	459.3	10.61	50.74	14.11
3H-1, 145–150	8	18.20	42	3.8	3.0	7.77	1.98	546.6	27.29	461.2	10.40	51.25	14.52
3H-3, 145–150	9	21.20	53	4.2	2.1	7.86	1.84	547.5	27.81	462.4	10.15	50.80	15.43
3H-5, 145–150	10	24.20	52	4.5	1.5	7.47	1.77	548.5	26.15	460.2	10.55	49.99	15.94
3H-7, 57–62	11	26.32	42	4.8	1.5	7.76	1.73	548.5	26.38	459.8	10.37	49.82	16.57
4H-1, 145–150	12	27.70	60	5.0	2.7	7.71	1.58	550.4	26.46	459.8	10.49	50.27	17.04
4H-3, 145–150	13	30.70	50	5.3	2.0	7.71	1.58	549.5	25.32	456.8	10.22	49.48	17.83
4H-5, 145–150	14	33.70	60	5.7	1.8	7.71	1.56	551.4	24.88	458.2	10.20	48.63	18.52
4H-7, 72–77	15	35.97	60	6.0	1.8	7.73	1.43	551.4	23.66	456.2	9.93	48.26	18.75
5H-1, 145–150	16	37.20	57	6.2	2.4	7.87	1.40	547.5	26.26	454.0	9.45	49.60	19.41
5H-3, 145–150	17	40.20	59	6.5	2.7	7.77	1.35	550.4	25.81	455.6	9.81	49.16	19.85
5H-5, 145–150	18	43.20	66	6.9	2.8	7.87	1.20	553.3	25.46	455.8	9.84	49.05	20.89
5H-7, 50–55	19	45.25	57	7.2	2.7	7.83	1.23	553.3	26.18	456.4	10.32	48.85	21.24
6H-1, 125–130	20	46.50	57	7.3	2.7	7.85	1.14	550.4	25.82	451.6	10.20	48.43	22.28
7X-3, 145–150	21	51.20	30	7.9	2.7	8.19	1.27	550.4	25.54	452.0	10.59	45.63	24.46
8X-3, 140–150	22	56.40	52	8.6	2.7	8.66	1.18	545.6	25.13	443.6	9.87	43.39	28.40
10X-1, 140–150	23	72.60	4	10.6	2.7			557.2	26.42	447.8	10.01	34.96	41.15
195-1201D-													
1R-2, 129–143	1	83.33	8	11.9		8.74	0.90	554.8	26.02	461.7	9.58	24.53	43.71
7R-CC, 0–12	2	146.77	35	19.9		8.86	0.42	569.9	19.87	346.8	3.19	3.19	126.80
8R-4, 124–140	3	153.21	54	20.6	2.0	9.42	0.48	580.5	20.02	348.5	3.28	2.00	132.63
9R-4, 128–148	4	163.14	28	21.9	2.0	9.45	0.71	586.4	19.28	348.6	3.09	0.13	136.81
11R-5, 124–140	5	183.41	11	24.4	2.0	8.49	0.33	594.1	19.43	325.2	2.69	0.00	152.71
13R-3, 116–135	6	199.66	22	26.4	2.0	9.12	0.52	598.0	17.92	298.2	2.15	0.00	167.01
17R-3, 120–133	7	238.04	40	31.2	2.0	9.15	0.55	610.6	17.30	259.4	1.06	0.00	192.67
20R-3, 140–150	8	267.16	9	34.9	2.0	9.52	0.55	620.3	17.69	230.5	0.87	0.00	212.45
22R-1, 122–141	9	283.71	28	36.9	2.0	9.23	0.61	618.4	17.00	229.3	0.90	0.00	211.41
23R-3, 116–132	10	296.08	40	38.5	2.0	9.39	0.90	625.2	18.01	220.2	0.86	0.00	220.50
24R-1, 123–138	11	302.88	18	39.3	2.0	9.33	0.62	621.3	18.20	222.5	0.89	0.00	217.47
26R-2, 130–145	12	323.54	54	41.9	2.0	9.55	0.71	626.2	16.62	218.7	0.80	0.00	220.31
27R-3, 138–148	13	334.22	22	43.3	2.0	9.45	0.74	627.1	18.04	220.7	0.76	0.00	221.26
28R-6, 89–105	14	347.97	18	45.0	2.0	9.50	0.79	611.6	17.80	208.1	0.74	0.00	219.55
30R-1, 0–9	15	359.19	25	46.5	2.0	9.59	0.93	625.2	17.71	197.6	0.38	0.00	231.77
32R-4, 120–130	16	383.96	44	49.5	2.0	9.41	0.85	631.0	18.68	202.4	0.78	0.00	233.00
33R-3, 113–129	17	392.08	32	50.5	2.0	9.45	0.60	628.6	17.93	190.2	0.38	0.00	237.26
35R-1, 125–140	18	408.50	30	52.5	2.0	9.95	1.24	633.9	17.77	189.4	0.78	0.00	240.29
37R-1, 0–12	19	426.52	8	54.9	2.0	9.51	0.99	624.2	17.81	189.3	0.76	0.00	235.36
38R-1, 114–127	20	437.27	34	56.1	2.0	9.77	0.93	633.0	17.11	160.1	0.00	0.00	254.02
40R-1, 0–23	21	455.53	8	58.6	2.0	9.47	0.80	632.0	16.74	157.9	0.38	0.00	254.02
42R-1, 0–18	22	474.68	8	61.0	2.0	9.46	0.88	633.9	16.86	168.1	0.00	0.00	250.23
44R-1, 0–11	23	493.81	25	63.4	2.0	9.44	0.77	635.9	16.37	166.3	0.76	0.00	251.18
44R-2, 135–150	24	496.70	10	63.5	2.0	9.48	0.88	641.7	15.45	156.7	0.00	0.00	258.37
44R-4, 135–150	25	499.70	4	63.9	2.0	9.37	0.86	646.5	16.13	133.2	0.00	0.00	273.24
44R-5, 135–150	26	501.20	6	64.1	2.0	9.12	0.67	644.6	16.56	152.2	0.00	0.00	263.10
45R-1, 135–150	27	504.80	20	64.6	2.0	10.03	1.15	644.6	15.84	140.1	0.85	0.00	268.22
45R-3, 90–106	28	507.36	0.05	64.9	2.0			638.0‡	15.43	139.1‡	0.00		
45R-5, 0–15	29	509.01	2	65.2	2.0			601.6‡	13.51	152.7‡	0.00		

Notes: * = Based on a bottom-water temperature of 1.51°C and a linear extrapolation from a measured temperature of 7.08°C at 44.6 mbsf in Hole 1201C. Methods: ISE = ion-specific electrode, ET = electrochemical titration, IC = ion chromatography, CT = colorimetric titration, Color = colorimetric spectrophotometry, ICP-AES = inductively coupled plasma–atomic emission spectroscopy. † = calculated from charge balance; these values average 2% higher than Na by IC because chloride by IC is 1% too high and Na by IC is 1% too low. ‡ = as measured by IC; these two samples were too small to analyze by other methods.

Table T8 (continued).

Core, section, interval (cm)		Depth	Na/Cl (mol/mol)	NH_3 (µmol/kg)	PO_4 (µmol/kg)	F (µmol/kg)	Sr (µmol/kg)	Mn (µmol/kg)	Fe (µmol/kg)	Al (µmol/kg)	Si (µmol/kg)	B (µmol/kg)	Li (µmol/kg)
Method:	IW#	(mbsf)	Calculated	Color	Color	ISE	ICP-AES	ICP-AES	ICP-AES	ICP-AES	ICP-AES	ICP-AES	ICP-AES
195-1201A-													
1H-1, 126–131	1	1.26	0.8591		0.98	66.7	78.8	0.26	0.04	2.9	225	594	32.2
195-1201B-													
1H-1, 145–150	1	1.50	0.8535	1.24	<0.25	23.6	81.3	0.33	0.05	0.0	227	605	29.2
1H-3, 145–150	2	4.50	0.8530	1.37	<0.25	14.1	79.4	0.22	0.01	0.0	155	630	25.8
1H-4, 145–150	3	6.00	0.8520	1.24	<0.25	13.6	81.3	0.22	0.59	0.6	140	620	26.5
2H-1, 145–150	4	8.70	0.8457	1.51	<0.25	17.7	82.7	0.27	0.73	0.0	129	646	25.4
2H-3, 145–150	5	11.70	0.8492	1.44	<0.25	20.5	79.2	0.12	0.00	0.0	97	600	25.4
2H-5, 145–150	6	14.70	0.8477	1.17	<0.25	20.1	83.2	0.11	0.00	1.6	80	582	25.4
2H-7, 86–91	7	17.11	0.8448	1.37	<0.25	5.6	83.5	0.36	0.06	0.0	111	715	26.5
3H-1, 145–150	8	18.20	0.8438	1.30	<0.25	6.5	85.2	0.19	0.00	0.8	100	610	25.9
3H-3, 145–150	9	21.20	0.8445	1.37	<0.25	5.3	87.4	0.37	0.00	1.2	105	622	26.2
3H-5, 145–150	10	24.20	0.8390	2.18	<0.25	6.2	89.5	0.72	0.00	1.0	109	681	25.6
3H-7, 57–62	11	26.32	0.8384	1.64	1.34	5.8	87.9	0.43	0.35	0.0	111	646	25.3
4H-1, 145–150	12	27.70	0.8354	1.44	<0.25	4.7	89.7	0.18	0.01	0.0	107	567	25.1
4H-3, 145–150	13	30.70	0.8314	1.51	<0.25	4.4	88.0	0.00	0.00	0.4	118	589	24.8
4H-5, 145–150	14	33.70	0.8310	1.64	<0.25	5.2	85.3	0.59	0.52	2.0	127	617	27.9
4H-7, 72–77	15	35.97	0.8274	1.10	<0.25	4.1	82.7	0.02	0.00	1.8	110	570	25.5
5H-1, 145–150	16	37.20	0.8291	1.57	<0.25	3.3	93.3	0.40	0.33	3.5	110	606	24.6
5H-3, 145–150	17	40.20	0.8277	1.44	<0.25	2.9	90.5	0.55	0.00	0.0	107	615	22.3
5H-5, 145–150	18	43.20	0.8236	1.10	<0.25	2.7	96.3	0.28	0.00	1.7	106	565	22.4
5H-7, 50–55	19	45.25	0.8249	1.30	<0.25	2.9	94.2	0.71	0.00	0.0	128	572	22.6
6H-1, 125–130	20	46.50	0.8204	1.51	<0.25	2.2	95.2	1.01	0.00	1.2	105	539	21.1
7X-3, 145–150	21	51.20	0.8212	1.51	0.25	3.3	93.7	1.40	0.00	2.3	422	471	24.2
8X-3, 140–150	22	56.40	0.8130	1.51	<0.25	3.2	96.7	2.72	0.00	0.0	284	216	20.8
10X-1, 140–150	23	72.60	0.8037	0.90	0.61	4.4							
195-1201D-													
1R-2, 129–143	1	83.33	0.8322	1.64	<0.25	20.0	107.4	11.32	0.00	3.2	520	260	13.3
7R-CC, 0–12	2	146.77	0.6086	1.64	2.78	10.5	114.7	8.54	0.00	9.0	200	91	3.5
8R-4, 124–140	3	153.21	0.6003	1.51	0.25	10.2	114.2	4.29	0.00	14.2	253	88	3.6
9R-4, 128–148	4	163.14	0.5946	1.51	0.25	13.0	105.4	4.03	0.00	14.7	261	84	3.9
11R-5, 124–140	5	183.41	0.5474	3.13	<0.25	15.9	83.8	7.72	1.05	19.2	261	100	3.6
13R-3, 116–135	6	199.66	0.4987	1.51	<0.25	14.5	66.1	3.76	0.90	18.4	255	113	3.2
17R-3, 120–133	7	238.04	0.4248	1.51	<0.25	3.6	47.3	1.10	0.00	23.1	218	224	5.6
20R-3, 140–150	8	267.16	0.3716	1.64	<0.25	4.5	49.4	0.61	0.00	27.1	204	265	6.1
22R-1, 122–141	9	283.71	0.3708	1.44	<0.25	3.3	52.9	0.51	0.00	28.2	218	261	6.4
23R-3, 116–132	10	296.08	0.3523	1.57	0.61	3.1	47.7	0.46	0.00	30.1	223	239	5.0
24R-1, 123–138	11	302.88	0.3581	1.57	0.61	3.6	51.6	0.47	0.00	31.7	200	230	5.1
26R-2, 130–145	12	323.54	0.3493	1.37	0.98	3.0	49.8	0.33	0.00	29.3	221	262	3.9
27R-3, 138–148	13	334.22	0.3519	1.57	0.61	2.9	48.2	0.52	0.02	26.2	199	281	3.7
28R-6, 89–105	14	347.97	0.3403	1.64	0.61	3.4	41.1	0.31	0.00	22.6	203	261	4.2
30R-1, 0–9	15	359.19	0.3161	1.57	<0.25	2.5	44.1	0.30	0.00	28.1	218	270	4.4
32R-4, 120–130	16	383.96	0.3208	2.05	<0.25	2.3	44.4	0.46	0.13	28.9	216	252	5.8
33R-3, 113–129	17	392.08	0.3025	1.64	<0.25	1.8	45.8	0.37	0.40	39.9	250	268	4.9
35R-1, 125–140	18	408.50	0.2987	1.57	<0.25	1.7	51.2	0.15	0.00	28.0	208	252	5.6
37R-1, 0–12	19	426.52	0.3033	1.78	<0.25	1.9	56.4	0.41	3.24	39.1	193	272	7.8
38R-1, 114–127	20	437.27	0.2529	1.78	0.25	1.3	53.3	0.34	0.00	35.3	246	262	8.2
40R-1, 0–23	21	455.53	0.2498	1.64	0.25	2.1	47.6	0.60	0.00	30.8	205	242	8.6
42R-1, 0–18	22	474.68	0.2651	1.57	0.25	2.2	56.5	0.11	0.00	30.8	214	251	8.0
44R-1, 0–11	23	493.81	0.2615	1.64	0.61	3.3	54.9	0.20	0.00	28.3	176	243	8.9
44R-2, 135–150	24	496.70	0.2442	1.57	0.25	2.6	53.7	0.31	0.00	24.5	147	236	10.8
44R-4, 135–150	25	499.70	0.2060	1.57	0.61	2.8	56.3	0.60	0.22	36.8	190	226	8.9
44R-5, 135–150	26	501.20	0.2361	1.91	0.61	2.8	54.4	0.71	0.00	28.8	162	213	9.6
45R-1, 135–150	27	504.80	0.2174	1.78	0.61	7.8	60.4	0.16	0.00	31.2	146	248	7.6
45R-3, 90–106	28	507.36	0.2180‡										
45R-5, 0–15	29	509.01	0.2538‡	2.18		9.0	45.6	0.68	0.00	28.5	203	147	5.5

Table T9. Composition of Hole 1201D basal sediment compared with lithogenous pelagic clay of Chester and Aston (1976).

Core, section:	45R-4	45R-4	45R-4	45R-5	45R-5	45R-5	Lithogenous pelagic clays, Chester and Aston (1976)
Interval (cm):	20–21	58–59	120–121	26–27	68–69	84–85	
Depth (mbsf):	507.56	507.94	508.56	509.12	509.54	509.7	
Rock type:	Sediment	Sediment	Sediment	Sediment	Sediment	Sediment	Sediment
Major element oxide (wt%):							
SiO_2	58.72	58.25	48.03	54.65	36.12	41.14	58.90
TiO_2	0.48	0.46	0.42	0.43	0.36	0.40	0.89
Al_2O_3	15.70	15.29	12.95	14.03	10.77	12.03	18.99
Fe_2O_3T	8.62	10.21	22.36	13.91	30.92	26.23	8.83
MnO	1.49	1.61	3.93	2.66	6.03	4.79	0.51
MgO	4.63	4.50	3.37	4.25	2.86	3.25	3.64
CaO	4.39	5.00	4.61	4.81	6.15	6.31	0.99
Na_2O	1.69	1.37	1.07	1.17	1.01	1.05	1.63
K_2O	1.52	1.34	1.18	1.49	1.05	1.26	3.47
P_2O_5	0.11	0.29	0.41	0.06	0.85	0.91	0.15
Total:	97.52	98.49	98.58	97.62	96.45	97.67	98.00
Trace element (ppm):							
Sc	24.72	23.26	20.25	20.62	18.91	20.54	
V	96.83	151.33	373.09	111.57	769.41	555.94	
Cr	86.39	50.46	68.34	53.69	36.77	39.04	
Ni	—	—	—	—	—	—	
Sr	132.28	115.37	274.43	322.73	810.92	668.61	
Y	20.49	44.22	89.10	59.48	133.87	119.56	
Ba	342.91	193.61	470.23	661.01	659.25	448.04	
Zr	28.24	71.04	105.83	94.85	158.73	145.26	
LOI (wt%)	12.1	13.3	11.3	14.1	–4.6	15.4	

Table T10. Mineral saturation indices (SI) vs. depth calculated from pore water composition, Site 1201.

Depth (mbsf)	Aluminum hydroxides		Alumina clay		Carbonates		Feldspars		Magnesian clay		Sulfates		Zeolites	
	Phase	SI	Phase	SI	Phase	SI	Phase	SI	Phase	SI	Phase	SI	Phase	SI
24.20	Boehmite	–0.2	Kaolinite	–1.6	Aragonite	–0.3	Albite	–7.3	Sepiolite	–12.0	Anhydrite	–0.6	Analcime	–4.9
	Diaspore	1.7			Calcite	–0.1	Anorthite	–10.8			Gypsum	–0.1	Laumontite	–12.4
	Gibbsite	–0.1			Celestite	–0.9	Microcline	–6.7			Strontianite	–1.7	Leonhardite	–11.5
51.20	Boehmite	0.1	Kaolinite	0.4	Aragonite	0.5	Albite	–4.4	Sepiolite	–7.4	Anhydrite	–0.4	Analcime	–2.6
	Diaspore	2.1			Calcite	0.6	Anorthite	–7.3			Gypsum	0.1	Laumontite	–7.7
	Gibbsite	0.3			Celestite	–0.9	Microcline	–3.8			Strontianite	–1.1	Leonhardite	–2.0
83.30	Boehmite	0.2	Kaolinite	0.7	Aragonite	1.0	Albite	–3.5	Sepiolite	–5.1	Anhydrite	–0.1	Analcime	–1.8
	Diaspore	2.1			Calcite	1.1	Anorthite	–5.5			Gypsum	0.3	Laumontite	–5.8
	Gibbsite	0.4			Celestite	–0.9	Microcline	–3.0			Strontianite	–0.8	Leonhardite	1.8
146.98	Boehmite	0.7	Kaolinite	0.8	Aragonite	1.0	Albite	–4.3	Sepiolite	–6.8	Anhydrite	0.1	Analcime	–2.1
	Diaspore	2.6			Calcite	1.2	Anorthite	–4.8			Gypsum	0.6	Laumontite	–5.8
	Gibbsite	0.8			Celestite	1–1.1	Microcline	–4.1			Strontianite	–1.2	Leonhardite	1.8
199.66	Boehmite	0.9	Kaolinite	1.6	Aragonite	1.2	Albite	–3.3	Sepiolite	–5.2	Anhydrite	0.2	Analcime	–1.3
	Diaspore	2.8			Calcite	1.4	Anorthite	–3.3			Gypsum	0.6	Laumontite	–4.0
	Gibbsite	1.0			Celestite	–1.4	Microcline	–3.2			Strontianite	–1.4	Leonhardite	5.4
267.16	Boehmite	0.9	Kaolinite	1.2	Aragonite	0.4	Albite	–3.7	(Mg = 0.0)		Anhydrite	0.3	Analcime	–1.5
	Diaspore	2.8			Calcite	0.6	Anorthite	–2.8			Gypsum	0.7	Laumontite	–4.0
	Gibbsite	1.0			Celestite	–1.6	Microcline	–3.9			Strontianite	–2.4	Leonhardite	5.5
302.88	Boehmite	1.1	Kaolinite	1.6	Aragonite	1.2	Albite	–3.7	Sepiolite	–5.0	Anhydrite	0.3	Analcime	–1.5
	Diaspore	3.0			Calcite	1.3	Anorthite	–2.8			Gypsum	0.7	Laumontite	–3.9
	Gibbsite	1.2			Celestite	–1.6	Microcline	–3.8			Strontianite	–1.7	Leonhardite	5.6
383.96	Boehmite	1.0	Kaolinite	1.4	Aragonite	1.4	Albite	–3.7	Sepiolite	–4.7	Anhydrite	0.3	Analcime	–1.6
	Diaspore	2.9			Calcite	1.7	Anorthite	–2.8			Gypsum	0.7	Laumontite	–3.9
	Gibbsite	1.1			Celestite	–1.6	Microcline	–3.9			Strontianite	–1.5	Leonhardite	5.6
456.76	Boehmite	1.0	Kaolinite	1.4	Aragonite	1.4	Albite	–3.8	Sepiolite	–5.0	Anhydrite	0.3	Analcime	–1.6
	Diaspore	2.9			Calcite	1.6	Anorthite	–2.7			Gypsum	0.7	Laumontite	–3.8
	Gibbsite	1.1			Celestite	–1.7	Microcline	–4.2			Strontianite	–1.6	Leonhardite	5.9
495.20	Boehmite	1.0	Kaolinite	1.3	Aragonite	1.4	Albite	–3.8	Sepiolite	–4.5	Anhydrite	0.2	Analcime	–1.6
	Diaspore	2.9			Calcite	1.6	–2.75	–2.5			Gypsum	0.7	Laumontite	–3.9
	Gibbsite	1.1			Celestite	–1.6	–3.93	–3.8			Strontianite	–1.5	Leonhardite	5.7

Table T11. Index properties of discrete samples, Holes 1201A, 1201B, and 1201D. (Continued on next five pages.)

Core, section interval (cm)	Depth (mbsf)	Density (g/cm³)		Porosity (%)	Water content (%)	Void ratio
		Bulk	Grain			
195-1201A-						
1H-1, 74–76	0.74	1.35	2.58	80.80	61.60	4.22
195-1201B-						
1H-1, 74–76	0.74	1.30	2.64	82.90	65.20	4.83
1H-2, 74–76	2.24	1.33	2.72	82.10	63.30	4.59
1H-3, 74–76	3.74	1.24	2.69	86.80	71.40	6.56
1H-4, 74–76	5.24	1.21	2.71	88.70	74.80	7.85
1H-5, 74–76	6.74	1.28	2.80	85.80	68.90	6.05
2H-1, 74–76	7.94	1.24	2.73	87.50	72.40	7.01
2H-2, 74–76	9.44	1.24	2.58	86.00	70.80	6.12
2H-3, 74–76	10.94	1.28	2.66	84.30	67.40	5.37
2H-4, 74–76	12.44	1.21	2.60	88.20	74.70	7.50
2H-5, 74–76	13.94	1.22	2.64	87.80	73.70	7.22
2H-6, 74–76	15.44	1.25	2.77	87.00	71.20	6.67
2H-7, 74–76	16.94	1.26	2.68	85.50	69.20	5.89
3H-1, 74–76	17.44	1.24	2.58	86.00	70.80	6.12
3H-2, 74–76	18.94	1.22	2.58	87.30	73.20	6.89
3H-3, 74–76	20.44	1.17	2.50	89.80	78.30	8.80
3H-4, 74–76	21.94	1.20	2.81	90.30	77.30	9.31
3H-5, 78–80	23.48	1.26	2.84	87.20	71.10	6.83
3H-6, 74–76	24.94	1.24	2.70	87.00	71.70	6.68
3H-7, 49–51	26.19	1.29	2.71	84.30	66.90	5.36
4H-1, 74–76	26.94	1.23	2.56	86.60	72.10	6.46
4H-2, 74–76	28.44	1.29	2.65	84.00	66.90	5.23
4H-3, 74–76	29.94	1.37	2.73	79.70	59.60	3.93
4H-4, 74–76	31.44	1.26	2.70	85.80	69.60	6.03
4H-5, 74–76	32.94	1.28	2.65	84.20	67.30	5.31
4H-6, 74–76	34.44	1.29	2.81	85.40	68.00	5.84
4H-7, 64–66	35.84	1.30	2.76	84.30	66.60	5.37
5H-1, 74–76	36.44	1.25	2.62	86.00	70.60	6.15
5H-2, 60–62	37.80	1.27	2.77	85.80	69.10	6.06
5H-3, 60–62	39.30	1.21	2.43	86.60	73.20	6.48
5H-4, 74–76	40.94	1.33	2.58	80.60	62.20	4.15
5H-5, 74–76	42.44	1.28	2.58	83.40	66.50	5.01
5H-6, 60–62	43.80	1.36	2.68	79.80	60.20	3.95
5H-7, 30–32	45.00	1.41	2.55	74.50	53.90	2.92
6H-1, 70–72	45.90	1.57	2.60	65.30	42.70	1.89
7X-1, 74–76	47.44	1.37	2.34	73.80	55.30	2.82
7X-2, 74–76	48.94	1.42	2.44	72.30	52.30	2.61
7X-4, 74–76	51.94	1.99	2.75	44.00	22.60	0.78
8X-1, 85–87	52.75	1.87	2.70	49.80	27.40	0.99
8X-3, 72–74	55.62	1.67	2.66	60.60	37.20	1.54
8X-4, 27–29	56.67	1.56	2.49	63.30	41.50	1.72
8X-6, 69–71	59.59	2.14	2.77	36.10	17.30	0.57
9X-1, 51–53	62.01	1.84	2.66	50.00	27.80	1.00
10X-1, 95–97	72.05	1.56	2.66	67.40	44.30	2.07
195-1201D-						
1R-1, 88–90	81.28	1.96	2.74	45.50	23.80	0.84
1R-2, 81–83	82.71	2.01	2.76	43.00	21.90	0.75
1R-3, 49–51	83.82	1.82	2.66	51.10	28.70	1.04
1R-4, 60–62	85.30	2.05	2.76	41.00	20.50	0.70
1R-5, 37–39	86.52	2.13	2.80	37.90	18.20	0.61
2R-1, 75–77	90.75	2.12	2.75	36.60	17.70	0.58
2R-2, 89–91	92.39	2.14	2.84	38.20	18.30	0.62
2R-3, 70–72	93.56	2.04	2.77	41.80	21.00	0.72
2R-4, 74–76	95.08	2.06	2.76	40.30	20.00	0.68
2R-5, 74–76	96.50	2.06	2.75	39.90	19.80	0.66
2R-6, 42–44	97.64	2.10	2.80	39.60	19.40	0.66
3R-1, 97–99	100.57	2.01	2.66	40.10	20.50	0.67
3R-2, 79–81	101.69	2.02	2.67	39.60	20.10	0.66
3R-3, 73–75	102.89	2.07	2.74	39.40	19.50	0.65
3R-4, 130–132	104.63	1.85	2.65	49.30	27.30	0.97
3R-5, 70–72	105.46	1.98	2.73	44.20	22.90	0.79
3R-6, 75–77	106.76	1.95	2.71	45.30	23.80	0.83
3R-7, 59–61	107.38	1.96	2.72	44.80	23.30	0.81

Table T11 (continued).

Core, section interval (cm)	Depth (mbsf)	Density (g/cm³)		Porosity (%)	Water content (%)	Void ratio
		Bulk	Grain			
4R-1, 111–113	110.31	1.96	2.72	45.00	23.50	0.82
4R-2, 71–73	111.27	1.96	2.68	43.20	22.60	0.76
4R-3, 81–83	112.80	1.93	2.65	44.00	23.30	0.79
4R-4, 55–57	114.05	1.91	2.56	42.00	22.50	0.73
4R-5, 78–80	115.58	1.93	2.62	42.80	22.70	0.75
4R-6, 98–100	116.86	1.88	2.51	42.80	23.40	0.75
4R-7, 72–74	117.90	1.85	2.58	47.00	26.10	0.89
5R-1, 82–84	119.62	1.87	2.50	42.80	23.40	0.75
5R-2, 76–78	120.97	1.88	2.48	40.90	22.30	0.69
5R-3, 71–73	122.23	1.92	2.46	37.50	20.00	0.60
5R-4, 73–75	123.61	1.92	2.50	39.00	20.70	0.64
5R-5, 57–59	124.88	1.87	2.51	42.80	23.40	0.75
5R-6, 74–76	126.40	1.70	2.44	52.40	31.60	1.10
6R-1, 76–78	129.16	1.67	2.50	56.00	34.20	1.27
6R-2, 73–75	130.52	1.78	2.44	46.40	26.70	0.87
6R-3, 76–78	132.05	1.81	2.40	43.30	24.50	0.76
6R-4, 81–83	133.45	1.81	2.39	42.60	24.10	0.74
6R-5, 43–45	134.06	1.87	2.61	46.90	25.70	0.88
6R-6, 40–42	135.30	1.87	2.47	41.70	22.90	0.72
6R-7, 73–75	136.52	1.92	2.57	41.90	22.40	0.72
7R-1, 30–32	138.30	1.73	2.60	55.50	32.90	1.25
7R-2, 79–81	139.97	1.67	2.17	43.50	26.70	0.77
7R-3, 69–71	141.11	1.83	2.58	48.10	26.90	0.93
7R-4, 101–103	142.75	1.65	2.12	42.60	26.40	0.74
7R-5, 71–73	143.85	1.81	2.60	50.10	28.30	1.00
7R-6, 73–75	145.16	1.71	2.74	60.00	35.90	1.50
7R-7, 85–87	146.09	1.82	2.74	53.50	30.10	1.15
8R-1, 75–77	148.35	1.71	2.61	56.60	33.80	1.31
8R-2, 76–78	149.81	1.89	2.69	47.80	25.80	0.91
8R-3, 71–73	151.02	1.61	2.69	64.90	41.30	1.85
8R-4, 56–58	152.37	1.75	2.67	55.80	32.60	1.26
8R-5, 23–25	153.44	1.86	2.70	50.10	27.60	1.01
8R-6, 65–67	155.23	1.67	2.68	61.10	37.60	1.57
8R-7, 78–80	156.69	1.94	2.74	46.90	24.80	0.88
9R-1, 71–73	157.91	1.96	2.73	45.00	23.50	0.82
9R-2, 71–73	159.41	1.81	2.61	50.20	28.40	1.01
9R-3, 76–78	160.92	1.72	2.21	40.90	24.30	0.69
9R-4, 82–84	162.48	1.94	2.69	45.00	23.80	0.82
9R-5, 77–79	163.91	1.87	2.67	48.90	26.80	0.96
9R-6, 73–75	165.19	1.89	2.67	47.60	25.80	0.91
10R-1, 85–87	167.65	1.69	2.21	43.80	26.60	0.78
10R-2, 81–83	169.11	1.90	2.70	47.70	25.70	0.91
10R-3, 72–74	170.52	1.94	2.69	45.20	23.90	0.83
10R-4, 59–61	171.88	1.94	2.61	42.20	22.30	0.73
11R-1, 79–81	177.19	1.90	2.60	44.20	23.80	0.79
11R-2, 64–66	178.39	1.90	2.58	44.00	23.70	0.79
11R-3, 79–81	180.04	1.92	2.59	42.60	22.70	0.74
11R-4, 74–76	181.45	1.95	2.58	40.60	21.40	0.69
11R-5, 72–74	182.73	1.95	2.58	40.90	21.50	0.69
11R-6, 65–67	184.06	1.94	2.59	41.30	21.80	0.70
11R-7, 37–39	185.28	1.87	2.46	41.40	22.70	0.71
12R-1, 60–62	186.70	1.91	2.59	43.30	23.20	0.76
12R-2, 71–73	187.91	1.93	2.66	45.00	23.90	0.82
12R-3, 68–70	189.18	1.98	2.68	42.30	21.90	0.73
12R-4, 65–67	190.50	1.89	2.66	47.00	25.50	0.89
12R-5, 96–98	192.24	1.93	2.63	43.70	23.20	0.78
12R-6, 102–104	193.60	1.99	2.62	39.60	20.40	0.66
12R-7, 39–41	194.43	1.93	2.60	42.70	22.70	0.75
13R-1, 63–65	196.33	1.96	2.60	40.90	21.40	0.69
13R-2, 54–56	197.39	1.97	2.62	40.80	21.20	0.69
13R-3, 64–66	198.95	1.78	2.54	49.70	28.60	0.99
13R-4, 72–74	200.38	1.91	2.60	44.00	23.60	0.78
13R-5, 96–98	201.72	1.90	2.58	43.50	23.40	0.77
13R-6, 101–103	203.27	1.94	2.61	42.40	22.40	0.74
13R-7, 72–74	204.28	1.78	2.51	49.00	28.20	0.96
14R-1, 78–80	206.08	1.71	2.52	53.70	32.10	1.16
14R-2, 76–78	207.36	1.79	2.48	47.30	27.00	0.90
14R-3, 74–76	208.84	1.92	2.56	41.60	22.20	0.71

Table T11 (continued).

Core, section interval (cm)	Depth (mbsf)	Density (g/cm³)		Porosity (%)	Water content (%)	Void ratio
		Bulk	Grain			
14R-4, 77–79	210.29	1.94	2.61	42.10	22.20	0.73
14R-5, 75–77	211.77	1.96	2.61	41.40	21.70	0.71
15R-1, 57–59	215.47	1.98	2.70	42.70	22.00	0.75
15R-2, 36–38	216.71	1.94	2.65	43.90	23.20	0.78
15R-3, 72–74	218.44	2.06	2.72	39.20	19.50	0.64
16R-1, 68–70	225.18	2.01	2.74	42.50	21.70	0.74
16R-2, 64–66	226.45	1.79	2.62	51.90	29.60	1.08
16R-3, 87–89	227.90	1.94	2.72	45.90	24.20	0.85
16R-4, 57–59	229.08	2.08	2.74	38.70	19.10	0.63
16R-5, 75–77	230.48	2.00	2.72	42.30	21.60	0.73
17R-1, 69–71	234.79	1.83	2.57	48.00	26.80	0.92
17R-1, 117–119	235.27	1.65	2.32	51.80	32.10	1.07
17R-2, 84–86	236.36	1.67	2.53	57.00	34.90	1.32
17R-3, 66–68	237.37	1.79	2.63	52.60	30.20	1.11
17R-4, 68–70	238.72	1.73	2.60	54.90	32.40	1.22
17R-5, 63–65	240.17	1.77	2.42	46.80	27.20	0.88
17R-6, 71–73	241.49	1.83	2.39	41.00	22.90	0.69
18R-1, 75–77	244.55	1.95	2.50	36.90	19.30	0.58
18R-2, 88–90	246.18	1.95	2.47	36.10	19.00	0.57
18R-3, 79–81	247.60	1.98	2.53	36.40	18.80	0.57
18R-4, 91–93	249.22	2.00	2.57	36.80	18.80	0.58
18R-5, 73–75	250.52	1.94	2.52	38.80	20.50	0.63
18R-6, 73–75	252.02	2.05	2.59	34.20	17.10	0.52
18R-7, 64–66	253.44	1.99	2.57	37.50	19.30	0.60
19R-1, 102–104	254.42	1.82	2.53	47.10	26.50	0.89
19R-2, 54–56	255.44	1.89	2.62	45.40	24.50	0.83
19R-3, 87–89	257.16	1.76	2.45	48.00	27.90	0.92
19R-4, 83–85	258.55	1.93	2.48	37.90	20.10	0.61
19R-5, 44–46	259.66	1.77	2.41	46.40	26.80	0.86
19R-6, 66–68	261.32	1.70	2.50	54.30	32.80	1.19
20R-1, 79–81	263.79	1.79	2.44	46.00	26.30	0.85
20R-2, 100–102	265.33	2.07	2.53	31.00	15.40	0.45
20R-3, 100–102	266.66	1.96	2.47	35.40	18.50	0.55
20R-4, 74–76	267.90	2.04	2.47	30.10	15.10	0.43
20R-5, 71–73	269.35	1.91	2.41	36.10	19.40	0.57
20R-6, 77–79	270.82	1.84	2.41	40.70	22.60	0.69
21R-1, 83–85	273.43	1.97	2.50	35.90	18.70	0.56
21R-2, 73–75	274.54	1.89	2.48	40.60	22.00	0.68
21R-3, 76–78	276.07	1.89	2.47	40.00	21.70	0.67
21R-4, 43–45	276.87	2.03	2.52	32.70	16.50	0.49
21R-5, 67–69	278.51	1.73	2.45	50.40	29.80	1.02
21R-6, 72–74	279.87	1.78	2.51	49.00	28.10	0.96
21R-7, 58–60	280.84	1.79	2.48	47.40	27.10	0.90
22R-1, 67–69	282.97	1.79	2.49	47.40	27.00	0.90
22R-2, 81–83	284.52	1.85	2.48	43.60	24.20	0.77
22R-3, 76–78	285.98	1.78	2.54	50.10	28.80	1.01
22R-4, 103–105	287.75	1.82	2.52	46.60	26.20	0.87
22R-5, 92–94	289.15	1.92	2.43	36.40	19.40	0.57
22R-6, 70–72	290.39	1.77	2.49	49.40	28.60	0.97
23R-1, 85–87	292.75	1.75	2.51	51.20	30.00	1.05
23R-2, 78–80	294.05	1.83	2.50	45.50	25.50	0.84
23R-3, 76–78	295.52	1.93	2.49	38.40	20.40	0.62
23R-4, 73–75	296.81	1.76	2.50	50.10	29.10	1.00
23R-5, 79–81	298.22	1.82	2.50	45.80	25.70	0.85
23R-6, 78–80	299.51	1.86	2.55	45.30	25.00	0.83
23R-7, 75–77	300.74	1.81	2.52	47.40	26.80	0.90
24R-1, 90–92	302.40	1.79	2.54	49.70	28.50	0.99
24R-2, 75–77	303.63	1.72	2.56	54.50	32.40	1.20
24R-3, 73–75	304.77	1.85	2.48	43.10	23.90	0.76
24R-4, 80–82	306.31	1.95	2.45	35.10	18.40	0.54
24R-5, 46–48	307.27	1.98	2.47	34.10	17.70	0.52
25R-1, 46–48	311.56	1.92	2.58	42.50	22.70	0.74
25R-2, 120–122	313.72	1.93	2.54	39.80	21.10	0.66
25R-3, 111–113	315.13	2.14	2.54	26.40	12.60	0.36
25R-4, 103–105	316.35	1.91	2.58	43.40	23.30	0.77
25R-5, 52–54	317.05	1.61	2.46	59.20	37.70	1.45
26R-1, 82–84	321.52	2.00	2.46	31.80	16.30	0.47
26R-2, 65–67	322.74	1.75	2.51	51.60	30.30	1.07

Table T11 (continued).

Core, section interval (cm)	Depth (mbsf)	Density (g/cm³)		Porosity (%)	Water content (%)	Void ratio
		Bulk	Grain			
26R-3, 64–66	324.18	1.90	2.51	40.80	22.00	0.69
26R-4, 73–75	325.45	1.79	2.50	48.10	27.50	0.93
26R-5, 75–77	326.97	1.74	2.52	52.30	30.90	1.10
26R-6, 55–57	328.18	1.91	2.48	39.50	21.20	0.65
26R-7, 102–104	330.15	1.79	2.46	46.50	26.60	0.87
27R-1, 68–70	330.98	1.83	2.47	44.20	24.80	0.79
27R-2, 60–62	332.09	1.95	2.51	37.70	19.80	0.61
27R-3, 64–66	333.38	1.78	2.60	52.20	30.10	1.09
27R-4, 66–68	334.88	1.84	2.54	45.90	25.50	0.85
27R-5, 61–63	336.17	1.84	2.70	51.30	28.60	1.06
27R-6, 73–75	337.80	1.87	2.62	46.80	25.60	0.88
27R-7, 81–83	339.32	1.82	2.59	49.30	27.70	0.97
28R-1, 74–76	340.64	1.79	2.55	49.50	28.20	0.98
28R-2, 73–75	342.04	1.73	2.52	52.70	31.20	1.12
28R-3, 52–54	343.22	1.87	2.54	44.50	24.40	0.80
28R-4, 62–64	344.62	1.95	2.57	39.90	20.90	0.66
28R-5, 81–83	346.23	2.00	2.58	37.60	19.30	0.60
28R-6, 78–80	347.70	1.82	2.61	50.10	28.30	1.01
29R-1, 88–90	350.38	1.74	2.47	50.80	29.90	1.03
29R-2, 81–83	351.40	1.77	2.64	54.00	31.30	1.17
29R-3, 74–76	352.73	1.68	2.33	50.20	30.70	1.01
29R-4, 73–75	354.00	1.63	2.42	57.00	35.90	1.32
29R-5, 74–76	355.48	1.84	2.51	45.10	25.20	0.82
30R-1, 75–77	359.85	1.88	2.47	41.00	22.30	0.69
30R-2, 70–72	361.30	1.91	2.51	40.20	21.50	0.67
30R-3, 58–60	362.68	1.95	2.49	37.00	19.40	0.59
30R-4, 58–60	364.18	1.92	2.50	39.60	21.20	0.66
30R-5, 73–75	365.83	1.61	2.62	63.20	40.10	1.72
30R-6, 22–24	366.82	1.84	2.57	47.50	26.50	0.90
30R-7, 43–45	368.53	1.86	2.51	43.70	24.00	0.78
31R-1, 75–77	369.45	1.87	2.49	42.70	23.40	0.75
31R-2, 60–62	370.80	1.77	2.40	46.20	26.80	0.86
31R-3, 78–80	372.48	1.91	2.53	41.50	22.30	0.71
31R-4, 77–79	373.87	1.93	2.55	40.80	21.60	0.69
31R-5, 53–55	375.14	1.84	2.51	45.20	25.20	0.83
31R-6, 69–71	376.79	1.89	2.52	42.20	22.90	0.73
31R-7, 37–39	377.88	1.83	2.42	42.30	23.70	0.73
32R-1, 76–78	379.06	1.94	2.54	39.50	20.80	0.65
32R-2, 79–81	380.59	1.91	2.45	37.70	20.20	0.61
32R-3, 66–68	381.92	1.78	2.42	46.00	26.50	0.85
32R-4, 71–73	383.37	1.95	2.42	34.10	17.90	0.52
32R-5, 76–78	384.72	1.72	2.48	52.60	31.40	1.11
32R-6, 73–75	386.03	1.85	2.44	41.90	23.30	0.72
32R-7, 60–62	387.06	1.80	2.44	45.10	25.60	0.82
33R-1, 74–76	388.64	1.74	2.34	45.80	27.10	0.85
33R-2, 65–67	390.02	1.89	2.53	42.50	23.00	0.74
33R-3, 54–56	391.33	1.84	2.54	46.30	25.80	0.86
33R-4, 73–75	392.81	1.81	2.52	47.70	27.10	0.91
33R-5, 83–85	394.38	1.70	2.58	56.80	34.30	1.32
33R-6, 71–73	395.76	1.70	2.62	57.90	34.90	1.37
33R-7, 75–77	396.72	1.72	2.54	54.30	32.40	1.19
34R-1, 75–77	398.25	1.84	2.46	43.30	24.20	0.76
34R-2, 77–79	399.55	1.86	2.50	43.50	24.00	0.77
34R-3, 62–64	400.73	1.71	2.53	54.80	32.90	1.21
34R-4, 74–76	402.26	1.86	2.50	43.60	24.10	0.78
34R-5, 74–76	403.77	1.77	2.64	53.60	30.90	1.15
34R-6, 81–83	405.21	1.80	2.61	51.20	29.10	1.05
35R-1, 92–94	408.02	1.86	2.56	45.60	25.10	0.84
35R-2, 40–42	408.90	1.80	2.56	49.50	28.10	0.98
35R-3, 72–74	410.30	1.76	2.47	48.80	28.40	0.95
35R-4, 69–71	411.46	1.86	2.49	42.70	23.50	0.75
35R-5, 82–84	412.74	1.92	2.47	38.40	20.50	0.62
35R-6, 81–83	414.03	1.92	2.55	41.20	22.00	0.70
35R-7, 52–54	414.77	1.85	2.47	42.90	23.70	0.75
36R-1, 104–106	417.74	1.77	2.39	45.00	26.00	0.82
36R-2, 71–73	418.69	1.80	2.37	42.30	24.00	0.73
36R-3, 87–89	420.24	1.86	2.30	35.10	19.40	0.54
36R-4, 73–75	421.46	1.80	2.37	42.20	23.90	0.73

Table T11 (continued).

Core, section interval (cm)	Depth (mbsf)	Density (g/cm³)		Porosity (%)	Water content (%)	Void ratio
		Bulk	Grain			
36R-5, 88–90	423.09	1.81	2.32	39.90	22.60	0.66
36R-6, 74–76	424.45	1.80	2.37	42.30	24.10	0.73
36R-7, 71–73	425.91	1.82	2.41	42.90	24.20	0.75
37R-1, 75–77	427.15	1.83	2.38	40.90	22.90	0.69
37R-2, 70–72	428.51	1.84	2.37	39.90	22.20	0.66
37R-3, 72–74	429.79	1.77	2.39	45.40	26.30	0.83
37R-4, 72–74	430.98	1.79	2.39	44.50	25.50	0.80
37R-5, 103–105	432.79	1.86	2.39	38.80	21.30	0.63
37R-6, 95–97	434.21	1.88	2.37	36.70	20.00	0.58
37R-7, 65–67	435.41	1.86	2.46	41.80	23.00	0.72
38R-1, 71–73	436.71	1.77	2.39	45.70	26.50	0.84
38R-2, 134–136	438.61	1.90	2.57	43.50	23.50	0.77
38R-3, 71–73	439.39	1.89	2.46	39.70	21.50	0.66
38R-4, 70–72	440.71	1.91	2.53	40.80	21.80	0.69
38R-5, 72–74	442.00	1.83	2.42	42.20	23.60	0.73
38R-6, 120–122	443.98	1.93	2.46	37.40	19.90	0.60
38R-7, 73–75	445.01	1.76	2.41	46.90	27.30	0.88
39R-1, 76–78	446.46	1.76	2.42	47.40	27.60	0.90
39R-2, 65–67	447.69	1.86	2.44	40.80	22.50	0.69
39R-3, 71–73	449.15	1.85	2.51	44.20	24.50	0.79
39R-4, 76–78	450.42	1.73	2.39	48.40	28.60	0.94
39R-5, 68–70	451.78	1.87	2.51	43.00	23.50	0.75
39R-6, 79–81	453.19	1.78	2.48	48.20	27.70	0.93
39R-7, 73–75	454.40	1.86	2.51	43.80	24.10	0.78
40R-1, 77–79	456.07	1.92	2.46	37.80	20.20	0.61
40R-2, 73–75	457.49	1.69	2.25	46.10	28.00	0.85
40R-3, 75–77	458.87	1.87	2.46	40.90	22.30	0.69
40R-4, 68–70	460.29	1.90	2.48	39.80	21.40	0.66
40R-5, 75–77	461.87	1.84	2.48	43.70	24.30	0.78
40R-6, 68–70	462.94	1.91	2.49	39.50	21.10	0.65
40R-7, 82–84	464.47	1.85	2.47	42.70	23.60	0.75
41R-1, 76–78	465.66	1.87	2.49	42.40	23.30	0.74
41R-2, 70–72	467.09	1.88	2.52	42.70	23.30	0.75
41R-3, 80–82	468.48	1.91	2.43	36.80	19.70	0.58
41R-4, 73–75	469.86	1.90	2.51	41.20	22.20	0.70
41R-5, 73–75	471.36	1.88	2.44	39.30	21.40	0.65
42R-1, 113–115	475.63	1.95	2.58	40.70	21.40	0.69
42R-2, 91–93	476.91	1.88	2.54	43.50	23.70	0.77
42R-3, 67–69	478.17	1.94	2.54	39.50	20.90	0.65
42R-4, 50–52	479.50	1.88	2.51	42.30	23.00	0.73
42R-5, 94–96	481.44	1.85	2.49	43.30	23.90	0.76
42R-6, 74–76	482.66	1.92	2.57	41.90	22.40	0.72
42R-7, 45–47	483.87	1.92	2.54	40.80	21.80	0.69
43R-1, 90–92	485.00	1.85	2.46	42.50	23.50	0.74
43R-2, 73–75	486.22	1.84	2.55	46.20	25.60	0.86
43R-3, 70–72	487.63	1.88	2.51	42.60	23.20	0.74
43R-4, 36–38	488.52	1.94	2.48	37.30	19.70	0.60
43R-4, 75–77	488.91	1.90	2.45	38.80	20.90	0.63
43R-5, 66–68	490.32	1.92	2.45	37.10	19.80	0.59
44R-1, 78–80	494.48	1.88	2.46	40.30	21.90	0.68
44R-2, 85–87	496.05	1.89	2.46	39.20	21.20	0.65
44R-3, 101–103	497.71	1.84	2.45	42.70	23.80	0.75
44R-4, 74–76	498.94	1.97	2.41	31.40	16.30	0.46
44R-5, 83–85	500.53	1.92	2.49	39.00	20.90	0.64
44R-6, 73–75	501.93	1.94	2.47	36.40	19.20	0.57
44R-7, 49–51	503.19	1.89	2.45	39.20	21.20	0.64
45R-1, 71–73	504.01	1.93	2.47	37.30	19.80	0.60
45R-2, 78–80	505.58	1.93	2.47	37.20	19.70	0.59
45R-3, 48–50	506.78	1.99	2.52	35.70	18.40	0.56
45R-4, 40–42	507.76	2.01	2.60	37.70	19.20	0.60
45R-4, 119–121	508.55	1.99	2.65	40.50	20.90	0.68
45R-5, 48–50	509.34	1.88	2.70	49.10	26.80	0.97
45R-CC, 16–18	510.17	2.52	2.72	11.80	4.80	0.13
46R-1, 76–78	513.66	2.47	2.61	9.30	3.90	0.10
46R-2, 75–77	515.15	2.45	2.67	13.10	5.50	0.15
46R-3, 101–103	516.81	2.36	2.52	10.90	4.70	0.12
46R-4, 84–86	518.10	2.47	2.65	11.00	4.60	0.12
46R-5, 74–76	519.50	2.43	2.61	11.50	4.90	0.13

Table T11 (continued).

Core, section interval (cm)	Depth (mbsf)	Density (g/cm³)		Porosity (%)	Water content (%)	Void ratio
		Bulk	Grain			
47R-1, 72–74	522.82	2.44	2.67	14.10	5.90	0.17
47R-3, 74–76	525.82	2.03	2.62	36.50	18.40	0.58
48R-1, 34–36	532.04	2.74	2.83	5.10	1.90	0.05
48R-2, 67–69	533.11	2.72	2.80	4.50	1.70	0.05
48R-3, 73–75	534.67	2.74	2.82	4.40	1.60	0.05
49R-1, 76–78	542.06	2.69	2.78	4.90	1.90	0.05
49R-2, 63–65	543.43	2.79	2.87	4.10	1.50	0.04
49R-3, 32–34	544.62	2.69	2.76	4.10	1.60	0.04
51R-1, 35–37	554.35	2.67	2.76	4.90	1.90	0.05
52R-1, 100–102	561.70	2.63	2.74	6.10	2.40	0.07
53R-1, 132–134	571.62	2.67	2.78	6.40	2.40	0.07
54R-1, 83–85	580.33	2.69	2.79	5.50	2.10	0.06
54R-2, 70–72	581.38	2.65	2.77	6.90	2.70	0.07

Table T12. Physical properties, Holes 1201A, 1201B, 1201C, and 1201D. (Continued on next seven pages.)

Core, section, interval (cm)	Depth (mbsf)	Thermal conductivity (W/[m·K])	Velocity (km/s)			Maximum shear strength (kPa)	Formation factor
			x	y	z		
195-1201A-							
1H-1, 18–22	0.20						2.53
1H-1, 75–75	0.75	0.83					
1H-1, 121–121	1.21				1.52		
1H-1, 124–124	1.24			1.62			
195-1201B-							
1H-1, 92–92	0.92					7.43	
1H-1, 102–102	1.01			1.61	1.60		
1H-1, 112–116	1.14						2.14
1H-2, 85–85	2.35			1.62	1.57		
1H-2, 95–95	2.45					21.40	
1H-2, 100–104	2.52						2.51
1H-3, 75–75	3.75	0.76					
1H-3, 83–83	3.83			1.64	1.59		
1H-3, 93–93	3.93					11.87	
1H-3, 96–100	3.98						2.71
1H-4, 63–67	5.15						2.41
1H-4, 84–84	5.34			1.64	1.60		
1H-4, 93–93	5.43					5.43	
1H-5, 36–40	6.38						2.65
1H-5, 52–52	6.52			1.65	1.62		
1H-5, 64–64	6.64					7.87	
2H-1, 44–48	7.66						2.67
2H-1, 53–53	7.73					6.76	
2H-1, 63–63	7.83			1.65	1.60		
2H-2, 53–57	9.25						2.86
2H-2, 66–66	9.36			1.66	1.62		
2H-3, 48–52	10.70						2.88
2H-3, 64–64	10.84			1.66	1.62		
2H-3, 80–80	11.00	0.77					
2H-3, 82–82	11.02					12.53	
2H-4, 65–65	12.35			1.66	1.61		
2H-4, 84–84	12.54					7.54	
2H-4, 93–97	12.65						2.86
2H-5, 65–65	13.85			1.67	1.62		
2H-5, 83–83	14.03					7.65	
2H-5, 94–98	14.16						2.92
2H-6, 66–66	15.36			1.69	1.61		
2H-6, 83–83	15.53					8.43	
2H-6, 94–98	15.66						2.87
2H-7, 39–43	16.61						3.18
2H-7, 61–61	16.81			1.67	1.63		
2H-7, 81–81	17.01					13.20	
3H-1, 64–64	17.34			1.65	1.61		
3H-1, 80–80	17.50					6.10	
3H-1, 91–95	17.63						2.98
3H-2, 61–61	18.81			1.65	1.60		
3H-2, 80–80	19.00					6.54	
3H-2, 86–90	19.08						2.63
3H-3, 62–62	20.32			1.63	1.59		
3H-3, 80–80	20.50	0.73				11.87	
3H-3, 90–94	20.62						2.21
3H-4, 49–49	21.69			1.65	1.61		
3H-4, 80–80	22.00					8.76	
3H-4, 90–94	22.12						2.42
3H-5, 63–63	23.33			1.68	1.63		
3H-5, 85–85	23.55					9.31	
3H-5, 90–94	23.62						2.44
3H-6, 63–63	24.83			1.64	1.61		
3H-6, 80–80	25.00					11.64	
3H-6, 90–94	25.12						2.56
3H-7, 20–20	25.90					10.42	
3H-7, 40–40	26.10			1.69	1.63		
4H-1, 61–61	26.81			1.66	1.61		
4H-1, 80–80	27.00					22.95	
4H-1, 90–94	27.12						1.92

Table T12 (continued).

Core, section, interval (cm)	Depth (mbsf)	Thermal conductivity (W/[m·K])	Velocity (km/s)			Maximum shear strength (kPa)	Formation factor
			x	y	z		
4H-2, 54–54	28.24			1.63	1.58		
4H-2, 80–80	28.50					17.74	
4H-2, 90–94	28.62						2.00
4H-3, 80–80	30.00	0.83					
4H-3, 82–82	30.02			1.63	1.58		
4H-3, 92–92	30.12					10.76	
4H-3, 100–104	30.22						2.25
4H-4, 62–62	31.32			1.62	1.58		
4H-4, 85–85	31.55					24.84	
4H-4, 100–104	31.72						2.52
4H-5, 61–61	32.81			1.61	1.57		
4H-5, 85–85	33.05					19.18	
4H-5, 90–94	33.12						2.12
4H-6, 58–58	34.28			1.61	1.57		
4H-6, 84–84	34.54					24.06	
4H-6, 95–99	34.67						2.08
4H-7, 52–52	35.72			1.61	1.57		
4H-7, 61–61	35.81					22.84	
5H-1, 61–61	36.31			1.68		3.88	
5H-1, 82–82	36.52				1.62		
5H-1, 90–94	36.62						2.63
5H-2, 47–47	37.67			1.69	1.63		
5H-2, 82–82	38.02					6.32	
5H-2, 93–97	38.15						3.36
5H-3, 37–37	39.07					19.41	
5H-3, 44–44	39.14			1.67	1.63		
5H-3, 43–47	39.15						2.84
5H-3, 75–75	39.45	0.86					
5H-4, 83–83	41.03			1.70	1.65		
5H-4, 98–98	41.18					23.29	
5H-4, 105–109	41.27						2.57
5H-5, 54–54	42.24			1.76			
5H-5, 63–63	42.33					53.78	
5H-5, 75–79	42.47						2.75
5H-6, 19–19	43.39			1.60			
5H-6, 33–33	43.53					40.92	
5H-6, 45–45	43.65				1.64		
5H-6, 46–46	43.66			1.60			
6H-1, 38–38	45.58		1.53	1.63			
6H-1, 39–39	45.59		1.64				
6H-1, 63–63	45.83					97.36	
6H-1, 65–65	45.85	0.85					
6H-1, 67–71	45.89						3.67
7X-1, 43–43	47.13		2.50				
7X-1, 107–107	47.77		2.58				
7X-2, 17–17	48.37		2.40				
7X-2, 80–80	49.00		1.85				
7X-3, 33–33	50.03		1.95				
7X-3, 75–75	50.45	0.75					
7X-3, 82–82	50.52		1.96				
7X-4, 20–20	51.40		2.17				
8X-1, 5–5	51.95		2.15				
8X-1, 12–12	52.02		2.21				
7X-4, 84–84	52.04		2.26				
8X-1, 78–78	52.68		2.21				
8X-1, 94–94	52.84		2.21				
8X-3, 44–44	55.34		1.97				
8X-3, 106–106	55.96		2.01				
8X-4, 25–25	56.65		2.17				
8X-5, 35–35	58.25		2.22				
8X-5, 74–74	58.64		2.19				
8X-5, 76–76	58.66		2.92				
9X-1, 70–70	62.20		2.33				
10X-1, 16–16	71.26		1.89				
10X-1, 103–103	72.13		1.68				
11X-CC, 6–6	80.76		2.62				
195-1201C-							
1H-3, 75–75	3.75	0.77					

Table T12 (continued).

Core, section, interval (cm)	Depth (mbsf)	Thermal conductivity (W/[m·K])	Velocity (km/s)			Maximum shear strength (kPa)	Formation factor
			x	y	z		
2H-3, 75–75	10.35	0.80					
3H-3, 75–75	19.85	0.73					
4H-3, 75–75	29.35	0.73					
5H-3, 75–75	38.85	0.75					
6H-3, 40–40	47.50	0.85					
195-1201D-							
1R-1, 88–88	81.28		2.61		2.45		
1R-2, 81–81	82.71		2.72		2.73		
1R-3, 15–33	83.48	1.09					
1R-3, 49–49	83.82		2.39		2.30		
1R-4, 61–61	85.31		3.00		2.84		
1R-5, 37–37	86.52		3.05		3.04		
2R-1, 75–75	90.75		3.12		3.10		
2R-2, 90–90	92.40		3.18		3.12		
2R-3, 37–51	93.23	1.13					
2R-3, 70–70	93.56		2.92		2.93		
2R-4, 75–75	95.09		2.95		2.94		
2R-5, 12–12	95.88		2.77				
2R-5, 74–74	96.50		3.02		2.97		
2R-6, 42–42	97.64		2.97				
3R-1, 97–97	100.57		2.98		2.89		
3R-2, 79–79	101.69		2.96		2.92		
3R-3, 37–58	102.53	1.21					
3R-3, 73–73	102.89		2.99		2.91		
3R-4, 130–130	104.63		2.43		2.31		
3R-5, 70–70	105.46		2.62		2.66		
3R-6, 75–75	106.76		2.49		2.48		
3R-7, 59–59	107.38		2.55		2.60		
4R-1, 110–110	110.30		2.53		2.51		
4R-2, 72–72	111.28		2.68		2.72		
4R-3, 18–46	112.17	1.00					
4R-3, 79–79	112.78		2.78		2.70		
4R-4, 55–55	114.05		2.79		2.75		
4R-5, 79–79	115.59		2.83		2.79		
4R-6, 99–99	116.87		2.81		2.81		
4R-7, 72–72	117.90		2.69		2.66		
5R-1, 81–81	119.61		2.79		2.76		
5R-2, 77–77	120.98		2.83		2.86		
5R-3, 27–35	121.79	1.04					
5R-3, 70–70	122.22		3.02		2.94		
5R-4, 73–73	123.61		2.91		2.89		
5R-5, 57–57	124.88		2.79		2.79		
5R-6, 75–75	126.41		2.49		2.45		
5R-7, 70–70	127.59		2.28		2.23		
6R-1, 75–75	129.15		2.32		2.31		
6R-2, 74–74	130.53		2.57		2.54		
6R-3, 76–76	132.05		2.70		2.67		
6R-3, 95–112	132.24	0.99					
6R-4, 80–80	133.44		2.75		2.70		
6R-5, 43–43	134.06		2.51		2.48		
6R-6, 42–42	135.32		2.76		2.65		
6R-7, 73–73	136.52		2.73		2.67		
7R-1, 29–29	138.29		2.36		2.27		
7R-2, 80–80	139.98		2.50		2.46		
7R-3, 24–48	140.66	0.99					
7R-3, 69–69	141.11		2.49		2.49		
7R-4, 103–103	142.77		2.52		2.45		
7R-5, 69–69	143.83		2.49		2.30		
7R-6, 75–75	145.18		2.21		2.13		
7R-7, 86–86	146.10		2.13		2.11		
8R-1, 75–75	148.35		2.21		2.18		
8R-2, 76–76	149.81		2.48		2.43		
8R-3, 28–45	150.59	0.98					
8R-3, 70–70	151.01		1.94		1.88		
8R-4, 56–56	152.37		2.15		2.14		
8R-5, 23–23	153.44		2.40		2.36		
8R-6, 66–66	155.24		2.06		2.03		
8R-7, 78–78	156.69		2.55		2.50		

Table T12 (continued).

Core, section, interval (cm)	Depth (mbsf)	Thermal conductivity (W/[m·K])	Velocity (km/s)			Maximum shear strength (kPa)	Formation factor
			x	y	z		
9R-1, 72–72	157.92		2.47		2.35		
9R-2, 71–71	159.41		2.41		2.39		
9R-3, 51–73	160.67	1.07					
9R-3, 76–76	160.92		2.60		2.59		
9R-4, 81–81	162.47		2.58		2.57		
9R-5, 77–77	163.91		2.39		2.36		
9R-6, 73–73	165.19		2.44		2.44		
10R-1, 84–84	167.64		2.38		2.34		
10R-2, 81–81	169.11		2.41		2.41		
10R-3, 72–72	170.52		2.36		2.38		
10R-3, 94–114	170.74	1.11					
10R-4, 59–59	171.88		2.84		2.74		
11R-1, 79–79	177.19		2.53		2.51		
11R-2, 65–65	178.40		2.55		2.54		
11R-3, 79–79	180.04		2.61		2.61		
11R-3, 99–119	180.24	1.07					
11R-4, 74–74	181.45		2.66		2.67		
11R-5, 73–73	182.74		2.69		2.77		
11R-6, 65–65	184.06		2.63		2.62		
11R-7, 37–37	185.28		2.61		2.60		
12R-1, 61–61	186.71		2.57		2.55		
12R-2, 71–71	187.91		2.46		2.43		
12R-3, 23–47	188.73	1.11					
12R-3, 68–68	189.18		2.64		2.62		
12R-4, 65–65	190.50		2.49		2.52		
12R-5, 96–96	192.24		2.61		2.54		
12R-6, 103–103	193.61		2.85		2.70		
12R-7, 39–39	194.43		2.64		2.61		
13R-1, 63–63	196.33		2.74		2.75		
13R-2, 54–5	197.39		2.80		2.86		
13R-3, 53–82	198.84	0.94					
13R-3, 64–64	198.95		2.43		2.46		
13R-4, 72–72	200.38		2.53		2.56		
13R-5, 96–96	201.72		2.45		2.55		
13R-6, 101–101	203.27		2.75		2.77		
13R-7, 72–72	204.28		2.43		2.48		
14R-1, 78–78	206.08		2.33		2.27		
14R-2, 76–76	207.36		2.43		2.43		
14R-3, 74–74	208.84		2.59		2.56		
14R-3, 93–110	209.03	1.08					
14R-4, 77–77	210.29		2.63		2.63		
14R-5, 75–75	211.77		2.73		2.77		
15R-1, 57–57	215.47		2.70		2.69		
15R-2, 36–36	216.71		2.75		2.75		
15R-3, 1–20	217.73	1.11					
15R-3, 72–72	218.44		2.89		2.87		
16R-1, 68–68	225.18		2.63		2.57		
16R-2, 5–5	225.86		2.61				
16R-2, 10–10	225.91		2.55				
16R-2, 15–15	225.96		2.56				
16R-2, 20–20	226.01		2.55				
16R-2, 25–25	226.06		2.54				
16R-2, 30–30	226.11		2.56				
16R-2, 38–38	226.19		2.54				
16R-2, 64–64	226.45		2.27		2.23		
16R-3, 10–30	227.13	1.15					
16R-3, 15–15	227.18		2.46				
16R-3, 20–20	227.23		2.44				
16R-3, 25–25	227.28		2.42				
16R-3, 30–30	227.33		2.39				
16R-3, 35–35	227.38		2.35				
16R-3, 50–50	227.53		2.37				
16R-3, 55–55	227.58		2.45				
16R-3, 70–70	227.73		2.34				
16R-3, 75–75	227.78		2.20				
16R-3, 87–87	227.90		2.48		2.45		
16R-3, 110–110	228.13		2.34				
16R-3, 115–115	228.18		2.40				

Table T12 (continued).

Core, section, interval (cm)	Depth (mbsf)	Thermal conductivity (W/[m·K])	Velocity (km/s)			Maximum shear strength (kPa)	Formation factor
			x	y	z		
16R-3, 120–120	228.23		2.33				
16R-3, 125–125	228.28		2.31				
16R-3, 135–135	228.38		2.26				
16R-3, 140–140	228.43		2.37				
16R-4, 57–57	229.08		2.58		2.59		
16R-5, 75–75	230.48		2.44		2.44		
17R-1, 69–69	234.79		2.38		2.30		
17R-1, 118–118	235.28		1.94		1.92		
17R-2, 84–84	236.36		1.98		1.95		
17R-3, 52–70	237.23	1.00					
17R-3, 66–66	237.37		2.32		2.19		
17R-4, 67–67	238.71		2.01		1.95		
17R-5, 63–63	240.17		2.37		2.35		
17R-6, 70–70	241.48		2.60				
18R-1, 74–74	244.54		2.68		2.61		
18R-2, 88–88	246.18		2.70		2.68		
18R-3, 67–95	247.48	1.08					
18R-3, 79–79	247.60		2.64		2.56		
18R-4, 91–91	249.22		2.64		2.59		
18R-5, 73–73	250.52		2.45		2.48		
18R-6, 72–72	252.01		2.64		2.62		
18R-7, 64–64	253.44		2.68		2.70		
19R-1, 101–101	254.41		2.44		2.35		
19R-2, 54–54	255.44		2.41		2.44		
19R-3, 87–87	257.16		2.23		2.20		
19R-3, 94–112	257.23	1.01					
19R-4, 83–83	258.55		2.62		2.63		
19R-5, 44–44	259.66		2.27		2.22		
19R-6, 66–66	261.32		1.91		1.90		
20R-1, 79–79	263.79		2.21		2.23		
20R-2, 100–100	265.33		2.66		2.59		
20R-3, 100–100	266.66		2.44		2.47		
20R-3, 121–140	266.87	1.11					
20R-4, 74–74	267.90		2.67		2.71		
20R-5, 71–71	269.35		2.67		2.64		
20R-6, 77–77	270.82		2.59		2.52		
21R-1, 83–83	273.43		2.56		2.56		
21R-2, 73–73	274.54		2.48		2.46		
21R-3, 44–62	275.75	1.01					
21R-3, 76–76	276.07		2.36		2.29		
21R-4, 43–43	276.87		2.53		2.48		
21R-5, 67–67	278.51		2.15		2.13		
21R-6, 72–72	279.87		2.20		2.05		
21R-7, 58–58	280.84		2.22		2.06		
22R-1, 68–68	282.98		2.20		2.09		
22R-2, 82–82	284.53		2.56		2.31		
22R-3, 76–76	285.98		2.17		2.14		
22R-3, 97–116	286.19	1.07					
22R-4, 103–103	287.75		2.26		2.25		
22R-5, 92–92	289.15		2.64		2.56		
22R-6, 71–71	290.40		2.15		2.00		
23R-1, 84–84	292.74		2.24		2.09		
23R-2, 78–78	294.05		2.20	2.21	2.10		
23R-3, 49–67	295.25	1.09					
23R-3, 76–76	295.52		2.32	2.63	2.46		
23R-4, 73–73	296.81		2.03	2.02	2.05		
23R-5, 79–79	298.22		2.22	2.19	2.13		
23R-6, 78–78	299.51		2.15	2.16	2.07		
23R-7, 75–75	300.74		2.14	2.10	2.01		
24R-1, 90–90	302.40		2.11		1.99		
24R-2, 75–75	303.63		2.03		1.98		
24R-3, 20–35	304.24	1.07					
24R-3, 73–73	304.77		2.74		2.25		
24R-4, 80–80	306.31		2.76		2.73		
24R-5, 46–46	307.27		2.88		2.77		
25R-1, 46–46	311.56		2.56		2.54		
25R-2, 120–120	313.72		2.67		2.60		
25R-3, 0–10	314.02	1.11					

Table T12 (continued).

Core, section, interval (cm)	Depth (mbsf)	Thermal conductivity (W/[m·K])	Velocity (km/s)			Maximum shear strength (kPa)	Formation factor
			x	y	z		
25R-3, 112–112	315.14		2.66		2.67		
25R-4, 103–103	316.35		2.53		2.42		
25R-5, 51–51	317.04		2.20		2.14		
26R-1, 82–82	321.52		3.01		2.90		
26R-2, 65–65	322.74		2.43		2.13		
26R-3, 36–56	323.90	1.02					
26R-3, 65–65	324.19		2.56		2.56		
26R-4, 72–72	325.44		2.24		2.16		
26R-5, 75–75	326.97		2.17		1.97		
26R-6, 55–55	328.18		2.60		2.58		
26R-7, 102–102	330.15		2.41		2.39		
27R-1, 68–68	330.98		2.53		2.54		
27R-2, 60–60	332.09		2.86		2.73		
27R-3, 65–65	333.39		2.09		2.04		
27R-4, 24–47	334.46	1.06					
27R-4, 66–66	334.88		2.43		2.40		
27R-5, 61–61	336.17		2.10		2.02		
27R-6, 73–73	337.80		2.52		2.51		
27R-7, 81–81	339.32		2.20		2.18		
28R-1, 73–73	340.63		2.16		2.02		
28R-2, 72–72	342.03		2.11		2.04		
28R-3, 51–51	343.21		2.32		2.29		
28R-4, 62–62	344.62		2.50		2.41		
28R-4, 88–102	344.88	1.08					
28R-5, 78–78	346.20		2.54		2.50		
28R-6, 78–78	347.70		2.14		2.13		
29R-1, 88–88	350.38		2.16		2.13		
29R-2, 81–81	351.40		2.11		2.03		
29R-3, 74–74	352.73		2.17		2.10		
29R-3, 103–118	353.02	1.03					
29R-4, 73–73	354.00		1.99		1.90		
29R-5, 73–73	355.47		2.38		2.35		
30R-1, 75–75	359.85		2.55		2.49		
30R-2, 70–70	361.30		2.54		2.46		
30R-3, 1–25	362.11	1.13					
30R-3, 58–58	362.68		2.65		2.54		
30R-4, 58–58	364.18		2.57		2.51		
30R-5, 73–73	365.83		1.96		1.90		
30R-6, 22–22	366.82		2.36		2.27		
30R-7, 43–43	368.53		2.47		2.42		
31R-1, 75–75	369.45		2.48		2.46		
31R-2, 61–61	370.81		2.29		2.28		
31R-3, 78–78	372.48		2.43		2.49		
31R-3, 114–124	372.84	1.09					
31R-4, 77–77	373.87		2.45		2.25		
31R-5, 53–53	375.14		2.47		2.25		
31R-6, 69–69	376.79		2.30		2.18		
31R-7, 37–37	377.88		2.65		2.63		
32R-1, 75–75	379.05		2.67		2.38		
32R-2, 78–78	380.58		2.39		2.29		
32R-3, 13–30	381.39	1.00					
32R-3, 66–66	381.92		2.34		2.32		
32R-4, 71–71	383.37		3.11				
32R-5, 76–76	384.72		2.07		2.07		
32R-6, 73–73	386.03		2.92		2.61		
32R-7, 60–60	387.06		2.44		2.49		
33R-1, 74–74	388.64		2.26		2.23		
33R-2, 65–65	390.02		2.44		2.44		
33R-3, 7–28	390.86	1.05					
33R-3, 54–54	391.33		2.31		2.27		
33R-4, 73–73	392.81		2.26		2.06		
33R-5, 84–84	394.39		2.13		2.03		
33R-6, 71–71	395.76		2.08		2.08		
33R-7, 75–75	396.72		2.23		2.16		
34R-1, 72–72	398.22		2.50		2.34		
34R-2, 77–77	399.55		2.48		2.41		
34R-3, 10–24	400.21	1.03					
34R-3, 62–62	400.73		2.12		2.07		

Table T12 (continued).

Core, section, interval (cm)	Depth (mbsf)	Thermal conductivity (W/[m·K])	Velocity (km/s)			Maximum shear strength (kPa)	Formation factor
			x	y	z		
34R-4, 73–73	402.25		2.44		2.36		
34R-5, 74–74	403.77		2.11		2.00		
34R-6, 81–81	405.21		2.16		2.11		
35R-1, 92–92	408.02		2.75		2.36		
35R-2, 34–34	408.84		2.26		2.15		
35R-3, 71–71	410.29		2.39		2.22		
35R-4, 69–69	411.46		2.45		2.29		
35R-4, 90–115	411.67	1.08					
35R-5, 81–81	412.73		2.61		2.46		
35R-6, 81–81	414.03		2.47		2.31		
35R-7, 52–52	414.77		2.57		2.60		
36R-1, 104–104	417.74		2.60		2.59		
36R-2, 71–71	418.69		2.57		2.48		
36R-3, 40–58	419.77	0.97					
36R-3, 87–87	420.24		3.01		3.14		
36R-4, 73–73	421.46		2.67		2.69		
36R-5, 88–88	423.09		2.85		2.81		
36R-6, 74–74	424.45		2.76		2.75		
36R-7, 71–71	425.91		3.02		2.57		
37R-1, 75–75	427.15		2.78		2.72		
37R-2, 70–70	428.51		2.87		2.87		
37R-3, 51–71	429.58	0.97					
37R-3, 71–71	429.78		2.51		2.40		
37R-4, 22–22	430.48		2.57		2.44		
37R-5, 103–103	432.79		2.75		2.73		
37R-6, 95–95	434.21		2.92		2.90		
37R-7, 65–65	435.41		2.70		2.70		
38R-1, 71–71	436.71		2.56		2.53		
38R-2, 134–134	438.61		2.54		2.34		
38R-3, 59–83	439.27	1.02					
38R-3, 71–71	439.39		2.55		2.49		
38R-4, 70–70	440.71		2.67		2.44		
38R-5, 72–72	442.00		2.67		2.59		
38R-6, 120–120	443.98		2.92		2.97		
38R-7, 73–73	445.01		2.43		2.32		
39R-1, 76–76	446.46		2.45		2.37		
39R-2, 65–65	447.69		2.76		2.70		
39R-3, 29–51	448.73	1.07					
39R-3, 71–71	449.15		2.61		2.53		
39R-4, 76–76	450.42		2.19		2.14		
39R-5, 67–67	451.77		2.51		2.50		
39R-6, 79–79	453.19		2.41		2.34		
39R-7, 73–73	454.40		2.44		2.40		
40R-1, 77–77	456.07		2.79		2.80		
40R-2, 73–73	457.49		2.25		2.23		
40R-3, 42–56	458.54	0.97					
40R-3, 77–77	458.89		2.49		2.42		
40R-4, 68–68	460.29		2.57		2.56		
40R-5, 74–74	461.86		2.39		2.33		
40R-6, 68–68	462.94		2.45		2.40		
40R-7, 82–82	464.47		2.52		2.40		
41R-1, 76–76	465.66		2.52		2.45		
41R-2, 70–70	467.09		2.32		2.13		
41R-3, 75–100	468.43	1.10					
41R-3, 79–79	468.47		2.84		2.73		
41R-4, 73–73	469.86		2.37		2.21		
41R-5, 73–73	471.36		2.74		2.68		
42R-1, 113–113	475.63		2.37		2.24		
42R-2, 91–91	476.91		2.39		2.33		
42R-3, 1–10	477.51	1.09					
42R-3, 67–67	478.17		2.48		2.28		
42R-4, 50–50	479.50		2.44		2.34		
42R-5, 93–93	481.43		2.42		2.26		
42R-6, 74–74	482.66		2.46		2.17		
42R-7, 45–45	483.87		2.55		2.23		
43R-1, 90–90	485.00		2.45		2.30		
43R-2, 73–73	486.22		2.26		2.07		
43R-3, 39–60	487.32	1.08					

Table T12 (continued).

Core, section, interval (cm)	Depth (mbsf)	Thermal conductivity (W/[m·K])	Velocity (km/s)			Maximum shear strength (kPa)	Formation factor
			x	y	z		
43R-3, 70–70	487.63		2.44		2.16		
43R-4, 35–35	488.51		2.24		2.11		
43R-4, 75–75	488.91		2.76		2.77		
43R-5, 66–6	490.32		2.86		2.85		
44R-1, 77–77	494.47		2.53		2.36		
44R-2, 85–85	496.05		2.50		2.28		
44R-3, 17–29	496.87	1.07					
44R-3, 101–101	497.71		2.43		2.28		
44R-4, 74–74	498.94		3.12		3.14		
44R-5, 83–83	500.53		2.44		2.31		
44R-6, 73–73	501.93		3.08		2.50		
44R-7, 49–49	503.19		2.47		2.28		
45R-1, 72–72	504.02		2.81		2.67		
45R-2, 79–79	505.59		2.66		2.60		
45R-3, 21–48	506.51	1.12					
45R-3, 49–49	506.79		2.77		2.71		
45R-4, 120–120	508.56		2.19		1.89		
45R-CC, 17–17	510.18		4.93				
46R-1, 90–90	513.80		4.92		4.85		
46R-2, 75–75	515.15		4.31	4.31	4.26		
46R-3, 20–36	516.00	1.41					
46R-3, 101–101	516.81		4.49	4.61	4.64		
46R-4, 84–84	518.10			4.60	4.45		
46R-5, 74–74	519.50		4.45	4.50	4.69		
47R-1, 72–72	522.82		4.48	4.43	4.32		
47R-2, 52–52	524.12		4.80	4.93	4.96		
47R-2, 91–102	524.51	1.52					
47R-3, 74–74	525.82		5.31	5.55	5.57		
48R-1, 34–34	532.04		5.41	5.13			
48R-2, 67–67	533.11		5.25	5.36	5.38		
48R-3, 0–16	533.94	1.47					
48R-3, 73–73	534.67		5.21	5.12	5.06		
49R-1, 76–76	542.06		5.20	5.32	5.39		
49R-2, 63–63	543.43		5.01	5.32	5.39		
49R-2, 88–103	543.68	1.66					
49R-3, 32–32	544.62		5.16	4.96	5.05		
51R-1, 35–35	554.35		5.21	5.24	5.15		
52R-1, 100–100	561.70		4.87	5.29	5.37		
54R-1, 83–83	580.33		4.83		4.99		
54R-2, 70–70	581.38		4.95	4.72	4.77		
54R-2, 95–111	581.63	1.74					
55R-1, 124–139	589.34	1.66					

Table T13. Logging operations summary, Hole 1201D.

	Run 1 triple combo (main)	Run 2 FMS-sonic-NGT (passes 1 and 2)	Comments
Water depth, seafloor, or mud line:			Logging operations commenced at 1115 hr on 12 Apr 2001. Wiper trip, hole displaced, 150 bbl of sepiolite was used; no KCl. Sea state/heave: average = 0.4 m; max = 0.92 m.
Mud line (mbrf; driller's depth)	5720	5720	Run into hole (RIH) speed = 4000–5000 ft/hr
Mud line (mbrf; logger's depth)	5723	5723	Triple combo uphole speed = 900 and 1800 ft/hr in sticky intervals (417–467 mbsf). FMS-sonic-NGT uphole speed, both passes = 900 ft/hr. Logging operations ceased at 1330 hr on 13 Apr 2001.
Drill pipe depth during logging:			
Pipe depth (mbrf; driller's depth)	5800	5800	
Pipe depth (mbsf; using driller's depth)	80	80	Initial pipe depth was set at 80 mbsf, and pipe remained at that depth throughout logging operations to prevent borehole collapse in the soft upper sediments.
Pipe depth (mbrf; depth from logs)	5799.5	5799.5	
Pipe depth (mbsf; using logger's depth)	76.5	76.5	
Sticking encountered during logging:			No ledges or bridges were encountered on the first RIH with the triple combo tool string, but sticky intervals that were slow to get through were encountered at 5830 and between 6140 and 6190 mbrf. The FMS-sonic-NGT runs were hampered by these same sticky intervals and only reached 6075–6090 mbrf, so the basement interval could not be logged.
Depth of first sticky interval (mbrf; winch)	5830	5830	
Depth of first sticky interval (mbsf)	107	107	
Depth of second sticky interval (mbrf; winch)	6140–6190	6075–6090	
Depth of second sticky interval (mbsf)	417–467	352–367	
Final tool depth:			Hole conditions were good, with the caliper reading on gauge in the basement section up to 6235 mbrf. In the sediments, hole size varied from 18 in to below bit size in the tight spot at 6140 mbrf.
Final tool depth (mbrf; winch)	6314	6089	
Final tool depth (mbsf; using logger's depth)	591	366	
Total hole depth (m):	600	600	Log data are generally good, although some problems were encountered as a result of a default speed correction applied by the acquisition software. See **"Data Quality,"** p. 41, in "Downhole Measurements" for further explanation.
Length of logging run (m):	514.5	289.5	

Note: Triple combo = triple combination tool string, FMS = Formation MicroScanner, NGT = natural gamma spectrometry tool.

Table T14. Logging data quality summary, Hole 1201D.

Tool string*:	HNGS (spectral gamma ray)	APS (porosity)	HLDT (bulk density)	DLL (resistivity)
First uplog				
First reading (mbsf):	560 (6283 mbrf)	566.5 (6289.5 mbrf)	572 (6295 mbrf)	570 (6293 mbrf)
Stop depth (mbsf):	396.5 (6119.5 mbrf)	413 (6136 mbrf)	396.5 (6119.5 mbrf)	408 (6131 mbrf)
	14.5-m data gap between uplogs	25.5-m data gap between uplogs	Splice of two main uplogs: no gap	Splice of second uplog curves: no gap
Second uplog				
Restart depth (mbsf):	382 (6015 mbrf)	387.5 (6110.5 mbsf)	396.5 (6119.5 mbrf)	408 (6131 mbrf)
Last reading (mbsf):	Seafloor (5723 mbrf)	Seafloor (5723 mbrf)	Seafloor (5723 mbrf)	93: repeat spliced in at 127 mbsf
Repeat				
First reading (mbsf):	150 (5873 mbrf)	155 (5878 mbrf)	166 (5889 mbrf)	172 (5895 mbrf)
Last reading (mbsf):	93 (5816 mbrf)	109 (5832 mbrf)	100 (5823 mbrf)	93 (5816 mbrf)
Comments:	Gamma ray values in lower portion of second uplog may be slightly elevated, due to prior activation of the formation by the neutron source.	Spike at 342 mbsf (6065 mbrf) may not be a real feature.	Density logs are unreliable between 451 and 444 mbsf (6174–6167 mbrf) due to unstable long-spacing voltage, but short-spacing curve is OK.	Spike at 413 mbsf (6136 mbrf) caused by downlog splice between 417 and 412 mbsf. The spike at 297 mbsf is not a real feature. Current to the DLL was lost at the top of the second uplog.

Note: * = All tool names are trademarks of Schlumberger. HNGS = hostile environment natural gamma ray sonde, APS = accelerator porosity sonde, HLDT = high-temperature lithodensity logging tool, DLL = dual laterolog.

Table T15. Glossary of NEREID-195 system terms.

Term	Definition
BIA	Borehole instrument assembly, commonly known as the Christmas tree.
CRM	Combiner/repeater module. This is part of the multiple-access expandable gateway (MEG-195).
DM24	Digitizer module consisting of a 24-bit analog-to-digital converter and microprocessor.
GCF	Guralp compressed format, used for data transmission and receiving on an RS-232C serial line.
GPS	Global positioning system.
LBS	Lithium battery system. Large-capacity lithium cells are housed in 65-cm titanium spheres.
LBU	Lithium battery unit. An LBS consists of two LBUs.
MEG-195	Multiple-access expandable gateway, commonly known as the G-Box. It serves as the control unit for power, signal, and timing.
OBH	Ocean borehole seismometer. Modified version of the feedback-type broadband seismometer (Type CMG-1T) made by Guralp Ltd., United Kingdom.
PAT	Power supply access terminal, commonly called the battery frame. It contains the titanium sphere lithium battery system and storage acquisition module (SAM-195) and also serves as a remotely operated vehicle or submersible platform.
PDM	Power conditioning/distribution module contained in the MEG-195.
PCB	Printed circuit board.
ROV	Remotely operated vehicle.
RTM	Real-time module, contained in the CRM.
SAM-195	Storage acquisition module. This is a seismic data recorder that can be recovered by an ROV or submersible.
UMC	Underwater mateable connector, produced by Ocean Design Inc., USA.

Table T16. Sensor sensitivity of Guralp seismometer.

Component	Stream identifier	Sensitivity	Unit
OBH T1023:			
Velocity channels (24-bit resolution):			
Vertical	D003Z6	2.015424E+09	Counts/m/s
North-south	D003N6	2.070694E+09	Counts/m/s
East-west	D003E6	2.044987E+09	Counts/m/s
Acceleration channels (16-bit resolution):			
Vertical	D003M8	1.198741E+07	Counts/m/s^2
North-south	D003M9	1.229458E+07	Counts/m/s^2
East-west	D003MA	1.250960E+07	Counts/m/s^2
Temperature:	D003ME	77.700078	Counts/K
OBH T1038:			
Velocity channels (24-bit resolution):			
Vertical	D417Z6	2.032134E+09	Counts/m/s
North-south	D417N6	2.052699E+09	Counts/m/s
East-west	D417E6	2.038560E+09	Counts/m/s
Acceleration channels (16-bit resolution):			
Vertical	D417M8	1.219381E+07	Counts/m/s^2
North-south	D417M9	1.297704E+07	Counts/m/s^2
East-west	D417MA	1.290025E+07	Counts/m/s^2
Temperature:	D417ME	77.700078	Counts/K

Note: velocity (V) for a digital sample (x) is given as (in terms of Laplace variable [s])

$$V(s) = [G \times A \times H(s)]\, x,$$

where

G = velocity output sensitivity as listed above.
A = normalizing factor to make the magnitude of $A \times H(s)$ unity. For the Leg 195 OBHs, A = –45.63 at 1Hz.
H(s) = the transfer function in factored form.

$$H(s) = \frac{\Pi(s - z_n)}{\Pi(s - p_n)}$$

z_n are the roots of the numerator polynomial, giving the zeroes of the transfer function, and p_n are the roots of the denominator polynomial giving the poles of the transfer function. The poles and zeroes for the CMG1Ts for all the velocity channels are as follows:

Poles (Hz)	Zeroes (Hz)
–1.964E–03 ± 1.964E–03 j	0
–80 ± 30 j	0
	160

Table T17. Mapping between sensor channels and stream identifier in Guralp compressed format.

Sensor channels	Stream identifier
Upper seismometer CMG1T T1023:	
Vertical (20 Hz)	d003z4
Vertical (100 Hz)	d003z2
Horizontal north-south (20 Hz)	d003n4
Horizontal north-south (100 Hz)	d003n2
Horizontal east-west (20 Hz)	d003e4
Horizontal east-west (100 Hz)	d003e2
Vertical mass position	d003m8
Horizontal north-south mass position	d003m9
Horizontal east-west mass position	d003ma
Temperature	d003me
Status message (clock offset/drift)	d00300
Lower seismometer CMG1T T1038:	
Vertical (20 Hz)	d417z4
Vertical (100 Hz)	d417z2
Horizontal north-south (20 Hz)	d417n4
Horizontal north-south (100 Hz)	d417n2
Horizontal east-west (20 Hz)	d417e4
Horizontal east-west (100 Hz)	d417e2
Vertical mass position	d417m8
Horizontal north-south mass position	d417m9
Horizontal east-west mass position	d417ma
Temperature	d417me
Status message (clock offset/drift)	d41700
MEG-195 status message	gbox00
SAM-195 status message	sam100

Notes: MEG = multiple-access expandable gateway, SAM = storage acquisition module. All of the records in the SAM are labeled with the SAM system identifier "LEG195." System identifiers are used for communication with the ocean borehole seismometer units (OBHT1038 = T1038; OBHT1023 = T1023) and the MEG-195 (LEG195).

Table T18. Explanation of status messages from the CRM in the MEG/SAM.

Readout	Explanation
Internal clock 18,000 microseconds slow	CRM internal clock is offset over its reference. In the example, the CRM internal clock is 18,000 µs behind the reference. The figure is for the last minute.
2001 Apr 17 06:06:00 o/s=1112521 drift= 21	Date/time (year month day hour:min:second), the internal clock offset (o/s) in a unit of 25/1536 (= 1000/1024/60) µs in a fraction of a second and the clock drift over a minute in the same unit as the offset.
Power 99Asecs 13.669Asecs 227mA 5.35W	MEG and OBH power consumption, including ampere seconds since the system was started, ampere seconds, average current, and power consumed in the last minute.
Temperature 23.06°C	Temperature in the MEG canister measured on the PDM board.
MIN MAX AVG STATUS #Blks #Naks Pkt# Space	The next three lines summarize the status of OBH power and the data link. The first single-digit number in each line indicates the PDM channel that corresponds to the measurement. Channel 0 is dedicated to SWB voltage measurement. Channels 1 and 2 are dedicated to the OBHs. Channels 3, 4, and 5 are available for connection to internal DM24s (not set in this example).
0 23.57V 23.59V 23.57V SWB >GOOD 50 0 46 511	LBU voltages (PDM channel 0) in the last minute, in order of minimum, maximum, and average, respectively. Comparison of these results with thresholds is given as follows: "high" = exceeding the higher threshold, "good" = between the two thresholds, and "low!" = below the lower threshold. The next four readings indicate the number of GCF blocks sent in the last minute, the number of error blocks (NAKs) in the transmission, the last GCF block sequence number, and the available space in the CRM buffer, respectively.
1 111.0mA 124.2mA 119.7mA ON ok 29 0	One-line summary of supply current and data link status for the first OBH sensor. A one-word diagnosis is given with each measurement similar to the LBU voltage measurement example in channel 0: "ok" = between high (160 mA) and low (40 mA) current thresholds, "low" = below the lower threshold, and "leak?" = higher than the upper threshold.
2 133.8mA 142.3mA 138.6mA ON ok 21 0	
The SAM status message includes the current measurements of PDM channel 1 (logic supply for the disks), channel 6 (5-V supply for disks), and channel 7 (12-V supply for disks [not in use during Leg 195]). A status message from the CRM in the SAM includes an additional 100-byte string as follows:	
Writing 5|1306 : Reading 3|4032 Bad Flash 0 0	This line indicates the status of buffer memory: the number of chip and block currently writing and reading and the number of error in writing and reading, respectively.

Notes: CRM = combiner/repeater module, MEG = multiple-access expandable gateway, SAM = storage acquisition module, OBH = ocean borehole seismometer, PDM = power distribution module, SWB = seawater battery, DM24 = digitizer module, LBU = lithium battery unit. GCF = Guralp compressed format.

Table T19. Available command set in the CRM, OBH, and SAM. (See table notes. Continued on next page.)

Command	Definition
CRM available command set:	
h8upload	Initiate uploading a firmware via serial link
ok-1	Enable FORTH vocabulary
set-id	
.ids	Show what instrument(s) are currently being talked to
streams?	List all streams and port numbers being received in format: StreamID SystemID Port#
port# (open)	Open pass-thru to the specified serial port
open sysID strID	Open other system terminal by pass-thru
(head 4 characters)	
close	Close the pass-thru terminal link
.boot	Display last reboot
run-hours?	Show time since last boot
running?	Show running status
.bauds	List baud-rate settings for each serial port
port# baud# baud	Change baud rate (to set the port to 115,200 bps, use 1,152 instead)
255 bauds 4 + c!	Set port #3 to "unused"
!config	Save the configuration
n activate	Enable serial port #*n*
/uarts	Initialize UARTS (do not use from data port!)
port# sync-on	Enable sending StreamSync character to the specified port
port# sync-off	Disable sending StreamSync character to the specified port
2 ~protect	Disarm protection of the flash memory
save-cmos	Save CMOS memory in EEPROM
.wpr	Check the state of the write-protect register in the EEPROM
.ext	Show external clock
.int	Display internal clock
.phase	Convert the latest available o/s figure to microseconds
.pwm	Show the clock offset and drift
@rtc .rtc	Fetch real-time clock setting and print
–1 ref-clk 2+ + !	Decrement internal clock by 1 s
ref-clk +time	Increment internal clock by 1 s
8 watch + !	Switch on monitoring StreamSync clock
–8 watch + !	Switch off monitoring StreamSync clock
time-ref ?	Restart synchronization
re-sync on	Enable resync to reference (resync requires 15 min of mismatch)
auto-trim on	Allow trimming of real-time module to reference time
interval on	Disable auto-calibration
bad-match ?	Display how many more consistent clock measurements are necessary to resynchronize
n gps-type	Set clock synchronization source (n; 2-GARMIN, 3-StreamSync)
sync-src ?	See settings by GPS-type commands
time set-rtc	Set real-time clock for time stamp in format: *yy mm dd hh mm ss*
set-clock	Set backup real-time clock (PCF8583)
rtc>sam	Set real-time clock (PCF8583) into internal clock (MEG, SAM)
: ?t cr begin 13 emit .int 30 30ms key? until;	Program to check the internal clock ticking
master-sync	Set internal clock (and backup real-time clock) to the RTM time (reboot does the same thing)
2400 /sci2	Set baud rate of the GPS serial port to 2400 bps for accessing the RTM
rtm-open	Enable access to the RTM module
+1ppm	Change the frequency of the RTM (precision clock)
–1ppm	Change the frequency of the RTM (precision clock)
cancel	Restore the RTM module to normal state using the calculated trim value
: slower 2400 /sci2 rtm-open 0 do -1ppm 3 30ms loop rtm-close;	Program to define "slower" and "faster" commands
: faster 2400 /sci2 rtm-open 0 do +1ppm 3 30ms loop rtm-close;	Program to define "slower" and "faster" commands
n slower	Change the RTM frequency by *n* ppm
n faster	Change the RTM frequency by *n* ppm (maximum adjustment is ~30–40 ppm)
rtm-close	Disable access to the RTM module
rtm-open 2400 /sci2 cancel rtm-close	Program to restore the RTM to normal operation
4800 /sci2	Restore baud rate for GPS connection
rtm-trim ?	Display a number for clock trim in the CMOS backup memory in the power distribution module
trim# dup -1 xor swap rtm-trim 2! rtm-trim backup!	Program to set the *trim#* to CRM CMOS register
?lithium	Report the state of both the battery comparator and the switch line
+rtm-battery	Switch the backup on and reports the status (before and after)
reminder	Set the clock into timer mode (sets a maximum off time of 10 min)
manual	Start the system in timer mode
sleep	Switch off the system using watch-dog reset
time wake-up	Set start time in format: *mm dd hh mm*
.limits	Display setting in the units shown in the status block
.mean	Show mean voltage of power supply

Table T19 (continued).

Command	Definition
.st	Status reading from power distribution module
n power-down	Switch off the channel
n power-up	Switch on the channel—if not disabled
n enable	Reenable switching on
n disable	Switch off the channel and prevent further operation; monitoring is not affected
n remove	Remove control and monitoring
n install	Adds the channel for control and monitoring
vl vh ch set-limits	Set limits of power control; vl = switch off voltage, vh = high limit, and ch = channel of PDM
o/p ?	Check the semaphore status; this should show zero (i.e., no task currently outputting to the display/status)
0 0 o/p 2!	Manually reset the semaphore when there is a problem to stop sending status messages
OBH available command set:	
.d-day	Show deploy date setting *day month year*
.soh	Request ocean borehole seismometer health status
component unlock	Unlock the component (component is of; e/w n/s z all)
component centre	Center mass
component lock	Mass lock the component
configuration show	Shows digitizer configuration
masses?	Shows mass positions continuously (type any key to stop)
mpos 2 + ?	Request mass position of N-S
mpos ?	Request mass position of Z
mpos 4 + ?	Request mass position of E-W
mpos n dump	Hex dump first n mass positions (each 2 bytes)
set-config	Set output channels of the digitizer (in a form; 0007 0700 4700)
tap0 tap1 tap2 tap3 samples/sec	Set sample rate
SAM available command set:	
.flash	Shows flash memory usage
2 /chunk	Change number of chips for buffering (2–14); maximum is 14 to allow time for disk operation
chunk ?	Check number of memory chip installed 1 chip = 4 MB
n target	Set current target HDD
target# ?	Show current target HDD
next-target	Increase SCSI ID of HDD
chk-disc	Spin up current disk and check
dir	Display directory of the HDD records
disc-on	HDD power supply up
disc-off	HDD power supply down (resulting spin down HDD)
stop-unit	Spin down, disk power remains ON
reset-disc	Initialize current disk
/flash#	Reset the pointers to 0|0
0 erase-card	Erase the whole card
0 erase-chip	Erase specified chip: 0–15, 4 MB each

Notes: Italics denote variables in the command string. GPS = Global Positioning System. MEG = multiple-access expandable gateway, SAM = storage acquisition module, RTM = Real-time module. CRM = combiner/repeater module. HDD = hard disk drive, ID = identifier. OBH = ocean borehole seismometer.

Table T20. Pin assignments of underwater mateable stab plate connectors.

OBH - MEG				
Function (OBH)	MSSK-8 #20-CCP	OCC cable	UMC pin/A, B	MEG Dsub9 (for OBH)
Power + Vin	1	Red/in	1/A	8 (Red)
0Vin	2	Black/in	2/A	9 (Green)
0Vin	3	Blue/out	2/B	9 (Green)
Signal GND	4	Green/out	1/B	5 (Black)
Rx (+)	5	Red/out	3/B	3 (Orange)
Rx (–)	6	Yellow/out	4/B	4 (White)
Tx (+)	7	Green/in	3/A	2 (Blue)
Tx (–)	8	Blue/in	4/A	1 (Pink)

MEG - SAM - LBU						
UMC 4p female (LBU out)	UMC 4p female (to MEG)	UMC 4p female (SAM stab plate)	Function (MEG/SAM)	MEG 4p male UMC	MEG Dsub15 female	SAM Dsub15 female
1	1	1	Power in (+24 V)	1	1, 2 (Red)	7, 8 (Red)
2	1					
3	2	2	GND	2	3, 4 (Green)	5, 6 (Green)
4	2					
	3	3	RS232C-Rx (SAM—>MEG)	3	12 (Orange)	11 (Blue)
	4	4	RS232C-Tx (MEG—>SAM)	4	11 (Blue)	12 (Orange)

SAM - ROV		
Function (SAM)	SAM DATA Dsub9 female (pigtail)	UMC 4p plug (cable)
NC		1
GND	5 (Black)	2
RS232C-Tx (SAM—>ROV)	3 (Orange)	3
RS232C-Rx (ROV—>SAM)	2 (Blue)	4

Notes: OBH = ocean borehole seismometer, MEG = multiple-access expandable gateway. OCC = Ocean Cable Cooperation. UMC = underwater mateable connector. Vin = power supply input, GND = ground, Rx = receive, Tx = transmit. LBU = lithium battery unit, SAM = storage acquisition module. ROV = remotely operated vehicle. NC = no connection.

Table T21. Recording configuration and estimated amount of data for the Site 1201 seismic observatory.

Information type	Amount of data (MB/day)
Status information from SAM/MEG:	1.31 (including GCF header)
Seismic data:	
3 channels × 2 systems × (100 + 20 sps) × 2 bytes (typical) × 3600 s × 24 hr + header	121
Slow seismic data:	
4 channels (mass, position, and temperature) × 2 systems × 4 sps × 1 byte × 3600 s × 24 hr	2.68
Total:	
186 days to fill 22.8-GB (5712 MB × 3 + 6176 MB × 1) hard disk storage in the SAM-195	125

Notes: SAM = storage acquisition module, MEG = multiple-access expandable gateway. GCF = guralp compressed format. sps = samples per second.

Table T22. Power consumption of the NEREID-195 system.

Subsystem	Condition	Power consumption (W)
CRM		0.70
OBH	T1038 + short cable, mass locked, measured at PDM	3.14
	T1023 + short cable, mass locked, measured at PDM	3.07
	T1038 + 550-m cable, mass unlocked, measured at PDM (prospect)	2.87
	T1023 + 550-m cable, mass unlocked, measured at PDM (prospect)	2.56
DC/DC for OBH	No supply for OBH	0.30
SAM-195	Steady-state	1.00
	Disk writing	11.00
Total average:		
MEG + 1 × OBH(T1023) + SAM		
	22-hr cycle average for a typical amount of incoming data: (100 sps + 20 sps) × 3 channels × 2 bytes	4.58
MEG + 2 × OBH + SAM		
	11-hr cycle average for a typical amount of incoming data: (100 sps + 20 sps) × 6 channels × 2 bytes	7.78

Notes: CRM = combiner/repeater module, OBH = ocean borehole seismometer, SAM = storage acquisition module, MEG = multiple-access expandable gateway, PDM = power distribution module. DC = direct current. Power consumption is shown for a typical supply voltage of 22.4 V.